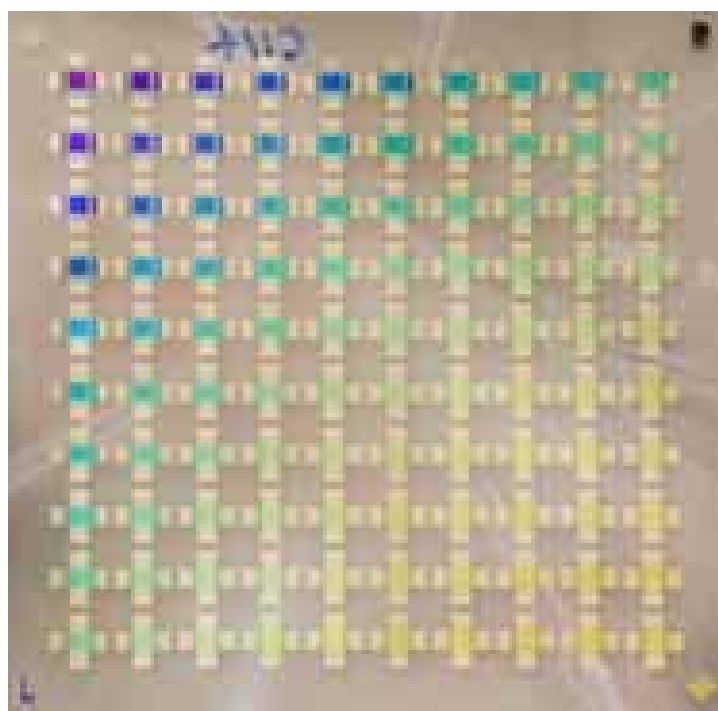


Tilman A. Beierlein

Combinatorial Methods for Organic Light-Emitting Materials and Devices



Cuvillier Verlag Göttingen

Combinatorial Methods for Organic Light–Emitting Materials and Devices

A dissertation submitted to the
University of Bayreuth

for the degree of

Doktor der Naturwissenschaften (Dr. rer. nat.)

by

Dipl.-Ing.

Tilman Artur Beierlein

from Bad Saulgau

Prof. Dr. Markus Schwoerer, examiner

Prof. Dr. Hans-Werner Schmidt, co–examiner

2003

Bibliografische Information Der Deutschen Bibliothek

Die Deutsche Bibliothek verzeichnet diese Publikation in der Deutschen Nationalbibliografie; detaillierte bibliografische Daten sind im Internet über <http://dnb.ddb.de> abrufbar.

1. Aufl. - Göttingen : Cuvillier, 2003
Zugl.: Bayreuth, Univ., Diss., 2003
ISBN 3-89873-834-5

Von der Fakultät für Mathematik und Physik
der Universität Bayreuth
als Dissertation am 9. April 2003 angenommen.

Erstgutachter: Prof. Dr. Markus Schwoerer
Zweitgutachter: Prof. Dr. Hans-Werner Schmidt
Tag der mündlichen Prüfung: 23. Juli 2003

© CUVILLIER VERLAG, Göttingen 2002
Nonnenstieg 8, 37075 Göttingen
Telefon: 0551-54724-0
Telefax: 0551-54724-21
www.cuvillier.de

Alle Rechte vorbehalten. Ohne ausdrückliche Genehmigung
des Verlages ist es nicht gestattet, das Buch oder Teile
daraus auf fotomechanischem Weg (Fotokopie, Mikrokopie)
zu vervielfältigen.

1. Auflage, 2003
Gedruckt auf säurefreiem Papier

ISBN 3-89873-834-5

Δεα γραθιας!

meiner lieben Sandra...

Contents

| | |
|--|----------|
| Zusammenfassung | v |
| 1 Introduction and Motivation | 1 |
| 1.1 Introduction | 1 |
| 1.2 Motivation | 4 |
| 2 Basics of Organic Electroluminescence | 7 |
| 2.1 Organic Semiconducting Materials | 7 |
| 2.2 Device Operation | 8 |
| 2.2.1 Basic Device Structure | 8 |
| 2.2.2 Charge Carrier Injection from Contacts | 9 |
| 2.2.3 Charge Carrier Transport | 12 |
| 2.2.4 Charge Carrier Recombination | 15 |
| 2.3 Excited States in Organic Materials | 16 |
| 2.3.1 Energy Transfer | 18 |
| 2.3.2 Exciton Diffusion | 19 |
| 2.3.3 Exciton Decay | 20 |
| 2.4 Optical Effects in OLEDs | 22 |
| 2.5 Efficiency and Color | 24 |
| 2.5.1 Photometric Efficiency | 24 |
| 2.5.2 Color | 24 |
| 2.6 Challenges for OLEDs | 26 |

| | | |
|----------|--|-----------|
| 3 | The Combinatorial System: Device Fabrication and Characterization | 29 |
| 3.1 | Motivation | 29 |
| 3.2 | Evaporation System “Columbus HPO” | 31 |
| 3.2.1 | Base chamber | 33 |
| 3.2.2 | Recipient | 36 |
| 3.2.3 | Load Locks and Storage Chamber | 36 |
| 3.2.4 | Glovebox | 39 |
| 3.3 | Combinatorial Device Configurations | 39 |
| 3.3.1 | Thickness-Dependent Device Series | 39 |
| 3.3.2 | Position-Dependent Device Series | 41 |
| 3.3.3 | Combinatorial Matrix | 41 |
| 3.3.4 | Further Sample Configurations | 42 |
| 3.4 | Device Fabrication | 45 |
| 3.4.1 | Substrates and Fabrication | 45 |
| 3.4.2 | Organic Materials | 46 |
| 3.5 | Device Characterization | 49 |
| 3.5.1 | Automated Measurement Setup | 49 |
| 3.5.2 | I - V / L - V Characteristics | 49 |
| 3.5.3 | EL and PL Spectra | 52 |
| 3.5.4 | Transmission and Reflection Measurements | 55 |
| 3.5.5 | Other Characterization Methods | 57 |
| 3.6 | Data Representation | 58 |
| 4 | Organic Multilayer Structures | 61 |
| 4.1 | Three-Layer OLEDs Based on Alq ₃ as Emitter Material | 61 |
| 4.1.1 | Thickness Variation and Optimization of NPB/Alq ₃ | 62 |
| 4.1.2 | Devices with Constant Thickness | 70 |
| 4.1.3 | Summary: Three-Layer OLEDs Based on Alq ₃ as Emitter Material | 74 |
| 4.2 | Potential Sensing | 76 |

| | | |
|----------|--|------------|
| 4.2.1 | Measurement Techniques | 76 |
| 4.2.2 | Direct Potential Sensing | 77 |
| 4.2.3 | Summary: Potential Sensing | 85 |
| 4.3 | Complex Multilayer Structures | 87 |
| 4.3.1 | Doped OLEDs: Width of Doped Region | 87 |
| 4.3.2 | Double-Doped OLEDs | 94 |
| 4.3.3 | OLEDs Based on Phosphorescence | 98 |
| 4.3.4 | Summary: Complex Multilayer Structures | 111 |
| 5 | Optical Interference Effects | 113 |
| 5.1 | Variation of Organic Layer Thickness | 114 |
| 5.1.1 | Spectral Changes in Alq ₃ -Emitting OLEDs | 115 |
| 5.1.2 | Optimization of Red OLEDs | 120 |
| 5.1.3 | Summary: Variation of Organic Layer Thicknesses | 125 |
| 5.2 | Anode: Influence on Spectral Emission and Device Performance | 126 |
| 5.2.1 | Highly Reflecting Anodes | 126 |
| 5.2.2 | Black Anode Structure | 136 |
| 5.2.3 | OLEDs on Black Anode Structure | 139 |
| 5.2.4 | Summary: Anode | 146 |
| 5.3 | Cathode: Influence on Spectral Emission and Device Performance | 147 |
| 5.3.1 | Semi-Transparent Metal Cathodes | 147 |
| 5.3.2 | Dielectric Capping Layer | 154 |
| 5.3.3 | Summary: Cathode | 156 |
| 6 | Diffusion of Excitons and Quenching at Interfaces | 157 |
| 6.1 | Quenching of Excitons | 157 |
| 6.1.1 | PL Quenching of Alq ₃ on Glass, ITO and Al | 158 |
| 6.1.2 | Description of PL Intensity using Lambert–Beer’s Law | 162 |
| 6.1.3 | Exciton Diffusion Model with Quenching at Surfaces | 168 |

| | | |
|----------|--|------------|
| 6.1.4 | Summary: Diffusion of Excitons and Quenching at Interfaces | 178 |
| 6.2 | Delta-Doped Devices | 179 |
| 6.2.1 | Exciton Sensing in Alq ₃ :DCJTB System | 180 |
| 6.2.2 | Summary: Delta Doped Devices | 188 |
| 7 | Summary | 189 |
| | Appendix | 195 |
| | References | 198 |

Zusammenfassung

Ein Ziel dieser Arbeit war die Schaffung der experimentellen Voraussetzungen, um technologische und wissenschaftliche Fragestellungen aus dem Gebiet organischer Leuchtdioden (OLEDs) mittels systematischer Experimentreihen zu erforschen. Dazu bedurfte es der Konzeption und des Aufbaus einer neuartigen Ultrahochvakuum (UHV) Aufdampfanlage für kombinatorische Probenherstellung, sowie eines umfassenden Charakterisierungssystems, wobei die Vielseitigkeit und Flexibilität beider Systeme von höchster Priorität war.

Mit Hilfe dieser neuen Systeme wurden auf kleinen Molekülen basierende OLEDs untersucht. OLEDs bestehen typischerweise aus drei Schichten, wobei Strukturen mit bis zu sechs Schichten und komplexere Systeme in der Regel zu höheren Effizienzen führen. Da es sich bei OLEDs um Dünnschichtbauelemente mit Gesamtschichtdicken von etwa 100 nm handelt, hängen sowohl elektrische als auch optische Eigenschaften in großem Maß von der Dicke der einzelnen Schichten ab. Folglich ist die Schichtdicke ein kritischer Parameter, welcher mit großer Präzision kontrolliert und reproduzierbar eingestellt werden muss. Die systematische Variation der Schichtdicke und ihr Einfluss auf die elektrischen und optischen Kenndaten können daher zur Untersuchung verschiedenster physikalischer Prozesse und Effekte eingesetzt werden. Mit Hilfe des neuen Aufdampfsystems können nun zuverlässige Schichtdicken- und Elektrodenvariationen mit einer bislang nicht gekannten reproduzierbaren Ausführlichkeit und Komplexität durchgeführt werden — und dies mit einer Leichtigkeit, wie sie allenfalls in Simulationen denkbar ist.

Die im Rahmen dieser Arbeit neu aufgebaute UHV-Aufdampfanlage erreicht einen Basisdruck von $<10^{-8}$ mbar. Sie besitzt 12 unabhängige, temperaturgeregelterte Effusionszellen, wobei aus bis zu vier Zellen gleichzeitig verdampft werden kann. Dank einer Vakuumschleuse sind kurze Ladezeiten für beliebige Substrate und Schattenmasken bis zu einer Maximalgröße von 80×80 mm² möglich. Eine weitere Ladekammer erlaubt das Nachfüllen und Austauschen

von Verdampfungsmaterialien ohne Fluten der Hauptkammer mit Umgebungsluft. Die neue Anlage erforderte ein neues Konzept für Effusionszellen, welche nun nicht nur als gesamte Einheit ein- und ausgebaut, sondern auch im Vakuum verschoben werden können, so dass sie während des Aufdampfens unter dem Substrat zentriert sind. Dadurch werden ausgezeichnete Uniformitäten in der Schichtdicke ($\pm 3\%$) im aktiven Bereich ($66 \times 66 \text{ mm}^2$) des Substrates erzielt. Das Herzstück der Anlage ist ein drehbarer Proben- und Maskenhalter im Rezipienten, welcher mittels einer von außen präzise steuerbaren Blende die Herstellung gestufter Schichten auf dem Substrat erlaubt. Des Weiteren können Substrat, Schattenmaske und die bewegliche Blende in 90° -Schritten relativ zueinander rotiert werden, so dass z.B. durch zwei orthogonale treppenartige Schichten eine sogenannte kombinatorische Matrix gebildet werden kann. In dieser sind 10×10 unterschiedliche Schichtdickenkombinationen zweier Materialien realisiert. In einem Aufdampfvorgang können auf einem Substrat 100 verschiedene Proben hergestellt werden. Zur Charakterisierung werden die Substrate anschliessend direkt in eine Handschuhbox transferiert, wo sie unter Inertgas (Argon , $\text{O}_2 < 1 \text{ ppm}$, $\text{H}_2\text{O} < 1 \text{ ppm}$) mit verschiedenen Methoden untersucht werden. Die rechnergesteuerte, automatisierte Charakterisierungseinheit erlaubt routinemäßige Messungen von Strom-Spannungs- und Helligkeit-Spannungs-Kennlinien ($I-V$ bzw. $L-V$) sowie der Photolumineszenz (PL), Transmission und Reflexion. Darüber hinaus können noch Messung von Photoströmen, transientser Elektrolumineszenz (EL) und Impedanzspektroskopie ($Z(\omega)$, $C-V$) durchgeführt werden. Der Aufbau wurde so flexibel gestaltet, dass grundsätzlich alle Arten von Messungen möglich sind, bei denen einerseits elektrisch oder optisch angeregt und andererseits elektrisch oder optisch detektiert wird. Neben dem sorgfältigen Erfassen der Messdaten ist die übersichtliche Darstellung der Rohdaten ein weiterer wichtiger Aspekt. Dafür wurden entsprechende Programme und Skripte erstellt, um die anfallende große Datenmenge zu verarbeiten, sowie abgeleitete Größen berechnen, extrahieren und darstellen zu können.

Ein solches kombinatorisches System in Verbindung mit derart vielseitigen Charakterisierungsmöglichkeiten hat in dieser Flexibilität bislang nicht existiert. Es ist zu erwarten, dass kommerzielle Anlagenhersteller in absehbarer Zeit mit ähnlichen Systemen nachziehen.

Eine weitere Zielsetzung dieser Arbeit war, anhand ausgewählter Beispiele die Leistungsfähigkeit kombinatorischer Methoden zur Herstellung von Schichtstrukturen und Bauelementen aufzuzeigen.

Als Modellstruktur dient anfangs eine aus drei Schichten bestehende OLED- Struktur, welche

bereits 1989 von Tang et al. vorgeschlagen wurde: CuPc¹, NPB² und Alq₃³. Dieses System wurde ausgewählt, weil zu dieser Struktur in der Literatur die größte Anzahl Daten vorhanden ist. Mit der Herstellung einer “kombinatorischen Matrix” kann in einem einzigen Aufdampfvorgang das effizienteste Bauelement bei Variation zweier Materialschichtdicken bestimmt werden. Mittels zwei-dimensionaler (2D) Effizienzplots ist sofort auch die Breite des Bereichs maximaler Effizienz ersichtlich, was beispielsweise in der Technologie als Prozessfenster von Bedeutung ist. Für das Verständnis der Funktionsweise des Bauelements erlaubt die Darstellung der Betriebsspannung bei einem gegebenem Strom als 2D-Plot Rückschlüsse auf die interne Spannungsverteilung im Bauelement. Hier wird mit dieser Struktur eindrücklich gezeigt, dass in ihr bei niedrigen Stromdichten ($<1 \mu\text{A}/\text{cm}^2$) die Betriebsspannung nahezu unabhängig von der Alq₃-Schichtdicke ist. Die Potentialverteilung ändert sich jedoch mit höheren Stromdichten ($20 \text{ mA}/\text{cm}^2$) derart, dass der Spannungsabfall über der Alq₃-Schicht vergleichbar mit demjenigen über NPB wird. Da die Löcherbeweglichkeit von NPB ($\mu_h = 10^{-3} \text{ cm}^2/\text{Vs}$) wesentlich höher als die Elektronenbeweglichkeit in Alq₃ ($\mu_e = 10^{-5} \text{ cm}^2/\text{Vs}$) ist, zeigt dies, dass die Injektion über die internen organischen Energiebarrieren, insbesondere über die CuPc/NPB-Grenzfläche, den Stromfluss und das interne Feld regulieren. Die internen Barrieren und die Feldverteilung dominieren somit maßgeblich die I - V -Kennlinie der OLEDs. Der Einfluss des Transports wird erst bei höheren Stromdichten ($>100 \text{ mA}/\text{cm}^2$) signifikant.

Die Herstellung der Bauelemente mittels des kombinatorischen Systems erlaubt das Einfügen einer dritten Elektrode, mit welcher direkt das Potenzial in einer Leuchtdiode unter typischen Betriebsbedingungen gemessen werden kann. Mit dieser komplementäre Methode, dem sogenannten “Potential Sensing”, kann auf die interne Potential- und Feldverteilung geschlossen werden. Die Tiefenauflösung (10 nm) ist durch die Dicke der dritten Metallelektrode bestimmt und kann noch verbessert werden. Aus den Messungen kann die interne Feldverteilung bestimmt werden, und die Ergebnisse dieser Methode bestätigen die mittels der oben erwähnten 2D-Spannungsplots gewonnenen Beobachtungen.

Oberstes Ziel für technische Anwendungen von OLEDs ist nebst einer Verlängerung der Lebensdauer die Steigerung der Effizienz. Prinzipiell wird dies durch die Verwendung geeigneter Dotierstoffe erreicht. Die Drei-Schichtstruktur CuPc/STAD⁴/Alq₃ wird um eine Dotier-

¹Kupfer-Phthalocyanin

²N,N'-Di(Naphthalen-1-yl)-N,N'-Diphenylbenzidin

³Tris(8-Hydroxyquinolinat) Aluminium

⁴2,2',7,7'-Diphenyl-amino-spiro-9,9'-bifluoren

schicht $\text{Alq}_3\text{:DCJTb}$ ⁵ ergänzt. Ein kombinatorisches Experiment zeigt, dass die Breite dieser dotierten Zone mindestens 150 Å betragen muss, so dass die Emission ausschließlich von DCJTb herrührt. Durch die Kenntnis dieser Minimaldicke kann die Effizienz möglichst hoch und die Betriebsspannung gleichzeitig möglichst niedrig gehalten werden. Die Flexibilität des neu aufgebauten Aufdampfsystems erlaubt auch einen direkten Vergleich verschiedener Dotierstoffe. Mittels gleichzeitigen Verdampfens aus drei Effusionszellen konnten rot emittierende OLED-Strukturen hergestellt werden, in welche zwei Farbstoffe (Rubren⁶ und DCJTb) in der Alq_3 Emissionszone eindotiert wurden. Durch diese Doppeldotierung wird bei leicht rotverschobenem Emissionsspektrum eine Effizienzsteigerung von etwa 15% erreicht. Der größere Vorteil dieser zweifach dotierten Strukturen zeigt sich jedoch in Messungen der Betriebslebensdauer, welche im Vergleich zu einfach dotierten Strukturen um einen Faktor drei auf extrapolierte 16'000 Stunden bei 100 cd/m^2 erhöht werden konnte.

Die Zukunft effizienter OLEDs liegt jedoch in der Verwendung phosphoreszierender Materialien, da bei diesen sowohl angeregte Singulett- als auch Triplett-Zustände zur Emission beitragen und die interne Effizienz theoretisch 100% betragen kann. Eine solche OLED-Struktur basierend auf dem phosphoreszierenden Dotierstoff Ir(ppy)_3 ⁷ wurde 1998 von Baldo et al. vorgeschlagen. Diese hocheffizienten Leuchtdiodenstrukturen benötigen allerdings eine zusätzliche Schicht, die verhindert, dass Triplett-Exzitonen während ihrer langen Lebensdauer in benachbarte Schichten diffundieren und dort mit geringerer Effizienz oder strahlungslos zerfallen. Mittels kombinatorischer Methoden wurden der Einfluss dieser Exzitonenblockierschicht sowie die Position und Breite der emittierenden Schicht untersucht. Eine Schichtdicke von 50 Å des Materials BCP⁸ ist beispielsweise ausreichend, um die Effizienz um einen Faktor zwei auf $\sim 20 \text{ cd/A}$ zu steigern, ohne dabei die Betriebsspannung wesentlich zu erhöhen. Hierbei hat die Position der Emissionszone einen großen Einfluss, während die Breite im Bereich von 150 bis 250 Å eine eher untergeordnete Rolle spielt.

Die in dieser Arbeit untersuchten OLEDs sind ausschließlich "top-emittierende" Strukturen, d.h. das Licht wird durch die zweite Elektrode nach oben emittiert. Die Ergebnisse verschiedener kombinatorischer Matrizen zeigen deutlich, dass die Effizienz von OLED-Strukturen eines gegebenen Materialsatzes überwiegend durch optische Interferenzeffekte be-

⁵4-(Dicyanomethylen)-2-*t*-Butyl-6(1,1,7,7-Tetramethyljulolidyl-9-enyl)-4*H*-Pyran

⁶5,6,11,12-Tetraphenylnaphthalen

⁷Tris(2-Phenylpyridin) Iridium

⁸2,9-Dimethyl-4,7-Diphenyl 1,10-Phenanthrolin

stimmt wird. Die Elektroden spielen dabei eine wichtige Rolle, weil die Reflektivität der Spiegel entscheidet, wie stark die Kavität ausgebildet ist. So kann mittels hochreflektierender Al/Ni-Zweischicht-Anoden die Reflektivität der Anode erhöht ($>85\%$) oder aber mittels einer Drei-Schicht-Anode (“black anode”) drastisch reduziert ($<5\%$) werden. Drei-Schicht-Anoden wurden in der Form Al/SiO_x/Ni hergestellt, und Reflexionsmessungen zeigen, dass numerische Simulationen die experimentellen Ergebnisse sehr gut reproduzieren können. Es reicht jedoch nicht aus, lediglich einzelne Komponenten, z.B. die Anode, auf hohe oder geringe Reflektivität zu trimmen, vielmehr muss die OLED als Gesamtstruktur betrachtet werden. Um auch bei Umgebungslicht gute Kontrastverhältnisse zu erzielen, muss die Reflektivität der Leuchtdiode im gesamten sichtbaren Bereich gering sein. Vorläufige Messungen an rot emittierenden Leuchtdioden zeigen, dass die effizienteste Leuchtdiode nicht notwendigerweise auch die geringste Gesamtreflektivität aufweist. Eine Abstimmung mittels einer zusätzlichen transparenten Schicht aus dielektrischem Material kann verwendet werden, um Effizienz und Gesamtreflexion anzupassen. In Leuchtdioden mit semi-transparenten Kathoden (“top-emitting”) spielen Transmission und Reflexion dieser Elektrode eine wichtige Rolle. Die optischen Eigenschaften von reaktiven Kathodenmaterialien, wie z.B. Ca und Mg, können mit Hilfe des aufgebauten Charakterisierungssystems unter Inertgasbedingungen vermessen werden und bilden die Datengrundlage für numerische Simulationen.

Neben technologischen Fragestellungen können mit Hilfe kombinatorischer Probenherstellung auch grundlegendere Eigenschaften von OLEDs untersucht werden. Lumineszenzlöschung an Grenzflächen ist ein Effekt, der in organischen Leuchtdioden zu einer drastischen Herabsetzung der Effizienz führen kann und daher unbedingt vermieden werden muss. Die Photolumineszenzintensität von Alq₃-Schichten als Funktion der Schichtdicke gibt Aufschluss darüber, welche kritischen Distanzen beachtet werden müssen. Zur Beschreibung der dickenabhängigen Photolumineszenzintensität wurde ein Modell aufgestellt, welches Exzitonendiffusion und Lumineszenzlöschung an der Substratgrenzfläche annimmt. Die experimentellen PL-Daten von Alq₃ auf Glass, ITO (Indium-Zinnoxid) und Aluminium werden damit sehr gut beschrieben. Desweiteren kann die Fluoreszenzlöschung an der Oberfläche quantifiziert werden und beträgt 15% bzw. 40% für unbehandeltes bzw. sauerstoffplasma-behandeltes Glas. Auf typischen Elektrodenmaterialien wie ITO und Al beträgt die Lumineszenzlöschung 60% bzw. 100% an der Grenzfläche. Basierend auf diesem Modell erhält man eine Exzitonendiffusionslänge in Alq₃ von $L = 220 \text{ \AA}$.

Als alternative Methode zur Bestimmung der Exzitonen-Diffusionslänge wurde die Methode des “Sensing layers” angewandt. Durch Einfügen einer extrem dünnen, dotierten Schicht (25 Å) an verschiedenen Positionen einer OLED, kann durch Messung der EL-Spektren die Verteilung der Emissionszone in OLED-Strukturen ausgemessen werden. Die relative Intensität der Emission des Dotierstoffes kann dabei näherungsweise als Maß für die lokale Exzitonendichte betrachtet werden. Im Falle von CuPc/NPB/Alq₃ OLEDs mit DCJTB als Dotierstoff zeigte sich jedoch, dass das erhaltene Profil stark von der Stromdichte abhängt, was auf Lumineszenzlöschung durch Ladungsträger hindeutet. Für den Grenzfall kleiner Stromdichten und unter Annahme einer Reihe von Vereinfachungen kann die Exzitonen-Diffusionslänge in Alq₃ zu $L \approx 200$ Å abgeschätzt werden. In der Vergangenheit wurden bereits verschiedene Experimente dieser Art durchgeführt, wobei die Datensätze allerdings limitiert und die Proben in der Regel meist seriell hergestellt wurden. Mittels kombinatorischer Methoden können solche Experimente nun jedoch ohne großen Aufwand mit verschiedenen Materialsystemen wiederholt werden, wobei sogar direkte Vergleiche von Materialkombinationen in einem Aufdampfvorgang möglich sind.

Alle hier vorgestellten experimentellen Ansätze machen Gebrauch davon, dass mittels kombinatorischer Methoden eine Vielzahl gezielt unterschiedlicher Proben hergestellt werden kann. Hierbei wird die Bauelementstruktur selbst als weiterer Parameter, quasi als zusätzliches “Mess-Instrument”, verwendet. Bei der Vielzahl organischer Materialien, Elektrodenkonfigurationen und deren möglicher Kombinationen muss allerdings bislang immer noch im Einzelfall untersucht werden, wie sich die Bauelemente genau verhalten. Für eine quantitative Simulation organischer Leuchtdioden, insbesondere ihres elektrischen Verhaltens, bedarf es nun ausgefeilter Modellbeschreibungen, die anhand reichhaltiger und verlässlicher Datensätze überprüft werden müssen. Daher sind für eine umfassende Beschreibung und das Verständnis systematische, experimentelle Daten unabdingbar, um zuverlässige Voraussagen treffen zu können. Somit muss das nächste Ziel sein, mittels kombinatorischer Experimente und anderweitig gemessener Materialparameter, quantitative Aussagen auch auf komplexere Systeme ausweiten zu können. Ein erster, wichtiger Schritt in diese Richtung ist hiermit getan, da mit Hilfe des im Rahmen dieser Arbeit aufgebauten kombinatorischen Aufdampfsystems die notwendigen experimentellen Daten mit sehr hoher Präzision und Reproduzierbarkeit auf sehr effizienter Weise gewonnen werden.

Chapter 1

Introduction and Motivation

1.1 Introduction

The fast and efficient exchange of knowledge is becoming increasingly important, and consequently, so is the access to rapidly changing information sources. As the interface between digitized information and human beings display plays a central role in this development. Research activities have therefore been focused on developing an ideal display. “The ideal display would modulate the ambient light when it is abundant, but would emit bright light in the dark; it would be capable of producing saturated colors at will, be visible from all angles, have high resolution, respond in microseconds but retain the image indefinitely if so desired, have contrast of 50:1 and 64 levels of gray, consume negligible power at low voltage” [Pankove 1980]. Furthermore, it should be portable, thin, lightweight and flexible. The cathode ray tube invented at end of the 19th century has been the predominant display type until now. However, liquid crystal displays which were developed in the 1970s, are about to take over the lead. Technologies which feature simplicity but at the same time offer high performance will prevail in the future. A candidate for next-generation displays is thought to be a technology based on organic electroluminescence (EL).

The basic discoveries of EL in organic materials were made in the early 1950s and thereafter [Bernanose et al. 1953; Pope et al. 1963]. Single crystals of anthracene were connected with electrolytic contacts, and EL was observed at voltages between 400 and 2000 V. Later, thin (≈ 600 nm) vacuum-sublimed films of anthracene were used with Al cathodes and Au anodes [Vincett et al. 1982]. Although the voltages were reduced significantly below 100 V

the devices exhibited extremely short lifetimes of the order of a few minutes. A breakthrough was achieved in 1987 when Tang et al. reported an organic two-layer structure with separate hole transport and electron transport layers [Tang and Van Slyke 1987]. The organic structures based on small molecule dyes showed bright yellow-green luminescence ($>1000 \text{ cd/m}^2$) below 10 V. This report triggered further research and development of this new type of organic light-emitting devices [Adachi et al. 1988a; Adachi et al. 1988b; Kido et al. 1991]. Another class of organic compounds attracted attention when Burroughes et al. observed EL in a conjugated polymer [Burroughes et al. 1990]. Since then the field of organic EL has been growing rapidly for both the polymers and the small molecules. The first products featuring organic light-emitting devices (OLEDs) have already been commercialized: a car radio with a passive matrix display based on small molecules (Pioneer 1997) and an electric razor with a display based on polymers (Philips 2002). In the meantime, various prototypes of full-color active matrix OLED displays based on a low-temperature poly-Si thin-film transistor (TFT) backplane have been demonstrated. The most prominent examples are a 13" diagonal panel by Sony with small molecules patterned by shadow masks and a 17" diagonal screen by Toshiba-Matsushita fabricated via ink-jet printing of polymers. A recent highlight was the demonstration of a 20" full-color active matrix OLED display based on amorphous-Si TFT developed in a collaboration of IDTech, CMO and IBM Research.

The attributes of OLEDs make them clearly favorable for displays of all sizes ranging from microdisplays (<1 " diagonal) to large screen (>15 " diagonal) applications. OLEDs are a self-emitting technology operating at low voltages (3 to 10 V), which is essential for battery-driven mobile displays. Fast switching speed $<1 \mu\text{s}$, high brightness (up to 10^6 cd/m^2) and a nearly Lambertian viewing angle make OLEDs also suitable for video applications. However, one of the most important issues for OLEDs to become a serious alternative to existing flat panel technologies are still efficiency and long-term stability. In order to further improve materials and devices it is necessary to understand the basic processes. Other criteria such as color purity and large viewing angle have to be fulfilled. Since fast switching speed and excellent form factor are inherent to these organic devices, they will not be addressed in this work. For success on the market, manufacturing costs are one of the most important issues that determine whether this technology will compete with or even replace existing ones.

Since 1995, the display group of the IBM Zurich Research Lab (ZRL) has focused on microdisplays based on crystalline silicon for head-mounted and direct-view displays. Figure 1.1 shows three display prototypes. Figure 1.1a shows a monochrome fixed pattern display with

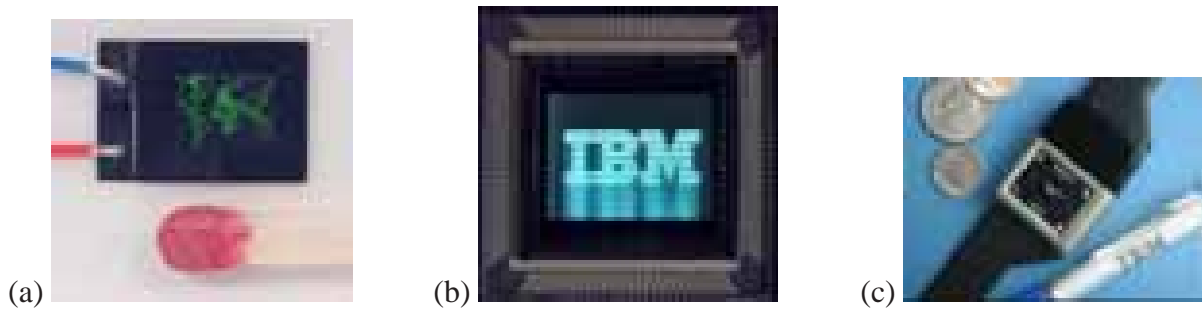


Figure 1.1: Examples of IBM prototype OLED displays: (a) fixed pattern with pixel size $4 \times 4 \mu\text{m}^2$; (b) actively driven VGA ($640 \times 480 \times 3$ pixel) display based on CMOS technology; (c) IBM/eMagin VGA display integrated in the IBM Linux wrist watch.

an active area of $4.8 \times 3.2 \text{ mm}^2$. It has a pixel number of 1024×768 (XGA), which corresponds to a pixel size of $4 \times 4 \mu\text{m}^2$. An example of an actively driven display is shown in Figure 1.1b which is a monochrome display integrated on CMOS technology with an active area of $12 \times 9 \text{ mm}^2$ and a pixel count of $640 \times 480 \times 3$. Figure 1.1c depicts an IBM/eMagin joint development of a direct-view display with an active area of $22 \times 16.5 \text{ mm}^2$ and VGA resolution (640×480), which results in 740 pixels/inch. The latter display was integrated into the IBM Linux wrist watch computer. In parallel, the OLED group at ZRL started in 1999 together with IBM Yorktown investigations on the feasibility of amorphous Si (a-Si) for AMOLED displays. In December 2000, the first functional, monochrome display (active area $40 \times 40 \text{ mm}^2$) based on a-Si was demonstrated with a resolution of 100 pixels per inch. By year-end 2001, the latter display was realized in full color. In March 2003, a collaboration of IDTech, CMO and IBM Research highlighted the capabilities of a-Si TFTs for large area OLED displays. Figure 1.2 shows an image of the world's largest full-color OLED display driven by amorphous Si-TFTs [IDTech 2003; Tsujimura et al. 2003]. The 20-inch prototype is a top-emitting, full-color, active-matrix display. It has WXGA resolution (1280×768 pixels) and a power consumption of 25 W at a brightness of 300 cd/m^2 (its desktop display brightness can exceed 500 cd/m^2). Improved color reproduction, which is better than that of CRTs, and extremely high efficiency have been achieved specifically by use of tailor-made organic materials in combination with a unique optical device architecture.

Besides OLEDs, organic materials can be used to implement transistors and even more complex circuitry [Bao et al. 1996; Lin et al. 1997]. All-organic displays have the potential to become a cheap alternative to screens having poly-Si or amorphous-Si TFT backplanes.



Figure 1.2: World's largest OLED display (20" diagonal) driven by a-Si TFTs developed in collaboration with IDTech, CMO and IBM Research [Tsumimura et al. 2003].

1.2 Motivation

Independent of the size of the targeted organic display, all basic investigations are initially done in simple test structures. It is therefore necessary to have efficient tools and methods to characterize new materials and new device structures. A single device or a simple one-by-one device fabrication is definitely not sufficient to evaluate a material set and determine the best device parameters. Furthermore, the understanding of many basic processes require systematic series of experiments and measurements. Therefore, many experiments on organic EL described in the literature rely on the measurement of either thickness-dependent or position-dependent device structures [Tang et al. 1989; So et al. 1999].

Thus, the motivation for this work was to provide the ability to fabricate series of devices in a reliable and comparable way in order to contribute to the understanding of the limiting effects and mechanisms in these devices. Within the framework of this thesis a new evaporation system and an automatized characterization tool has been established for systematic studies of electro-optical aspects of organic materials and light-emitting devices.

Chapter 2 gives a brief introduction to the most important mechanisms and processes that are

relevant for OLEDs, i.e. injection, transport and recombination in organic materials.

The new evaporation system with all its peculiarities for combinatorial device fabrication, which was designed and set up during this PhD research, is described in detail in Chapter 3. The flexibility of the system and the high quality of the fabricated devices will be emphasized. Chapter 4 focuses on electrical properties of multilayer structures. In particular, the internal potential distribution is addressed using combinatorial 2D layer variations and a complementary measurement method, i.e. direct potential sensing. Furthermore, more complex double-doped and phosphorescent OLED structures are investigated with respect to maximum efficiencies.

In Chapter 5 optical interference effects are addressed considering organic stacks, two- and three-layer anodes as well as semitransparent cathodes.

Chapter 6 addresses exciton diffusion as an elementary process in organic materials. Quenching is investigated on different substrates and described with an exciton diffusion model including quenching based on exciton diffusion.

Finally, Chapter 7 contains the summary of this work.

Chapter 2

Basics of Organic Electroluminescence

2.1 Organic Semiconducting Materials

Organic electroluminescent materials can in principle be divided into two groups: conjugated polymers, which are deposited from solution, and small molecules, which are usually evaporated under vacuum conditions. Both material classes possess a conjugated π -electron system, i.e. alternating single and double bonds, which are aromatic rings in the case of small molecules. In such conjugated systems, the carbon atoms are sp^2 hybridized and as a result the π -electrons are delocalized which easily allows electron rearrangement on one molecule. The following discussion focuses on small molecules. Molecules in organic crystals or amorphous films interact only via weak Van-der-Waals forces or hydrogen bridges, which leads to a weak overlap of the molecular orbitals. This results in narrow bands, a high effective mass and hence low mobility. Similar to the valence and conduction band in inorganic semiconductors the energetic levels relevant for charge carrier transport correspond to the HOMO (highest occupied molecular orbital) and LUMO (lowest unoccupied molecular orbital) in organic semiconductors, respectively. Typical energy gaps between the HOMO and LUMO of organic materials range between 1.6 and 3.6 eV (see Appendix, Table A.1).

2.2 Device Operation

2.2.1 Basic Device Structure

Figure 2.1 shows a schematic view of a basic OLED structure. One or several organic layers are sandwiched between two electrodes, which serve as electron and hole-injecting contacts. The most widely used electrode configuration is a transparent indium-tin-oxide (ITO) layer on glass as the anode and a low-work-function metal (e.g. Ca, Mg:Ag, Al) as the reflective top cathode. This type of configuration which emits through the substrate is called “bottom emitting”. Other electrode configurations are possible, e.g. two transparent contacts or a reversed structure having a top anode and a bottom cathode. The device configuration investigated in this work is a so-called “top-emitting” structure and has a reflective bottom anode and a semi-transparent top cathode (see Fig. 2.1). The advantage of a top-emitting structure is that the substrate may contain thin-film transistors buried below the OLED structure as switching elements for active matrix displays.

The fundamental processes occurring in an OLED structure are sketched in Figure 2.2. The basic processes comprise:

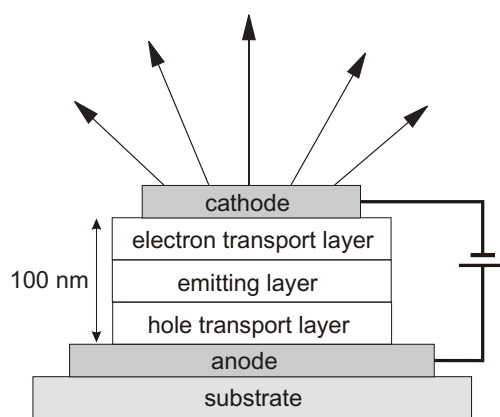


Figure 2.1: Basic OLED device structure. One or several organic layers (total thickness typically ≈ 100 - 150 nm) are sandwiched between two electrodes. The structures investigated in this work have a reflective bottom anode and a semitransparent top cathode.

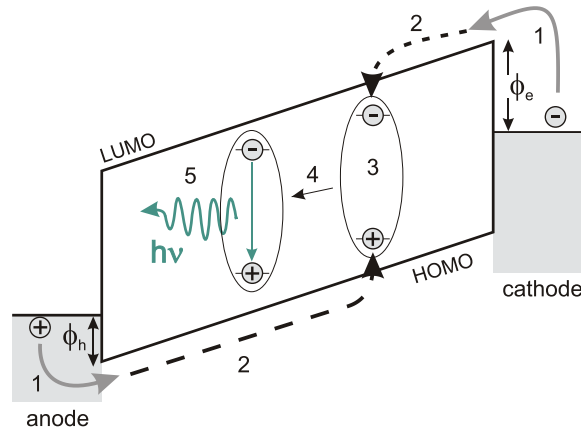


Figure 2.2: Basic mechanisms in an OLED structure. (1) charge carrier injection, (2) charge carrier transport, (3) electron and hole capture and formation of an exciton, (4) exciton diffusion, (5) decay of the excited state.

- (1) injection of holes and electrons from the anode and cathode, respectively,
- (2) charge carrier transport,
- (3) electron-hole capture and formation of an excited state (exciton)
- (4) diffusion of excitons
- (5) decay of the excitons.

In the simplest case the organic stack consists of only one material. However, the breakthrough in efficiency and lifetime in OLED technology based on small molecules was achieved by introducing an organic heterostructure based on two or three organic layers [Tang and Van Slyke 1987; Adachi et al. 1988a]. As shown in Figure 2.1 a typical OLED structure consists of a hole transport, electron transport and an emitting layer. Via the separation into layers with different functionality, each layer can be dedicated to specific processes.

The above-mentioned processes will be discussed in more detail in the following sections.

2.2.2 Charge Carrier Injection from Contacts

Most of the organic EL materials have a large gap (>2 eV) and hence their intrinsic free charge carrier density is negligible ($n < 10^{10}$ cm $^{-3}$) at room temperature. The resistivity $\rho = 1/\sigma = 1/(qn\mu)$ of pure organic compounds is in the range of 10^{10} to 10^{16} Ω cm [Kao and

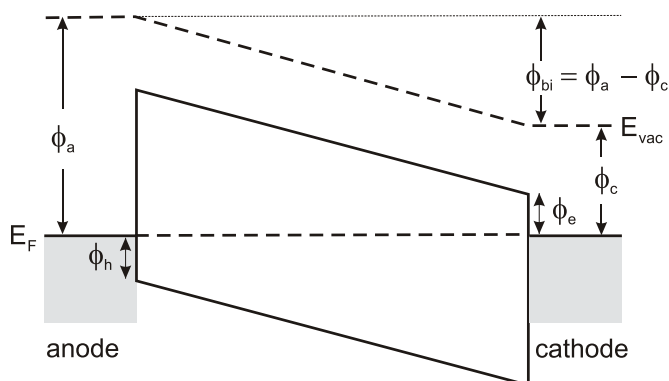


Figure 2.3: Energy diagram of an organic material in contact with two electrodes having different work functions. $U_{bi} = (\phi_a - \phi_c)/e$ is the resulting built-in voltage.

Hwang 1981]. Nevertheless, charge carriers can be injected from electrodes by applying high fields of the order of 10^5 to 10^6 V/cm. Figure 2.3 shows a simplified organic layer sandwiched between two metal electrodes having different work functions ϕ_a and ϕ_c . When zero bias is applied, the Fermi levels E_F of the electrodes are aligned to the same height, resulting in a tilt of the HOMO and LUMO levels and hence a field across the organic layer. The potential difference is also called built-in voltage U_{bi} and depends on the differences between the work functions of the electrodes $U_{bi} = \frac{1}{e}(\phi_a - \phi_c)$. For example, a structure having ITO ($\phi_a = 4.9$ eV) and Mg ($\phi_c = 3.6$ eV) and a 100-nm-thick organic layer results in a field of 2×10^5 V/cm. In general, holes and electrons have to overcome barriers ϕ_h and ϕ_e , which depend on the relative alignments of the HOMOs and LUMOs with respect to the Fermi levels E_F of the electrodes. A contact with no barrier, i.e. negligible impedance, is called ohmic. In this case, the current density j obeys Ohm's law and is written

$$j = en\mu F, \quad (2.1)$$

where e is the electronic charge, μ the mobility and F the electric field.

Commonly used electrodes, however, are usually not ohmic. In the case of ITO ($\phi_a = 4.9$ eV) and Mg ($\phi_c = 3.6$ eV) electrodes and an Alq₃ (HOMO 5.8 eV, LUMO 3.1 eV) layer this would lead to a energy barrier of 0.9 and 0.5 eV for holes and electrons, respectively. The work functions of some metals are listed in Chapter 5 in Table 5.3 and Table 5.4. A selection of HOMO and LUMO energies of organic materials is given in Table A.1 (page 197). It has to be mentioned that this simplified picture neglects surface states and dipole layers at the interfaces,

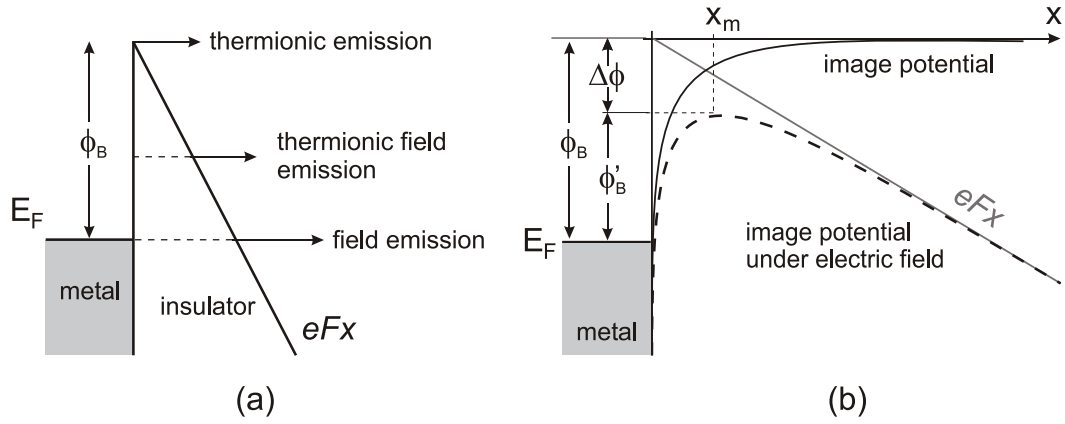


Figure 2.4: Schematic energy-level diagram showing (a) various emission processes, i.e. thermionic emission, thermionic field emission, and field emission. (b) Barrier lowering due to an image charge potential [Sze 1981].

which may lead to considerable shifts in the energy alignment. In Figure 2.4 different injection mechanisms are shown as examples of electrons. Rigid bands in insulators are assumed, which results in a triangular energy barrier. Electrons that have enough thermal energy are injected over the barrier ϕ_B into the semiconductor. This process is called thermionic injection and the current scales according to

$$j = j_s \left[\exp \left(\frac{eU}{kT} - 1 \right) \right], \quad (2.2)$$

where j_s is the saturation current density

$$j_s = A^* T^2 \exp \left(- \frac{e\phi_B}{kT} \right) \quad (2.3)$$

and A^* the Richardson constant ($120 \text{ A/cm}^2/\text{K}^2$) for thermionic emission of electron emission into vacuum [Sze 1981]. At lower temperatures and higher fields F there is a probability that electrons will tunnel through the thin barrier. This mechanism has been treated by Fowler and Nordheim [Fowler and Nordheim 1928] and the injection current across such an interface writes:

$$j = \frac{A^*}{\phi_B} \left(\frac{eF}{\alpha kT} \right)^2 \exp \left[- \frac{2\alpha\phi_B^{3/2}}{3eF} \right] \quad (2.4)$$

where

$$\alpha = \frac{4\pi(2m^*)^{1/2}}{h} \quad (2.5)$$

with an effective mass m^* of the charge carrier. Experimental results showing a linear relation between $\ln j/F^2$ versus $1/F$ indicate that field emission is the predominant process. Under normal conditions, injection will be thermally assisted, i.e. carriers have a certain thermal energy so that they tunnel from an energy above the Fermi level and encounter a thinner barrier. For detailed treatment of this thermionic field emission process, see [Kao and Hwang 1981]. When the injected carrier density exceeds the intrinsic charge carrier density the transport of the carriers may become the limiting process for current flow.

2.2.3 Charge Carrier Transport

Hopping Transport in Organic Materials

Owing to the narrow band width of organic materials and the resulting large effective mass and hence low mobility of charge carriers, the mean free path is of the order of the molecular spacing. Injected excess charge carriers are basically localized on the molecules and undergo a random hopping process from one molecule to the next. Nevertheless, the mobility μ of a charge carrier can be defined via $v_d = \mu F$, where v_d is the drift velocity and F the applied field. In organic semiconductors the mobility μ is generally strongly field dependent and increases with increasing fields. This is explained by the Poole-Frenkel effect, which is based on the assumption that charge carriers trapped in a Coulomb potential are detrapped more easily by high electric fields. Figure 2.5 illustrates this barrier lowering $\Delta\phi$ at high electric fields. The mobility can be written

$$\mu = \mu_0 \exp\left(-\frac{E_a - \beta_{PF} \cdot \sqrt{F}}{kT}\right), \quad (2.6)$$

whereby the Poole-Frenkel factor β_{PF} is given by $\beta_{PF} = \sqrt{e^3/\pi\epsilon_r\epsilon_0}$ and E_a is the activation energy without electric field. The field dependence of the mobility of organic materials is often expressed by an exponential increase with \sqrt{F} . Detailed models have been developed by Baessler et al. describing the random walk of charge carriers through a disordered solid [Bässler 1993]. However, in order to describe current–voltage characteristics, for example, all relevant processes such as electron/hole injection depending on the electrodes and interfaces as well as recombination have to be taken into account.

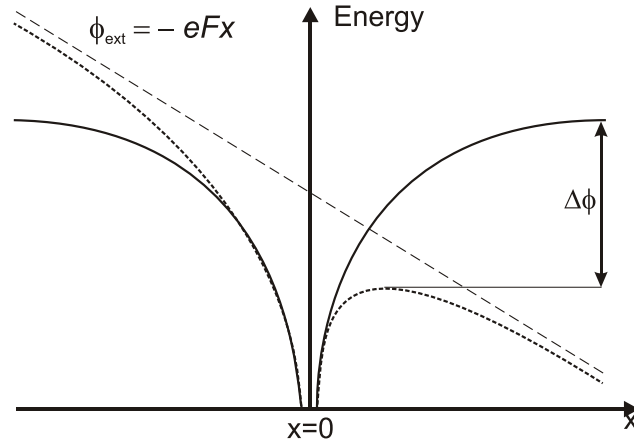


Figure 2.5: Poole-Frenkel effect: barrier lowering for a charge carrier in a Coulomb potential due to an external field.

Space-Charge-Limited Conduction and Traps

Especially in low mobility materials, the occurrence of space-charge-limited conduction (SCLC) can be observed. In this case, an ohmic or nearly ohmic contact injects more charge carriers than can be transported and recombined in the bulk. The excess charge will form a space charge which screens the electric field and hence reduces the rate of charge carrier injection from the contacts [Kao and Hwang 1981]. In order to describe the functional behavior, single-carrier injection and no traps ($n_t = 0$) are assumed. For simplicity, the mobility is regarded as field independent and diffusion terms are neglected. The field in the semiconductor is calculated via Poisson's equation in one dimension

$$\frac{dF}{dx} = (n_0 + n_t) \frac{e}{\epsilon_0 \epsilon_r}. \quad (2.7)$$

At low voltages the intrinsic, thermally generated carriers n_0 dominate over the injected carriers such that the field in the sample is constant. In that regime the drift current density scales linearly with the field according to Ohm's law (Eq. 2.1)

$$j = e\mu n_0 F = e\mu n_0 \frac{V}{d}, \quad (2.8)$$

where d is the thickness of the sample. Integration of Equation (2.7) by using Equation (2.1) results in the relationship known as Child's law or the Mott-Gurney equation:

$$j_{SCL} = \frac{9}{8} \epsilon_0 \epsilon_r \mu \frac{V^2}{d^3}. \quad (2.9)$$

Assuming $\mu \approx 10^{-6} \text{ cm}^2/\text{Vs}$ and $\epsilon_r = 4$, the maximum current density which can pass a 100-nm-thick organic layer at 10 V is about 40 mA/cm². This estimation shows that in principle SCLC can be observed in typical OLEDs structures. Equation (2.9) is the description of a trap-free material. However, if traps are present the mobility can be replaced by an effective mobility assuming a discrete shallow trap level, i.e. close to the LUMO level for electrons [Kao and Hwang 1981].

$$\mu_{\text{eff}} = \theta \mu, \quad (2.10)$$

where θ is the ratio of the free carrier density to the total carrier density

$$\theta = \frac{n}{n + n_t}. \quad (2.11)$$

For the trap-free case $n_t = 0$ this factor is $\theta = 1$ and with traps it could be as small as $\theta = 10^{-7}$ [Kao and Hwang 1981]. In real organic materials, however, traps will have a certain distribution in energy. In some special cases an analytical solution of the current-voltage relation can be given, see [Kao and Hwang 1981, p. 150ff]. In the case of an exponential distribution of traps the current density is given as

$$j = e^{1-l} \mu N_e \left(\frac{2l+1}{l+1} \right)^{l+1} \left(\frac{l}{l+1} \frac{\epsilon_0 \epsilon_r}{n_t} \right) \frac{V^{l+1}}{d^{2l+1}}, \quad (2.12)$$

where N_e is the density of states in the LUMO level and $l = T_c/T$ with $l \geq 1$ where T is the temperature and T_c a characteristic constant of the trap distribution. A Gaussian distribution of traps will modify the parameters in Equation (2.12) but the current density still follows the relationship

$$j \sim \frac{V^{l+1}}{d^{2l+1}}. \quad (2.13)$$

For deep traps $l > 2$, whereas for shallow traps $l = 1$, which reproduces Equation (2.9). The different regimes in a current-voltage characteristic are summarized in Figure 2.6 in a double logarithmic representation. This is strictly valid only for single carrier injection; these equations have to be modified for double carrier injection. Double carrier injection causes a higher current flow than predicted by space-charge-limited theory [Kao and Hwang 1981]. In order to

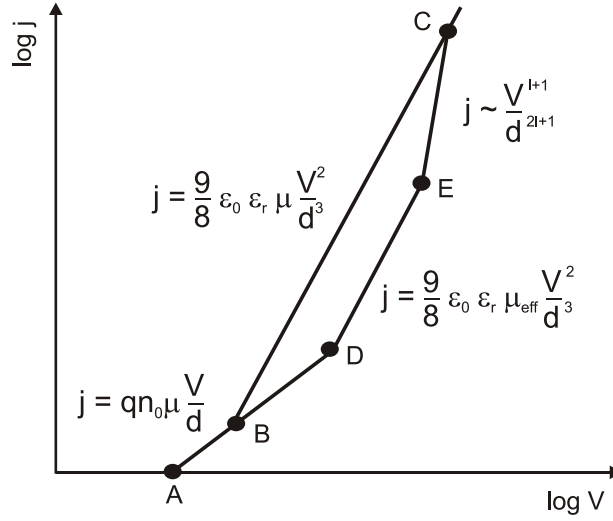


Figure 2.6: Current-voltage characteristics for space charge and trap limited transport. (A-B) ohmic region without traps. (B-C) SCLC without traps. (B-D) Ohm's law with traps. (D-E) SCLC with shallow traps. (E-C) SCLC with deep traps.

describe and predict current–voltage characteristics, more sophisticated models have been developed taking into account double carrier injection, recombination, field-dependent injection and field-dependent mobility.

2.2.4 Charge Carrier Recombination

When electrons and holes are produced statistically independent of each other, then recombination is a random process and is kinetically bimolecular. This type of recombination is called *Langevin* recombination [Pope and Swenberg 1999]. The initial requirement is that the main free path λ of the carriers is less than the radius of capture of one carrier by the other. This condition is fulfilled in narrow-band conductors with carrier mobilities $\leq 1 \text{ cm}^2/\text{Vs}$ at room temperature. In these conductors, the scattering length is of the order of the lattice parameter. The coulombic capture radius r_c is the distance at which the kinetic energy of the particle is equal to the Coulomb potential attractive potential energy. Using $\epsilon_r = 3.4$ it is written

$$r_c = \frac{e^2}{4\pi\epsilon_0\epsilon_r kT} \approx 17 \text{ nm.} \quad (2.14)$$

The recombination may be viewed as the drift of two carriers together under the action of the coulombic field. For simplicity, the electron is considered stationary and the hole moves with the total mobility $\mu_t = \mu_e + \mu_h$. The hole drift current density j attracted by an electron is therefore, at r_c ,

$$j = e n_h \mu_T F = e n_h \mu_T \frac{e^2}{4\pi\epsilon_0\epsilon_r kT}, \quad (2.15)$$

where n_h is the density of holes. The area of the spherical surface of radius r_c is $4\pi r_c^2$ and the total current entering the sphere is

$$i = n_h \mu_T e^2 / \epsilon_0 \epsilon_r. \quad (2.16)$$

All of this current recombines with the negative charge, for which the recombination rate is $\gamma_{eh} n_h e$, where γ_{eh} is the bimolecular rate constant for free electron–hole recombination. This yields $\gamma_{eh} n_h e = n_h \mu_T e^2 / \epsilon_0 \epsilon_r$ or

$$\gamma_{eh} = e n_h \mu_T / \epsilon_0 \epsilon_r. \quad (2.17)$$

In this Langevin model the factor γ_{eh} is dependent only on the material parameters μ and ϵ_r . At high external fields the electron–hole pairs can be dissociated. The external field necessary to dissociate an electron–hole pair can be estimated by calculating the field at r_c assuming a typical exciton binding energy of $E_B = 0.2$ eV and $\epsilon_r = 3.4$:

$$F = 4\pi\epsilon_0\epsilon_r \frac{E_B^2}{e^3} \quad (2.18)$$

This results in a field of the order of 10^6 V/cm. Taking typical thicknesses of organic layers of the order of 100 nm and assuming an average field within the device corresponds to a voltage of only 10 V where dissociation of excitons and hence reduction of efficiency might become significant. It is therefore important for OLED structures to keep the voltage drop over the recombination zone as small as possible.

2.3 Excited States in Organic Materials

Recombination of charge carrier results in excited crystal states called excitons. These excitons exist either in a singlet or triplet state. In the case of optical excitation (photoluminescence) only singlet excitons are created, whereas by electrical excitation (electroluminescence), triplets and singlets are created according to the quantum mechanical selection rules

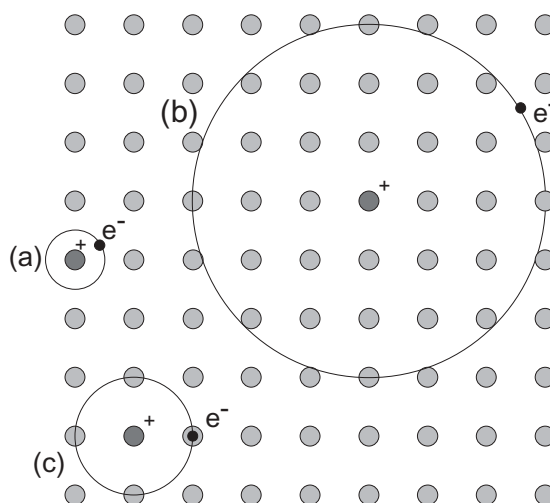


Figure 2.7: Schematic illustration of different types of excitons: (a) Frenkel, (b) Wannier–Mott, and (c) charge transfer. In reality, the hole and consequently the exciton itself are mobile as well.

with a ratio of 3:1. This limits the theoretical efficiency of a material that utilizes only the decay of singlet excitons (fluorescence) to 25% neglecting triplet-triplet annihilation. A schematic overview of the photophysical processes is given in Section 2.3.3. Classically, these excitons can be viewed as bound electron–hole pairs. Depending on the binding radius and the binding energy these excitons are classified into three groups, which are schematically illustrated in Figure 2.7.

Frenkel exciton: Organic semiconductors usually have a low dielectric constant $\epsilon_r \approx 3$, which means that the Coulomb interaction is rather strong, i.e. the electron–hole pair will be close together. This is called a Frenkel exciton and is the most relevant for organic semiconductors. Its radius is $\sim 10 \text{ \AA}$, which is basically located on one molecule and has a binding energy in range of 0.1 to 1 eV.

Wannier exciton: In inorganic semiconductors due to their larger dielectric constants and delocalization, the excitons have a much larger binding radius ($\sim 100 \text{ \AA}$) of the order of several lattice constants and a binding energy of $\sim 10 \text{ meV}$.

Charge-transfer (CT) exciton: There exist excited states where the hole and electron are located on nearest or next-nearest neighboring molecular sites but still retain their correlation [Pope and Swenberg 1999]. These CT excitons play a role as intermediate steps in charge carrier-recombination. In the initial state of EL the electron-hole pairs are located separate and uncorrelated, but in the final state they are on one molecule, i.e. a Frenkel exciton. Therefore, an intermediate Wannier or CT exciton must exist [Kao and Hwang 1981].

2.3.1 Energy Transfer

Energy transport in organic films can occur via several radiative and non-radiative processes. They are especially important in doped systems where an efficient energy transfer from the excited host molecule to a dopant molecule is desired.

Reabsorption

The “trivial” mechanism is a radiative two-step process. A photon with the energy $E = h\nu$ is emitted from the excited donor molecule D^* , which is then absorbed by another acceptor molecule A .



The transfer rate will depend on (1) the quantum yield of the emission by D^* , (2) the concentration of A in the path of photons by D^* , (3) the light-absorbing ability of A , and (4) the overlap of the emission spectrum of D^* and the absorption spectrum of A . Because of the low concentration of the dopant (typically $\approx 1 - 5\%$) in the host matrix this process can be neglected in OLED structures.

Förster transfer

The Förster transfer is a non-radiative resonant process due to dipole–dipole interaction [Förster 1948]. The rate constant for energy transfer by the dipole–dipole mechanism is related to the distance R of the donor D^* and the acceptor A

$$k_{ET} \sim \frac{1}{\tau_D} \left(\frac{R_0}{R} \right)^6, \quad (2.20)$$

where τ_D is the actual mean lifetime of D^* and R_0 is the critical separation of donor and acceptor for which energy transfer from D^* to A and radiative emission from D^* are equally probable [Turro 1991]. Both the donor and acceptor transitions must be allowed and occurs only via singlet-singlet energy transfer. For efficient energy transfer, the donor emission and the acceptor absorption must overlap. Typical Förster radii R_0 are in the range of 50 to 100 Å [Rabek 1996].

Dexter transfer

Another theory for energy transfer was proposed by Dexter [Dexter 1953]. This mechanism involves electron exchange through overlapping electron clouds of molecules. The energy transfer rate k_{ET} is written as

$$k_{ET} \sim J \exp(-2R_{DA}/L), \quad (2.21)$$

where J is a normalized spectral overlap integral, R_{DA} is the distance between donor D^* and acceptor A relative to their Van-der-Waals radii L . Owing to the exponential decrease the transfer rate k_{ET} drops to negligibly small values for distances larger than two molecular dimensions (for Alq₃ 15 – 20 Å) [Shoustikov et al. 1998]. The Dexter and the Förster theories both predict a direct dependence of k_{ET} on J , which is the spectral overlap integral.

2.3.2 Exciton Diffusion

One of the most important properties of excitons is their capability of transporting energy without transporting net charge [Kao and Hwang 1981]. Excitons are mobile within their lifetime τ and therefore migrate through the organic material until they decay radiatively. The diffusion length L is defined as

$$L = \sqrt{D\tau}. \quad (2.22)$$

Strictly speaking, the relationship between the diffusion coefficient D , the diffusion length L and the exciton life time τ depends on whether the diffusion is restricted to one, two or three dimensions [Pope and Swenberg 1999, p. 122] but commonly the relationship in Equation (2.22) is used. The one-dimensional case of the rate equation for excitons is written as

$$\frac{\partial S(x,t)}{\partial t} = g(x,t) + D \cdot \frac{\partial^2 S(x,t)}{\partial x^2} - \frac{S(x,t)}{\tau}. \quad (2.23)$$

The first term $g(x,t)$ describes the exciton generation and is assumed to be proportional to the current density as long as the current balance between holes and electrons does not change. The second term stands for the diffusion and the last term takes the decay of excitons by radiative recombination into account.

In order to describe the temporal and spatial distribution of excitons Equation (2.23) has to be solved. A special case for the generation is a stepwise turn-on of a Dirac-like confined exciton generation

$$g(x,t) = \xi \cdot \theta(t - t_0) \cdot \delta(x - x_0), \quad (2.24)$$

where ξ is a scaling factor, θ the Heaviside function and x_0 the location of the delta source. The offset in time t_0 in Equation (2.24) corresponds to the time it takes for charges to penetrate and meet in an actual device. For the special case of a dirac-delta exciton generation there is an analytical solution [Ruhstaller 2000].

$$S(x,t) = \frac{\xi \cdot \tau}{4L} \cdot \left[2e^{-\frac{x}{L}} - e^{-\frac{x}{L}} \left(1 - \operatorname{erf} \left(\sqrt{\frac{\tau}{t}} \left(\frac{t}{\tau} - \frac{x}{2L} \right) \right) \right) + e^{-\frac{x}{L}} \left(-1 + \operatorname{erf} \left(\sqrt{\frac{\tau}{t}} \left(\frac{t}{\tau} - \frac{x}{2L} \right) \right) \right) \right], \quad (2.25)$$

where the error function is defined as $\operatorname{erf}(x) = \frac{2}{\sqrt{\pi}} \int_0^x e^{-y^2} dy$. For the approach to equilibrium $t \rightarrow \infty$, Equation (2.25) simplifies to

$$S(t \rightarrow \infty) = \frac{\xi \cdot \sqrt{\tau}}{\sqrt{D}} \cdot e^{-\frac{|x|}{\sqrt{D\tau}}} = \frac{\xi \cdot \tau}{L} \cdot e^{-\frac{|x|}{L}}. \quad (2.26)$$

Equation (2.25) only describes the solution for $x > 0$, whereas for $x < 0$ the solution is analogous and is therefore consistent with the experimental OLED, where diffusion is assumed to be unidirectional away from the interface with the HTL. Thus the exciton distribution decays exponentially according to the diffusion length L , starting from a density at $x = 0$ which is dependent on ξ , τ and L .

2.3.3 Exciton Decay

Figure 2.8 gives an overview of the possible decay paths of an excited state (after [Turro 1991]). The Frenkel excitons located on one molecule can be regarded as a molecular excited state which and can either have a spin $S = 0$ (singlet S) or $S = 1$ (triplet T). The stable ground state of a molecule is the S_0 state. These processes are either “allowed” (high probability) or “forbidden” (low probability) by quantum mechanical selection rules.

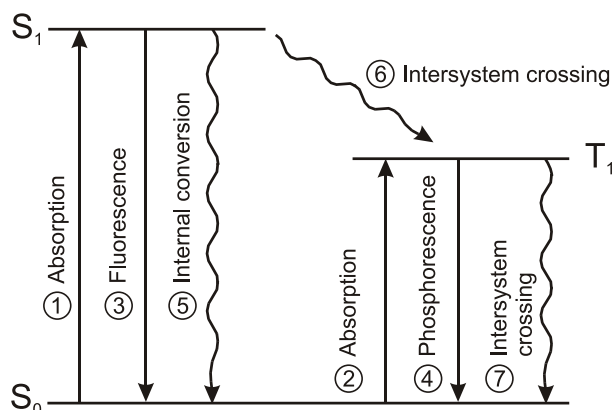


Figure 2.8: Radiative and non-radiative decay processes in a typical organic molecule, after [Turro 1991].

- 1 “Allowed” or singlet-singlet absorption $S_0 + h\nu \rightarrow S_1$.
- 2 “Forbidden” or singlet-triplet absorption $S_0 + h\nu \rightarrow T_1$.
- 3 “Allowed” singlet-singlet emission, called *fluorescence* $S_1 \rightarrow S_0 + h\nu$, characterized by a radiative rate constant, k_F . Typical lifetimes of the excited states are of the order of 10^{-9} to 10^{-6} s.
- 4 “Forbidden” triplet-singlet emission, called *phosphorescence* $T_1 \rightarrow S_0 + h\nu$, characterized by a radiative rate constant, k_P . Typical lifetimes of triplet states are of the order of 10^{-3} to ~ 20 s.

Further processes are non-radiative and involve the generation of phonons $\hbar\Omega$.

- 5 “Allowed” transitions between states of the same spin, called *internal conversion* (e.g., $S_1 \rightarrow S_0 + \hbar\Omega$), characterized by a rate constant, k_{IC} .
- 6 “Forbidden” transitions between excited states of different spin, called *intersystem crossing* (e.g., $S_1 \rightarrow T_1 + \hbar\Omega$), characterized by a rate constant, k_{ST} .
- 7 “Forbidden” transitions between triplet states and the ground state, also called intersystem crossing (e.g., $T_1 \rightarrow S_0 + \hbar\Omega$), characterized by a rate constant, k_{TS} .

Quenching

In addition to the processes described above, there are more non-radiative processes that can lead to a decrease in efficiency in OLED structures.

- Quenching by metal surfaces. Energy of excitons is transferred efficiently to metal surfaces [Chance et al. 1978].
- Quenching by radical ions. Radical cations and anions are known to have a different spectral absorption, which can lead to suppression of EL [Kao and Hwang 1981, p. 473].
- Quenching by impurities. This can be viewed basically an energy transfer to a dopant molecule with a lower quantum efficiency.
- Excimer and exciplex formation. Because of different decay channels the emission is shifted to longer wavelength and often is less efficient [Klessinger and Michel 1995].
- Field-induced dissociation of excitons at high fields ($> 10^6$ V/cm) may occur in EL devices [Popovic and Menzel 1979].

2.4 Optical Effects in OLEDs

As OLEDs are thin-film structures sandwiched between two electrodes they always form a more or less strong cavity. The devices investigated in this work are top-emitting devices, i.e. they have a reflecting anode and a semitransparent top cathode. Figure 2.9 illustrates two types of interference effects that occur in such devices. In the case of wide-angle interference (Fig. 2.9a) light from the emitter interferes with the reflected light from the bottom mirror. The distance d determines which wavelengths will interfere constructively and destructively. In the case of a partly reflecting semitransparent top electrode (Fig. 2.9b), multiple beam interference determines which wavelengths are enhanced and which are suppressed. Here, the length L of the cavity is the relevant parameter. In reality, the emission spectrum of an OLED will be influenced by both types of interference and hence depend on d as well as on L . As a general rule for top-emitting devices, the emission zone should be located roughly $\lambda/4n$ from the

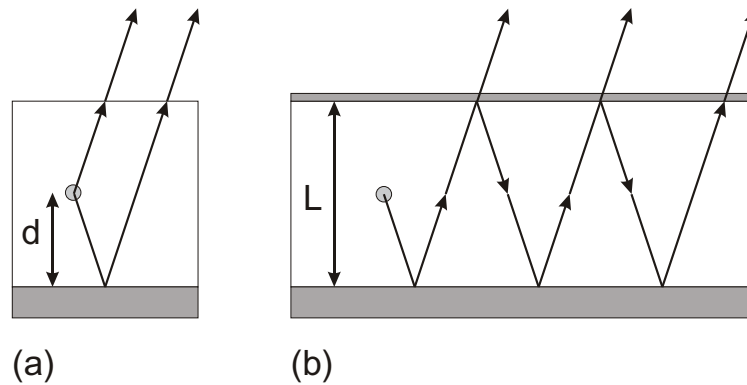


Figure 2.9: Interference effects: (a) wide angle interference (b) multiple beam interference.

bottom mirror, whereby λ is the peak wavelength and n the refractive index of the organic material. In this simple picture phase shifts at the metal interfaces are not considered. For a more precise optical description of the OLED stack one has to know the exact thicknesses of the individual layers and their optical constants, i.e. the complex refractive indices $n + i\kappa$. These values can easily be determined by spectral ellipsometry. Therefore, pure optical simulations are usually in good agreement with the experimental data. If the recombination zone is confined to a very thin region the present optical models show good agreement in most cases with experimental data. The simulation tool used in this work was developed by H. Nakamura [Nakamura 2002]. This program solves the electromagnetic field created by a radiative dipole located in a layered structure. Sommerfeld was the first to treat this with the classical electromagnetic theory, and Chance et al. made systematic and comprehensive studies by using the Dyadic Green's function method [Chance et al. 1978]. Combined with the inclusion of non-radiative processes, the simulator gives a quantitative prediction of outcoupling efficiency, which is defined as a far-field radiant intensity (for a given viewing angle) normalized with the power loss of the dipole. It also gives surface reflection, which is calculated considering the Fresnel coefficients of all the interfaces [Born and Wolf 1999]. This approach is slightly different from the program developed by K. Neyts [Neyts 1998] and used in [Riel 2002]. For a detailed discussion of optical interference effects, see [Neyts 1998; So et al. 1999; Neyts et al. 2000].

2.5 Efficiency and Color

2.5.1 Photometric Efficiency

An important parameter in describing OLED performance is efficiency. For display applications the sensitivity of the human eye (see Fig. 2.10) has to be considered when calculating intensities and efficiencies. Hence, each radiometric unit has its photometric equivalent. For more details see e.g. [Keller 1997]. The efficiency is measured in candela/Ampere (cd/A) and is calculated as follows:

$$\eta_{\text{cd/A}} = \frac{L}{j}, \quad (2.27)$$

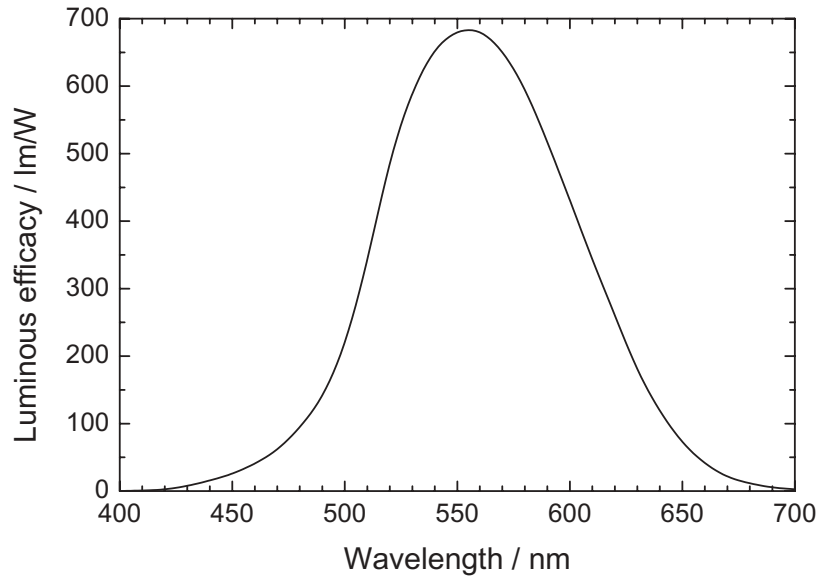
where L is the luminance (in cd/m^2) measured in forward direction and j is the current density (in A/m^2). Technologically of interest is also the efficiency in Lumen/Watt, which relates the optical output (scaled with the human eye response) in Lumen (lm) with the electrical input power in Watts (W). The calculation of this parameter is simple if one presumes Lambertian emission (which is justified in most cases for OLEDs). Hence the luminous efficiency is

$$\eta_{\text{lm/W}} = \frac{\pi \cdot L}{j \cdot V}, \quad (2.28)$$

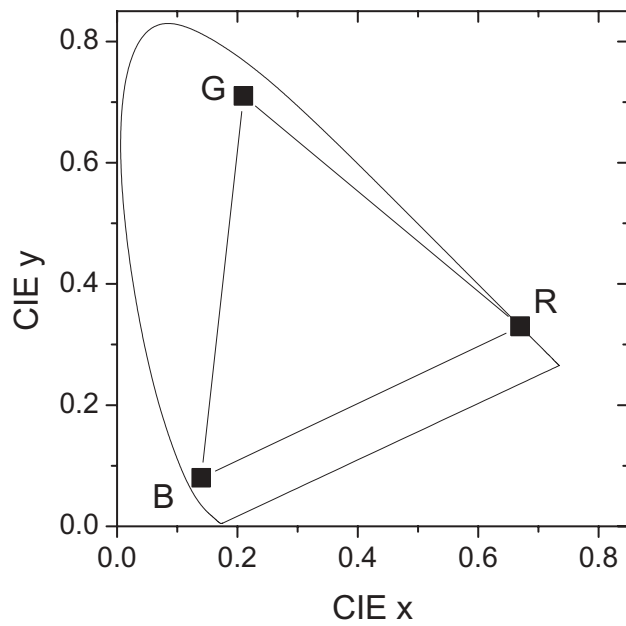
with luminance L , current density j and applied voltage V . Nevertheless, to correctly determine luminous efficiencies of different samples the validity of Lambertian emission has to be confirmed for each diode structure [Tsutsui and Yamamoto 1999].

2.5.2 Color

Any color that can be seen by the human eye can be specified by the 1931 Commission Internationale de l'Eclairage chromaticity diagram (CIE 1931) as a pair of coordinates x, y (see Fig. 2.10). An important standard for display applications is the NTSC (National Television Standards Committee), which defines three primary colors for red, green, and blue. The theoretical limit in lm/W is determined by the human eye's sensitivity (see Fig. 2.10), which has a maximum of 683 lm/W at a wavelength of 555 nm for a day-adapted eye. As a consequence, there will be always a trade-off between saturated color and efficiency. To give an impression of this trade-off, Figure 2.11 shows the maximum theoretical efficiency in lm/W achieved as a function of peak wavelength and full width at half maximum (FWHM) of the spectrum. The NTSC CIE1931 color coordinates are included for comparison. For this calculation a Gaussian



(a)



(b)

Figure 2.10: (a) Eye response curve for the daylight-adapted human eye with a maximum luminous efficacy of 683 lm/W at 555 nm. (b) CIE 1931 x,y chromaticity diagram with NTSC color coordinates for red (0.67, 0.33), green (0.21, 0.71) and blue (0.14, 0.08).

emission spectrum was assumed. Figure 2.11 can be used to estimate the expected maximum efficiency. It is obvious that any RGB emitter should be as narrow as possible to ensure saturated emission. The FWHM of typical OLED emitters in the range of 60 to 100 nm. For example, a red emitter with a FWHM of 100 nm will hardly achieve NTSC red. A green emitter that exactly matches NTSC green has to have a peak wavelength of 530 nm and a FWHM of 50 nm. A reasonable choice for a NTSC blue emitter would have the emission maximum at 465 nm with a FWHM of 60 nm. Whereas for green and blue there is one Gaussian spectrum which exactly matches the NTSC coordinates, the red spectrum can be as broad as 100 nm and still achieves NTSC, but at the expense of efficiency. The maximum theoretical efficiencies for Gaussian spectra that match the NTSC color coordinates are listed in the following table:

| Color | CIE x | CIE y | max. lm/W |
|-------|-------|-------|-----------|
| Red | 0.67 | 0.33 | ~200 |
| Green | 0.21 | 0.71 | ~500 |
| Blue | 0.14 | 0.08 | ~80 |

As a guideline, the synthesis of new materials and the tuning of the spectra should always take into account the above-mentioned trade-off between color coordinates and efficiency.

2.6 Challenges for OLEDs

This section very briefly lists the major challenges encountered in the research and development of organic EL for display applications.

Modeling: A detailed understanding of electrical and optical OLED characteristics will definitely support the synthesis of new materials as well as the design of new device structures. Optical modeling of OLEDs is only one part of the complete description of the device. The electrical description of OLEDs is much more complex because many different processes such as injection, transport and recombination have to be taken into account. Furthermore, the electrical parameters necessary for numerical simulations are usually less well defined than the optical constants. In addition, there is a strong need for appropriate and accurate model descriptions in order to gain a quantitative understanding.

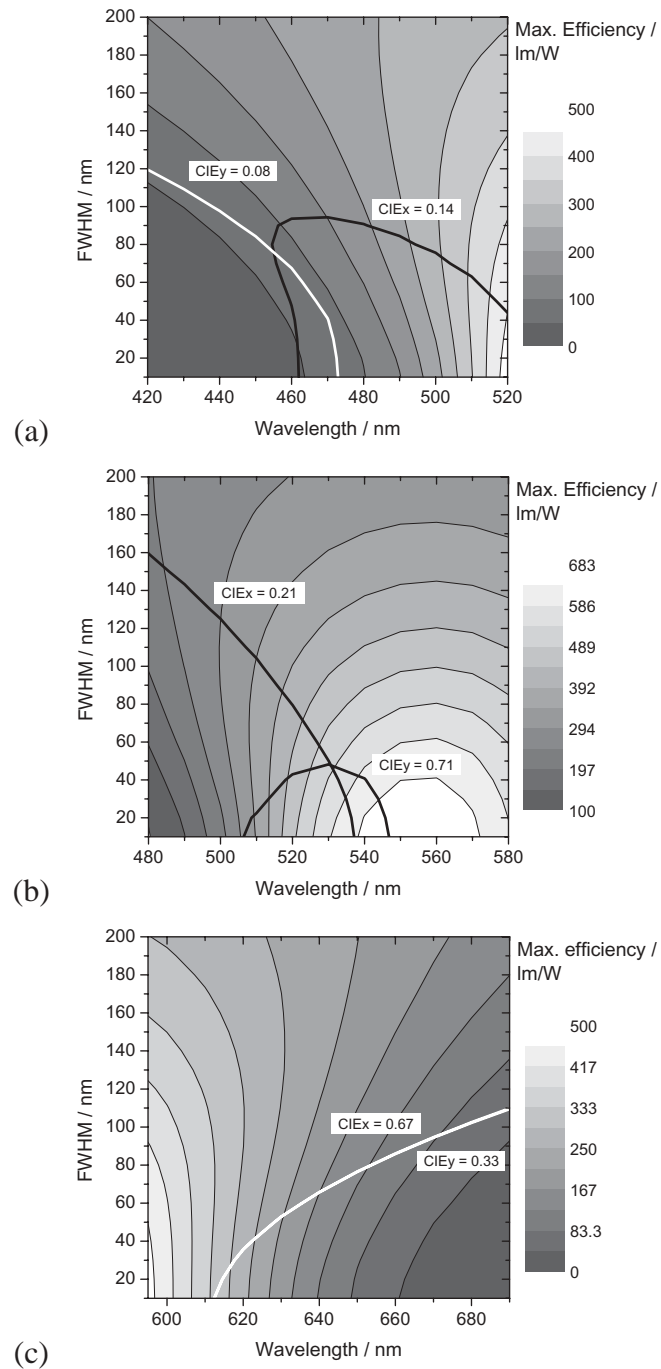


Figure 2.11: Maximum theoretical efficiency in lm/W of a Gaussian emission spectrum as a function of peak wavelength and spectral width. (a) Blue, (b) green, and (c) red spectral range. The $\text{CIE}_{x,y}$ coordinates for NTSC are shown for comparison.

Lifetime: The lifetime of an OLED is usually defined as the time $t_{1/2}$ elapsing from the start of measurement to the time where the luminance reaches half the initial value. For display applications, differential aging is the most severe challenge, i.e. a difference of $\sim 2\%$ in intensity at neighboring pixels can already be detected by the human eye. Therefore, the challenge for a high-quality display is to have less than 2% degradation in intensity within 10,000 h of continuous operation. The detailed origins of device degradation are still the subject of intensive investigations [Sato et al. 1998; Aziz et al. 1999; Kondakov et al. 2003].

Patterning: From a technology point of view, color patterning is a major issue in determining whether OLEDs will become a low-cost technology. Full color with high resolution will be essential for such advanced applications as medium-size and large monitors. Shadow masking for small molecules or spin-coating for polymers are extremely material-consuming processes that waste roughly 90% of the materials. Inkjet printing promises to be more economical and can basically be applied to polymers and small molecules. Other techniques, e.g. silk printing and thermal dye transfer, are still under investigation.

Chapter 3

The Combinatorial System: Device Fabrication and Characterization

3.1 Motivation

The basic approach of any experimentalist is to compare different measurements and draw appropriate conclusions. To facilitate deducing the correct implications it should be ensured that as few parameters as possible are changed between the measurements, ideally only one. In this case, the new measurement result can be associated with the change of this one parameter. Therefore, it has to be the aim of any experiment to provide a basis upon which such comparisons can be made.

OLEDs consist of several (usually three to six) extremely thin organic layers with a total thickness of ~ 100 nm (which corresponds to around 150 molecular layers). Therefore, it is obvious that a change in thickness of one or more layers can have a tremendous impact on the overall performance of the device. In fact, many questions dealing with basic processes and mechanisms in these type of materials and devices can to a certain extent be reduced or translated to the measurement of the thickness dependence of a specific quantity, e.g. operating voltage, current density, efficiency, reflectance, or spectral emission characteristic. However, this implies the ability to fabricate series of devices which are comparable and differ only in one parameter. Therefore, the starting point is to deposit all these individual devices on one substrate in one process run in order to minimize uncertainties due to substrates variations and deposition conditions.

The approach called “combinatorial methods” was deduced from combinatorial chemistry which has become an active field in materials research in recent years, e.g. see [Danielson et al. 1997]. In combinatorial chemistry the main goal is to combine many different components or building blocks systematically in a highly parallel way in order to test or synthesize new materials with the desired properties and superior performance. High parallelism can also be realized in the area of thin film devices where the individual film thicknesses play the essential role. Simple shutter mechanisms can be used during sputtering or thermal evaporation to create wedged or stepped layers on one substrate. In the field of magnetism, layers as thin as monolayers of Fe, Co, Ni, and Cu are of interest and have been investigated by a combinatorial approach [Bloemen et al. 1994].

For device fabrication of small molecule OLEDs, these combinatorial methods were first introduced by Schmitz et al. [Schmidt et al. 1999; Schmitz et al. 1999; Schmitz 2001] for the efficient screening of different organic materials. Recently, this technique has attracted more attention since it has proved to be a powerful tool for optimizing OLEDs and organic solar cell structures [Zou et al. 2001; Sun and Jabbour 2002; Beierlein et al. 2002; Hänsel et al. 2002]. Nowadays, a variety of different OLED materials is available, which drastically increases the possibilities for combining them in different layered structures to achieve stable and efficient devices. Although the basic idea of this combinatorial approach is very simple, it can tackle and answer a variety of challenging scientific and technological questions.

During the research described here, performed at the IBM Zurich Research Lab, several organic materials were investigated not only in terms of the best material combinations but also to understand the electrical and optical dependencies on the materials and the detailed layer sequence. The aim was now to build up a system which can efficiently provide such sets of devices and therefore sets the basis for answering specific questions related to different aspects of OLEDs. Since such a system is not (yet) commercially available a completely new system was designed and set up at IBM ZRL during this thesis research. Besides the device fabrication system, an automated characterization system for electrical and optical measurements is indispensable. Another important task is the processing and appropriate representation of a huge amount of data. This was realized by customized scripts and plotting routines. Since all the mechanical details and the components were designed and developed in house, a major part of the thesis depicts the system in more detail. The next sections will describe the aspects of device fabrication, characterization and representation.

3.2 Evaporation System “Columbus HPO”

At the beginning of this thesis research there were three different evaporation systems available in the Display Technology group to fabricate OLED structures. First, an old MBE system (Varian), which was modified for organic deposition and basically capable of fabricating one sample at a time. Second, there was a simple thermal evaporator (Edwards) with six boats for fabricating identical devices on three substrates. Third, a more advanced evaporation system (Leybold) was available having ten thermal sources and a shutter mechanism to allow the deposition of three different devices on three substrates. Besides incorporating combinatorial device fabrication into the new evaporation system, another task was to combine the advantages and eliminate the weak points of the older systems. One weak point of these systems is clearly the limited amount of devices concerning organic layer thickness variations. In the latter two systems the whole evaporation chamber has to be vented since no load-lock for substrates is available. Since these single devices are characterized sequentially by hand, care has to be taken to avoid statistic measurement errors. As mentioned above, one crucial point of device investigation is always either to have a reference device or even better to have a series of devices to observe certain trends. In order to overcome the uncertainty of successive evaporation runs and different substrates, many intentionally different samples are incorporated on one single substrate. Compared to polymeric devices small molecule OLEDs have the advantage that complex multilayer structures can be easily fabricated by sequential deposition of many different layers.

Figure 3.1 shows a photograph of the setup (called “**Columbus HPO**”) which consists of a temperature and rate control rack, a vacuum chamber and a glovebox (from left to right). The system can be divided into fabrication and characterization parts with four major components

- 1) the base chamber with the effusion cells
- 2) the recipient with the rotating substrate holder and sliding shutter mechanism
- 3) the load/storage chambers for mask, sample and cell transfer and storage
- 4) the glovebox with the characterization system under inert atmosphere.

These components will be described in more detail in the following sections.

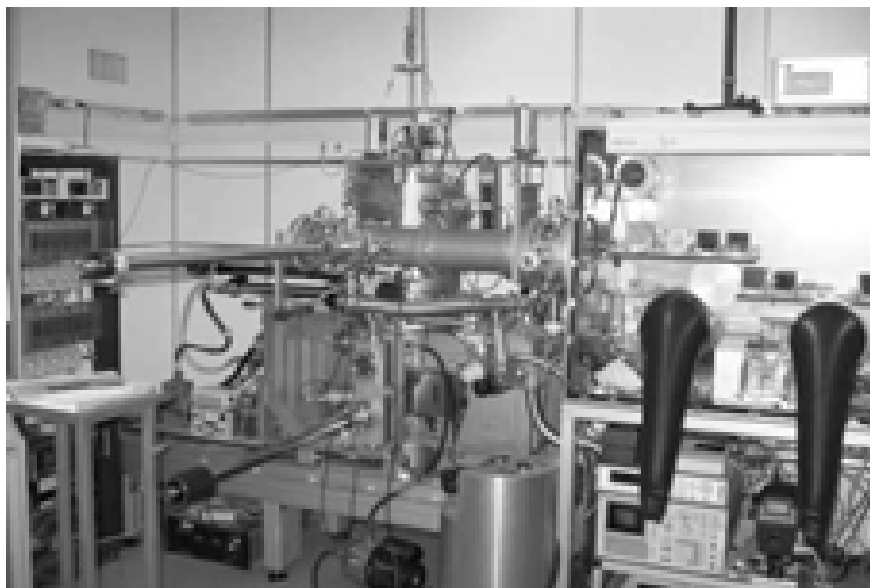


Figure 3.1: Photograph of “Columbus HPO” system consisting of temperature and rate control rack, evaporation chamber, glovebox with characterization equipment (from left to right).

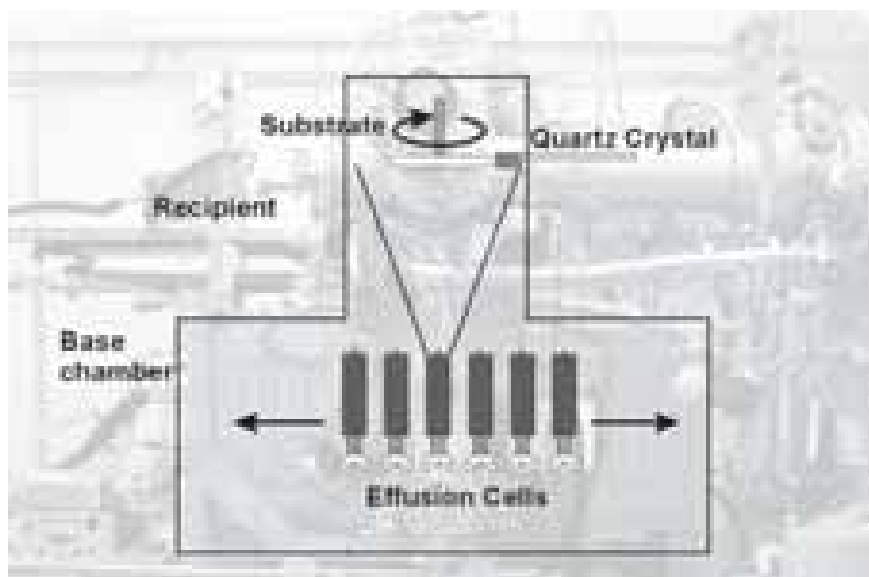


Figure 3.2: Schematic front view of the evaporation chamber. The distance between the evaporation sources and the substrate is approximately 400 mm.

3.2.1 Base chamber

The base chamber shown in Figure 3.2 as a schematic front view is rectangular in shape with dimensions of about $1200 \times 500 \times 500 \text{ mm}^3$. Water lines are welded to the outside of the chamber to allow the walls to be heated in case the system is vented to prevent water condensation to ensure short pump-down times. It is equipped with a turbo pump (Pfeiffer TMU 1601) which has a delivery rate of about 1600 l/s for N_2 . This molecular drag pump is backed with an oil-free backing pump (Leybold EcoDry L), which has a delivery rate of $40 \text{ m}^3/\text{h}$ and reaches a backing pressure of $4 \times 10^{-2} \text{ mbar}$. The turbo pump is mounted horizontally below the main chamber to save space. There is a mesh in front of the rotary blades for protection. This reduces the flow rate by about 30%, but it is still enough to reach a base pressure well below $1 \times 10^{-8} \text{ mbar}$ in the main chamber. During evaporation of the organic materials the pressure stays below $3 \times 10^{-8} \text{ mbar}$ and during evaporation of metals it is below $1 \times 10^{-7} \text{ mbar}$. The pressure is monitored either by a hot cathode (Varian UHV 24) Bayard-Alpert type or cold cathode (Varian 525) ionization gauge. A leak valve is attached to the base chamber for either venting the system or adjusting a certain pressure in the range of 10^{-8} to 10^{-5} mbar to investigate the influence on device performance of different base pressures during evaporation.

The system is equipped with twelve effusion cells, each with individual temperature control. Usually, eight of them are used for organic materials and four are used to evaporate metals or materials with a higher vapor pressure. The cells have up to three Ta heat shields, depending on their operating temperature, wrapped around the heating filaments to reduce radiation losses and avoid heating neighboring cells. To ensure accurate temperature control and stable evaporation rates all effusion cells feature a thermocouple (ten cells with type K, and two with type C for temperatures as high as 1350°C). The organic materials are evaporated from quartz glass crucibles with typical rates from 0.01 to $2 \text{ \AA}/\text{s}$. A Leybold Inficon XTM/2 quartz balance is used to monitor the evaporation rates. The temperature to reach these rates naturally depend on the organic material but typically ranges between 180 and 500°C . Metals are evaporated from pyrolytic boron nitride (pBN) crucibles, and the temperature range for rates of $\approx 1 \text{ \AA}/\text{s}$ is 450°C (Mg) to 630°C (Ca) and 1100 – 1350°C for Ag and Al. The cells are controlled by Eurotherm 2408 temperature controllers and powered by Eurotherm TE 10A thyristors.

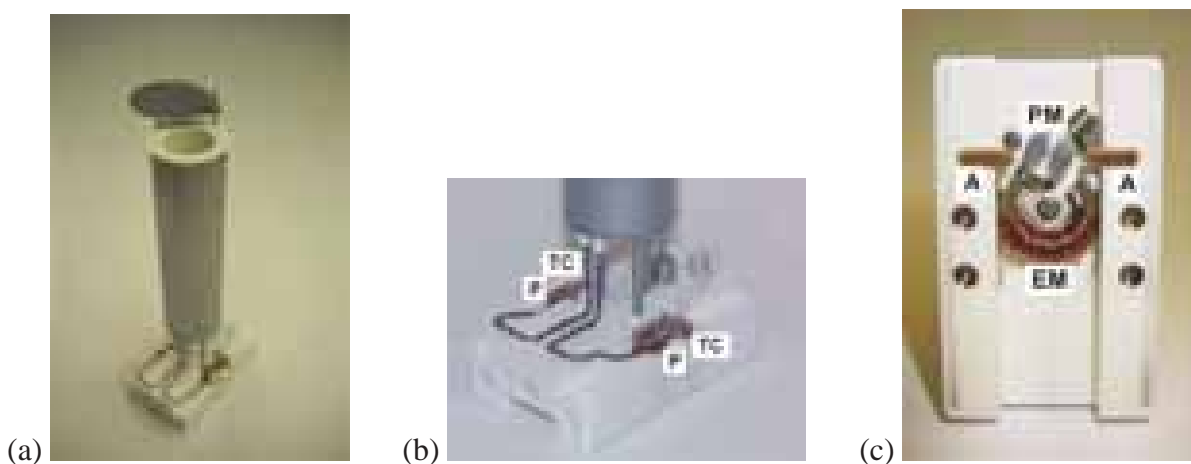


Figure 3.3: Details of the custom-built effusion cell. (a) Cell with individual shutter. (b) Socket with power (P) and thermocouple (TC) contacts. (c) Shutter actuator contacts (A), permanent magnet (PM) and electromagnet (EM) of the bistable shutter mechanism. See text for details.

Each cell has its own shutter to minimize cross contamination. Figure 3.3 shows details of such a cell and its socket. This socket has six electrical contacts in total: one pair for power (P), one pair for the thermocouple (TC) (Fig. 3.3b), and one pair for the shutter actuator (A) (Fig. 3.3c). The shutter actuator (Fig. 3.3c) was home built and consists of a permanent magnet (PM) and an electromagnet (EM), which is shaped like a 270° torus. A short current pulse (≈ 1 A for ≈ 0.5 s) turns the permanent magnet to one of the bistable positions, whereas a current pulse with reversed polarity forces it into the opposite position. By this 90° rotation of the permanent magnet and the attached shutter, each cell can be opened and closed individually. The cell shutter mechanism and the cell socket are a proprietary design and development necessary to transfer the evaporation cells as a unit into vacuum (see Sec. 3.2.3).

The necessary number of evaporation cells is given by the complexity of the organic multilayer structures. For example, a direct comparison of different host/guest systems requires at least six or more cells. For a highly efficient structures, this would comprise the following materials: hole injection, hole transport, host, guest 1, guest 2, electron transport, and usually one or two cathode materials. In a conventional evaporation system with spatially fixed cells the arrangement of the cells would lead to a large evaporation angle and hence non-uniform layers. An increase of the cell–substrate distance could improve the uniformity, but the material

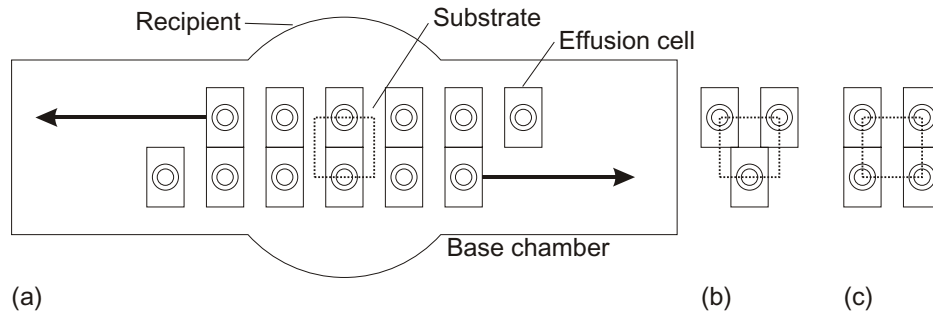


Figure 3.4: Top view of the arrangement of the effusion cells in the base chamber (diameter of recipient in dotted line). The alignment of the substrate (located in the recipient 400 mm above the cells) is shown in dotted lines. Cell alignment for (a) single material or co-evaporation (b) double doping (c) triple doping experiments.

consumption will increase with the square of the distance, which is definitely not practicable when only small amounts of materials are available.

In the new “Columbus HPO” system, the effusion cells are arranged in two rows of six cells (see Fig. 3.4a). These two rows can be moved sideways independently, which allows the alignment of the cells laterally below the substrate in different positions. Figure 3.4a shows the cell alignment for normal evaporation of a single material or for co-evaporation of two materials. The cells in the front and the back rows, which contain the dopant and host material, respectively, are centered with respect to the substrate. For double or triple doping experiments the cells are aligned as shown in Figure 3.4b and c, respectively. The tooling factors for each cell are determined at its actual position. For doping experiments the host cell is placed in the back row, whereas different dopants cells can be placed in the front row and shifted to the appropriate position as needed. Since there is only one quartz crystal monitor in the system, doping experiments are carried out in the following way: the dopant rate is measured alone right before the cell shutter of the host material is opened. Since the cells are temperature-controlled, a constant dopant flux is achieved during co-evaporation. In order to verify that the dopant flux has not changed during deposition, the dopant flux is measured again after the deposition. Owing to the precise temperature control, it stays constant within a few percent of the initial rate.

For reliable device comparisons, a certain degree of uniformity on the substrate must be

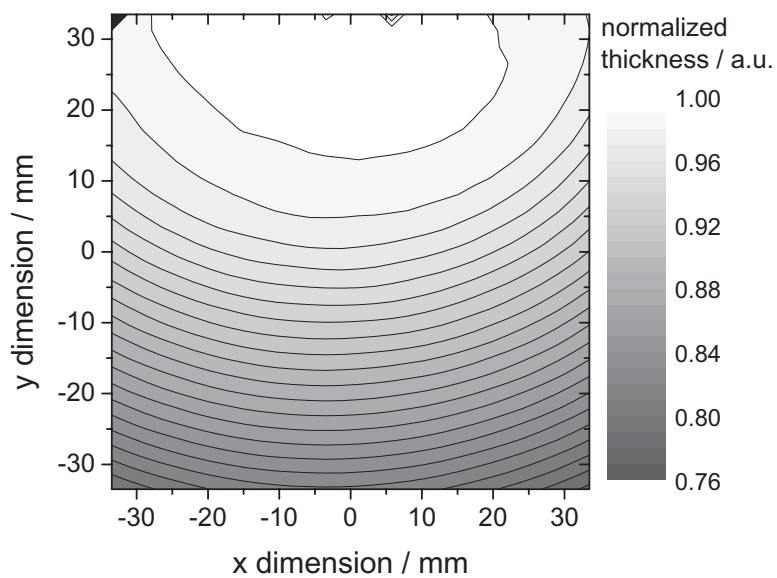
verified and guaranteed. The uniformity of organic layers is measured by ellipsometry using silicon substrates. Figure 3.5a and b show the normalized thickness of a nominally 1000-Å-thick film of Alq₃. These uniformity maps are based on 400 measured data points. The substrate in Figure 3.5a was not rotated during evaporation, which yields in a non-uniform layer with 24% difference between minimum and maximum thickness. This thickness distribution represents the off-center position (see Fig. 3.4a) of the cell below the substrate. It is clearly visible from Figure 3.5b that substrate rotation leads to a much more uniform layer, which shows a uniformity of better than $\pm 3\%$ over an area of $66 \times 66 \text{ mm}^2$. This emphasizes that rotation is absolutely necessary for excellent layer uniformity. The influence of the described thickness non-uniformity on I - V EL characteristic and efficiency of OLED structures is shown in Section 3.5.2.

3.2.2 Recipient

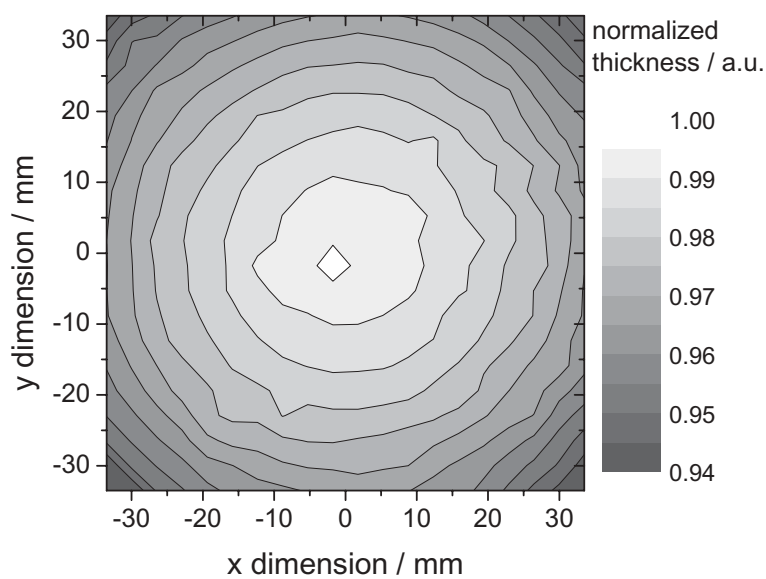
The core piece of the recipient is the rotating sample holder, which has a sliding shutter in close proximity ($\approx 0.5 \text{ mm}$) to the shadow mask and the substrate. Again, this sample holder is a proprietary design and development and allows a maximum in flexibility in terms of device fabrication. Figure 3.6 shows a photograph and a schematic view to visualize the function of the sliding shutter on the rotating sample holder. The shutter is controlled from outside by a stepper motor via a UHV linear transfer. With this mechanism it is possible to deposit staircase-like structures as they are shown and explained in Section 3.3. The maximum substrate size is $80 \times 80 \text{ mm}^2$, and typical substrate patterns and details are shown in Section 3.4.1.

3.2.3 Load Locks and Storage Chamber

As pointed out above, another advantage of “Columbus HPO” over the older systems is a small load lock attached to the glovebox to minimize substrate transfer and pump-down times to the vacuum chamber. Furthermore, shadow masks can also be transferred via the same load lock and the main chamber does not have to be vented, which makes the system even more flexible. This load lock reduces the loading procedure to about 10 minutes. As a consequence, the main evaporation chamber always stays under vacuum, which means that the materials need not be outgassed before evaporation. A table with integrated heater in the load lock chamber can be



(a)



(b)

Figure 3.5: Uniformity of organic layers ($\sim 1000 \text{ \AA}$ Alq₃) over an area of $66 \times 66 \text{ mm}^2$. (a) Without substrate rotation $\pm 12\%$ and (b) with substrate rotation $\pm 3\%$.

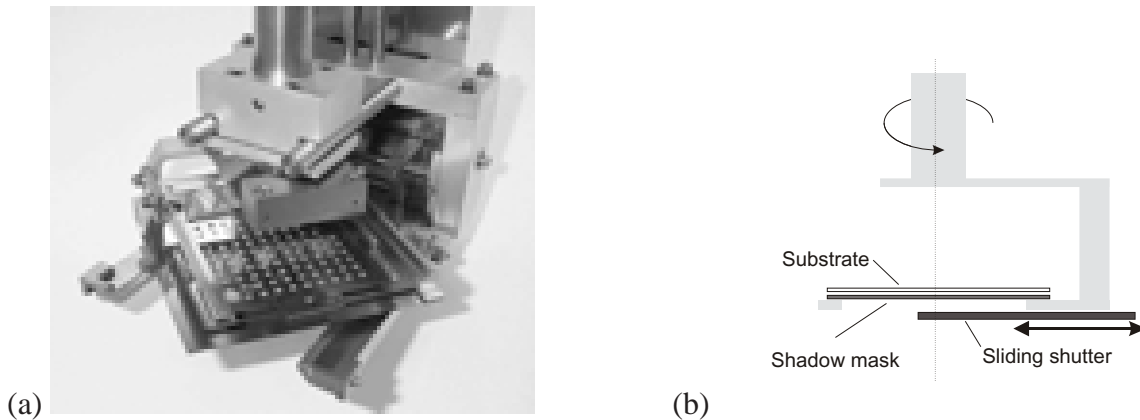


Figure 3.6: (a) Rotating substrate and shadow mask holder with sliding shutter for fabricating staircase-like structures. (b) Schematic view.

heated up to 300°C either in argon atmosphere or under vacuum. This feature is important to efficiently remove residual moisture or other contaminants on the substrate. An additional gas inlet can also be used for special treatments, e.g. annealing steps under various atmospheres.

The storage chamber contains a trolley, which can store up to six shadow masks and two substrates. These masks (see Fig. 3.7) consist of a frame and a thin (0.05–0.2 mm) sheet metal, which is patterned by laser cutting for various complex device architectures. With a linear transfer system these masks and substrates can be exchanged arbitrarily under vacuum conditions. Therefore, even complex device structures with more than two mask steps, e.g. three terminal devices, transistors or other structures can be fabricated (see Fig. 4.8, p. 78).

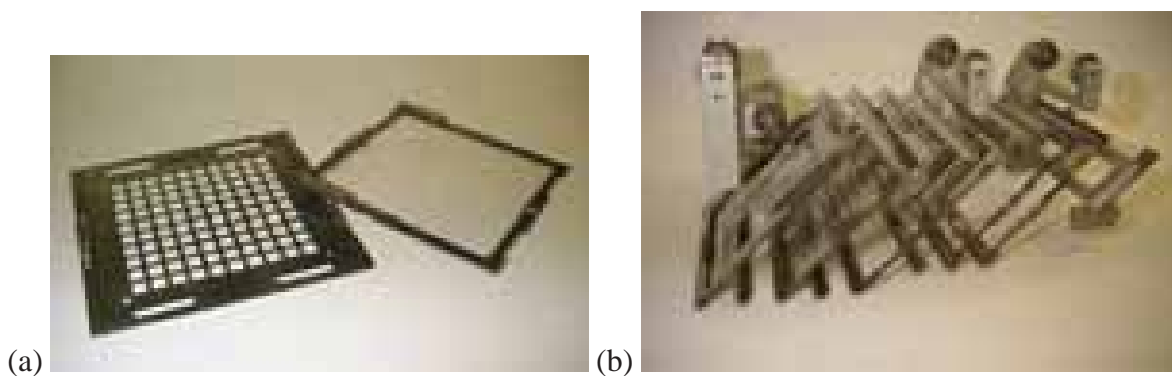


Figure 3.7: (a) Shadow mask and substrate holder frame and (b) trolley for storage and transfer of six masks and two substrates.

Another special feature of the “Columbus HPO” is the load lock for materials. This is basically a small antechamber separated by a rectangular valve from the main chamber and equipped with a linear transfer system, which serves to load and unload effusion cells. Thus, entire effusion cells can be exchanged without venting the main chamber. This allows the refill and exchange of material within less than half an hour without contaminating the other cells by exposing them to atmosphere.

3.2.4 Glovebox

OLEDs are prone to degrade when operated or stored under ambient conditions. Therefore, the evaporation chamber is directly connected to an argon glovebox (Mecaplex Special) to avoid exposure to oxygen or moisture. This inert gas system has a gas purification unit which reaches less than 1 ppm O₂ and H₂O. Figure 3.8 shows a photograph of the whole glovebox system comprising an automated device characterization setup inside the box, which will be described in Section 3.5 in more detail. The control and characterization equipment including *xy*-stage control, parameter analyzer and spectrophotometer are located below the glovebox.

3.3 Combinatorial Device Configurations

This section will give an overview about the possibilities of typical combinatorial device structures. As mentioned above, a sliding shutter with additional suitable manipulation capabilities allows the fabrication of a variety of different device series.

3.3.1 Thickness-Dependent Device Series

The staircase structure (Fig. 3.9a top) forms the basic element of combinatorial device fabrication. Such structures can be used to investigate the thickness dependency of single layer structures, e.g. not only the current flow, but also the photoluminescence of Alq₃ (see Sec. 6.1). Other examples are multi-layer stacks where one component is varied in thickness whereas the other layers are kept constant (Fig. 3.9a bottom), e.g. bilayer anodes (see Sec. 5.2). These staircase structures are the building blocks for all further combinatorial device architectures.

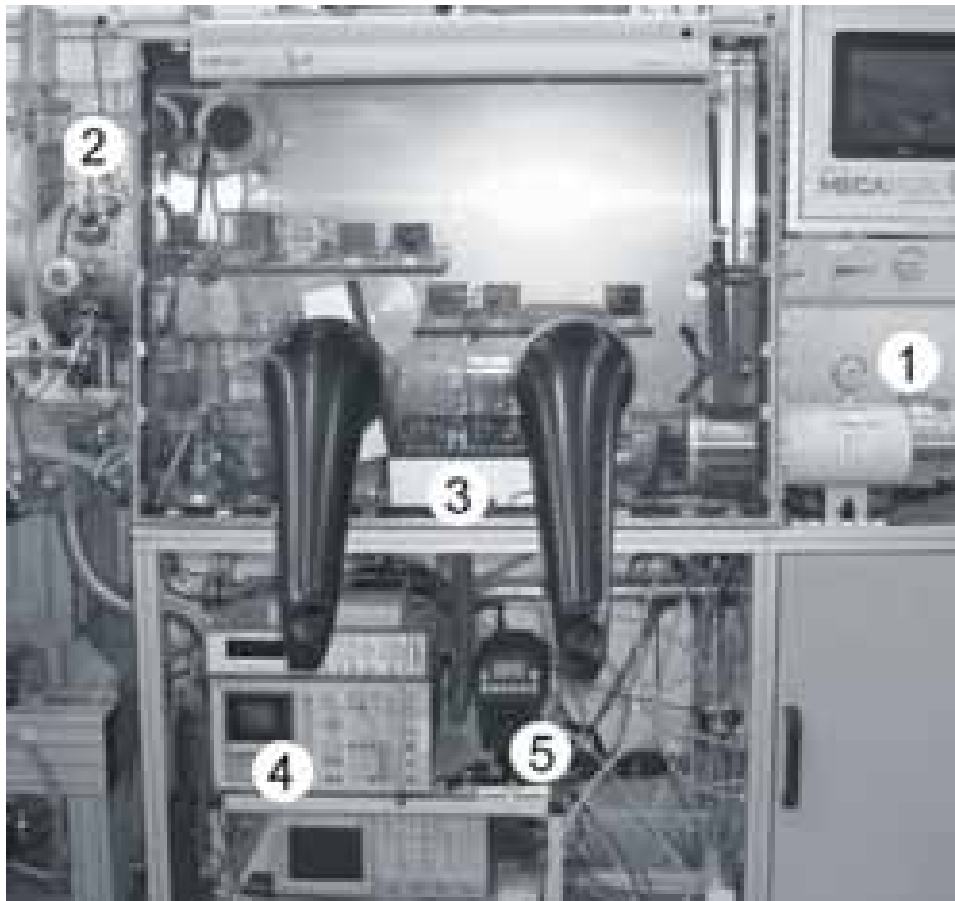


Figure 3.8: *Glovebox system with characterization setup: (1) load lock to ambient, (2) load lock to vacuum, (3) xy-stage characterization system, (4) parameter analyzer, and (5) spectrophotometer.*

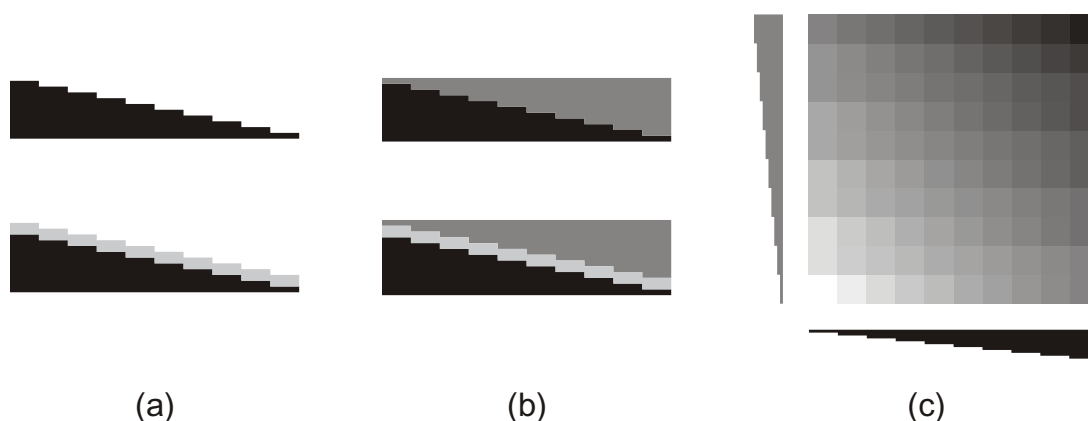


Figure 3.9: Schematic view of staircase-like device structures, which can be created with a stepwise sliding shutter. (a) Single-layer staircase deposition, (b) double layer with 180° rotation of shutter after deposition of the first layer, and (c) double layer with 90° rotation after the first layer. Constant layers can be added to each structure. In practice, besides the sliding shutter a mask with the appropriate openings is used to define the organic or electrode patterns.

3.3.2 Position-Dependent Device Series

The substrate holder is designed in such a way that the shutter can be rotated in 90° steps with respect to the substrate. In the case of a 180° rotation an opposing staircase of a second material can be deposited, e.g. in such a way that the total layer thickness is constant. Such device structures allow one to investigate position-dependent characteristics of structures and devices. One example is a two-layer structure where the interface of the first and the second layer is located at various distances from the substrate (Fig. 3.9b top). A second example (Fig. 3.9b bottom) is to shift a third layer through the organic stack whilst keeping the rest of the structure unchanged. This type of architecture is used for example, in delta-doped devices where the dopant layer is shifted within the host layer. This will be discussed in more detail in Section 6.2.

3.3.3 Combinatorial Matrix

As mentioned in the previous section the shutter can be rotated in 90° steps with respect to the substrate. After the deposition of the first staircase the shutter is rotated by 90° and a staircase

of a second material is deposited. This results in structures having all possible combinations of layer thicknesses arranged in a matrix (Figure 3.9c). This enables detailed studies of the influence of layer thicknesses in a two and multi-layer material system. A matrix where hole and electron transport layers are varied as described above will be discussed in Section 4.1.1.

3.3.4 Further Sample Configurations

Split Matrices

For a standard OLED structure two shadow masks, i.e. the organic mask and the cathode mask, are generally sufficient. However, for more sophisticated structures and direct comparisons more than just two shadow masks are needed. The “Columbus HPO” system was designed with extreme flexibility such that up to six different masks can be exchanged without breaking the vacuum. This allows the deposition of split combinatorial matrices, e.g. where two materials can be directly compared on one substrate.

As an example, the direct combinatorial comparison of single/double-doped devices (see Sec. 4.3.2) will be explained. First, the hole transport layer is varied step-wise in y -direction for all devices. By changing to a shadow mask with openings only on every other column, a uniform layer of the first host/guest system is deposited exclusively on the even columns. Then, this mask can be rotated by 180° with respect to the substrate, and the second host/guest system is deposited only on the odd columns. By changing back to the original organic mask a staircase of electron transporting material in x -direction is deposited. The result is the interdigitation of two 5×10 matrices having identical anodes, cathodes, staircased hole transporters and electron transporters and differing only in the doped emission layers. This is a very efficient way to optimize and directly compare two host/guest system emission layers.

For completeness, an example of an even more complex combinatorial matrix will be given. The substrate is split twice in two orthogonal directions, i.e. two different anode materials deposited on the even/odd columns and two different cathode materials for the even/odd rows. Figure 3.10 visualizes a general case of such a complex structure. First, two anode materials (1,2) are deposited in alternating columns followed by a first organic staircase of double step size (3) and a perpendicular staircase of a second organic material (4). Finally, two different cathode materials (5,6) in alternating rows are evaporated. This results in a 5×5 organic combinatorial matrix where each of its 25 individual cells consists of four devices

(grouped with dotted squares in Fig. 3.10) which have identical organic structures but four combinations of electrode configurations. With respect to charge carrier injection capabilities of the electrodes these four combinations could be realized in hole-only, hole-electron (standard OLED structure), electron-hole (inverted OLED structure) and electron-only configurations. It is obvious that this general structure is very helpful in investigating thickness dependencies of the organic layers combined with the influence of injection from the different electrodes. With a conventional evaporation system with sequential runs this would be an extremely time consuming if not impracticable experiment because of uncertainties due to run-to-run variations.

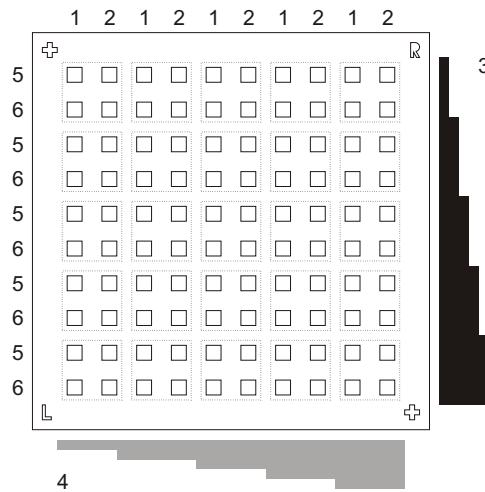


Figure 3.10: Schematic view of a complex combinatorial matrix. Two anode materials (1,2) are deposited in columns, an organic combinatorial matrix (3,4) is followed by evaporation of row-wise cathode materials (5,6). This results in a 5×5 matrix having 4 subsets of four different electrode combinations. See text for details.

Split Substrates

The substrate frame holder is designed in such a way that instead of a $80 \times 80 \text{ mm}^2$ substrate it can also hold, for example, 10 individual stripes of $8 \times 10 \text{ mm}^2$. This allows the deposition of identical organic stacks by a single evaporation run on top of ten differently treated anode

substrates. This enables the optimization of, for example, plasma treatment parameters such as gas mixture, plasma power, pressure, and time.

Potential Sensing Devices

More complex device structures, e.g. those with more than two electrodes, can be fabricated due to the capability of changing masks *in situ*. A schematic device configuration with a third electrode in addition to the anode and the cathode is shown in Figure 4.8 (page 78). This third electrode can be inserted into the organic stack at various positions and senses the potential as discussed in Section 4.2. The structures are basically created as described in Section 3.3.2 except that the mask is changed for evaporating the thin intermediate metal pad. To ensure a direct comparison, reference devices with the same organic structure but without the third metal pad are fabricated in the same evaporation run.

3D Combinatorial Devices

In special cases the samples under investigation can be modified after initial characterization and the parameter of interest can be remeasured. This modifications include uniform treatments or evaporation of additional layers of constant thickness. For example, the bottom electrode can be oxygen-plasma-treated several times and the change in reflectivity can be measured after each oxidation step. These successive modifications and characterizations in combination with a 2D matrix lead basically to a 3D combinatorial matrix. For example, a capping layer for outcoupling improvement can be added to a top emitting structure. First, the optical output of devices on a substrate having an organic 2D matrix stack (see Sec. 3.3.3) is measured. Second, a uniform capping layer is evaporated on top of all 2D devices and the output is remeasured. By repeating the second step several times, essentially a third dimension is added in the parameter space. Especially in the case of photoluminescence, transmission or reflection measurements it is easy to add a third dimension. As mentioned above, to some degree it is also possible to add a third dimension via electro-optical measurements on completed OLED structures, e.g. top-emitting devices when an additional cathode or capping layer is successively added. Because of the short pump down times (≈ 10 min) of the “Columbus HPO” load-lock system such 3D combinatorial matrices can easily be realized.

3.4 Device Fabrication

3.4.1 Substrates and Fabrication

The evaporation system was designed to handle any substrate size up to $80 \times 80 \text{ mm}^2$. The substrates for the 10×10 matrix were either Corning 1737 or Schott AF45 glass plates with a dimension of $80 \times 80 \text{ mm}^2$ and a thickness of 1.1 mm. Commonly used substrate layouts (anode pattern and cathode pad) are shown in Figure 3.11. The substrates for combinatorial devices consist of a regular pattern of individual electrically isolated devices arranged in a 10×10 matrix (Fig. 3.11a). The OLEDs are defined by the intersection of the vertical anode stripe with the horizontal cathode stripe, which results in an active area of $2 \times 2 \text{ mm}^2$ (see Fig. 3.11b). This 10×10 layout is difficult to encapsulate and therefore all measurements (see Sec. 3.5) on these matrices are carried out in the glovebox. For extensive lifetime measurements other substrate patterns (shown in Fig. 3.11b and c) are used which can be easily encapsulated and are compatible with devices from other evaporation systems, the encapsulation procedure and the lifetest setups.

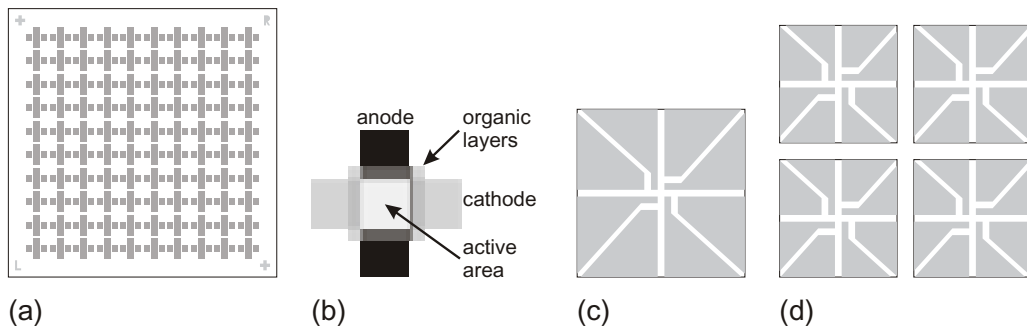


Figure 3.11: Substrates used in “Columbus HPO” system. (a) Substrate $80 \times 80 \text{ mm}^2$ for 10×10 combinatorial devices. (b) Detailed device structure. (c) Standard $50 \times 50 \text{ mm}^2$ pre-patterned glass substrates (d) Four $35 \times 35 \text{ mm}^2$ pre-patterned substrates.

The cleaning procedure of the substrates is as follows: the blank glass plates are successively cleaned for 5 minutes each in an ultrasonic bath in acetone and iso-propanol (VSLI grade). After blowing dry with nitrogen they are exposed to an oxygen plasma for 3 minutes in a barrel asher (TePla Plasma System 200). Immediately afterwards, they are transferred into an electron beam evaporator (base pressure $< 10^{-7}$ mbar), where the anode metals are

deposited. Typical anode metals such as Ti, Al, Ni, Mo, Pt, Ir and others are evaporated, however, Ti 50 Å/ Ni 700 Å is the preferred anode structure. These anode substrates are stored under inert glovebox conditions until they are used for sample preparation. Shortly before organic deposition the anode substrates are exposed to an oxygen plasma to increase the work function, to improve reproducibility, and to achieve better overall performance [Beierlein et al. 2000]. Typical plasma conditions are 0.2 mbar O₂ pressure, 300 W plasma power for 10 minutes. By means of pyrometer measurements it has been quantified that the temperature of the substrate rises to around 60°C during this treatment. The substrates are immediately loaded via the glovebox into the vacuum load lock, where they are transferred through the storage chamber into the evaporation chamber. About 15 minutes later, the evaporation of the organic material can be started at a base pressure of 10⁻⁸ mbar. A Leybold Inficon XTM/2 quartz balance is used to monitor the evaporation rates. The organic materials are typically deposited at rates ranging between 0.01 to 2 Å/s. After finishing the organic stack the organic mask is exchanged *in situ* by the cathode mask and typically Ca/Mg is evaporated as cathode. The evaporation rates of these metals are kept around 1 Å/s and the thickness is usually Ca 150 Å/ Mg 50 Å for semi-transparent cathodes.

3.4.2 Organic Materials

This section gives a brief overview of the organic materials used in this work. The chemical structure of these materials are depicted in Figure 3.12.

Alq₃ (tris(8-hydroxyquinolate) aluminum) is the archetype material of OLEDs. It was used as emitter material in the first publication of efficient low-voltage operation in organic materials [Tang and Van Slyke 1987]. Since then, it has been widely used in various structures, and many different methods have been applied to investigate its properties. Alq₃ is used as electron transport material and exhibits a field-dependent electron mobility of $\mu_e = 10^{-7} - 10^{-5} \text{ cm}^2/\text{Vs}$ at fields between 10⁵ and 10⁶ V/cm [Tang and Van Slyke 1987; Kepler et al. 1995; Barth et al. 2001]. A zero field hole mobility on the order of $\mu_{0,h} = 10^{-11} \text{ cm}^2/\text{Vs}$ was determined by time-of-flight measurements. The hole mobility μ_h at fields on the order of 10⁶ V/cm is still more than two orders of lower than the electron mobility [Naka et al. 1999].

N,N'-di(naphthalene-1-yl)-N,N'-diphenylbenzidine (NPB) or 2,2',7,7'-diphenyl-amino-spiro-9,9'-bifluorene (STAD) were used as hole-transporting material. These triphenylamines

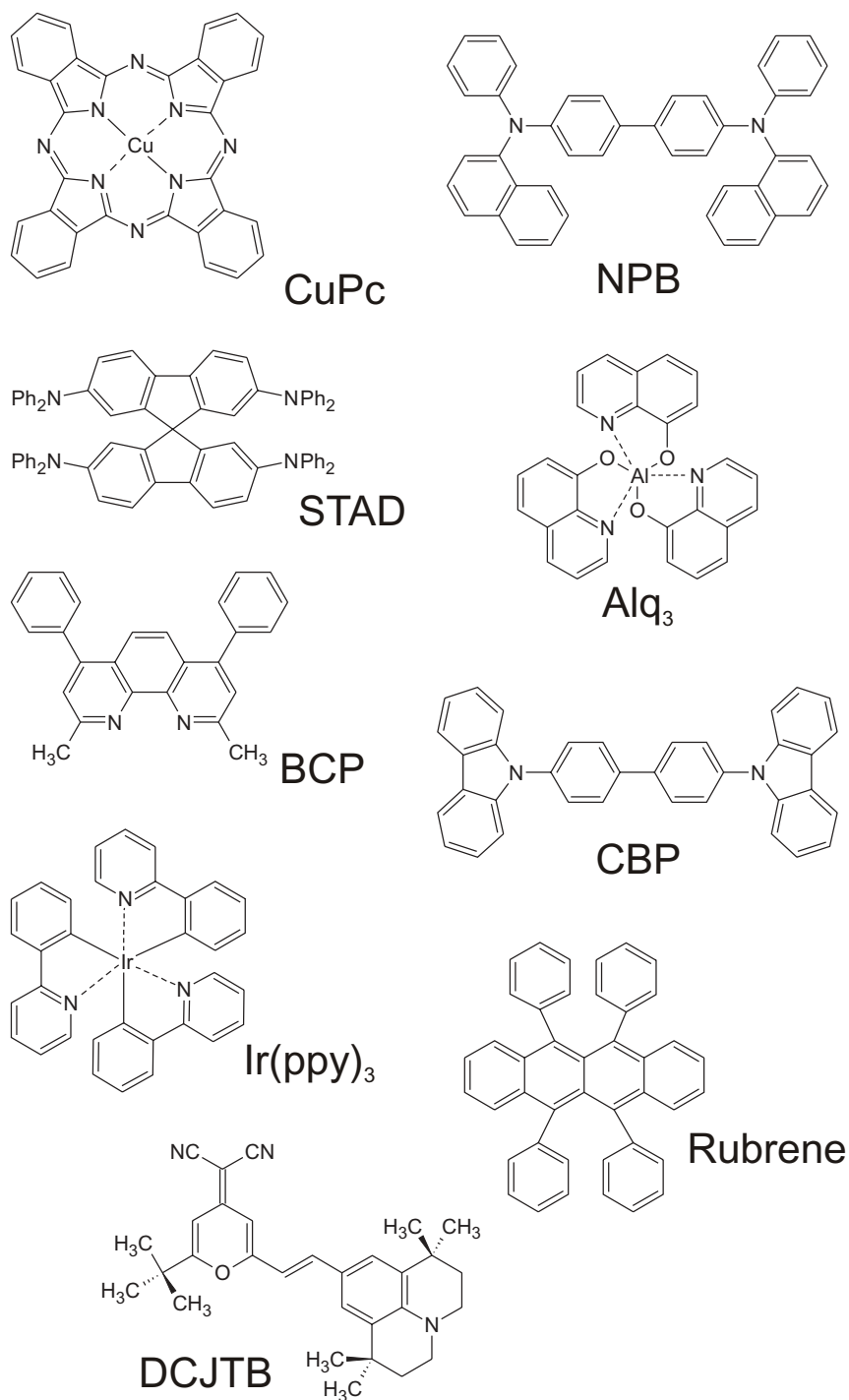


Figure 3.12: Organic materials used for device fabrication. For HOMO and LUMO values see Table A.1 on page 197.

are good hole-transporting layers (HTLs) and show hole mobilities on the order of $\mu_h \approx 10^{-3} \text{cm}^2/\text{Vs}$ [Bach et al. 2000]. Since STAD shows a higher glass transition temperature of $T_g = 133^\circ\text{C}$ than NPB ($T_g = 96^\circ\text{C}$) it is advantageous for achieving devices with higher thermal stability [Spreitzer et al. 1999].

CuPc (copper phthalocyanine) is used as buffer layer between the anode and the HTL and improves the stability and reproducibility of the devices [Van Slyke et al. 1996]. As CuPc exhibits excellent film-forming properties, many different phthalocyanines with different central metal atoms have been synthesized and investigated in detail [Simon and André 1985].

Doped structures have been realized with two fluorescent dopants 5,6,11,12-tetraphenyl-naphthacene (Rubrene) and 4-(dicyanomethylene)-2-*t-butyl*-6(1,1,7,7-tetramethyljulolidyl-9-enyl)-4*H*-pyran (DCJTB). Rubrene is a highly fluorescent dye [Mattoussi et al. 1998] and has been used to fabricate long-term stable devices [Sato et al. 1996; Sano et al. 1996; Vestweber and Rieß 1997]. DCJTB was introduced recently as an efficient red dopant with a PL emission maximum around 615 nm [Chen et al. 2000]. DCJTB is used together with Rubrene in double-doped structures to enhance efficiency and prolong their lifetime (see Sec. 4.3.2).

More efficient and in general more complex OLED structures use phosphorescent materials which harvest singlet and triplets [Baldo et al. 1998]. The iridium complex tris(2-phenylpyridine) iridium ($\text{Ir}(\text{ppy})_3$) has been reported as a green emitter [Baldo et al. 1999]. In the meantime many other Ir-complexes emitting in the visible range have been synthesized [Lamansky et al. 2001]. $\text{Ir}(\text{ppy})_3$ used in this work was obtained from Covion Organic Semiconductors GmbH. Since $\text{Ir}(\text{ppy})_3$ utilizes also the triplet states, an organic wide-gap material has to be used as host.

CBP (4,4'-N,N'-dicarbazole-biphenyl) with its HOMO–LUMO gap of 3.1 eV is well suited for this purpose, the emission layer consists of CBP co-evaporated with typically $\approx 5\%$ $\text{Ir}(\text{ppy})_3$. CBP is believed to have a rather high electron mobility (even higher than that of Alq_3) although it has not been reported. Typical triplet lifetimes are on the order of 500 ns to 100 μs and thus the exciton diffusion length is usually much greater than the typical device thickness of 100 nm. Therefore, an additional layer which efficiently blocks excitons is necessary [Baldo et al. 1999].

BCP (2,9-dimethyl-4,7-diphenyl 1,10-phenanthroline) is a material with a HOMO–LUMO gap of 3.4 eV, which is larger than that of CBP and efficiently blocks excitons from reaching the adjacent layer. Owing to the extremely low HOMO level, BCP also blocks holes from reaching the cathode and thereby improves the charge balance.

HOMO and LUMO levels of the above and further organic materials are compiled in Table A.1 on page 197.

3.5 Device Characterization

3.5.1 Automated Measurement Setup

After device fabrication the substrate is characterized in the glovebox under argon atmosphere. Since there are 100(!) samples on a single substrate it is necessary to perform automated measurements and data processing. For this task, a proprietary multipurpose computer controlled characterization system has been designed and set up. Various programs written with the software tool LabViewTM are used to configure the setup and acquire the data [Hofmann 2001]. The computer-controlled *xy*-stage features a special probe head which can be moved in the *z*-direction. This probe head has four electrically independent needle contacts, which make electrical contact to individual devices on the substrate. In addition, it can be equipped with either a photodiode or a quartz glass fiber for optical detection. The whole *xy*-stage is located in a separate metal box, which shields the sample against ambient light and electro-magnetic noise. With this setup, a large variety of different measurements can be performed, which are combinations of electrical/optical excitation and electrical/optical detection. A summary of the possible measurements is compiled in Table 3.1.

Figure 3.13 shows a schematic view of the automated characterization setup. The details are described in the following sections.

3.5.2 *I–V/L–V* Characteristics

A semiconductor parameter analyzer (Hewlett-Packard HP4145A) is used to measure the *I–V* characteristics of the individual devices. Typical sweep parameters are from -5 to $+10$ V in steps of 0.1 V. Current compliance is usually set to 20 mA, which corresponds to a current

| | | excitation | |
|-----------|------------|--|--|
| | | electrical | optical |
| detection | electrical | Current–voltage ($I-V$), Transient $I-V$, Impedance $Z(\omega)$ Capacitance–Voltage ($C-V$) 4-point probe (resistivity) | Photo currents |
| | optical | Luminance–Voltage ($L-V$), EL spectra, Transient EL | PL-spectra, Transmittance, Reflectance |

Table 3.1: Measurements that can be performed with the automated characterization table. Basically, any combination of electro-optical excitation and electro-optical detection is feasible.

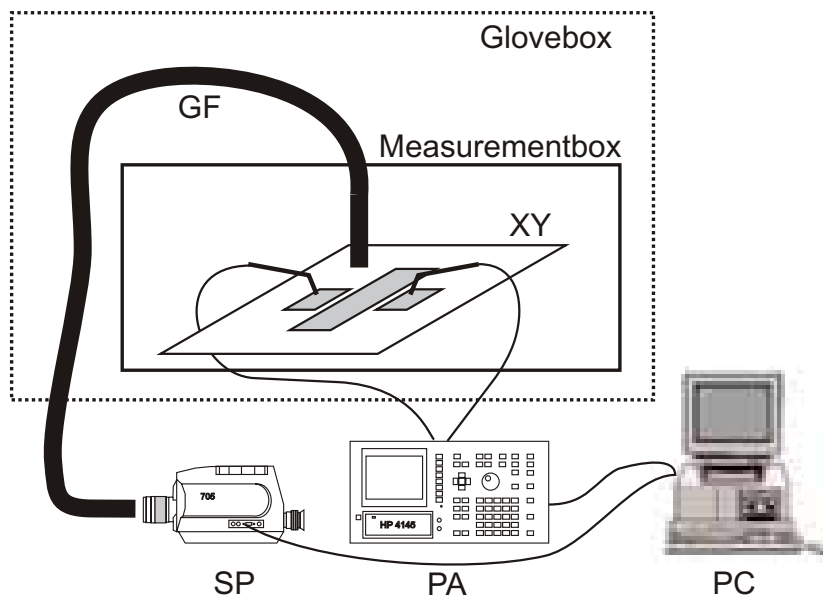


Figure 3.13: Schematic view of the proprietary multipurpose setup. xy -stage (XY), glass-fiber (GF), spectrophotometer (SP), parameter analyzer (PA) and personal computer (PC).

density of 500 mA/cm^2 . The HP4145A has four source measure units (SMU), which can be used either as voltage or current source. When used as voltmeter, the impedance of the SMU is $>10^{12} \Omega$. The EL signal was detected by a Si photodiode (Hamamatsu S1336-1010BR) biased with zero volts. Later a photometer head (P09F00, LMT Lichtmesstechnik Berlin GmbH) was used, driven under the same conditions. This sensor incorporates a filter matched to the human eye response curve within a precision of 2% (see Fig. 3.14). This allows the direct conversion of the measured photocurrent into luminance values by multiplication with a constant calibration factor. In this configuration, the dark current noise level is $\approx 10 \text{ pA}$. This corresponds to a minimum luminance of 10^{-3} cd/m^2 , which can be recorded with this detection system.

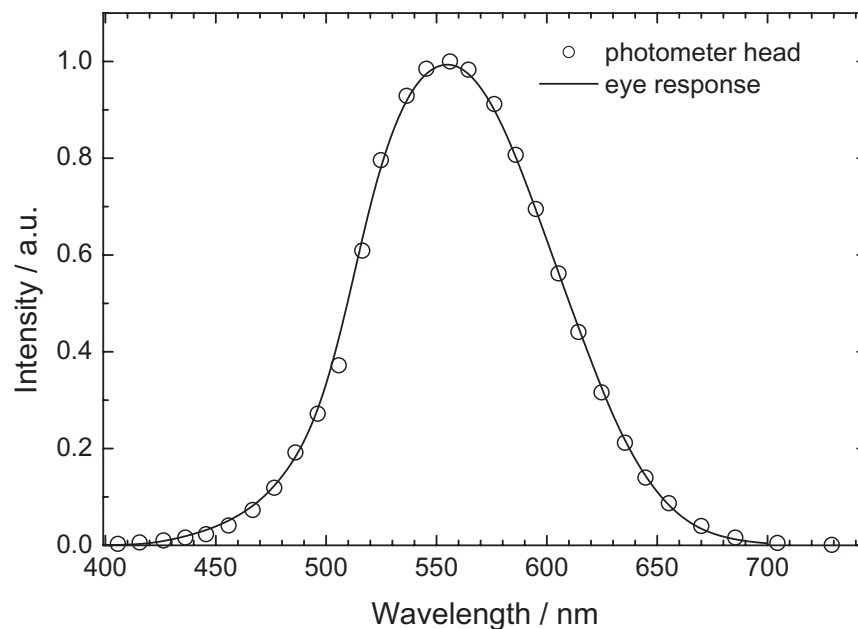


Figure 3.14: Response of photometer head (P09F00, LMT Lichtmesstechnik Berlin) (circles) compared with human eye response (line). Maximum sensitivity of the day-adapted human eye is in the yellow-green range at 555 nm. The conversion factor between the photometric and radiometric units at the maximum corresponds to 683 lm/W .

In order to check the uniformity of devices on the substrate, 100 identical diodes have been fabricated with the following structure:

| Material | Ni | CuPc | NPB | Alq ₃ | Ca |
|---------------|-----|------|-----|------------------|-----|
| Thickness / Å | 700 | 150 | 500 | 500 | 200 |

Figure 3.15 illustrates the uniformity of the electrical characteristics of the 100 devices. The uniformity of the EL spectra is shown later in Section 3.5.3. All devices show the typical diode characteristics (Fig. 3.15), i.e. a low reverse current and a sharp current onset at 2.2 V, which is accompanied by light onset. The rectification ratio of all devices is on the order of 10^5 at ± 5 V. In order to illustrate the spatial distribution, the current density at 6 V is depicted in a 2D plot in Figure 3.15b. The current density at 6 V shows excellent uniformity and is 16 ± 3 mA/cm². It has to be mentioned that besides the thickness uniformity of the organic layers, the uniformity of the electrodes, especially the uniformity of the plasma treatment can lead to a greater variation in the characteristics.

In Figure 3.16a the efficiency in cd/A of the 100 devices is plotted versus voltage. Extremely good uniformity of about 3.25 ± 0.05 cd/A at 6 V is achieved measured through a semi-transparent cathode. Since OLEDs are current-driven devices, the efficiency at a certain constant current density is of interest. Figure 3.16b shows the distribution in efficiency of the 100 devices at a current density of 20 mA/cm². This distribution is extremely narrow, ranging from 3.16 to 3.32 cd/A.

In conclusion, these results of I - V EL measurements on 100 nominal identical devices show that exceptional uniformity is achieved. This proves that the devices on a substrate can be compared directly and that effects in an intentionally staircased matrix as small as ± 3 can rightly be attributed to changes in thickness.

3.5.3 EL and PL Spectra

Electroluminescence (EL) or photoluminescence (PL) spectra are recorded with a highly sensitive spectrophotometer (PR-705 SpectraScan, Photo Research, Inc.), which is computer controlled via RS-232 interface. This spectrophotometer provides photometric and radiometric quantities, i.e. the spectral intensity in W/(sr·m²·nm) and deduced quantities of luminance as well as Commission International de l'Eclairage (CIE) x, y color coordinates. The minimum detectable light level is 0.003 cd/m². Light emission of the OLED structures is extracted via a quartz glass fiber bundle (see Fig. 3.17a), which exhibits a wavelength-independent transmission spectrum in the visible range. This bundle has a diameter of 1.5 mm. The top-emitting

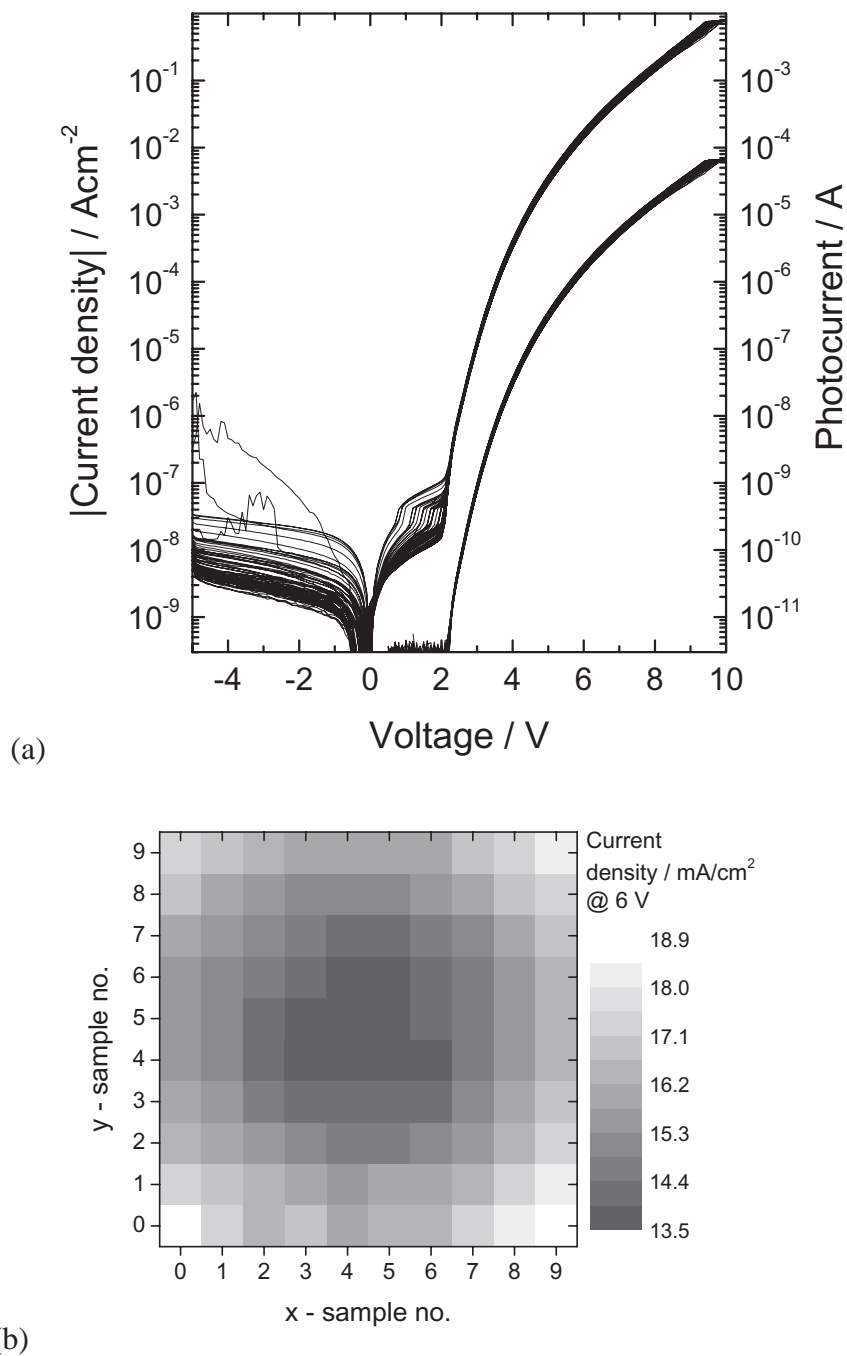
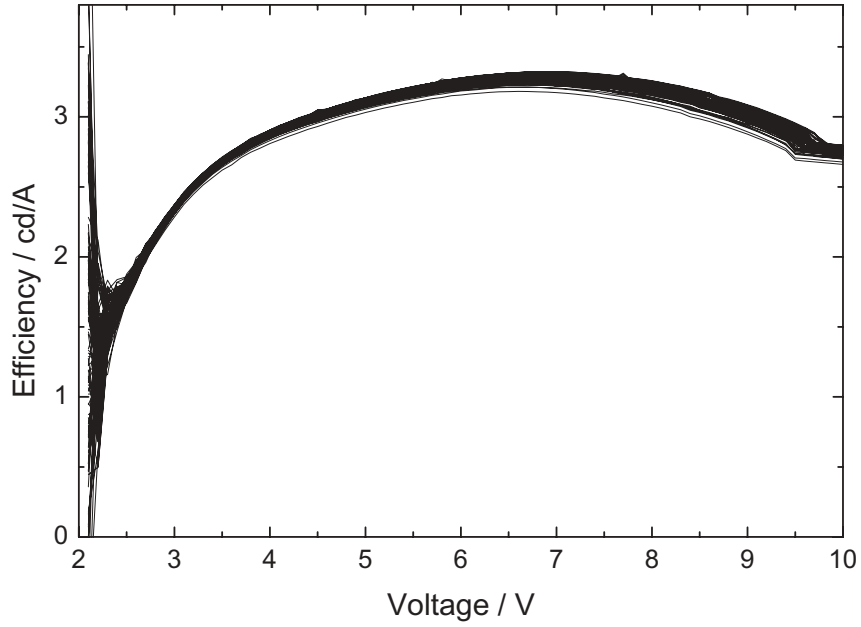
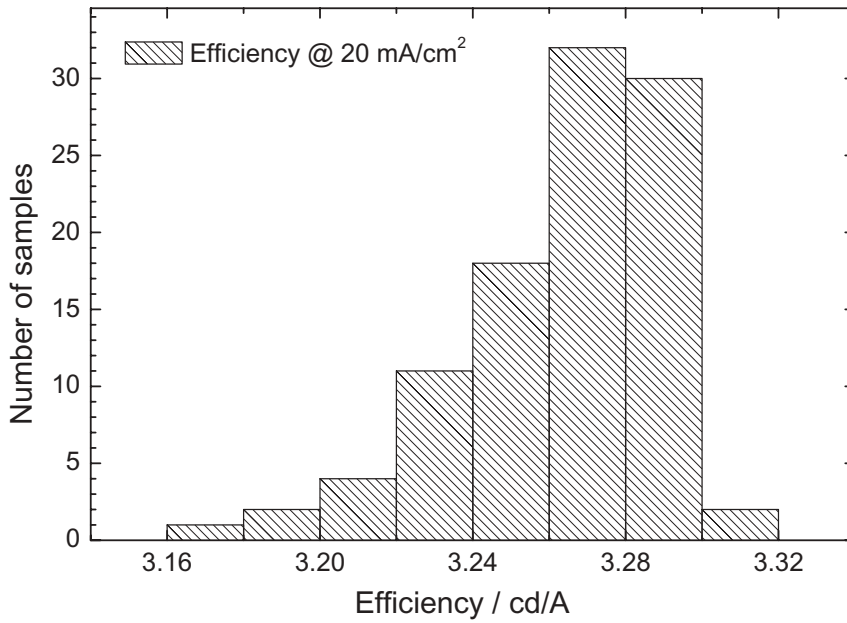


Figure 3.15: Uniformity of 100 nominal identical devices. (a) I - V EL characteristics. (b) Uniformity of current density at 6 V, which largely corresponds to the layer thickness uniformity (cf. Fig. 3.5) but might also be affected by the uniformity of the anode treatment.



(a)



(b)

Figure 3.16: Reproducibility on a single substrate with 100 nominal identical OLED structures. (a) Efficiency versus voltage. (b) Statistical distribution of efficiency at 20 mA/cm².

devices on the substrate are centered about 5 mm below by moving the xy stage. Another fiber can be placed below the substrate to measure spectra from bottom-emitting devices. The EL intensity is calibrated by directly measuring the luminance of several devices and calculating an average calibration factor taking into account a measured loss of 12% through the glove-box window. The automated measurement setup can take several spectra at either constant voltage or current density to investigate the influence of the driving conditions on the spectral characteristics.

For PL measurements the samples are excited with a frequency-tripled laser (NanoUVTM, Nanolase) emitting at 355 nm. The output power is 1 mW with a pulse width of <700 ps and a repetition rate of 12 to 16 kHz. Since the materials used, e.g. Alq₃, are highly fluorescent they show high PL intensity, which can easily be detected by the SpectraScan PR705 even at thicknesses down to 20 Å. The laser intensity is specified to have a stability better than $\pm 5\%$ over 1 h, whereby the measurement of 100 PL spectra takes only about 20 minutes. The PL intensity is measured in reflection mode, which will be described in the next section (see Fig. 3.17b).

3.5.4 Transmission and Reflection Measurements

The measurement of transmission and reflection of different samples on one substrate can also be carried out with the automated characterization setup. Here, an inorganic white LED was used as an excitation source, which allows the measurement of transmittance and reflectance in the range of 440 to 660 nm. The long-term stability of the LED intensity has been tested and found to be better than $\pm 2\%$ during 10 hours of continuous driving.

Transmission measurements are carried out in a setup as depicted in Figure 3.17c. The white inorganic LED is placed below the substrate and illuminates the sample whereas the quartz glass fiber is aligned on the opposite side and detects the remaining intensity. The spectral intensity was measured by the PR-705 SpectraScan via the fiber. To obtain absolute values, a blank glass substrate is taken as reference in transmission measurements. Figure 3.18 shows the comparison of results obtained by the automated setup and a commercial instrument (HP8452 UV-Vis spectrometer). The transmittance of gold layers with different thicknesses has been measured with both setups. The agreement is excellent, which justifies the use of this equipment and the validity of the measured data. Since the proprietary setup operates under inert gas conditions, even the transmittance of oxygen and moisture-sensitive materials, such as Ca, can be measured.

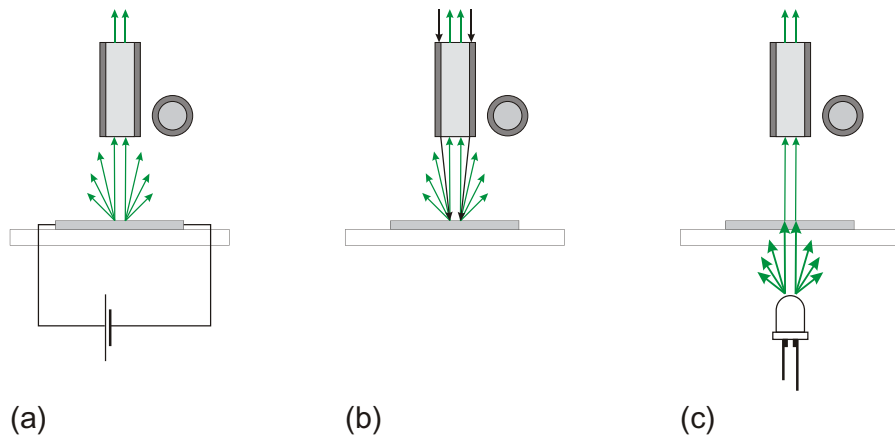


Figure 3.17: Schematic view of the setup for electro-optical measurements (a) electroluminescence (EL), (b) photoluminescence (PL) and reflection, and (c) transmission.

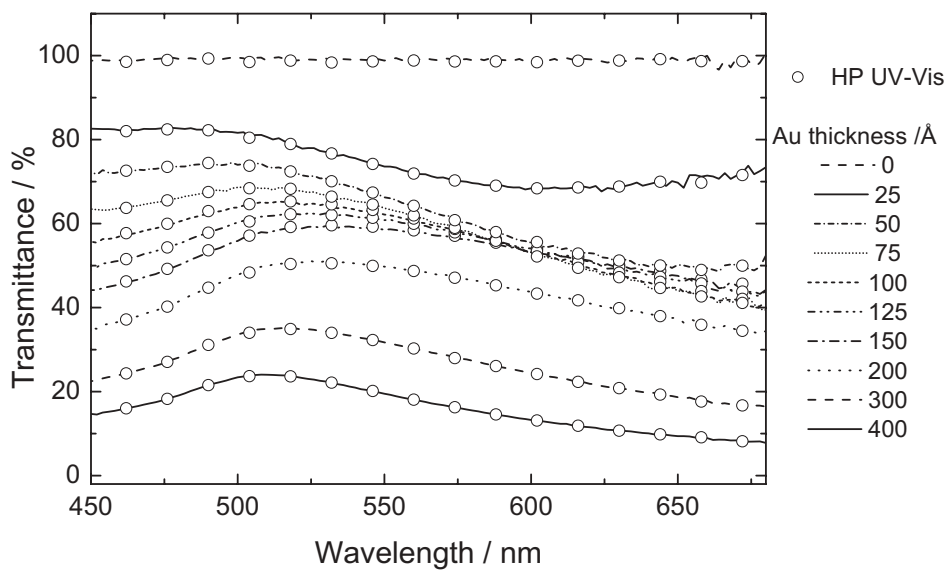


Figure 3.18: Thickness-dependent transmission data of Au layers on glass. Comparison between the new proprietary automated setup and the HP8452 UV-Vis spectrometer. Excellent agreement is achieved and verifies the data obtained by the automated setup.

Reflection measurements are carried out in a slightly modified arrangement depicted in Figure 3.17b. A specially designed coaxial Y-quartz glass fiber bundle is used where the inner core has a diameter of 1.5 mm (area 2 mm²) and the outer ring exhibits the same area of 2 mm². In reflection and PL measurement mode the outer ring is used for excitation whereas the inner core is used for detection. Either glass (8%) or Al (92%) can be used as a reflection reference. Glass is considered as the better choice since it has the advantage of wavelength independent reflection spectrum in the visible range. Excellent agreement is achieved when glass is taken as a 8% reference and consistent values for highly reflecting metals, e.g. Al (91%) or Ni (60%) at 530 nm have been measured (see Sec. 5.2).

3.5.5 Other Characterization Methods

Outside the glovebox further methods are available to characterize the samples.

Thickness Measurements:

Thickness measurements are carried out with a surface profiler (Tencor Alpha-Step 200) for determining and calibrating the thicknesses of metal layers. This gives reliable measurement results when the layer thicknesses exceed 100 nm. To get reliable results on reactive metals like Ca or Mg they have to be covered with a known thickness of Ag or Al in order to prevent oxidation. Since organic layers are often too soft to be measured precisely with the profiler technique, they are also covered with a metal clad of known thickness.

A more reliable method for the determination of organic film thicknesses, however, is ellipsometry. For uniformity maps a single wavelength ellipsometer (Plasmos SD) at a wavelength of 632 nm is used. A spectral ellipsometer (Woollam WVASE 32) is employed for thickness calibration and gathering optical constants of organic films. This allows the determination of the complex refractive index $\tilde{n} = n + i\kappa$ in the range of 380 to 780 nm, which is crucial for optical simulations.

Fluorescence and Absorbance:

Photoluminescence of organic materials is also measured in thin films on a glass substrate with a fluorescence spectrometer (Hitachi F-4500) in the range of 200 to 900 nm. The absorption spectra of the materials is either measured with the Hitachi F-4500 (as excitation scan) or with a spectrophotometer (Perkin Elmer Lambda 900).

3.6 Data Representation

Every substrate contains 100 samples, most of which are intentionally different. The characterization of this large number of devices is done automatically as described in Section 3.5. From each individual OLED a current–voltage sweep is taken and usually several (up to ten) EL spectra are taken at different current densities. This generates a large amount of raw data (roughly 1 MByte per substrate).

First of all, to facilitate the observation of certain trends all this data has to be displayed in clear overviews. For this purpose the software tool OriginTM is utilized. Customized LabTalkTM scripts have been written to accommodate the data obtained from the combinatorial matrix arrangements. Parameters such as the efficiency are automatically derived from the diode current and photodiode signal. Furthermore, the data has to be normalized, extracted or interpolated, and compiled into meaningful plots.

Figure 3.19 gives an overview of how the raw data is displayed.

In that experiment the NPB and the Alq₃ layers were varied in a 10×10 combinatorial matrix. The example shows 10 plots where the *I*–*V*-curves of devices with constant Alq₃ thickness but varying NPB thickness are bundled into one graph. Such overviews provide first hints about certain trends and allow one to extract or interpolate single values which in turn are displayed in either 3D plots or 2D color-coded plots. As an example, Figure 3.20 shows in a 2D plot the efficiency in lm/W at 20 mA/cm² calculated from this raw data. Two types of 2D representations will be used in this work. The first is shown in Figure 3.20a, where the value is directly mapped by the color, and the second in Figure 3.20b, where interpolated contour lines correspond to values of the same magnitude. The latter is favorable for viewing data, but it might falsely suggest a continuous data set. It has to be stressed that this plot is also based on 100 individual data points. Another way to display the data is a 3D bar plot, which sometimes allows a better visual comparison of all the magnitudes than a color-coded 2D plot. An example of such a plot is given in Figure 4.2 (page 65).

Ti 5 nm / Ni 70 nm / CuPc 15 nm / NPB / Alq / Ca 20 nm

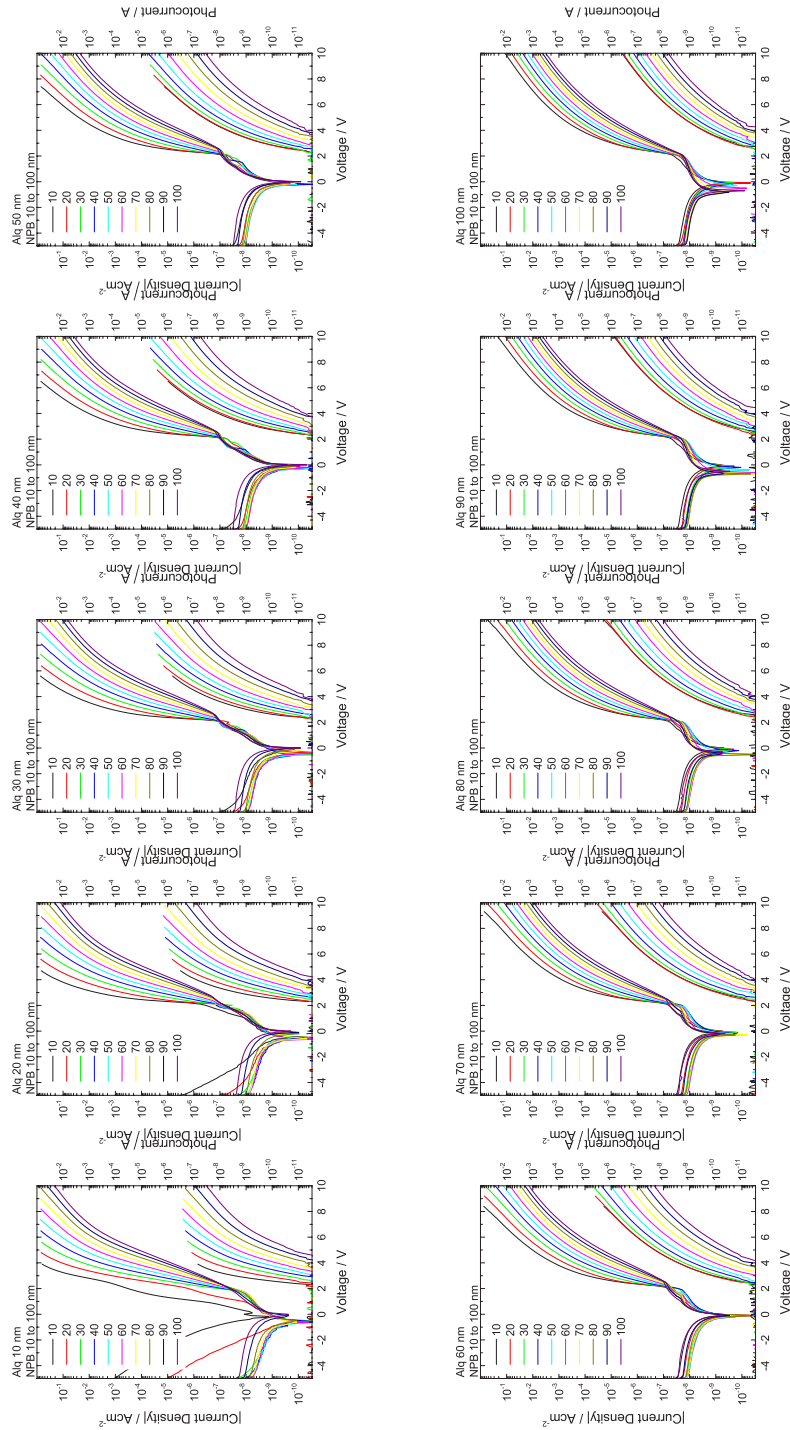


Figure 3.19: Example of an overview of raw data. The 100 $I-V$ EL curves of a combinatorial matrix are displayed either column-wise or row-wise in groups of 10 devices, which allows one to identify trends of the combinatorial substrate readily.

C034

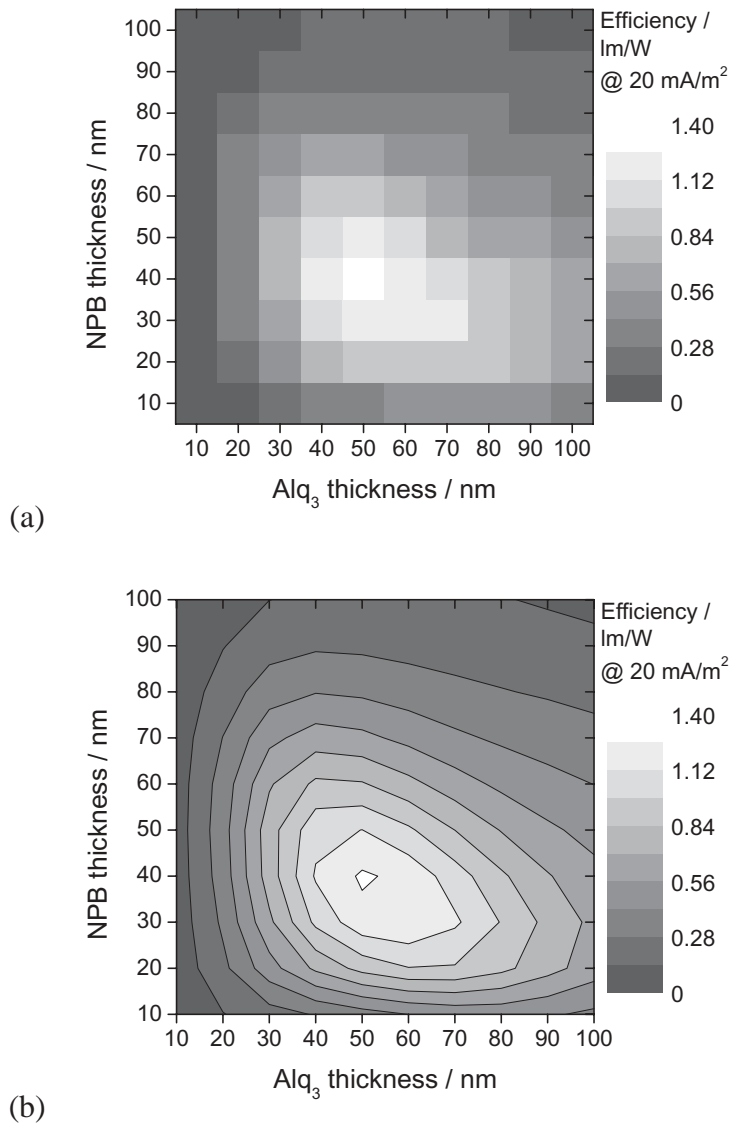


Figure 3.20: Two representations of identical 2D combinatorial data: (a) a gray-scale coded plot and (b) contour lines. The y- and the x-axes correspond to the thickness of the first and second staircased material deposited, respectively. Although the displayed data is the same, the contour-lines graph gives a clearer impression of the trends.

Chapter 4

Organic Multilayer Structures

4.1 Three-Layer OLEDs Based on Alq₃ as Emitter Material

The first efficient organic light-emitting structures to operate at low voltages (<10 V) were reported by Tang and van Slyke [Tang and Van Slyke 1987]. The novelty of this device structure was the use of an organic heterostructure which used separate hole and electron transport layers. This approach resulted in much higher efficiencies and lower voltage operation than the previously reported structures [Vincett et al. 1982]. The insertion of an additional hole injection layer of copper phthalocyanine (CuPc) led to more reproducible device characteristics and drastically improved device lifetime [Van Slyke et al. 1996]. However, the introduction of an additional layer makes a detailed description and understanding of device operation much more difficult. This device structure (CuPc/ NPB/ Alq₃) has become a widely investigated structure studied with respect to injection, transport and recombination processes [Shi and Tang 1997; Riel et al. 1998; Matsumura and Miyamae 1999; Forsythe et al. 2000; Forsythe et al. 2000; Brütting et al. 2001; Brütting et al. 2001; Riel et al. 2003].

In order to improve and maximize the performance of OLED architectures a detailed understanding of the operation mechanisms is absolutely necessary. This is a demanding task; a two-layer system requires that numerous effects be taken into account, and a multi-layer system even more so. First, electrical parameters of the organic materials determine the device characteristic, e.g. the mobilities of the charge carriers, barriers to the electrodes as well as internal barriers, whereby typically the injection and transport processes are generally strongly field dependent. Second, optical effects influence or even dominate the device performance.

These effects will be discussed in Section 5. The interplay between different processes can become very complex and can hardly be elucidated with only a limited set of experimental data. Therefore, for a broader view of the interrelations there is a need for a set of samples with well-defined modifications, e.g. layer thickness. In the following section, this will be illustrated using the OLED structure CuPc/ NPB/ Alq₃ as an example. The reason why this structure was chosen is because of the most comprehensive data set in the literature. Nevertheless, certain aspects need more insight. Furthermore, this device structure is long-term stable, which allows general statements to be drawn and applied to other systems.

4.1.1 Thickness Variation and Optimization of NPB/Alq₃

In the past, efforts to achieve optimum performance were carried out by time-consuming sequential evaporations with limited reproducibility. Such sets of data, however, should be interpreted with caution, especially when small effects are addressed. An efficient way to achieve optimum performance is the combinatorial approach described in detail in Section 3.3. The optimum thicknesses in a two-layer structure and a given material set can be found in a single evaporation run. Uncertainties occurring in sequential fabrication due to run variations are largely eliminated. As described above, this evaporation tool makes it easy to scan two thickness parameters in two dimensions. This allows a complete overview of a two-layer material system which is hard to achieve in serial experiments. With the same tool, the influence of CuPc on the device performance has been studied in detail [Riel 2002; Riel et al. 2003]. In this section the influence of the thickness of hole transport (NPB) and electron transport (Alq₃) layers will be discussed.

Experimental

The CuPc/ NPB/ Alq₃ sample structure is fabricated as described in Section 3.3.3 in a combinatorial matrix. The layer thicknesses of the complete structure is given in the following table:

| Material | Ni | CuPc | NPB | Alq ₃ | Ca |
|----------------|----|------|--------|------------------|----|
| Thickness / nm | 70 | 15 | 10–100 | 10–100 | 20 |

I - V and L - V characteristics are taken from all of these devices from -5 to 10 V in steps of 0.1 V. Spectra are taken at different current densities between 2 and 20 mA/cm² and will be discussed in Section 5.1.

Results and discussion

The resulting 100 I - V and L - V characteristics are shown as an overview in Figure 4.1. The total device thickness ranges from 35 to 215 nm. Although the thickness changes by less than one order of magnitude, the current density at a given voltage, e.g. 4 V, varies by more than six orders of magnitude. The photocurrent exhibit a similar broad variation and the light onset

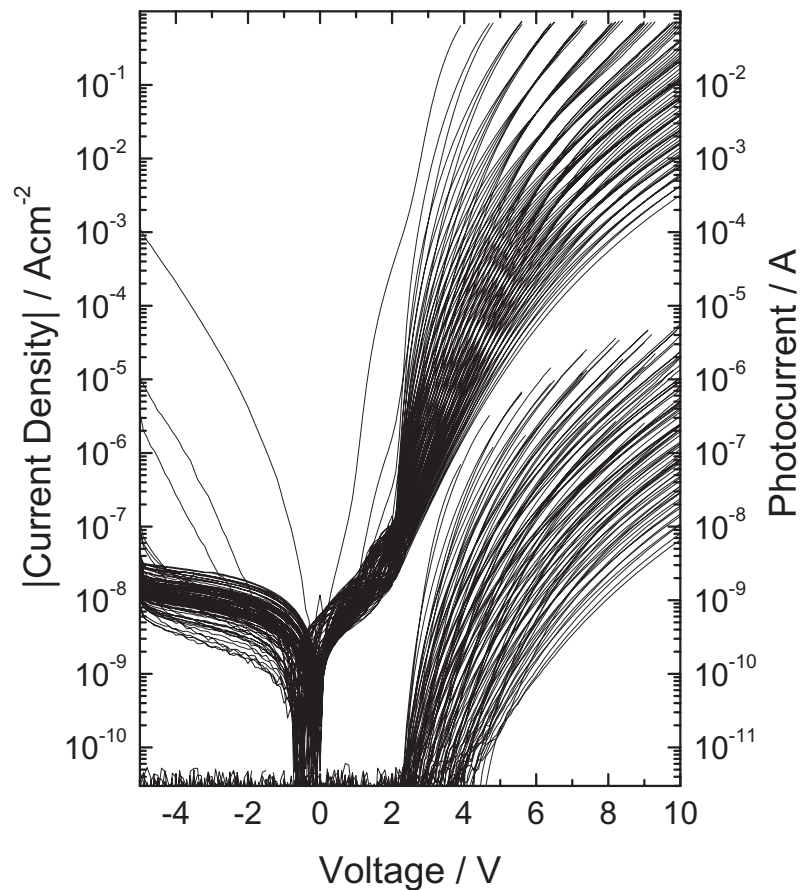


Figure 4.1: Raw data overview of I - V EL curves of 100 intentionally different combinatorial devices. NPB and Alq₃ thicknesses are varied from 10 to 100 nm each. Detailed device structure see text.

shifts between 2.2 and 4.2 V. All the devices exhibit low leakage currents in reverse direction. The rectification ratio at 4 V is as large as 10^6 and is still more than 5000 for even the thinnest device with only 35 nm. In order to avoid damaging the thin samples, the current limit was set to 750 mA/cm² during the voltage sweep.

For a better assignment of the current density and the luminance to the individual layer thicknesses they are displayed in three-dimensional semi-logarithmic plots (Figure 4.2a and b). To cover the thin as well as the thick devices this representation has been plotted for an applied voltage of 4 V. As one could expect, the current density decreases monotonically with increasing total device thickness (Figure 4.2a). Looking at the devices with the thinnest Alq₃ layer (Figure 4.2a, A-B), the current density varies by five orders of magnitude when the NPB layer is changed from 10 to 100 nm, whereas it changes by less than four orders of magnitude when NPB is thinnest and Alq₃ is varied (Figure 4.2a, A-C). In the case of thick NPB (Figure 4.2a, B-D) and thick Alq₃ (Figure 4.2a, C-D) layers, the described trend is similar but not as pronounced. In the thickness range investigated, at a voltage of 4 V the total current is more sensitive to the NPB layer thickness. At first glance, this result appears unexpected because the voltage drop across the NPB layer with a relatively high hole mobility ($\mu_h \approx 10^{-3}$ cm²/Vs) should be lower than that across the Alq₃ layer with an electron mobility of $\mu_e \approx 10^{-5}$ cm²/Vs [Barth et al. 2001]. This straightforward argument, however, neglects the existence of internal energy barriers. In the tri-layer device two internal interfaces have to be taken into account with different energy barriers at the CuPc/NPB and the NPB/Alq₃ interface. Recently, it was shown that it is the interplay between barriers for holes at the CuPc/NPB and the NPB/Alq₃ interface that controls the charge balance [Riel et al. 2000; Rieß et al. 2001]. By increasing the thickness of the NPB layer the electrical field at the CuPc/NPB interface is reduced, leading to a reduced hole current flow through the NPB layer. Since the hole current crucially affects the electron current, the increasing thickness of NPB leads to a significant reduction of the total current, i.e. the devices are injection-limited by the CuPc/NPB interface.

Figure 4.2b displays the dependency of the luminance at 4 V on the different individual layer thicknesses. Although the thinnest device has the highest luminance, the maximum is far less pronounced than in the current. The luminance increases monotonically with decreasing NPB thickness when the Alq₃ thickness is kept constant. However, with decreasing Alq₃ thickness at constant NPB thickness, the luminance also increases, but at Alq₃ thicknesses below 20 nm a clear drop in intensity is detected. This decrease has been explained by quenching

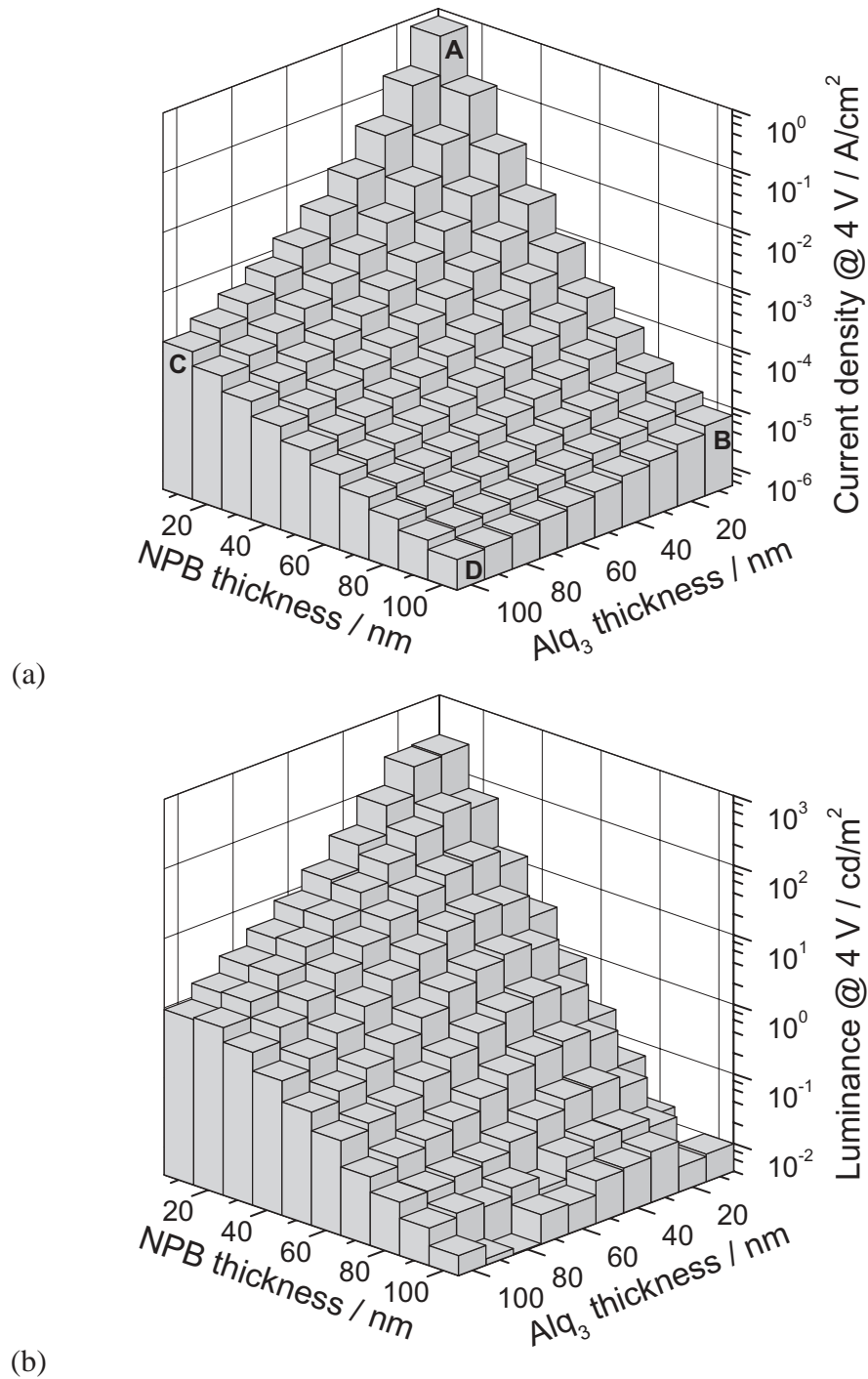


Figure 4.2: (a) Current density and (b) luminance at 4 V of 100 combinatorial devices based on CuPc/NPB/Alq₃. Detailed device structure see text.

effects due to dipole coupling to a metallic surface [Chance et al. 1978; Becker et al. 1997; Burin and Ratner 2000]. Quenching and exciton diffusion will be addressed in Section 6.1 using PL measurements on Alq₃ layers. Because a 15 nm CuPc buffer layer is inserted at the anode and NPB acts as exciton blocker, this quenching effect is not as pronounced at thin NPB thicknesses. Nevertheless, this quenching mechanism explains the similar luminance despite the higher current flow at low NPB thickness.

From the luminance and current density the efficiencies of the devices are calculated. Since OLEDs are usually driven under constant current conditions, the efficiencies are extracted for typical current densities of 1 and 20 mA/cm². Figure 4.3 shows the efficiency in cd/A of the combinatorial NPB/ Alq₃ matrix devices. These two-dimensional gray-scale plots are based on 100 values. For sake of clarity the contour lines are interpolated between these values. The device with 60 nm Alq₃ and 40 nm NPB gives the maximum efficiency with a value of 2.9 cd/A at 20 mA/cm² through a 20-nm-thick semitransparent Ca electrode. As will be shown in Section 5.3, the transmittance of such a cathode is around 50–70%. A drop in efficiency below 0.3 cd/A can be observed for devices having an Alq₃ layer thinner than 30 nm. The similar but weaker trend can be observed for NPB thicknesses below 20 nm. As mentioned above, the more pronounced drop with thin Alq₃ layers can be attributed to a quenching of excitons near the cathode, whereas for thin NPB layers the additional CuPc layer reduces quenching at the anode side. It is important to note that the shape of the efficiency map changes does not change significantly with current densities (see Figure 4.3b), i.e. at all current densities the 60 nm Alq₃ and 40 nm NPB structure with 15 nm CuPc is the most efficient device.

In device applications, minimization of the operating voltage is always an important issue. Naturally, there will be always a trade-off between maximum efficiency and lowest voltage operation. Figure 4.4 shows the voltage necessary to drive a current density of 20 mA/cm² through a device. This is again a 2D-contour plot based on 100 devices. A monotonic increase in voltage for increasing total device thickness is observed. This representation shows that at a current density of 20 mA/cm² the dependence of the voltage on NPB and Alq₃ layer thickness is almost equal. This tells us that the voltage drops across the NPB and Alq₃ layer must be similar. However, this changes for different current densities. Figure 4.5a, b, c, and d show the dependence of driving voltage necessary for different current densities ranging from 1 μ A/cm² to 1 mA/cm². Starting from the 2D-representation in Figure 4.5a, the contour lines of equal voltage are nearly horizontal, which means that the driving voltage is almost

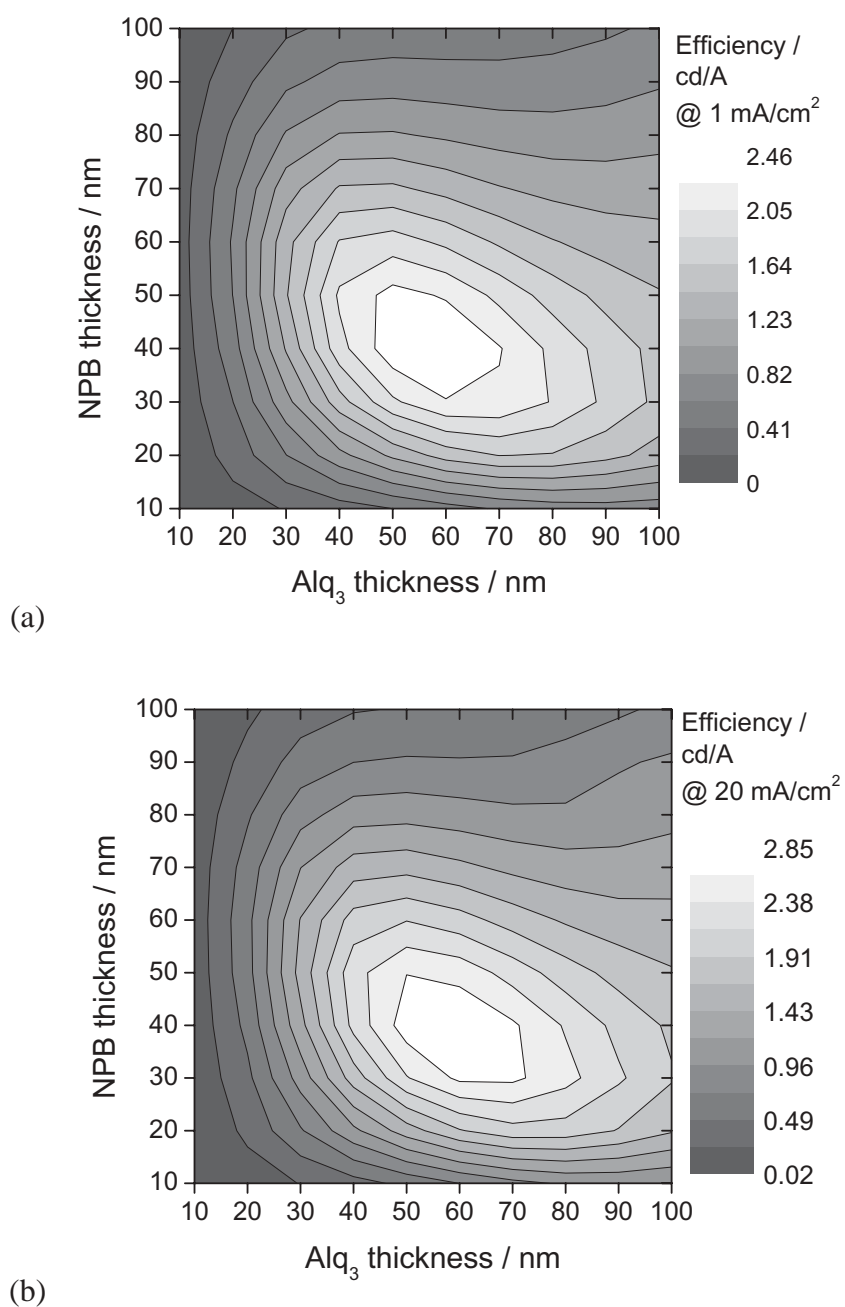


Figure 4.3: Efficiency in cd/A of 100 combinatorial devices based on CuPc/NPB/Alq₃ at (a) 1 mA/cm² and (b) 20 mA/cm². A clear maximum in efficiency is observed for 60 nm Alq₃ and 40 nm NPB. Note that there is no significant shift in maximum with current density.

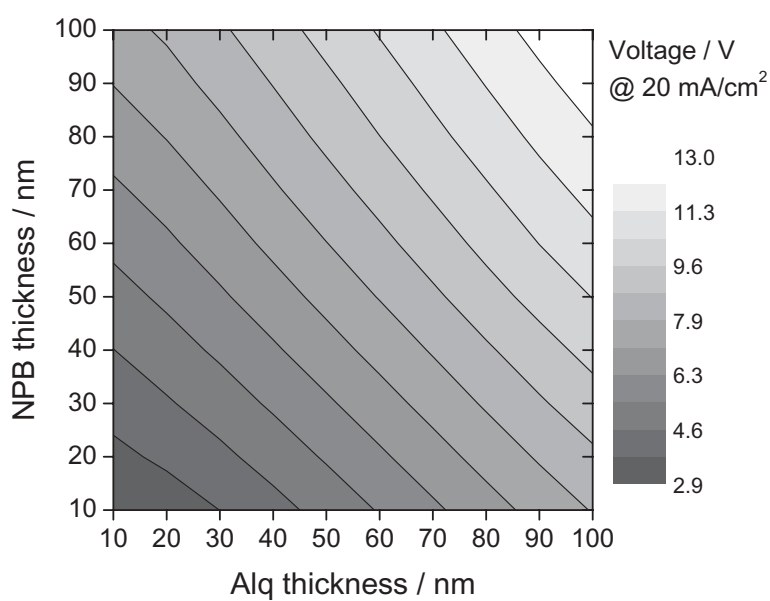


Figure 4.4: Driving voltage of 100 combinatorial CuPc/NPB/Alq₃ devices for achieving a current density of 20 mA/cm².

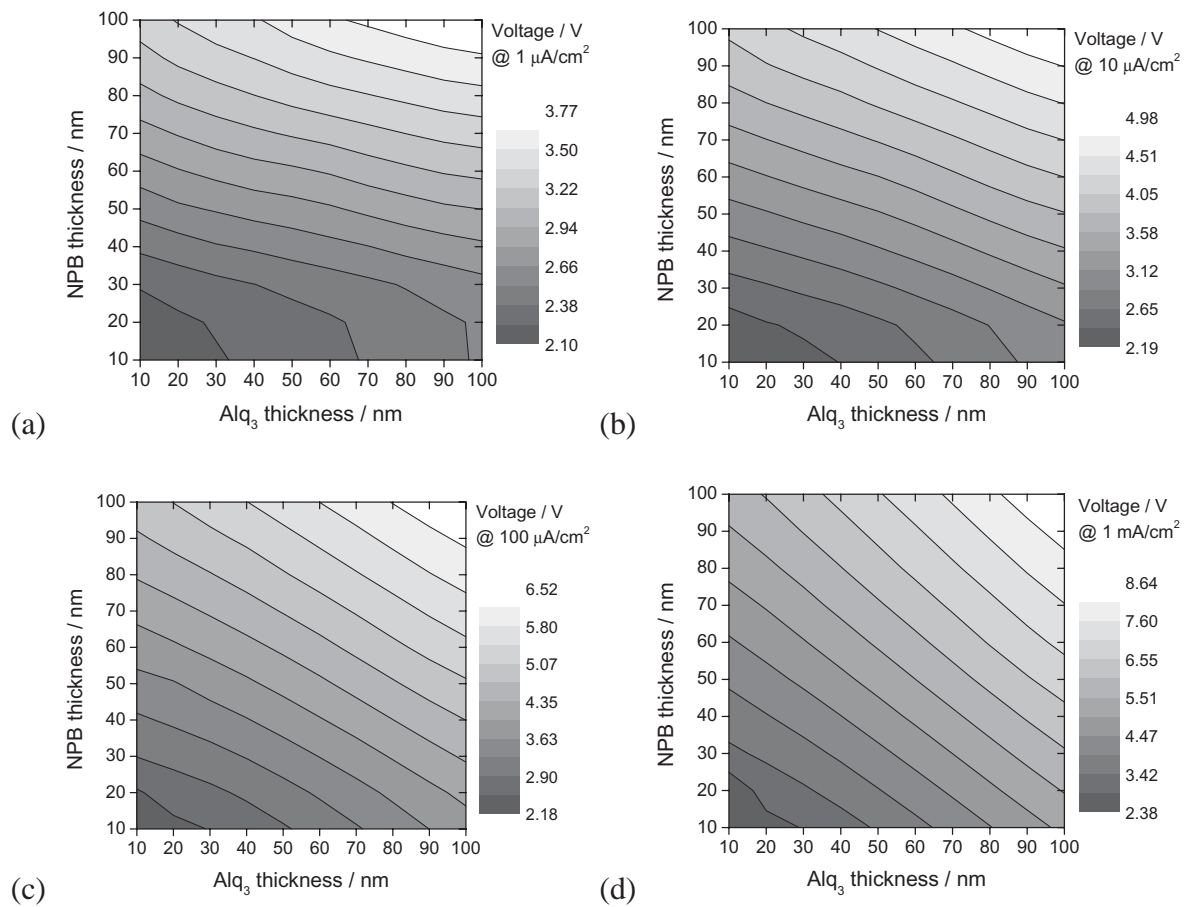


Figure 4.5: Dependence of drive voltage on NPB and Alq₃ layer thicknesses at constant current densities (a) $1 \mu\text{A}/\text{cm}^2$, (b) $10 \mu\text{A}/\text{cm}^2$, (c) $100 \mu\text{A}/\text{cm}^2$, (d) $1 \text{mA}/\text{cm}^2$.

independent of the Alq₃ layer thickness. In other words, an increase in NPB layer thickness causes a much greater rise in driving voltage than the same increase in Alq layer thickness. It is clearly noticeable that with higher current densities (Fig. 4.5b, c, d) the operating voltage becomes more and more dependent on the Alq₃ layer thickness. This indicates that a change in the dominating mechanism occurs. In this combination, it is the NPB layer thickness which basically determines the total current flow. Since the hole mobility in NPB is rather high ($\mu_h \approx 10^{-3} \text{ cm}^2/\text{Vs}$), this again suggests that not the transport of holes through NPB but the injection of holes from CuPc into NPB is the limiting factor. A way to circumvent this limitation to mix or grade organic layers whereby the operation voltage can be reduced. To a certain extent, the efficiency and lifetime can thus be increased [Strite and Beierlein 1997; Riel 1997; Popovic et al. 1998; Riel 2002; Ma et al. 2002].

4.1.2 Devices with Constant Thickness

In this section, a special subset of ten devices out of this matrix will be considered in more detail. The I - V overview of the combinatorial matrix (Fig. 4.1, p. 63) showed that the 100 individual I - V curves are bundled into several groups. A closer look reveals that all devices of a certain bundle have the same total device thickness. Therefore, the following discussion will concentrate on the devices with a constant total organic layer thickness of 125 nm:

| Material | Ni | CuPc | NPB | Alq ₃ | Ca |
|----------------|----|------|-----|------------------|----|
| Thickness / nm | 70 | 15 | x | $110 - x$ | 20 |

Since anode, cathode and the CuPc layer of all devices on this substrate are identical, these devices distinguish only in the position of the NPB/ Alq₃ interface within the organic stack.

Results

Figure 4.6 shows the I - V EL characteristics of ten devices with a constant thickness of 125 nm. All the devices show an identical I - V onset, which is expressed by a sharp kink in the I - V curves at 2.2 V. The second striking feature of this subset is a crossover of the I - V curves at a voltage of ca. 7 V. At low voltages (2 – 7 V) the curves with the thin NPB and thick Alq₃ exhibit the highest current, whereas at voltages higher than 7 V this behavior is reversed. Similar behavior can also be observed for subsets with other constant total thicknesses. The

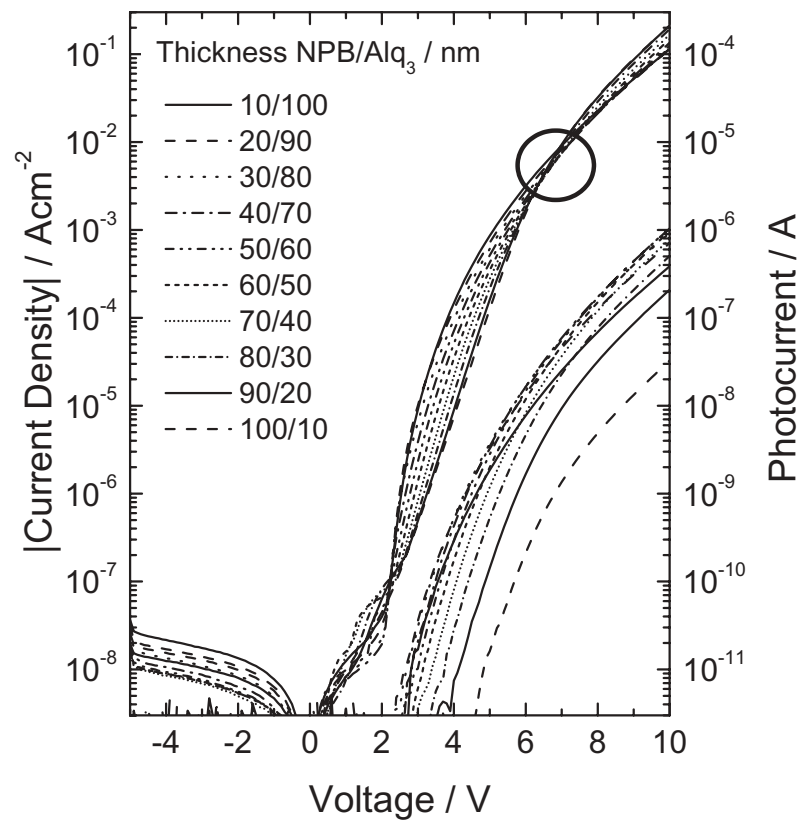


Figure 4.6: *I-V* EL curves of ten devices with an identical total thickness of 125 nm. CuPc 15 nm / NPB x nm / Alq₃ 110 - x nm.

EL onset, which is determined by the sensitivity of the photodiode, is shifted from 2.5 to 4.8 V for thin Alq₃ layer thicknesses. The reduction in EL signal is attributed to quenching at the cathode.

Figure 4.7 shows the efficiency as a function of current density normalized to the maximum for devices having a constant total thickness of 125 nm. All efficiencies curves show an increase with current density and exhibit their maximum at current densities in the range from 10 to 100 mA/cm². The efficiencies of the devices with 10 and 20 nm NPB thickness have not reached a maximum up to the measured current density, therefore their maximum values are extrapolated in order to normalize these curves. With an increasing NPB/Alq₃ thickness ratio the position of the maximum in efficiency shows a monotonic shift from 100 to 10 mA/cm², i.e. devices with thick NPB reach their maximum efficiency at lower current densities than those with a thin NPB layer.

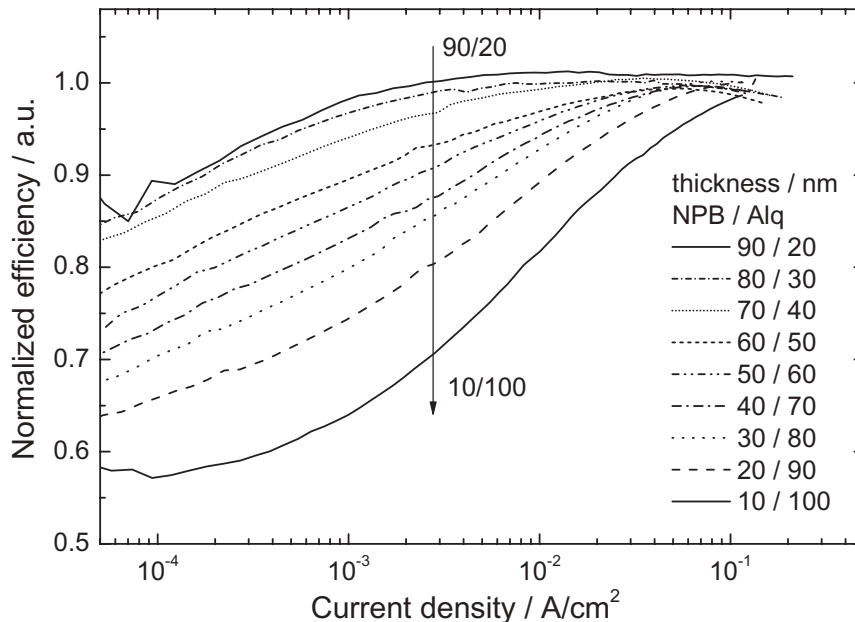


Figure 4.7: Normalized efficiency vs. current density of devices with constant organic layer thickness: CuPc 15 nm / NPB x nm / Alq₃ 110 – x nm.

Discussion

As oxidized Ni is a high-work-function material (~ 5.5 eV), it is justified to assume that the injection of holes into CuPc (LUMO 5.1 eV) is ohmic. Therefore, the kink in the I - V curves at 2.2 V corresponds to the injection of electrons from the cathode into Alq₃. Since the devices differ only with regard to the positions of the NPB/ Alq₃ interface, the changes in current flow can purely be associated with different internal charge and field distributions. The I - V characteristics of thick (200 nm) single-layer NPB devices have shown that the current density does not depend on layer thickness at low voltages, which indicates that injection rather than transport limits current flow [Riel 1998]. Therefore, the steeper I - V characteristics at low voltages in Figure 4.6 for the devices with thin NPB layer points to limitation by injection. Once holes are injected over the CuPc/ NPB interface, the transport to the NPB/ Alq₃ interface is not limiting because of the relatively high hole mobility $\mu_h = 10^{-3}$ cm²/Vs in NPB. At higher voltages (>7 V), however, it is the transport through the materials which will restrict the current flow. Especially the devices with thicker Alq₃ layer exhibit reduced current flow, which suggests that electron transport in Alq₃ restricts the total current density.

The shape of the efficiency curve (Fig. 4.7) is indicative of the current balance in the device. Holes are the first carriers to enter the device, and they are the major carriers through the device at low currents. The current balance γ is the ratio of the recombination current density j_r and the total current density j_{total} in the device.

$$\gamma = \frac{j_r}{j_{\text{total}}}, \quad (4.1)$$

where

$$j_r = j_{e,\text{cathode}} - j_{e,\text{anode}} = j_{h,\text{anode}} - j_{h,\text{cathode}}, \quad (4.2)$$

and

$$j_{\text{total}} = j_{e,\text{cathode}} + j_{h,\text{cathode}} = j_{h,\text{anode}} + j_{e,\text{anode}}. \quad (4.3)$$

Unbalanced electron and hole currents reduce the efficiency in the device, simply because injected charge carriers reach the opposite electrode without recombining and without generating light. To the first order, it can be assumed that the maximum in the efficiency curve corresponds to the point of charge balance ($\gamma \approx 1$). Other effects which lead to a reduction in efficiency are not considered here. Nevertheless, it has to be mentioned that at high current densities (>100 mA/cm²) high concentrations of ionic species, especially cations of Alq₃

lead to quenching of luminescence and hence a reduction in efficiency [Popovic et al. 2001]. The absolute values of the maximum efficiency for the ten individual devices (Fig. 4.6) varies considerably between 0.05 and 2.7 cd/A. This is due to optical interference effects since the position of the emission zone which is known to be close to the NPB/ Alq₃ interface in these devices is shifted over a large distance. In contrast to the absolute efficiency value, the shape of the efficiency curve for an individual device should not be influenced by interference effects, as long as the position of the emitting zone in Alq₃ does not shift within the Alq₃ layer with different driving conditions. Therefore, the normalized efficiencies allow a comparison of the current balance as it is shown in Figure 4.7. All efficiency curves show an increase to 10 mA/cm², which corresponds to the region above the crossover at 7 V in Figure 4.6. This is exactly the range where the transport in Alq₃ becomes limiting. The device with the thinnest NPB layer is the least balanced device, and the balance increases steadily with increasing NPB layer thickness. Again, this shows that the supply of holes over the CuPc/ NPB barrier determines the device characteristic and efficiency. This also illustrates the complex interplay between injection and transport in such multilayer structures.

4.1.3 Summary: Three-Layer OLEDs Based on Alq₃ as Emitter Material

An introductory example was given in this section to show how combinatorial methods can be applied to optimize and investigate OLED structures efficiently. Two-dimensional thickness variations on a three-layer structure CuPc/ NPB/ Alq₃ reveal that their device operation is a complex interplay between interfaces and bulk phenomena. Although the mobilities of the different materials in a given device structure can differ by orders of magnitude ($\mu_{h, \text{NPB}} \approx 10^{-3} \text{ cm}^2/\text{Vs}$ and $\mu_{e, \text{Alq}} \approx 10^{-5} \text{ cm}^2/\text{Vs}$), these values do not necessarily control the device characteristics. From systematic variation of NPB/Alq₃ layer thicknesses in a wide range it is suggested that by increasing the thickness of the NPB layer the electrical field at the CuPc/NPB interface is reduced, leading to a reduced hole current flow through the NPB layer. Since the hole current crucially affects the electron current, the increasing thickness of NPB leads to a significant reduction of the total current. The three-layer top-emitting CuPc/ NPB/ Alq₃ structures investigated here showed a clear maximum efficiency at 2.9 cd/A for NPB and Alq₃ thicknesses of 40 nm and 60 nm, respectively. The individual layer thicknesses determine the driving voltage for a given current flow, but the device efficiency is governed by

optical interference and quenching effects. Quenching plays the dominant role at either low NPB or low Alq₃ thicknesses. Optical interference effects will be discussed in more detail in Section 5. Experiments on quenching will be addressed in Section 6.1.

It is convincingly shown by combinatorial layer variations that the electrical field in this CuPc/NPB/Alq₃ structure is redistributed between NPB and Alq₃ with increasing bias. Whereas at low bias the largest voltage drop is across NPB, the voltage is nearly equally distributed between NPB and Alq₃ at higher voltages. The knowledge of the internal field distributions in these multilayer devices is of great interest for a deeper understanding of device characteristic and device operation. A method to measure the field distribution directly in devices under normal operation conditions will be described in the following section.

4.2 Potential Sensing

In the previous section, the importance of the internal electric field distribution was emphasized because the electric field distribution in an OLED structure is the essential parameter for the theoretical understanding and the numerical modeling of device characteristics. A measurement of the electric field as a function of applied voltage will therefore be a valuable link between experiment and theory. Evidently, the field distribution in a multilayer device is governed by the transport properties of the individual materials and the injection properties controlled by electrodes and internal barriers. The mobilities of charge carriers in organic materials are generally strongly field-dependent. In addition, the process of injection from electrodes or from adjacent organic layers in heterostructures is also determined by the local electric field and accumulated space charges. Various approaches have been used to quantify the internal field distribution in a working OLED and three of them will be described briefly in the next section.

4.2.1 Measurement Techniques

Electroabsorption Measurements

Electroabsorption measurements (EA) have been used by various researchers to determine the internal electrical field in operating OLEDs [Cambell et al. 1995; Giebeler et al. 1999; Rohlfing et al. 1999; Moderegger et al. 2000; Yamada et al. 2000]. The principle is based on the linear and nonlinear Stark effect, i.e. a change in absorption of the organic material under an applied field. A dc-field is superimposed with a small ac-field and applied to the device. Via changes in absorption due to the electric field, conclusions about the field in the material can be drawn. This technique was also used for multilayer structures where the spectral EA responses of the different materials were associated with the field in the different layers [Rohlfing et al. 1999]. However, a disadvantage of this measurement technique is that extremely small changes in transmittance ($\delta T/T \approx 10^{-5}$) have to be detected. Furthermore, no spatial resolution can be obtained, i.e. the resulting fields are averaged over the material film thickness.

Capacitance–Voltage Measurements

Via frequency-dependent capacitance–voltage (C – V) measurements insight into the electric field distribution of a multi-layer stack can be gained. With a proper equivalent circuit consisting of a series circuit of various RC elements, assumptions about the voltage and charge distribution can be made. However, this technique can only be used either in reverse bias or in forward direction before double carrier injection occurs. This means that the field distribution under real device operation cannot be measured. Moreover, again only an averaged field can be extracted. Nevertheless, it has been shown that below the onset of double carrier injection most of the applied voltage is dropped over the Alq₃ layer [Rieß et al. 2001; Berleb 2001; Riel 2002].

Direct Potential Sensing Method

Direct potential sensing is a straightforward method to measure the potential in a device under operating conditions in reverse and forward bias. A third metal pad is inserted between the organic layers and used to directly sense the potential [Hiramoto et al. 2000]. The experimental structure is shown in Figure 4.8. This approach has been adopted in this work because the combinatorial device fabrication is ideally suited to insert thin layers at various positions as discussed in Section 3.3.2. This method of direct potential sensing is capable of spatially resolving the potential within a working device. In the next section, the experimental details are described in more detail.

4.2.2 Direct Potential Sensing

The direct potential sensing method uses a third metal pad sandwiched between the organic layers [Hiramoto et al. 2000]. As the flexibility of the combinatorial system allows the insertion of thin layers at various positions in the devices (see Sec. 3.3.2) this approach has been adopted in this work. The schematic device structure is shown from top and side views in Figure 4.8. Similar to conventional devices, the area is still $2 \times 2 \text{ mm}^2$ but a thin metal pad 0.5 mm in width is inserted, extending through the device, which reduces the active device area by 25% (see Fig 4.8a). The investigated OLED structure has the following three-layer sequence.

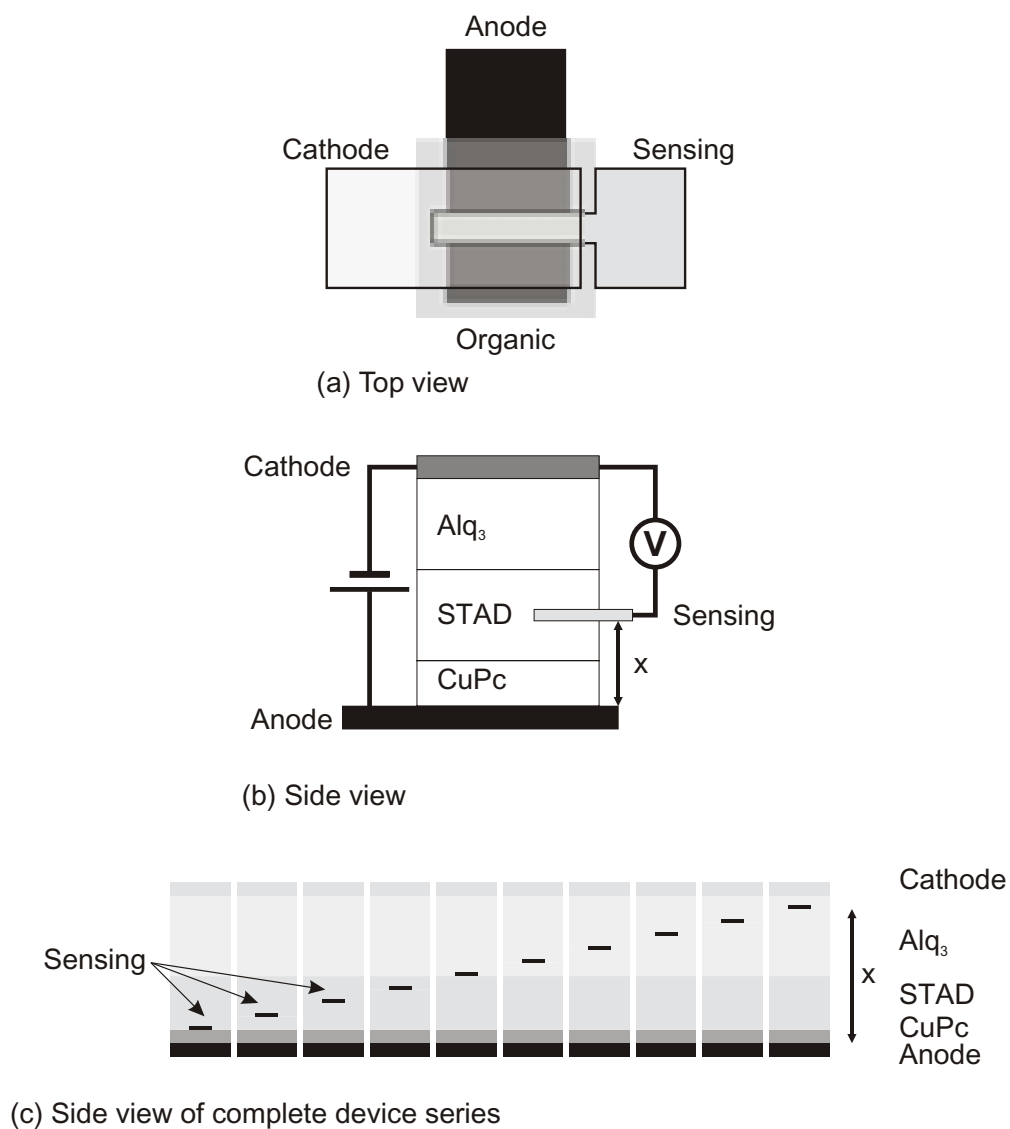


Figure 4.8: Schematic structure of a three-terminal device with intermediate electrode. The sensing pad is inserted at various positions x from the anode.

| Material | Ni | CuPc | STAD | Alq ₃ | Ca/Mg |
|---------------|-----|------|------|------------------|--------|
| Thickness / Å | 700 | 150 | 400 | 600 | 150/50 |

The devices are fabricated by staircasing the first layers of the organic stack, followed by inserting the metal sensing pad and finally completing the entire OLED structure (see Figure 3.9b, bottom). Recently, Hiramoto et al. [Hiramoto et al. 2000] demonstrated this method and chose Au as the third pad metal. Since Au diffuses easily, they had to use a device thickness of 8000 Å in total to avoid electrical shorts. In the experiments here, Ca/Mg or Al are used as intermediate electrodes, and devices with realistic thicknesses of 1100 Å can be investigated. The sensing pads have a thickness of 100 Å (Ca 50 Å/ Mg 50 Å), which enables the potential to be mapped in ten equidistant steps of 100 Å. For reference, there are ten control devices on the same substrate with identical structure but without the metal sensing layer. As sketched in Figure 4.8b, the voltage measurements are taken in a three-point configuration with a HP4145 parameter analyzer. Owing to the high impedance of the SMU ($\geq 10^{12}$ Ω), instrument loading is negligible. In order to exclude non-equilibrium effects the potential of this third pad is measured with reference to both the cathode and the anode.

Results

The I - V characteristics of ten devices having a metal pad are shown in Figure 4.9a. All devices show typical diode behavior, have low reverse currents, and show a sharp increase in the current density at around 2.1 V, which corresponds to double carrier injection. All the devices show rather steep characteristics and reach a current density of about 180 mA/cm² at 10 V. The onset of light emission is detected at 3 V, which is determined by the sensitivity of the photodiode. Figure 4.9b compares two devices with and without a sensing pad and shows that the current density is reduced by approximately 25% in the device having a metal pad. A reduction in this range is expected since the metal pad covers 1/4 of the active device area. The nominal identical 10 reference devices with without metal pad (not all shown here) show a variation of only $\pm 10\%$ in current density, whereas devices with metal sensing pad show a somewhat higher variation of about $\pm 30\%$. An exception is the device having the sensing layer located at the CuPc/ NPB interface, which exhibits more than one order of magnitude less current. This reduction in current is also observed in the corresponding reference device. A possible explanation can be given recalling the fabrication procedure of this series of devices

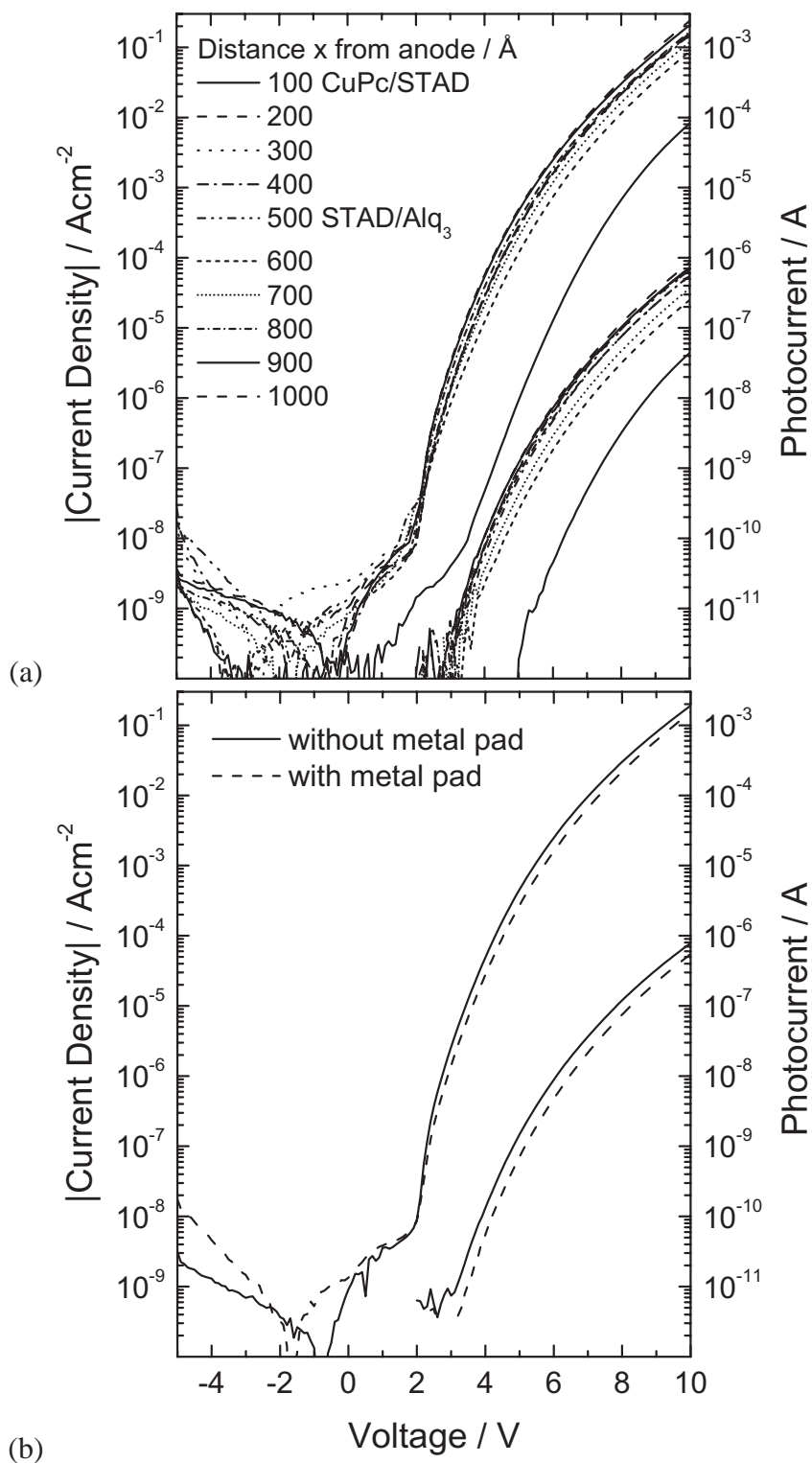


Figure 4.9: (a) $I-V$ EL characteristics of 10 devices having a metal sensing pad at various distances from the anode. (b) Comparison of this three terminal devices to the control device without metal pad. The insertion of the metal pad reduces the active area but does not disturb device operation.

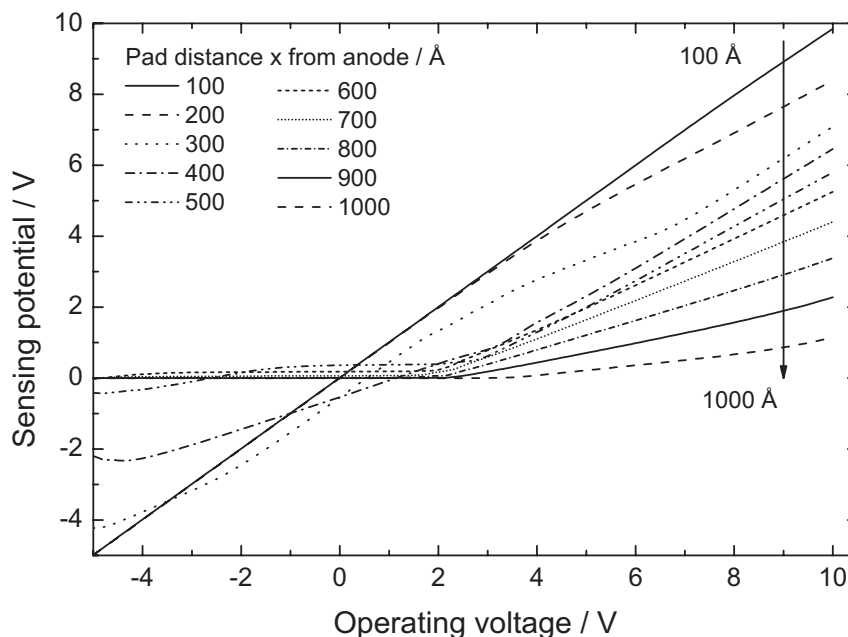


Figure 4.10: Sensing pad potential as a function of device operating voltage. Measurements on 10 devices which have the sensing pad at various positions.

(see Fig. 4.8c), which is first the deposition of an organic staircase, then the metal pad, and finally an opposing staircase of organic materials. The procedure of inserting the metal pad interrupts the evaporation process and might lead to contamination of that interface due to outgassing of the metal cell. As the CuPc/NPB interface is the most critical one as discussed in Section 4.1.1 a contamination of this interface will affect the I - V characteristic most severely. Although the variation in current density in the devices with sensing pad is slightly higher than in the corresponding reference devices, the change in voltage is only about ± 0.3 V at higher current densities. This justifies the assumption that the insertion of the third metal pad does not drastically influence the function of the device and the potential of the third pad can be regarded as a measure of the actual potential in the device.

Figure 4.10 shows the potential of the sensing electrode with reference to the grounded cathode as a function of operating voltage. This measurement is done for ten devices having the sensing layer at different positions. Above the onset (ca. 2.1 V) the potential of all sensing pads show a monotonic increase with applied device voltage, whereby the slope depends on the pad position in the device. For example, the pad at a distance of 100 Å from the anode

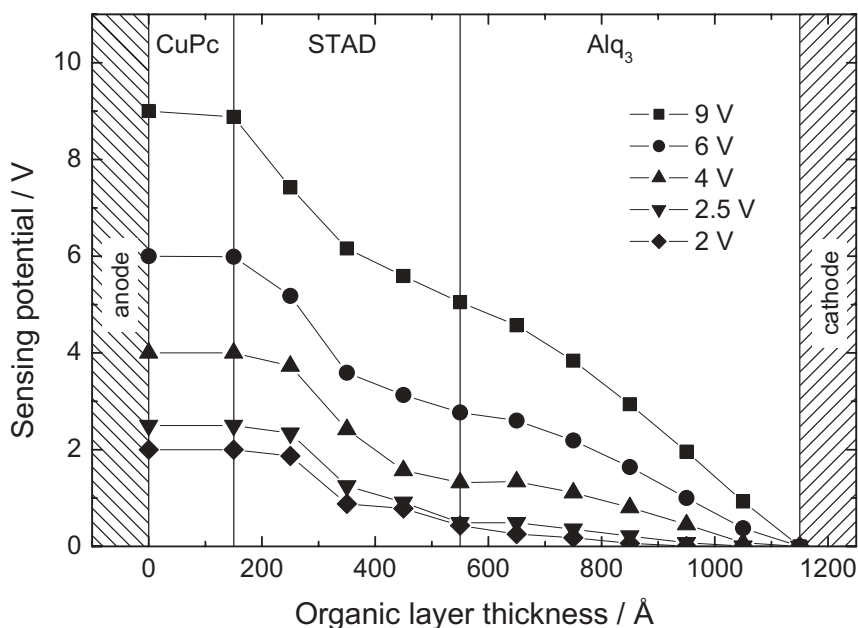


Figure 4.11: Sensing potential as function of sensing layer position at different applied operating voltages.

shows almost a straight line, which is nearly identical to the potential of the anode itself. With increasing distance from the anode the potential of the sensing pad approaches that of the cathode. In reverse bias the sensing potential stays at 0 V except in those devices where the pad is close to the anode. Not all the potential curves cross the origin, which can be explained by the fact that the minimum current in the I - V characteristics (Fig. 4.9) is not at 0 V either. This can be assigned in turn to non-equilibrium effects, i.e. the presence of trapped charges influencing the I - V curve at low voltage and current levels [Rieß et al. 2001; Brütting et al. 2001].

The potential distribution in this CuPc/ STAD/ Alq₃ device for a given operating voltage can now be extracted from Figure 4.10 by plotting the sensing potential versus the pad position. Figure 4.11 shows the results for different voltages from 2.5 to 9 V. The topmost curve corresponds to the potential distribution at 9 V which will serve as an example. As the cathode is grounded, the potential of anode and cathode corresponds to 9 V and 0 V, respectively. A voltage drop of only 0.1 V occurs between the anode and the first metal pad, which is located at the CuPc/STAD interface. The potential difference across the STAD layer is 3.8 V, whereby

the larger fraction drops in the first half close to the CuPc layer. Across the Alq₃ layer there is a voltage drop of about 5.1 V. Here, the slope of the potential curve is less steep close to the STAD/Alq₃ interface and becomes steeper towards the cathode. The described trend is generally true for other operating voltages. However, for lower voltages the relative voltage drop over the STAD layer becomes larger than that across the Alq₃ layer. For example, at an operating voltage of 2.5 V, almost 2.0 V is dropped over the STAD layer.

The low voltage drop over the CuPc layer might be caused by a low resistance path to the anode created during metal deposition when the metal penetrates the thin ($<300 \text{ \AA}$) organic layers. However, it has been shown in Section 4.1 that with this evaporation setup high-quality samples with extreme low leakage currents can be fabricated. Therefore, a short or low resistance path from the third pad to the bottom electrode or from the cathode to the third pad is believed to be unlikely. At 9 V there is a voltage drop of 0.15 V over the CuPc layer observed, which suggests that there is no low resistance path and possibly confirms ohmic injection into CuPc. In fact, experiments with a thicker CuPc layer should be used to rule out shorts and show that there is negligible voltage drop in the CuPc layer.

Discussion

The CuPc/STAD and the STAD/Alq₃ interfaces represent energy barriers for holes, whereas electrons have to overcome a barrier from the Alq₃ into the STAD layer. Positive and negative space charges will accumulate at these interfaces during device operation. This process will be further enhanced by the mobility discontinuities of the different materials. As Ni is a good hole-injecting electrode having a work function of about $\sim 5.5 \text{ eV}$ it is assumed to form an ohmic contact with CuPc. The voltage drop in CuPc is then solely determined by the transport properties and accumulated charges at the CuPc/STAD interface. This interface controls the current flow through the STAD layer and is responsible for the large voltage drop across the STAD layer. As it can be seen from Figure 4.11, the voltage does not decay linearly with thickness over the STAD layer, which is most likely due to the feedback of accumulated charges at the STAD/Alq₃ interface. Within the spatial resolution of the measurement technique this region of accumulated charges seems to extend more than 200 \AA into the STAD layer. On the cathode side no ohmic contact is achieved by the Ca electrode, particularly at low voltages. In addition, the rather low mobility of electrons in Alq₃ of the order of $\mu_e = 10^{-6} \text{ cm}^2/\text{Vs}$ [Barth et al. 2001] leads to a significant voltage drop across the Alq₃ layer. As the STAD/Alq₃ inter-

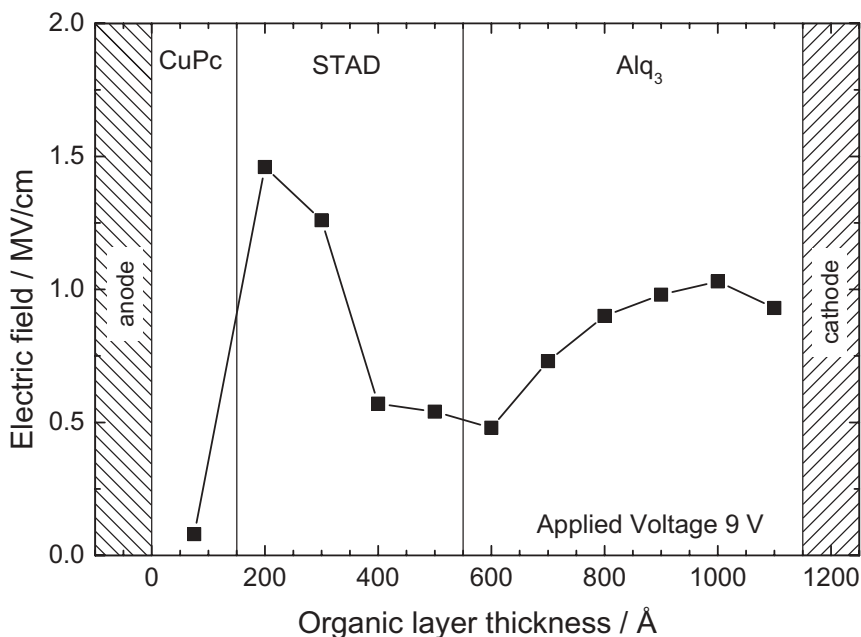


Figure 4.12: Internal fields in an OLED structure at forward bias of 9 V derived by the potential sensing method. The average fields in STAD and Alq₃ are 0.95 and 0.85 MV/cm, respectively. The average field in the device is 0.78 MV/cm.

face prevents electron penetration into STAD the recombination of electrons and holes takes place in the Alq₃ layer. As the hole mobility in Alq₃ is at least one order of magnitude lower than the electron mobility [Naka et al. 1999], recombination is restricted to a region close to the STAD interface. Consequently, the voltage drop in this region is lower as it can be detected by the potential sensing method (see Fig. 4.11). The measured potential distribution is consistent with the results on 2D-layer variations of the CuPc/NPB/Alq₃ structures (see Sec. 4.1.1). Although two different hole transport materials have been used in these experiments, they will be comparable since the energy levels as well as the transport properties of STAD and NPB are very similar.

Figure 4.12 shows the internal fields in an OLED structure at forward bias of 9 V derived by the potential sensing method. A low field in the CuPc layer is actually expected since Ni is assumed to form an ohmic contact. The highest field in the device is observed in STAD layer close to the CuPc interface. As mentioned above, accumulation of charges will reduce the local field at the STAD/Alq₃ interface. The field in Alq₃ is low close to the STAD/Alq₃ interface

but increases towards the cathode and decreases again in close proximity to the cathode.

Figure 4.13 summarizes the results by showing the schematic energy diagram based on the potential measurement for a forward bias of 9 V. For this schematic, the work functions of the electrodes and the HOMO and LUMO levels for the organic materials are taken from Tables 5.3,5.4 and Table A.1 in the Appendix.

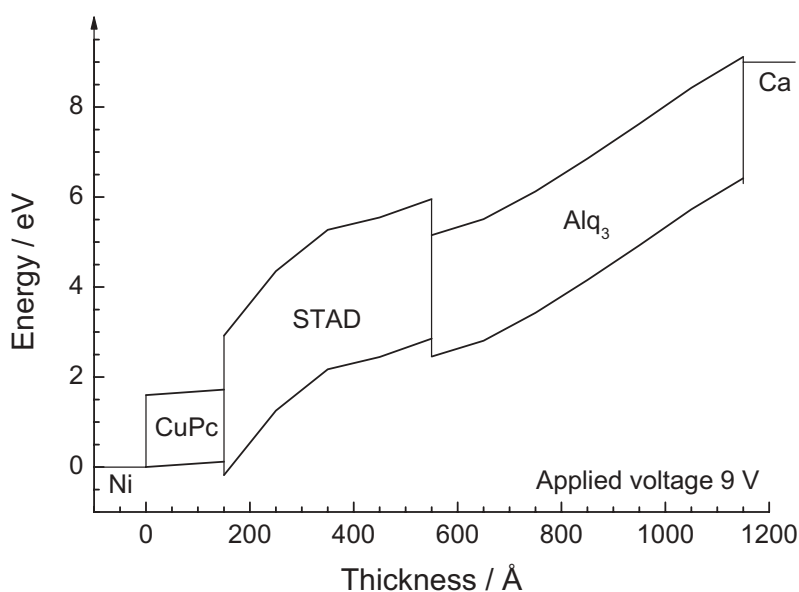


Figure 4.13: Schematic energy level diagram extracted from potential sensing data with a third intermediate electrode at forward bias of 9 V.

4.2.3 Summary: Potential Sensing

The described method of potential sensing can directly map the potential in an operating OLED. In contrast to other methods, i.e. electroabsorption and capacitance–voltage measurements, which only measure an averaged electric field over the whole layer, this technique allows the determination of the electric field distribution with a spatial resolution down to 100 Å. An increase in spatial resolution could be achieved with thinner sensing pads consisting of Al or similar electrode materials. The potentials determined by this method are consistent with simple considerations taking energy barriers and space charge accumulation into

account. These findings are also consistent with two-dimensional layer thickness variations as discussed in Section 4.1.1. With this method the spatially resolved fields in the individual layers of a CuPc/STAD/Alq₃ OLED structure have been determined. Although this method has been applied to a rather complex multilayer structure, experiments especially on single layer structures with unipolar current flow will help to separate the effects of injection and transport. In a next step, these findings have also to be compared with theoretical models in order to gain a more complete picture of internal fields in organic light-emitting structures.

4.3 Complex Multilayer Structures

In the previous sections, three-layer structures based on Alq₃ emission layers have been discussed. In order to achieve higher efficiencies, device structures usually become more complex, i.e. devices often consist of five or six materials. This requires systematic investigations in order to understand the interplay between these layers and to find the appropriate parameters for optimum device performance. Device structures with improved device performance will be discussed in the next sections. First, the influence of the width of the doped region is investigated in single doped devices. Second, devices with two fluorescent dopants are fabricated via co-evaporation from three effusion cells. Third, high-efficiency devices with materials based on phosphorescence are discussed.

4.3.1 Doped OLEDs: Width of Doped Region

Doping of the host material with highly fluorescent dyes is a well established method to significantly increase the efficiency of OLEDs [Tang et al. 1989]. Moreover, the emission color can be tuned within a certain range by choosing the appropriate dopant. Depending on the energy levels of the dopant with respect to the host material these dopants can act as efficient recombination centers but in parallel can also introduce charge carrier traps which deteriorate the transport properties in the host material. This in turn leads to an increase of the operating voltage for the same current flow. Maximizing the benefit of the doping material in terms of efficiency and color, but minimizing the operating voltage often requires a compromise. Apart from optical considerations (see Sec. 5.1) the dopant should only be inserted at the location where excitons in the host material are mainly created and recombination takes place. First guesses about the location where recombination will take place can already be made considering the HOMO and LUMO levels of the organic materials used [Adachi et al. 1991; Aminaka et al. 1996]. Nonetheless, the charge carrier transport capabilities of the used materials also have to be considered. For example, the recombination zone in a two-layer heterostructure based on hole transporting NPB and electron transporting Alq₃ is known to be located in Alq₃ close to the HTL/ ETL interface [Tang et al. 1989]. However, additional doping or emission layers may change the system considerably. In fact, most fluorescent materials show a high quantum yield when they are doped into a host matrix with low concentrations, typically from 0.1 to 10%. Recently, doping of Alq₃ with DJCTB was reported to result in efficient and

long-term stable devices [Hatwar et al. 2000]. In order to determine the width of the doped region appropriate to compromise efficiency and operation voltage, a series of devices with varying width of the doped region is fabricated. The detailed structure of this device series is the following:

| Material | Ni | CuPc | NPB | Alq ₃ :DCJTB | Alq ₃ | Ca |
|---------------|-----|------|-----|-------------------------|------------------|-----|
| Thickness / Å | 700 | 150 | 500 | x | $500 - x$ | 200 |



The thickness of the doped Alq₃ layer is increased from 0 to 500 Å whereas the sum of the doped and undoped Alq₃ layer thickness layer is kept constant at 500 Å. With the combinatorial setup a direct comparison of 1 and 5% DCJTB concentration is realized on one substrate.

Results and Discussion

Figure 4.14 shows the I - V characteristics which exhibit excellent diode like behavior with extremely low reverse currents ($< 10^{-8}$ A/cm²) and an EL onset at ≈ 2.2 V for all devices. With increasing thickness of the doped layer the current flow is reduced, e.g. the current density at 8 V of the fully doped devices with reference to the undoped device is decreased by a factor of ~ 7 for the 1% doped and a factor of ~ 15 for the 5% doped devices. This is tantamount to an increase of driving voltage for achieving the same constant current density. Figure 4.15a shows the driving voltage necessary for achieving a current density of 20 mA/cm² as a function of doped layer thickness. For the undoped devices, a voltage of 6.8 V is required to achieve 20 mA/cm². With increasing thickness of the doped layer this voltage steadily increases up to 8.5 and 9.2 V at a thickness of 400 Å for the 1% and the 5% doped samples, respectively. This can be understood by the fact that dopants act as traps, which deteriorate the transport through the host material. However, the driving voltage for the fully doped devices (500 Å) is lower than might be expected from the extrapolation of the increasing voltage with a rate of ~ 0.6 V per 100 Å and 0.42 V per 100 Å for the 1 and 5% doped samples, respectively. In the fully doped cases, the dopant is also in contact with the cathode and facilitates electron injection, thereby reducing the operating voltage.

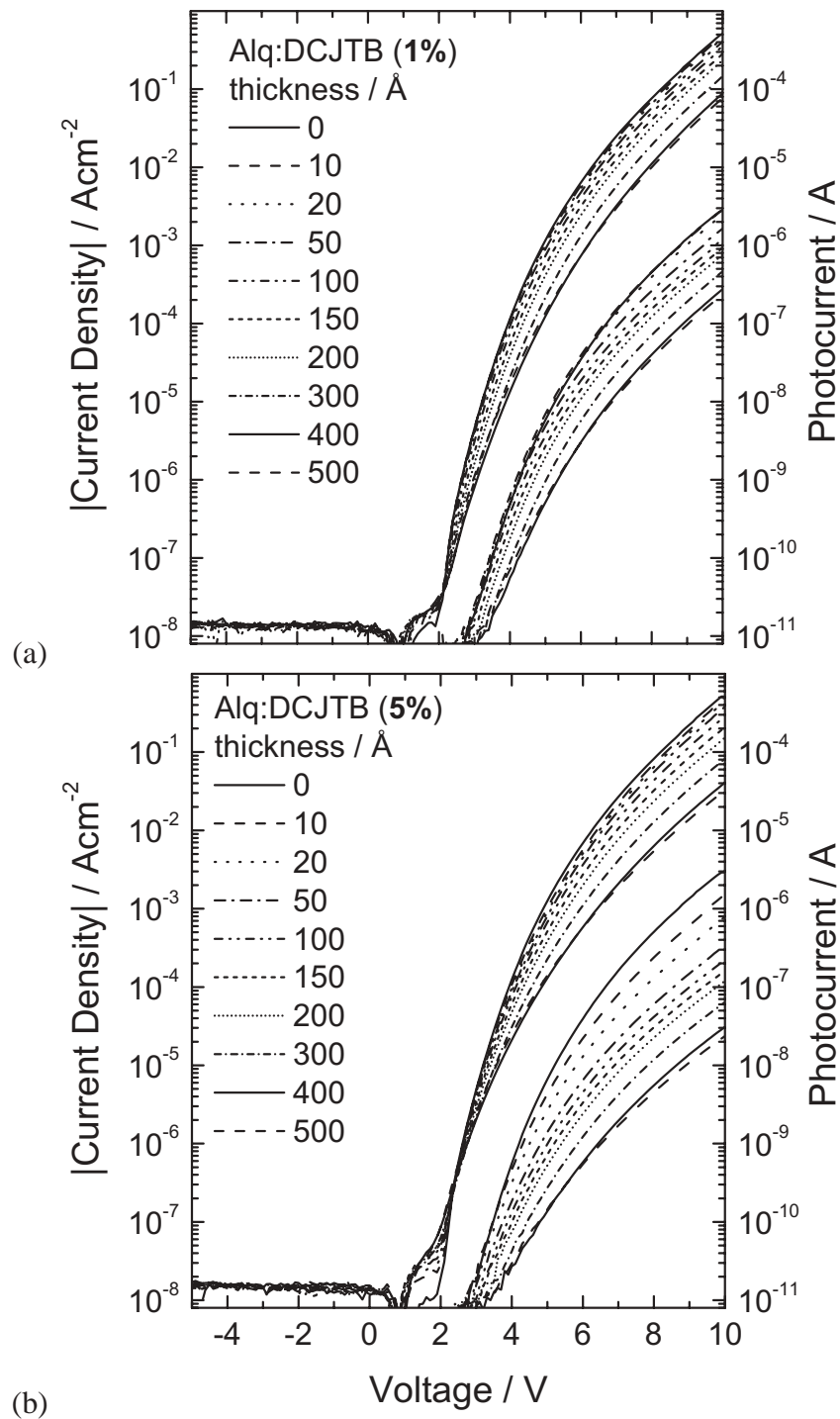


Figure 4.14: I - V EL characteristics of red-emitting devices with varying width of the doped Alq₃:DCJTB region; (a) DCJTB 1% and (b) DCJTB 5% concentration.

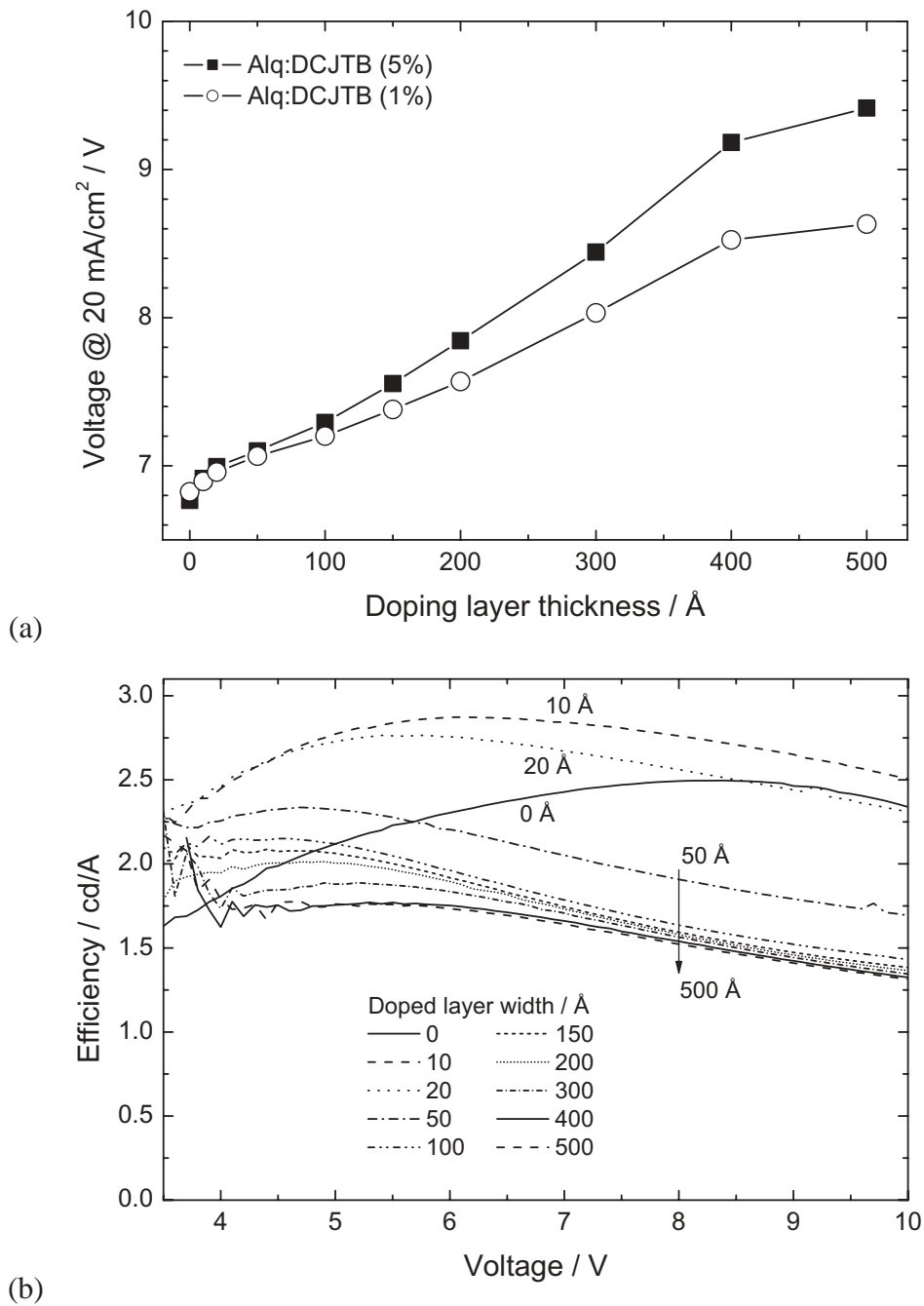


Figure 4.15: CuPc/ STAD/ Alq₃:DCJTBS/ Alq₃ OLEDs with various widths of the doped region. (a) Driving voltage at 20 mA/cm². (b) Efficiency versus voltage.

Figure 4.15b shows the efficiency versus voltage characteristic of the 1% doped Alq₃:DCJTB devices. Remarkable is the general functional behavior of the efficiency versus voltage curves. The efficiency of the undoped Alq₃ device (0 Å) increases to its maximum at 8.4 V and slightly drops afterwards. The doped samples, however, especially with a doped region >50 Å, show their maximum in efficiency at voltages below 5–6 V and steadily decrease toward higher voltages. For example, the efficiency of the device with a 100-Å-thick doped region (DCJTB 1%) reaches 2.15 cd/A at 4.5 V and drops to 1.43 cd/A at 10 V. This decrease in luminescence efficiency has been associated with quenching by cationic species either DCJTB⁺ or Alq₃⁺ [Young et al. 2002].

Figure 4.16 shows the spectra of the devices with increasing width of the doped region for two different concentrations of DCJTB. The Alq₃ reference devices ($x = 0$) show the emission maximum at 544 nm with a FWHM of 100 nm. The 10-Å-thick DCJTB doped layers at the NPB/Alq₃ interface result in a red-shifted spectrum with a peak wavelength of 596 and 616 nm for the 1 and 5% doped devices, respectively. These spectra exhibit a shoulder on the short wavelength side, indicating that some Alq₃ host emission is still present, however less pronounced in the higher doped samples. With increasing width of the doped region the spectrum is further red-shifted and Alq₃ emission is further suppressed. At widths greater than 150 Å no significant change in the spectral characteristic can be detected. The peak wavelengths for the 500-Å-thick 1 and 5% doped DCJTB structures are 616 and 644 nm, respectively. The spectral widths (FWHM) are decreased to 86 and 76 nm, respectively.

Figure 4.17 shows the efficiency as a function of width of the doped layer. The Alq₃ reference devices show an efficiency of ~ 2.7 cd/A. For the 5% doped DCJTB samples the efficiency rapidly drops to a value of 0.5 cd/A at a thickness of 50 Å and slowly decreases to 0.34 cd/A at 500 Å. Devices of the lower doped sample series (DCJTB 1%) show an increase in efficiency to 3.1 cd/A at 10 Å and a subsequent monotonic decay to 1.8 cd/A at 100 Å and 1.5 cd/A at 500 Å. The sharp drop in efficiency at small doping widths is mainly due to the red-shift of the spectrum and the lower sensitivity of the eye response curve. At doping layer thicknesses above 50 Å, the efficiencies of the 5% doped samples are generally a factor of ~ 3 lower than those of the 1% DCJTB samples. Since the efficiencies are given in cd/A, the red-shift accounts for a factor of 2 because the human eye is less sensitive in the red spectral range (see Fig. 3.14, page 51). The additional decrease in efficiency might be caused by concentration quenching at the relatively high concentrations of 5% DCJTB. It was shown in Figure 4.16 that there is no significant shift in spectrum for doping widths greater than

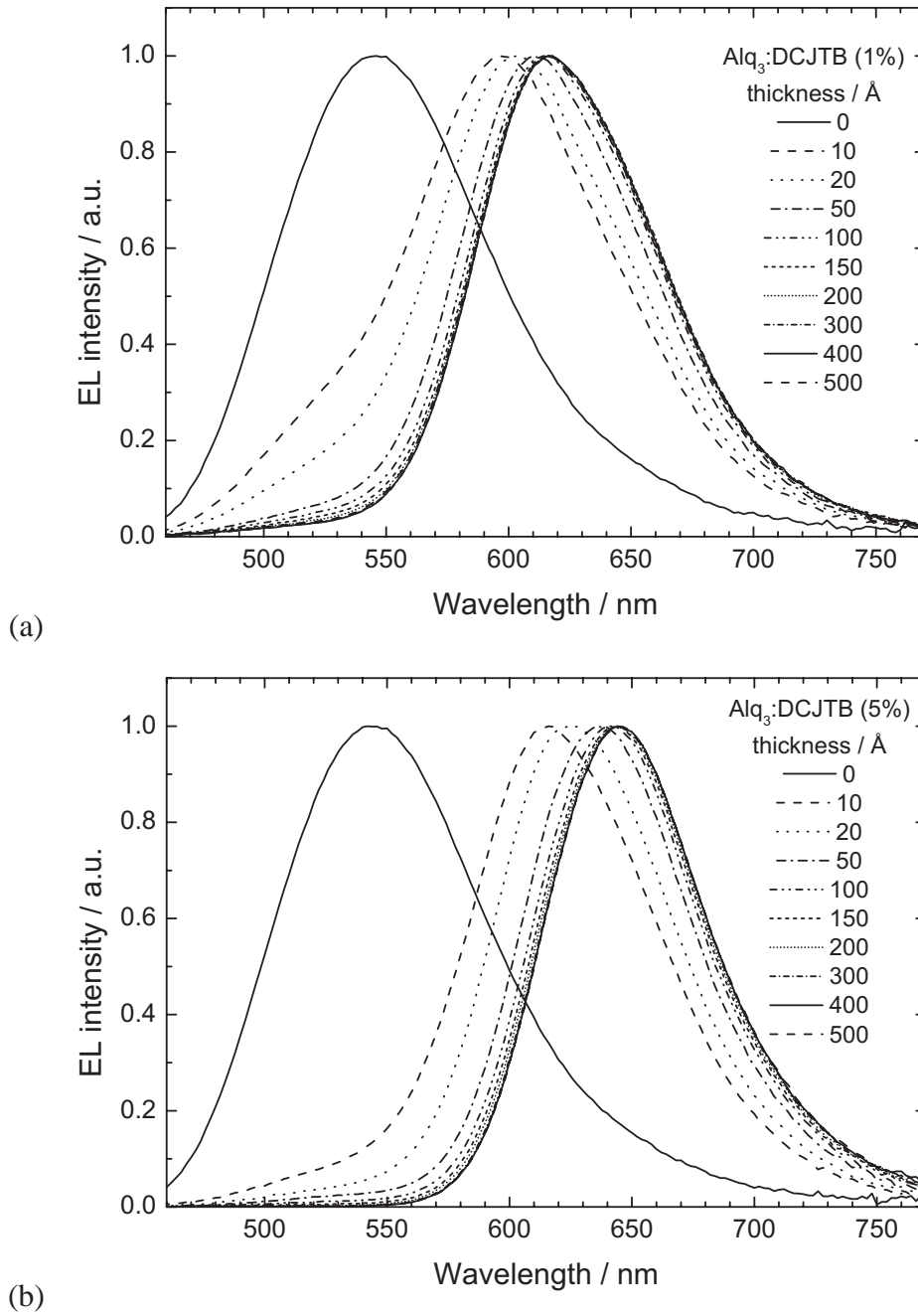


Figure 4.16: Normalized spectra of DCJTB doped structures at 20 mA/cm^2 with different doping region width and doping levels: (a) DCJTB 1%, (b) DCJTB 5%. The spectra are clearly red-shifted with increasing doping region width and doping concentration.

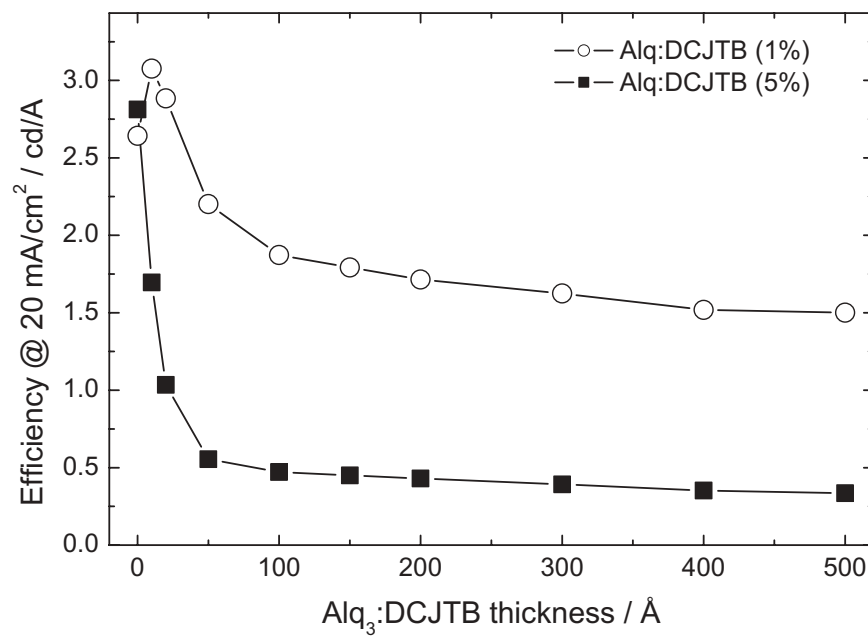


Figure 4.17: Luminance at 20 mA/cm² of Alq₃:DCJTB structures with varying width of doped region. Upper curve 1%, lower curve 5% DCJTB concentration.

150 Å. Consequently, the width of the doping region need not to be larger than 150 Å in order to achieve the pure dopant spectrum and maintain the highest possible efficiency and lowest driving voltage. This holds for this special case of the Alq₃:DCJTb system, and can be easily checked by combinatorial methods for other host/dopant systems.

4.3.2 Double-Doped OLEDs

Recently, a concept was proposed to improve the efficiency of red OLEDs by doping the Alq₃ host layer with two dopants (Rubrene and DCM) [Hamada et al. 1999]. In order to directly compare single versus double doping, a combinatorial experiment has been performed to study the impact of the second dopant on device performance. The comparison is carried out in a single evaporation run, i.e. two combinatorial matrices of 50 devices each are fabricated on one substrate (see Sec. 3.10). The complete device structure is listed in the following table:

| Material | Al/Ni | CuPc | STAD | Alq ₃ (:Rub):DCJTb | Alq ₃ | Ca/Mg |
|---------------|--------|------|---------|-------------------------------|------------------|--------|
| Thickness / Å | 700/50 | 150 | 300–750 | 250 | 200–600 | 100/50 |

The hole transporter (STAD) and the electron transport layer (Alq₃) are varied in two dimensions in order to find the optimum position of the emission zone in the cavity. As shown in Section 4.3.1, an increase of the width of the doped zone beyond ~150 Å does not lead to a significant increase in efficiency nor to a change in color. Therefore, the width of the doped region was set a bit larger to 250 Å. The devices differ only in the single-doped (Alq₃:DCJTb 2%) and double-doped (Alq₃:Rubrene 5%:DCJTb 2%) emission layer; all other layers are identical, including anode and cathode.

Results and Discussion

Figure 4.18 shows a selection of the *I*–*V* EL characteristics of single and double-doped structures. The devices shown here have a constant Alq₃ layer thickness of 750 Å including the doped region of 250 Å and a varying STAD thickness from 300 to 750 Å. All devices show extremely low reverse currents ($< 10^{-8}$ mA/cm²) and a uniform current onset at about 2.1 V. In general, the current decreases with increasing STAD layer thickness. For example, the current density at 10 V ranges from 20 to 135 mA/cm² and from 35 to 210 mA/cm² for the single

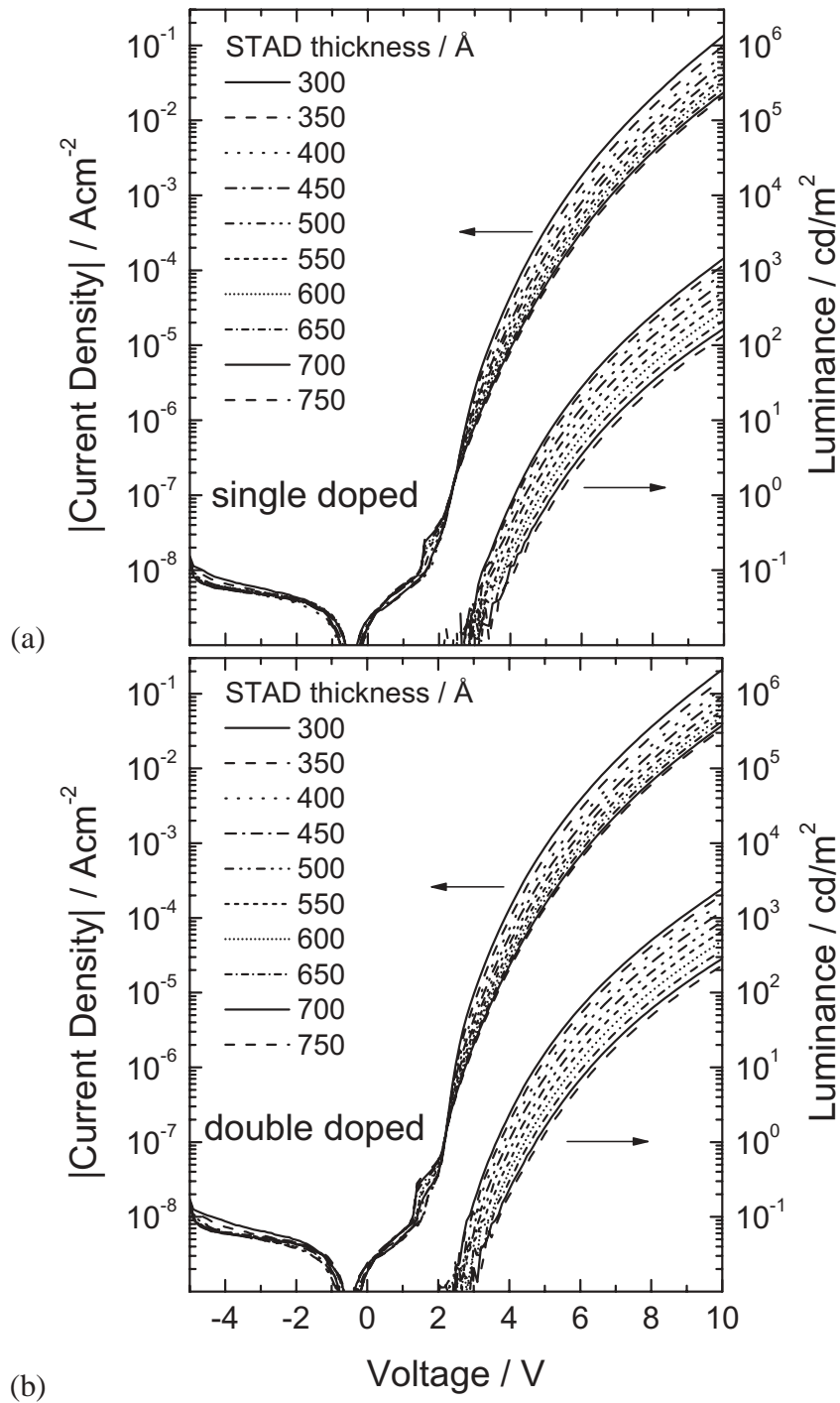


Figure 4.18: I - V EL characteristics of single and double-doped OLED structures. (a) Alq_3 :DCJT B (2%) and (b) Alq_3 :Rubrene (5%):DCJT B (2%). Double-doped structures exhibit a 50% higher current density at a given voltage. Detailed device structure see text.

and double-doped structures, respectively. The steepness of the I - V characteristics at low voltages is slightly higher for the double-doped structures than for their single-doped counterparts. This can be attributed to an improved injection of holes from STAD into the Alq_3 layer via the Rubrene dopant sites at this interface. All double-doped structures exhibit a roughly 50% higher current density than to their single-doped equivalents. The increased current density in the double-doped samples might be caused by improved hole transport via the relatively high concentration (5%) of Rubrene. Figure 4.19 compares the efficiencies at 20 mA/cm^2 of the two combinatorial matrices. The maximum efficiencies are 1.5 and 1.8 cd/A for the single and double-doped structures, respectively. In both matrices, the most efficient devices have a STAD thickness of 400 \AA and a Alq_3 layer thickness of 500 \AA . Since the same scale is used in both plots, it can directly be seen that the double-doped samples are on average $\sim 15\%$ more efficient than their single-doped counterparts. In Figure 4.20, the spectra of the two most efficient devices from each submatrix are compared. The single-doped device exhibits an intensity

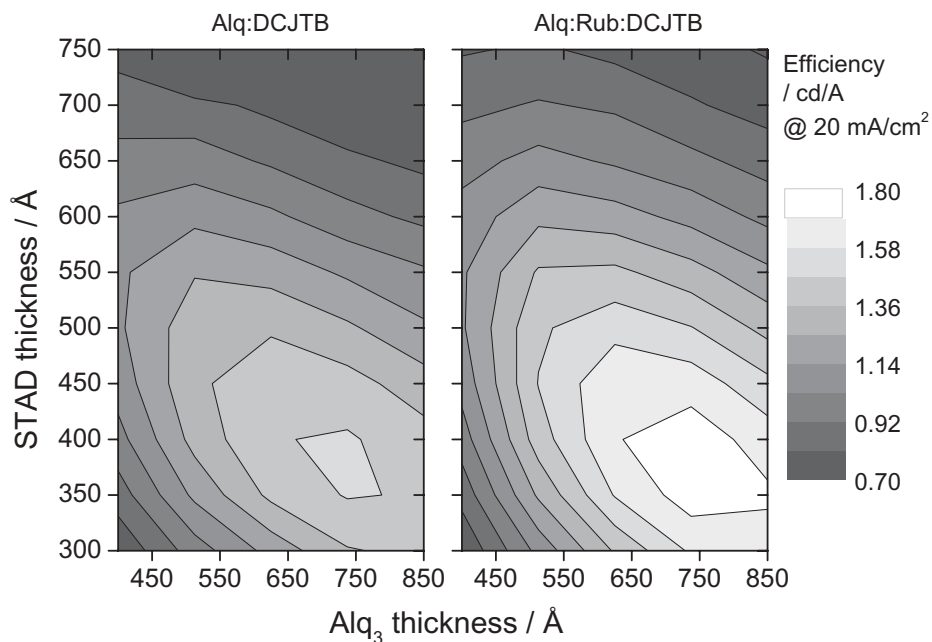


Figure 4.19: Comparison of efficiency of (a) single-doped (Alq_3 :DCJTb) and (b) double-doped (Alq_3 :Rub:DCJTb) OLEDs that differ only in the 250 \AA emission zone. The same scale in (a) and (b) shows that the double-doped samples are on average 15% more efficient than their single-doped counterparts.

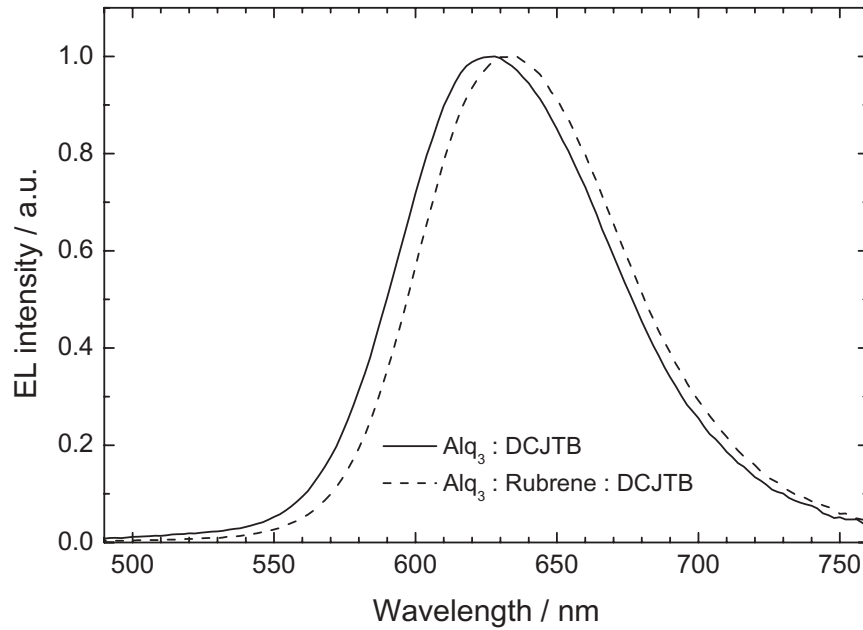


Figure 4.20: Spectra of single ($\text{Alq}_3:\text{DCJTb}$) and double-doped ($\text{Alq}_3:\text{Rub}:\text{DCJTb}$) OLEDs that differ only in the emission zone. A red-shift (6 nm) of the spectrum is observed in the double-doped case.

maximum at 628 nm and a FWHM of 88 nm, whereas the double-doped device exhibits an intensity maximum at 634 nm with a FWHM of 84 nm. Since the layer thicknesses of these two devices are identical, the observed red-shift cannot be attributed to optical interference effects (see Sec. 5.1). Hence, this red-shift in DCJTb emission spectrum is solely caused by the presence of rubrene. Similar spectral shifts were observed in high concentration doped $\text{Alq}_3:\text{DCM}$ samples and were interpreted as polarization-induced spectral shifts [Bulović et al. 1998]. The spectra do not show a shoulder around 530 nm, indicating that emission from Alq_3 is completely suppressed and only DCJTb contributes to the emission spectrum.

Another important aspect of double-doping is the impact on the operating lifetime. Figure 4.21 shows the operating stability of single and double-doped OLED structures from the above matrices. The half life of the device is thereby defined as the time $t_{1/2}$ elapsing from initial luminance to half luminance. A current density of 100 mA/cm^2 results in a starting luminance of 1050 and 1200 cd/m^2 for the single-doped and double-doped devices, respectively. Although the initial drop in luminance is faster for the double-doped device, the degradation

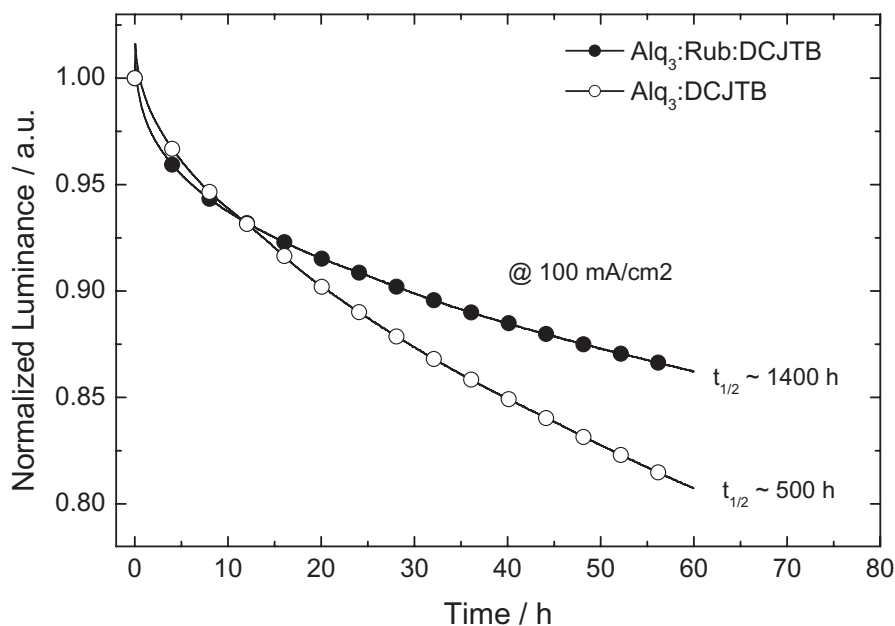


Figure 4.21: Lifetime comparison of single-doped ($\text{Alq}_3\text{:DCJTb}$) and double-doped ($\text{Alq}_3\text{:Rub:DCJTb}$) OLEDs. Assuming coulombic ageing, this results in extrapolated operating lifetimes $t_{1/2}$ at 100 cd/m^2 of 6.500 and 16.000 h, respectively.

rate is smaller after ~ 10 h. After 60 h of continuous driving, the luminance drops to about 80% and 86% for the single and double-doped samples, respectively. Assuming coulombic ageing, this results in extrapolated operating lifetimes $t_{1/2}$ at 100 cd/m^2 of 6.500 and 16.000 h, respectively. In conclusion, double-doping is a promising way to increase the efficiency and drastically extend device lifetime.

4.3.3 OLEDs Based on Phosphorescence

In the previous section two dopants have been used to increase the efficiency and stability of devices. However, fluorescent molecules limit the internal quantum efficiency to 25% according to the selection rules of spin statistics. Therefore, OLEDs based on phosphorescence have recently attracted attention since they are much more efficient than OLED structures based on fluorescence [Hoshino and Suzuki 1996; Baldo et al. 1999; Tsutsui et al. 1999; Ikai et al. 2001]. Unlike fluorescent materials, phosphorescent materials makes use of both the singlet

and the triplet states, which could lead to a theoretical internal efficiency of 100% [Adachi et al. 2001]. The archetype phosphorescent materials in OLEDs are PtOEP (Octaethyl-porphine platinum(II)) and Ir(ppy)₃ (tris(2-phenylpyridine) iridium) [Baldo et al. 1998; Baldo et al. 1999]. Recently, many different Ir complexes with various ligands have been synthesized to adjust the emission wavelength [Lamansky et al. 2001]. Although these materials offer significantly higher efficiencies the device structures are generally more complex. In other words, four or more layers are typically used and each layer is needed for specific purposes. The phosphorescent structures investigated in this work consist of the following five layers:

- (1) hole injection layer (HIL): CuPc
- (2) hole transport layer (HTL): STAD
- (3) emission layer (EML): CBP:Ir(ppy)₃
- (4) hole/exciton blocking layer (HBL): BCP
- (5) electron transport layer (ETL): Alq₃

Figure 4.22 sketches the energy diagram of such a device. CBP is a wide-gap host material ($E_g = 3.1$ eV) with triplet energy levels favorable for energy transfer to the phosphorescent material Ir(ppy)₃. BCP is a material with a wider gap ($E_g = 3.4$ eV) and a HOMO level below the HOMO of CBP, which makes it suitable as a hole-blocking as well as an exciton blocking layer. In order to maximize the efficiency of such complex device structures a detailed under-

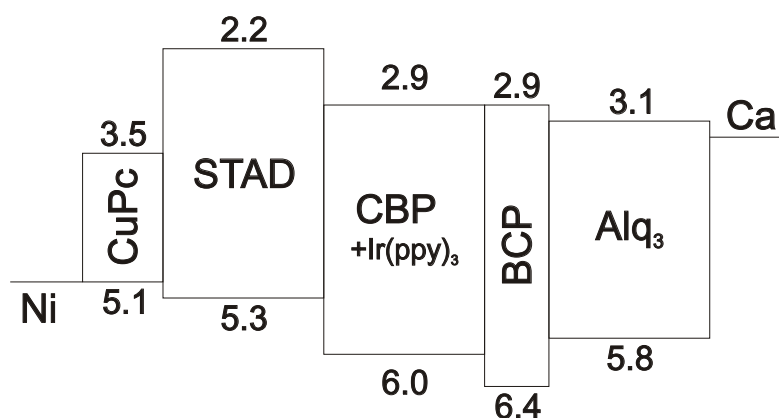


Figure 4.22: Schematic energy level diagram of phosphorescent device. HOMO and LUMO values are given in eV. For references see Table A.1, page 197.

standing of the influence of the individual layers is absolutely necessary. In the following, the influence of the individual layers is investigated systematically. The impact of interference effects on the shape spectral characteristics has been discussed elsewhere [Riel 2002]. Here, the function of the hole transport layer (STAD) and of the electron transport layer (Alq_3) on device performance is considered first. The thickness variation of the emission layer (CBP:Ir(ppy)_3) and of the hole blocking layer is discussed afterwards.

Variation of STAD and Alq_3 Layer Thickness

The emission in the phosphorescent structure described above takes place in the Ir(ppy)_3 doped CBP layer. In order to determine the optimum position of the CBP layer in this top emitting structure, the STAD and the Alq_3 are systematically varied over a wide range from 100 to 1000 Å. The CBP:Ir(ppy)_3 thickness and CBP thickness are set to fixed values 200 Å and 100 Å, respectively. Similar values for Alq_3 and BCP have been reported in the literature [Baldo et al. 1999]. The doping concentration of Ir(ppy)_3 in CBP is about 6% and the detailed device structure is listed in the following table:

| Material | Ni | CuPc | STAD | CBP:Ir(ppy)_3 | BCP | Alq_3 | Ca/Mg |
|---------------|-----|------|----------|------------------------|-----|----------------|--------|
| Thickness / Å | 700 | 100 | 100–1000 | 200 | 100 | 100–1000 | 150/50 |

Results and Discussion

Figure 4.23 shows 20 selected I - V curves out of the 100 in the combinatorial matrix. In Figure 4.23a, the devices have a fixed Alq_3 thickness of 300 Å and varying STAD thickness, whereas in Figure 4.23b the STAD thickness is fixed at 300 Å and Alq_3 thickness varied from 100 to 1000 Å. The onset in current flow, which is characterized by a steep increase of the I - V characteristic and accompanied by the onset of light emission, is around 3.0 V. Compared to the standard three-layer structure CuPc/NPB/Alq_3 (see Sec. 4.1.1), in this case, the current flow is more dependent on the thickness of the electron transporter (Alq_3) than on the hole transporter (here it is STAD). For example, at 10 V the current density decreases from 210 to 3.6 mA/cm^2 with increasing STAD layer thickness from 100 to 1000 Å (Fig. 4.23a). In contrast, varying the Alq_3 layer thickness in the same range, the current density drops from 380 to 1.4 mA/cm^2 . The light output is reduced by almost two orders of magnitude when

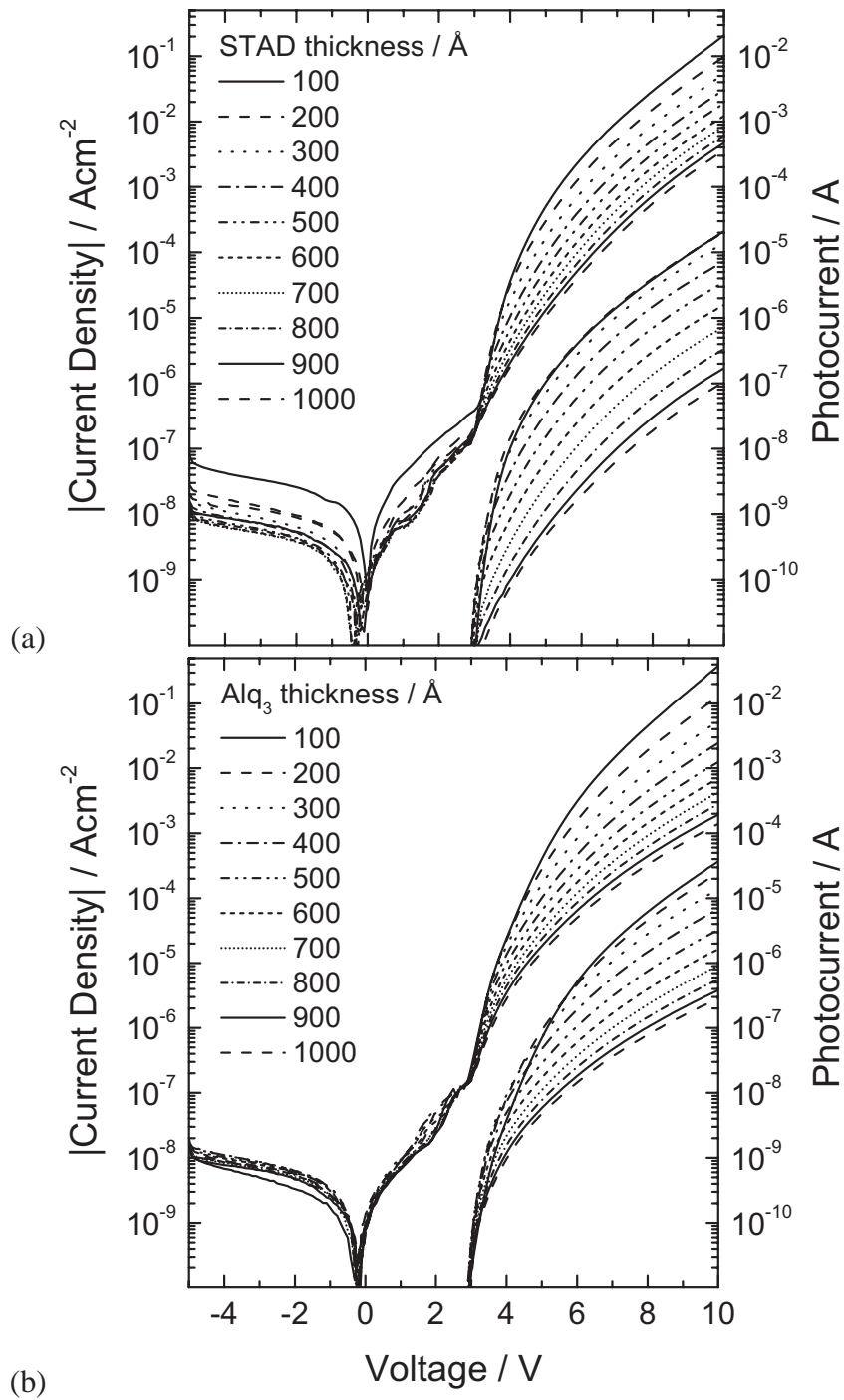


Figure 4.23: I - V EL curves of 20 out of 100 combinatorial multilayer devices based on $\text{Ir}(\text{ppy})_3$. (a) Fixed Alq_3 thickness of 300 Å and varying STAD thickness. (b) Fixed STAD thickness of 300 Å and varying Alq_3 thickness.

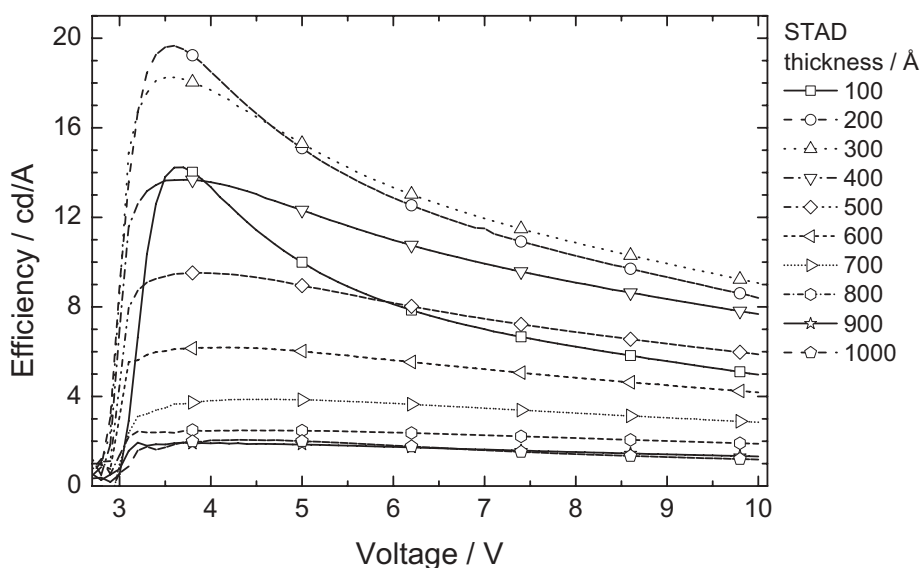


Figure 4.24: Efficiency in cd/A as a function of voltage of CuPc/ STAD/ CBP:Ir(ppy)₃/ BCP/ Alq₃ OLEDs. A maximum value of 19.7 cd/A at 3.6 V and a luminance of 1 cd/m² is achieved. The luminance of 100 cd/m² is reached at 7 V where the efficiency is 11.5 cd/A.

increasing the STAD and the Alq₃ layer from 100 to 1000 Å (Fig. 4.23a and b). Especially at lower voltages (<5 V), the reduction of the light output is more pronounced if the thickness of STAD is increased by the same amount as the Alq₃ layer thickness.

Figure 4.24 is an example of efficiency versus voltage for one row of the combinatorial matrix (constant Alq₃ 400 Å), which includes the most efficient device. The efficiency curves show a sharp increase above 3 V, which corresponds to the EL onset. A maximum efficiency of 19.7 cd/A at 3.6 V is achieved for the device with 200 Å STAD thickness. Especially for devices with thin (< 500 Å) STAD layers, a pronounced decrease in efficiency with increasing voltage is observed. For example, the efficiency of the latter device drops to 8.5 cd/A at 10 V. At higher voltages the device with 300 Å STAD layer thickness is the most efficient. A practical luminance, e.g. 100 cd/m², is reached at 6 V with an efficiency of 12.9 cd/A. This trend of decreasing efficiency is less pronounced for thicker STAD layers (see Fig. 4.24).

Figure 4.25 shows the efficiency in cd/A in a 2D overview as a function of STAD and Alq₃ layer thicknesses for all phosphorescent devices. Figure 4.25a and b show the efficiency

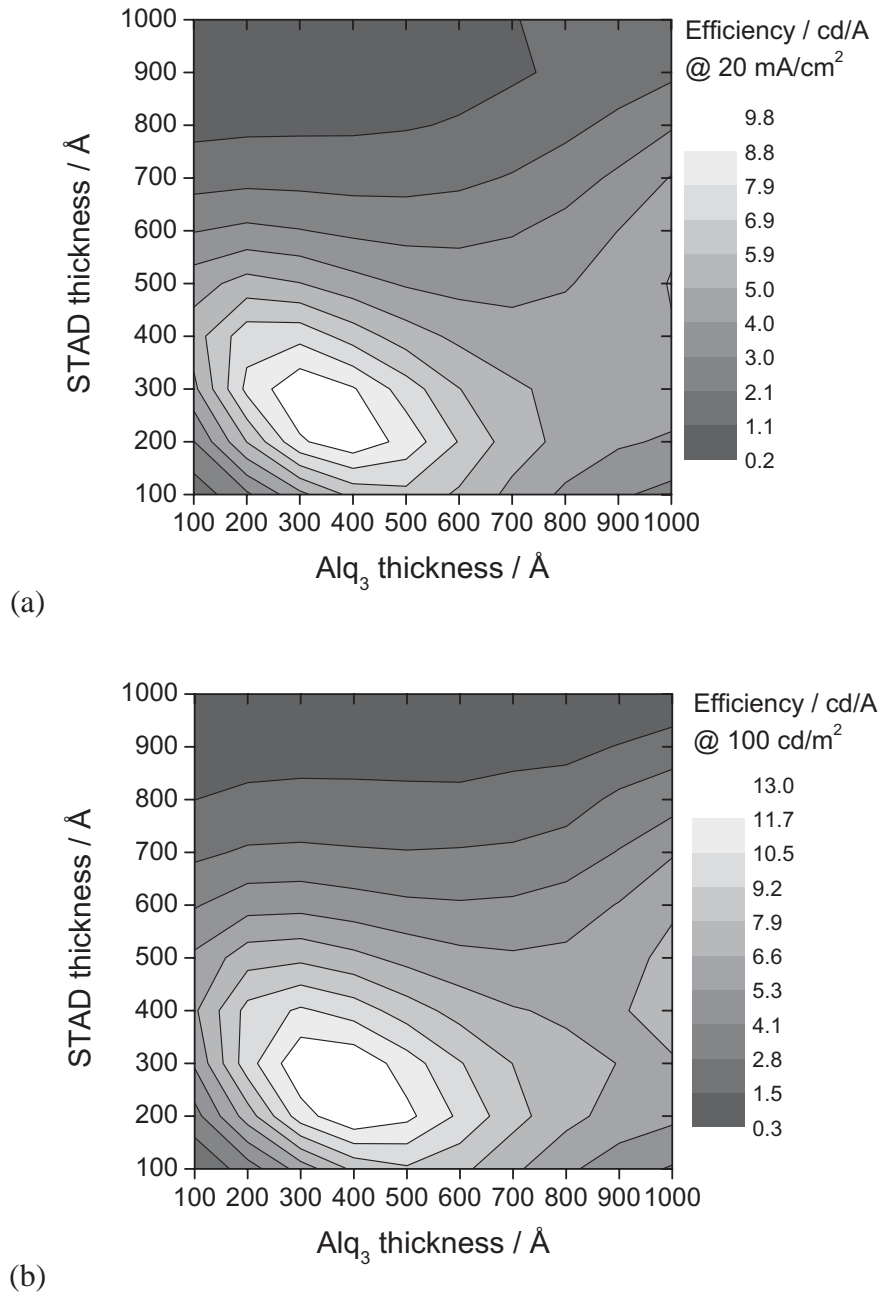


Figure 4.25: Efficiency of CuPc/ STAD/ CBP:Ir(ppy)₃/ BCP/ Alq₃ OLEDs as a function of STAD and Alq₃ layer thickness. (a) Efficiency in cd/A at 20 mA/cm². (b) A maximum efficiency of 12.7 cd/A at 100 cd/m² is achieved for STAD 300 Å and Alq 400 Å.

at 20 mA/cm² and 100 cd/m², respectively. The shape of the contour plot does not change significantly and the efficiency values are approximately 50% higher in the latter case. A maximum efficiency of 12.7 cd/A at 100 cd/m² is achieved for the device with STAD 300 Å and Alq₃ 400 Å. The efficiency is clearly more dependent on the STAD layer thickness than on the Alq₃ layer thickness. An increase in STAD to 1000 Å results in a drastic decrease below 1 cd/A whereas the same increase in Alq₃ layer thickness results in 6.5 cd/A.

The decrease in efficiency with increasing STAD layer thickness (Fig. 4.24) is associated with destructive interference effects in the device when the emission zone is shifted away from the reflecting bottom anode. Optical interference effects will be discussed in more detail in Section 5.1. However, the drastic decrease in cd/A with increasing voltage and current flow (Fig. 4.24) cannot be attributed to interference effects. There are several effects which might account for the drastic decrease in efficiency: Since the decrease in efficiency is only observed for thin STAD layer thicknesses, there may be a change in charge balance with increasing current flow as discussed in Section 4.1.1. There, an increase of the efficiency was ascribed to a change in charge balance. However, a reduction of the efficiency could also have other reasons. Since phosphorescent materials exhibit relatively long lifetimes of the excited states ($\tau = 500$ ns for Ir(ppy)₃) [Baldo et al. 1999], saturation of the dopant might lead to a reduction in efficiency. However, a rough estimation suggests a noticeable saturation effect only above 1 A/cm². Adachi et al. interpreted the reduction in efficiency at higher current densities as triplet-triplet annihilation [Adachi et al. 2000; Baldo and Forrest 2000].

Variation of Emission Layer and Blocking Layer Thickness

The importance of the position of the emission zone in the OLED structure was evaluated in the previous section. Here, the width of the doped emission layer (CBP:Ir(ppy)₃) and the layer thickness of the hole/exciton blocker (BCP) are varied to study the effect on device performance. In order to minimize interference effects, both the distance of the emission zone to the bottom mirror as well as the total device thickness are kept constant. In this device the distance of the STAD/ CBP:Ir(ppy)₃ interface from the reflecting bottom anode is kept constant (see Sec. 5.1). The device thickness was fixed at 1100 Å since it has been shown in the previous section that this device thickness exhibits the highest efficiency. Thus, a combinatorial matrix is realized by staircasing the CBP and BCP layers in two dimensions and backfilling with Alq₃ in such a way that all 100 devices exhibit the same total thickness of 1100 Å. The Ir(ppy)₃

concentration is 6% in the CBP layer. The detailed device structure is given in the following table:

| Material | Ni | CuPc | STAD | CBP:Ir(ppy) ₃ | BCP | Alq ₃ | Ca/Mg |
|---------------|-----|------|------|--------------------------|----------|------------------|--------|
| Thickness / Å | 700 | 100 | 300 | y=0..400 | x=0..300 | 700-(x+y) | 150/50 |

Results and Discussion

Figure 4.26 shows the I - V EL curves of 20 devices selected out of 100 in order to illustrate some of the general trends. The first series of devices (Fig. 4.26a) exhibit a constant BCP thickness of 100 Å, whereas the CBP:Ir(ppy)₃ layer thickness is varied from 0 to 400 Å. In these devices, the current onset is almost unaffected by the CBP layer thickness and varies between 2.8 and 3.1 V. The second set of devices (Fig. 4.26b) has a constant CBP:Ir(ppy)₃ thickness of 200 Å, whereas the BCP layer thickness was varied from 0 to 300 Å. Here, the current onset is 2.3 V for a BCP thickness of 0 Å and steadily increases up to 3.2 V for a BCP thickness of 300 Å. It is noteworthy that the I - V curves in Figure 4.26b show multiple steps (three in this case) below the current onset, which is characteristic of devices with a multi-layer stack and internal barriers. Below the onset, charge carriers are injected from the electrodes and blocked at internal barriers, thereby reducing the steepness of the I - V characteristics until the field is increased to overcome the barrier. This peculiarity occurs only when the I - V curve is swept with a certain speed, which confirms that this behavior is part of non-equilibrium processes. For a more detailed treatment of these processes see [Rieß et al. 2001; Brütting et al. 2001]. Although all 100 devices (in Fig. 4.26) have the same total thickness the current density varies between 4 and 130 mA/cm². The influence of the BCP layer on the operating voltage is clearly seen in Figure 4.26b pointing to the hole blocking function of this layer. At a current density of 1 mA/cm² the voltage increases from 6.2 to 7.3 V when the BCP layer is increased from 0 to 300 Å.

Figure 4.27a and b show the efficiency in a 2D representation at 20 mA/cm² and 100 cd/m², respectively. A maximum efficiency of 16.5 cd/A is achieved in a broad CBP and BCP layer thickness range. The efficiency is close to the maximum value when the CBP:Ir(ppy)₃ layer and the BCP layer have thicknesses above 150 and 50 Å, respectively. Comparing the efficiency maps at different operating modes, i.e. at a constant current density of 20 mA/cm² (Fig. 4.27a) and a luminance of 100 cd/m² (Fig. 4.27b), it can be observed that the range of

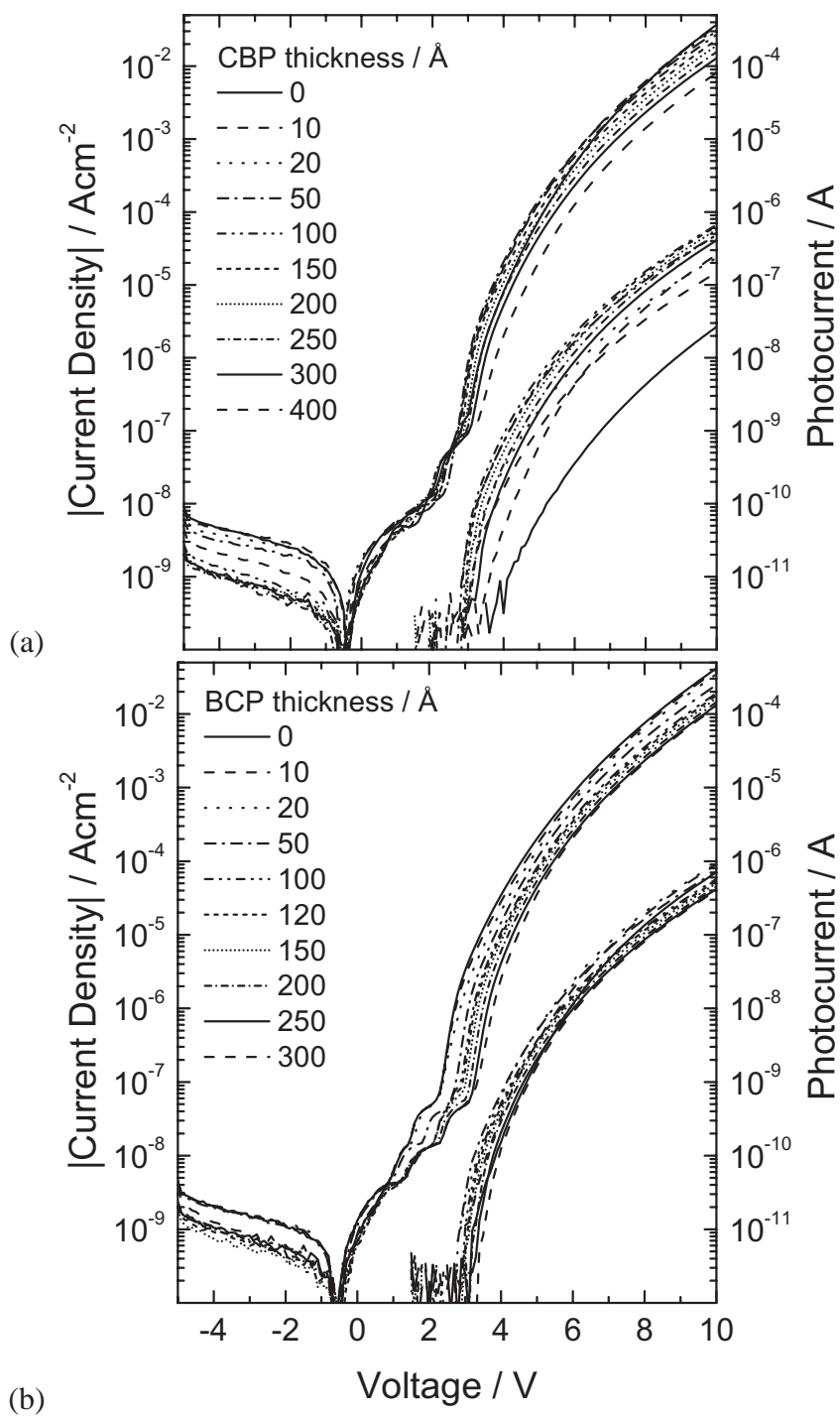


Figure 4.26: I - V curves of 20 out of 100 combinatorial multilayer devices based on $Ir(ppy)_3$. (a) Fixed BCP thickness of 100 Å and varying CBP: $Ir(ppy)_3$ thickness. (b) Fixed CBP: $Ir(ppy)_3$ thickness of 100 Å and varying BCP thickness.

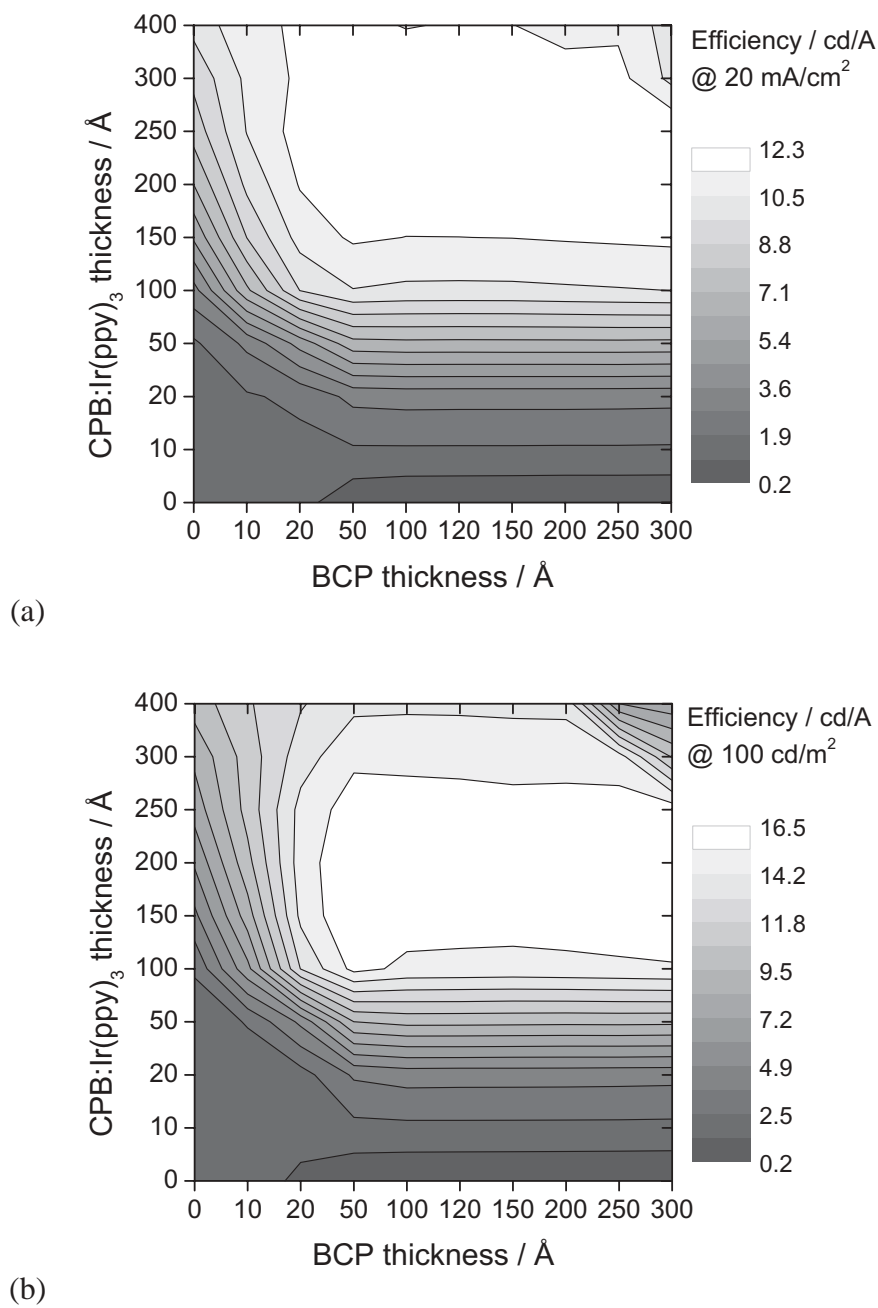


Figure 4.27: Efficiency map of CuPc/STAD/CBP:Ir(ppy)₃/BCP/Alq₃ OLEDs (a) at a current density of 20 mA/cm² and (b) a luminance of 100 cd/m². Note the CBP and BCP layer thickness steps are not equidistant.

maximum efficiency is extended to devices with a thicker CBP:Ir(ppy)₃ layer in the former case. This could be explained by a shift in the location of the recombination zone at higher driving conditions. The efficiency drastically drops when the BCP layer is thinner than 50 Å which clearly shows that this is the minimum thickness of the blocking layer for efficient device operation. The thickness of the CBP:Ir(ppy)₃ emission zone shows a minor impact on device efficiency.

Figure 4.28 shows a selection of four different spectra of OLED structures of the investigated combinatorial matrix having different emitting and blocking layer thicknesses. As expected, the device having no CBP (0 Å) and no BCP (0 Å) clearly shows pure Alq₃ emission since this structure is simply the conventional three-layer CuPc/STAD/Alq₃ structure. The introduction of a blocking layer efficiently reduces the number of holes entering the Alq₃ layer. This is illustrated in the case of CBP (0 Å) and BCP (100 Å) where the emission of Alq₃ is suppressed and the main emission originates from STAD (peak 406 nm). Inserting a 100-Å-thick CBP:Ir(ppy)₃ in a structure without BCP (0 Å) leads to a narrowing of the spectrum and a shoulder at 520 nm indicating that the emission is partly originating from Ir(ppy)₃. The additional introduction of a BCP layer (100 Å) increases the efficiency; emission originates

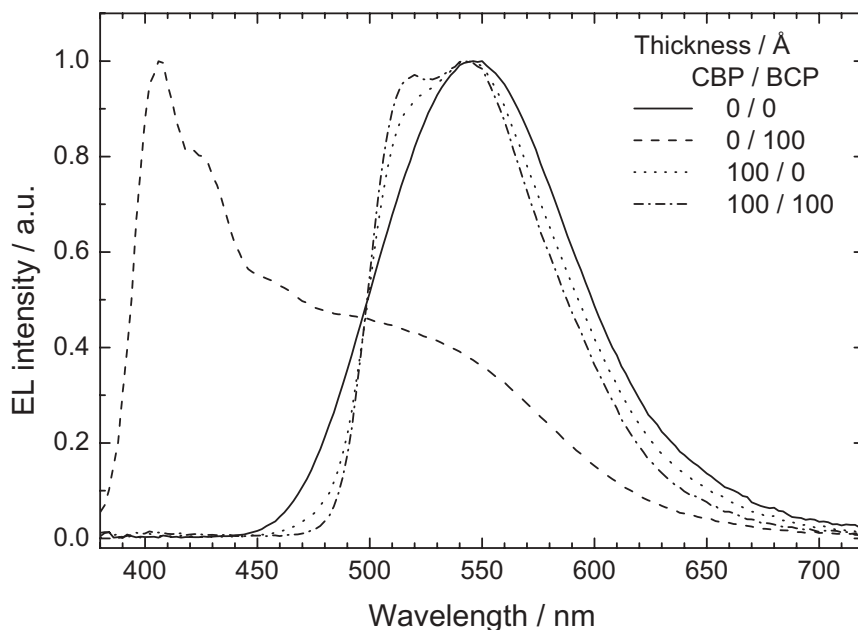


Figure 4.28: EL-spectra of CuPc/STAD/CBP:Ir(ppy)₃/BCP/Alq₃ OLEDs having different emitting layer (CBP:Ir(ppy)₃) and blocking layer (BCP) thicknesses.

exclusively from the CBP:Ir(ppy)₃ layer.

Figure 4.29 show some preliminary lifetesting of various phosphorescent structures carried out in sequential measurements on the *xy*-stage under inert conditions. All devices are driven at a constant current density of 20 mA/cm². The Alq₃ reference device (CBP 0 Å and BCP 0 Å) is the most stable device with a starting luminance of 370 cd/m² and a decay in luminance of 8% within 4 hours. Figure 4.29a demonstrates clearly that devices without blocking layer (BCP 0 Å) show a degradation which is dependent on the CBP layer thickness. The decay in luminance after 4 hours is 21, 47, 68, and 73% for CBP thicknesses of 50, 150, 200 and 300 Å, respectively, and seems to saturate for CBP thickness above 200 Å. Figure 4.29b compares the lifetime of devices having a hole blocker (BCP>0 Å) with the Alq₃ reference. Although the devices with and without CBP:Ir(ppy)₃ layer have different degradation behavior, their luminance decay does not depend on the BCP layer thickness. In the case of CBP 0 Å, the emission takes place in STAD as it could be seen in the EL spectrum in Figure 4.28. This might explain the difference in the decay curve and indicates that a different ageing process occurs in the STAD layer. The degradation of the devices with a CBP:Ir(ppy)₃ (200 Å) is independent for a wide range of BCP layer thicknesses (10 to 300 Å). These results suggest that the degradation is primarily inherent to the emitting CBP:Ir(ppy)₃ layer or the interfaces to the STAD or BCP layer. Anode and cathode can be excluded as the primary origin of degradation since they are identical for all devices. These observations point to the possible origins of degradation, although a definite explanation of the mechanism cannot be given yet. Degradation has been the subject of recent reports, and the presence of interfacial charges has been identified as a source of degradation in fluorescent devices [Kondakov et al. 2003]. In general, the device structure, i.e. the individual layer thicknesses, might be used as a parameter in lifetime measurements and combined with other measurement techniques in order to identify some of the degradation processes in fluorescent and phosphorescent OLEDs. These investigations have to be combined with complementary measurements, for example the recording of spectral changes of aged devices. With the combinatorial tool such systematic investigation of the influence of layer thicknesses on the degradation of OLEDs will be carried out in future to help identify degradation mechanisms.

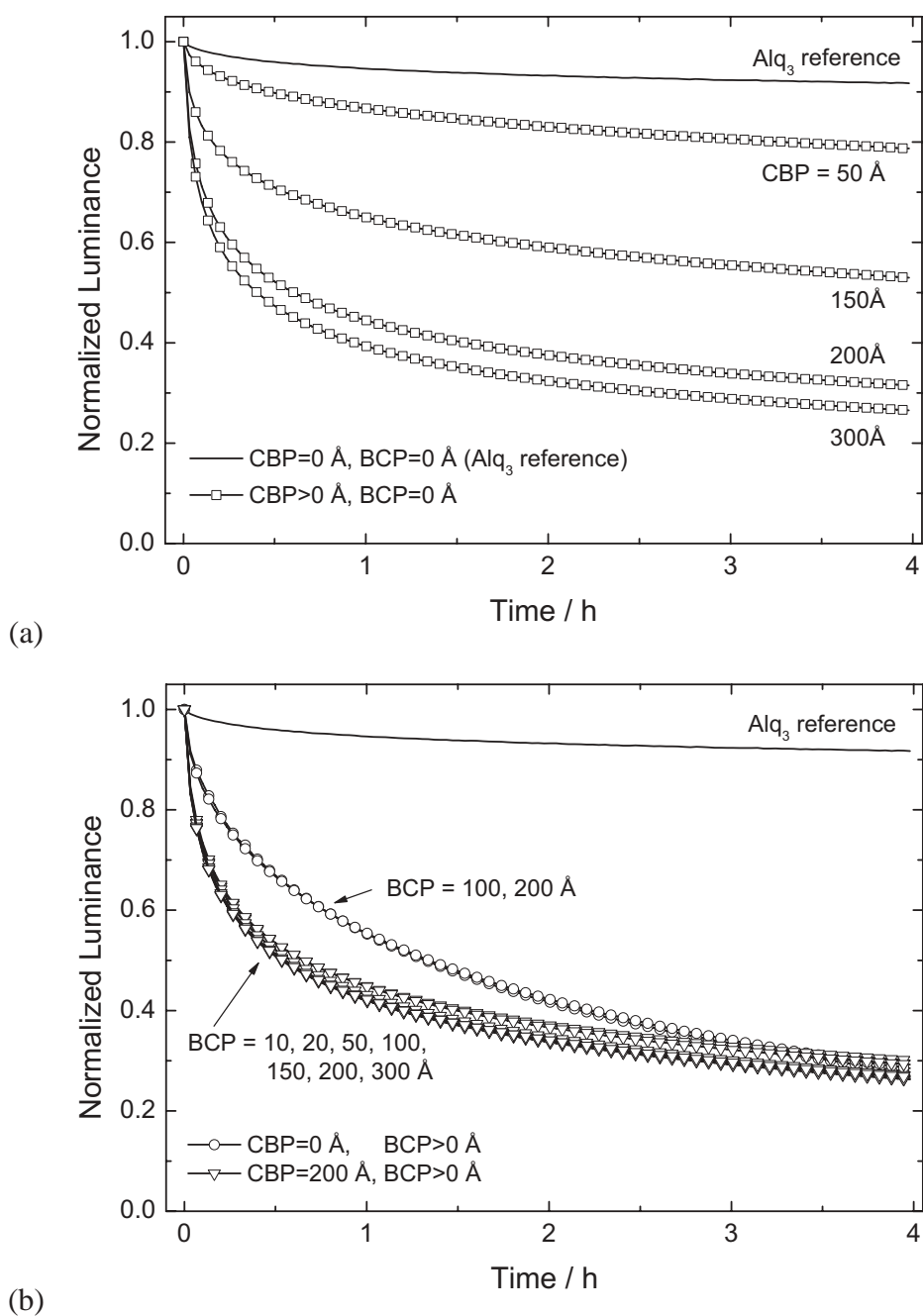


Figure 4.29: Lifetime of CuPc/STAD/CBP:Ir(ppy)₃/BCP/ Alq_3 OLEDs having different emitting layer (CBP:Ir(ppy)₃) and blocking layer (BCP) thicknesses. Driving conditions constant current density 20 mA/cm². A reference device without CBP and BCP is on the same substrate. Structures (a) without and (b) with blocking layer.

4.3.4 Summary: Complex Multilayer Structures

The extension of the standard three-layer structure by means of a doped layer introduces additional parameters for device optimization. A combinatorial investigation on the width of the doped region of a CuPc/STAD/Alq₃:DCJTb/Alq₃ structure showed that the thickness of the doped layer need not be larger than 150 Å in order to achieve the pure dopant spectrum. This maintains the highest possible efficiency and lowest driving voltage.

Red double-doped OLED structures (CuPc/STAD/Alq₃:Rubrene:DCJTb) have been fabricated via combinatorial methods and directly compared with single-doped structures (CuPc/STAD/Alq₃:DCJTb). An efficiency increase of about 15% in the double-doped devices was achieved compared to the single doped-equivalents. More strikingly, the lifetime is increased via double-doping by a factor of 3 compared to the single-doped devices. A lifetime of 16,000 h at 100 cd/m² can be extrapolated.

Combinatorial experiments on phosphorescent CuPc/STAD/CBP:Ir(ppy)₃/BCP/Alq₃ structures reveal the influence of the individual layers, in particular STAD, CBP, BCP and Alq₃, on device performance. The largest impact on efficiency is caused by the BCP layer of 50 Å, which is sufficient to efficiently confine holes and excitons within the CBP:Ir(ppy)₃ emission layer and thereby increase the efficiency from 6 to 16.5 cd/A at 100 cd/m². Ageing studies on these devices show that the origin of degradation is located in the emission layer itself or at its interfaces rather than at the electrodes. Future parallel lifetesting for the combinatorial substrate will be a powerful tool to quantify the ageing behavior as a function of individual layer thickness, thus helping to identify the layers, interfaces and processes which limit the lifetime.

Chapter 5

Optical Interference Effects

OLEDs basically consist of one or several organic layers sandwiched between two electrodes, whereby one of them is usually a highly reflecting mirror and the other one is transparent. Typical thicknesses of OLED structures (~ 100 nm) are on the order of $\lambda/4$ of the emitted light and therefore the spectral emission, and consequently the performance, will be influenced or even dominated by interference effects. Figure 5 shows extreme cases of idealized OLED structures, i.e. bottom-emitting, top-emitting, transparent and a strong cavity. A real OLED,

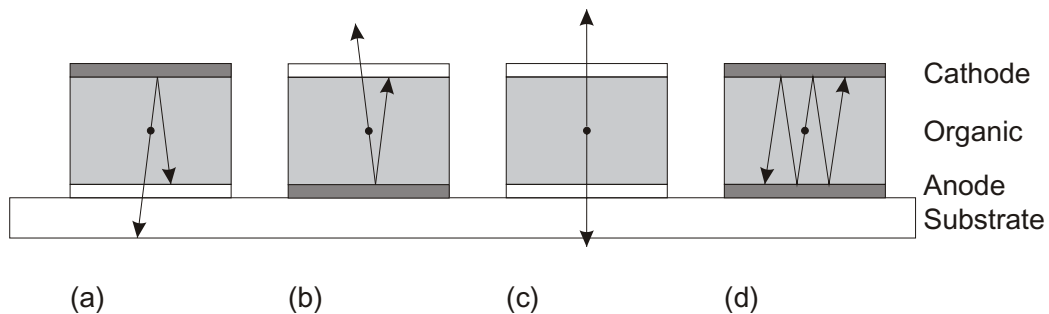


Figure 5.1: Four structures to investigate interference effects: (a) bottom emission, (b) top emission, (c) transparent device, (d) strong cavity.

however, will always be an intermediate between these idealized cases. In this work, only top-emitting structures as depicted in Figure 5b are investigated because of the focus on opaque substrates for microdisplays on crystalline silicon (see Sec. 1, Fig. 1.1). In addition, top emis-

sion OLEDs on Si-TFT backplanes offer the advantage of a higher pixel fill factor compared to bottom emission. In the devices investigated here, the bottom contact is the anode and the top contact is implemented as the cathode. In such top-emitting structures, thin semitransparent metal cathodes are used, thus forming a weak microcavity.

The following sections will address three aspects of individual components of the OLED structure: (1) the organic stack, (2) the bottom anode, and (3) the top cathode. First, it is shown that the individual organic layer thicknesses determine the position of the emission zone and thereby influence the spectral characteristic. Second, highly reflecting anodes for maximum light output are discussed with respect to their optical and electrical properties. In contrast, layer sequence with low reflectance is identified and used as anode in combinatorial OLED structures and characterized by their spectra and efficiency. Third, different cathode structures are studied with respect to their influence on the spectral emission.

5.1 Variation of Organic Layer Thickness

In this section, the influence of the organic layer thicknesses on the spectral characteristic will be illustrated in several examples. OLEDs always form a more or less distinct microcavity, and the output spectrum of the emitter will be changed due to constructive and destructive interference effects. The emission zone in an OLED structure is typically confined within a narrow region (~ 10 nm) and the position of this emission zone within the cavity will crucially affect the emission characteristic. By varying the individual layer thicknesses via combinatorial methods, the shift of this emitter region within the cavity can easily be studied. The experimental data will be used for illustrating general trends that can be applied to other material systems as well. As a first example, the CuPc/NPB/Alq₃ device, which was described by means of electrical characteristics (see Sec. 4.1.1), will now be considered by means of spectral characteristics. In the second example, a red-emitting OLED structure based on Alq₃ doped with DCJTb will be optimized with respect to efficiency, chromaticity and reflection by using the combinatorial approach.

5.1.1 Spectral Changes in Alq₃-Emitting OLEDs

It is well known that the emission in CuPc/NPB/Alq₃ structures originates from Alq₃ from a region close to the NPB interface [Tang and Van Slyke 1987]. Hence, the position of this interface within the cavity plays an important role and will determine the efficiency and the spectral output characteristics. The detailed structure of the combinatorial matrix is shown in the following table:

| Material | Ni | CuPc | NPB | Alq ₃ | Ca |
|----------------|----|------|----------|------------------|----|
| Thickness / nm | 70 | 15 | 10 – 100 | 10 – 100 | 20 |

For all 100 devices, the emission spectrum has been measured at constant current densities from 2 to 200 mA/cm² and no dependence of the spectral characteristic was observed. This indicates that there is no shift in the location of the emission zone in this undoped device structure, which would lead to a measurable change in spectral output.

As pointed out in Section 2.4, two different interference effects occur in microcavity structures: the wide angle interference, which depends on the distance d of the emission zone to the reflecting mirror, and the multiple beam interference, which depends on the length L of the cavity. Figure 5.2 sketches the investigated structure and the relevant distances. Since the combinatorial matrix covers all layer combinations of each NPB and Alq₃ in the range of 10 to 100 nm, the influence of d and L on the spectral characteristic can be displayed in

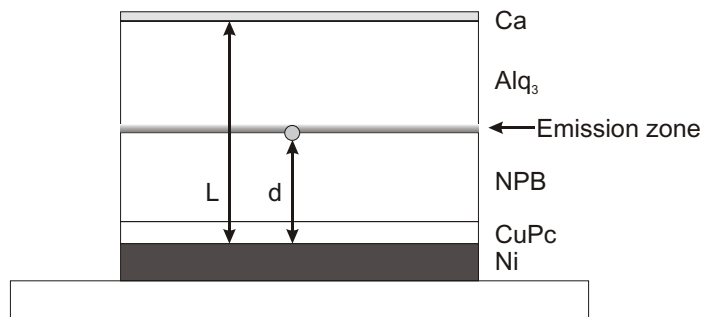


Figure 5.2: Schematic view of OLED device structure with significant distances concerning interference effects. Distance d from the bottom mirror and the cavity length L . Emission originates from Alq₃ close to the NPB/Alq₃ interface at distance d from the mirror.

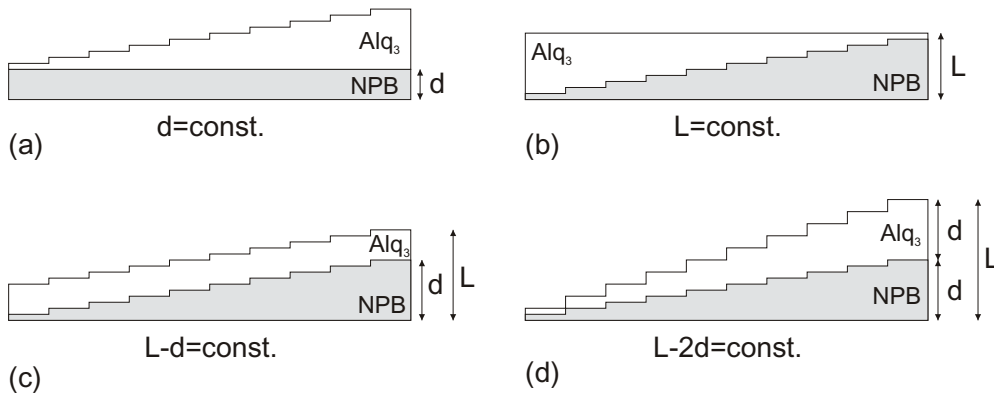


Figure 5.3: Simplified view of the selected device series with varying NPB and Alq₃ layers. Note that all devices have an additional CuPc (15 nm) layer below the NPB layer.

different ways. The spectra of four selected device series (10 devices each) will be shown in order to illustrate the influences of the individual layer thicknesses. Note that all devices have a 15 nm CuPc layer in common. Figure 5.3 visualizes the device series in a simplified way. These four device series represent basically four cross sections through the combinatorial matrix (see Fig. 3.9c, page 41), i.e. centered cuts (Fig. 5.3a and c) and two diagonal cross section (Fig. 5.3b and d). Figure 5.4a shows the EL spectra of devices with a NPB layer thickness of 50 nm and an Alq₃ layer variation from 10 to 100 nm. A fixed NPB thickness corresponds to a constant distance d of the emitter to the bottom mirror. In this series, the emission peak varies between 520 and 550 nm with increasing Alq₃ thickness and the spectral width (FWHM) shows a steady increase from 96 to 128 nm. Figure 5.4b shows spectra of devices having a constant cavity length L . In these devices, the sum of the NPB and the Alq₃ layer thicknesses is always 110 nm and the CuPc layer adds another 15 nm, resulting in a total cavity length of $L = 125$ nm. These devices exhibit a monotonic shift of the emission peak from 540 to 572 nm with increasing NPB layer thickness. Although the distance of the emission zone is shifted over 90 nm, the FWHM is basically constant within 108 and 114 nm. This clearly shows that the spectral width is not affected when the length of the cavity is kept constant.

Figure 5.5a shows the EL spectra for the device with varying NPB layer thickness (10 - 100 nm) and a fixed Alq₃ thickness of 50 nm. Here, the emission peak exhibits an extremely large shift from 520 to 574 nm when the NPB thickness is increased. The FWHM is also

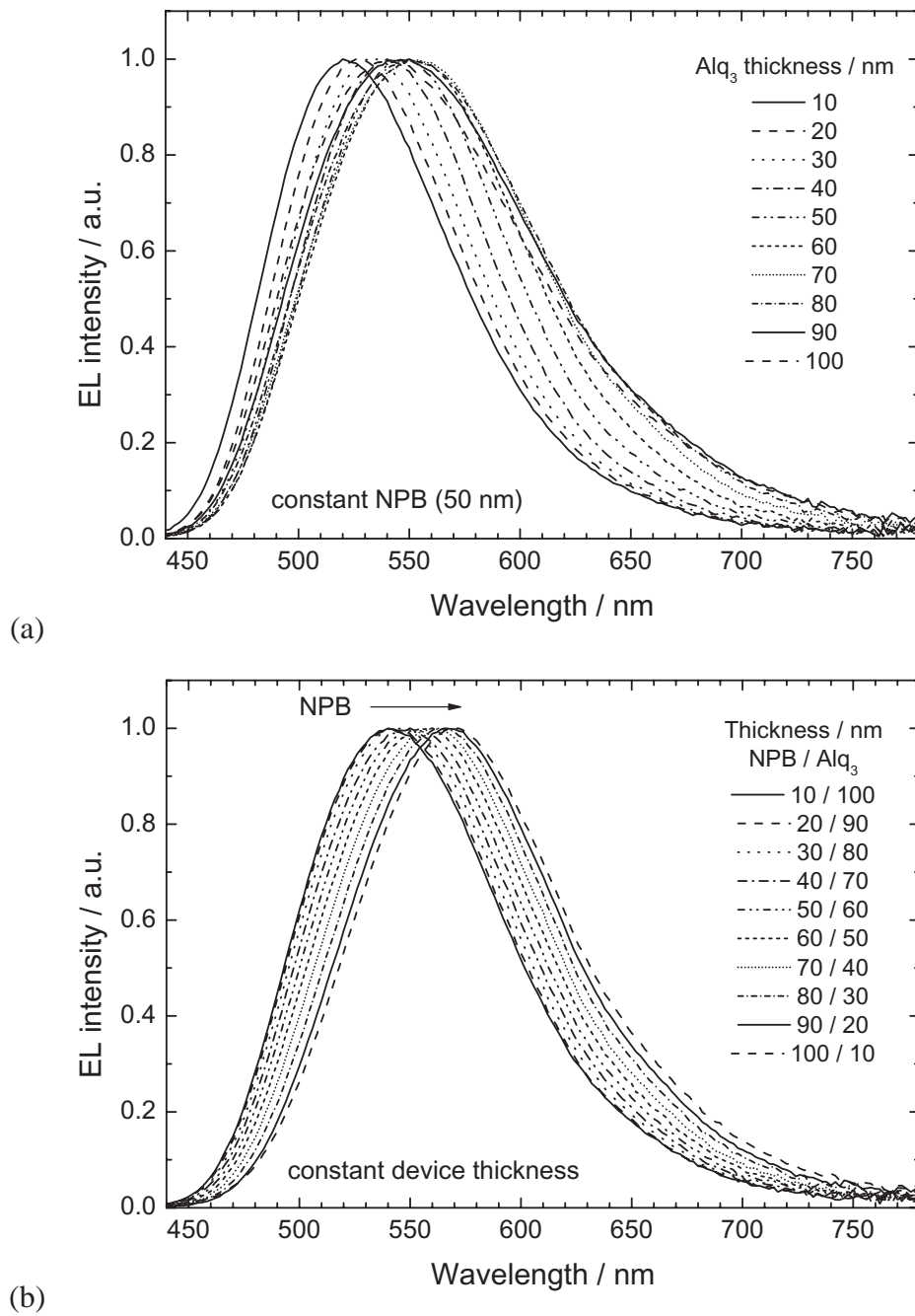


Figure 5.4: EL spectra of CuPc/NPB/Alq₃ OLEDs. (a) Fixed NPB thickness, i.e. fixed distance d of the emission zone from the bottom mirror. (b) The sum of NPB and Alq₃ thickness is constant, i.e. fixed cavity length L .

drastically increased from 92 to 138 nm. In this case, the distance d and the cavity length L are increased at the same time and the distance to the top cathode ($L - d$) is constant. Figure 5.5b depicts the spectra of devices having the same NPB and Alq₃ thickness. The distance d of the emission zone from the bottom mirror increases by the same value as the distance of the emission zone to the top cathode ($L - d$). Hence $L - 2d$ is constant (see Fig. 5.3d). These spectra are basically separated into two groups, namely devices with NPB (<40 nm) and NPB (>40 nm). The former devices show maximum emission at ~ 520 nm whereas the emission peak the latter is located at ~ 550 nm. The spectrum of the device with NPB 40 nm and Alq₃ 40 nm peaks at 530 nm. It is noteworthy that this spectrum resembles the PL emission of Alq₃ and is one of the devices with the highest efficiency on this substrate.

Table 5.1 summarizes the shifts in peak wavelength $\Delta\lambda_{\max}$ and in spectral width ΔFWHM as a function of changes in distance Δd and total cavity length ΔL . It can be seen that the

| Constant layer | | d | L | Δd | ΔL | $\Delta\lambda_{\max}$ | ΔFWHM |
|-----------------------------------|--------------------------------------|----------|----------|------------|------------|------------------------|---------------------|
| d_{NPB} | $\rightarrow d=\text{const.}$ | 50 | 75...165 | 0 | 90 | 30 | 28 |
| $d_{\text{NPB}} + d_{\text{Alq}}$ | $\rightarrow L=\text{const.}$ | 25...115 | 125 | 90 | 0 | 32 | 6 |
| d_{Alq} | $\rightarrow L - d=\text{const.}$ | 25...115 | 75...165 | 90 | 90 | 54 | 46 |
| $d_{\text{NPB}} - d_{\text{Alq}}$ | $\rightarrow L - 2d = \text{const.}$ | 25...115 | 35...215 | 90 | 180 | 46 | 30 |

Table 5.1: Shifts of peak wavelength and spectral width (FWHM) as function of changes in distance d from mirror and total cavity length L . Note, that all devices have a CuPc layer (15 nm) in common.

largest spectral shifts $\Delta\lambda_{\max}$ (54 and 46 nm) are observed when d and L are varied at the same time, whereas smaller shifts (30 and 32 nm) are detected when either d or L is kept constant. A very small broadening ΔFWHM of only 6 nm is observed when the cavity length L is kept constant.

The strong influence of layer thickness on the spectral emission characteristics has been illustrated in CuPc/NPB/Alq₃ device structures. The most critical dimension in the device that determines the spectral shift is the distance to the reflecting bottom anode. Naturally, the above-described trends of spectral changes with layer thickness can also be translated to other material systems and allow qualitative predictions to be made.

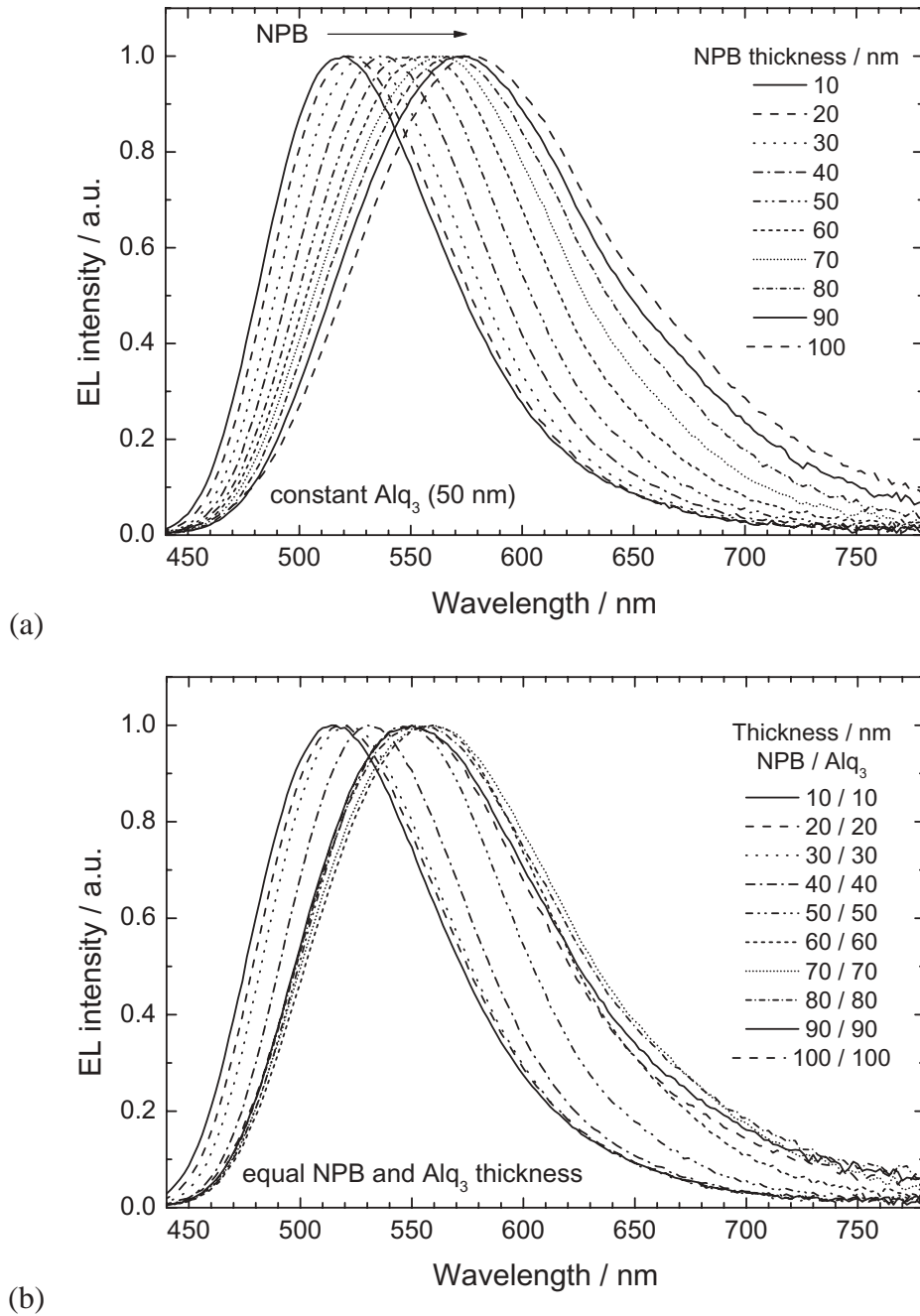


Figure 5.5: EL spectra of CuPc/NPB/Alq₃ OLEDs. (a) Varied NPB layer thickness and fixed Alq₃ thickness, i.e. distance to the top cathode ($L - d$) is constant. (b) Increase of NPB and Alq₃ layer thickness by the same amount.

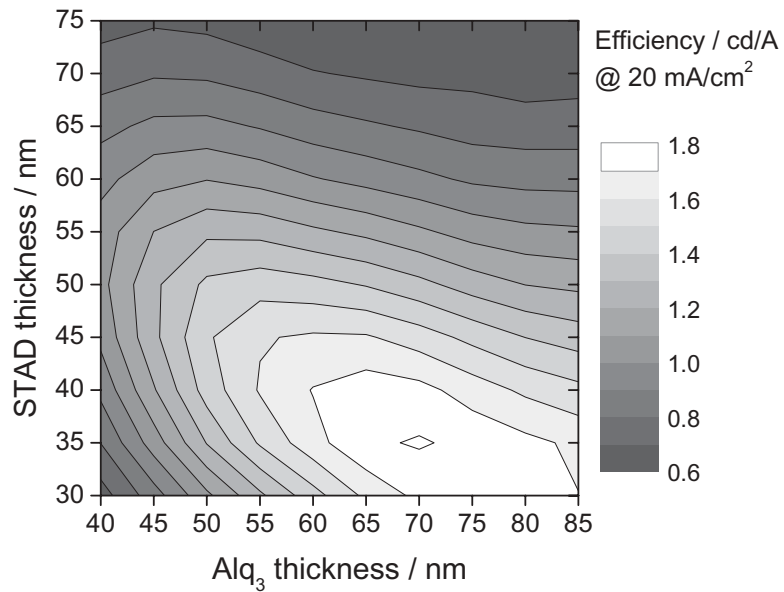
5.1.2 Optimization of Red OLEDs

The shift of the emission spectrum due to layer thickness variations will now be used to tune the spectral characteristic of a red-emitting OLED structure. This is especially important for display applications where efficient and saturated colors are required. In particular, the power consumption of a full color display is determined primarily by the efficiency of the red OLED. Here, it will be demonstrated that an OLED structure with a given material set can be easily optimized with help of combinatorial methods. The selection criteria for the optimum layer thicknesses are manifold: efficiency, driving voltage, spectral characteristic, color coordinates and reflectance spectrum. The aim is to facilitate the decision about a device structure by having all data available and finding the best compromise between the relevant parameters. The following double-doped combinatorial matrix has been fabricated:

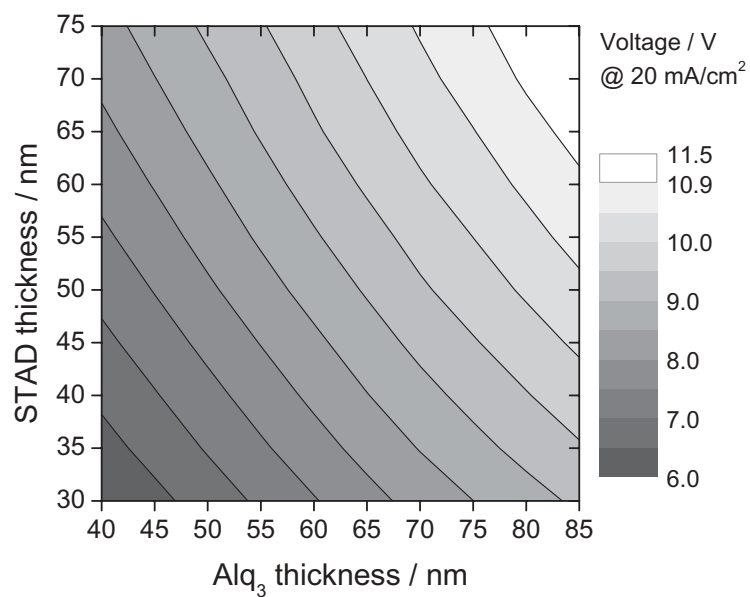
| Material | Al/Ni | CuPc | STAD | Alq ₃ :Rub:DCJTB | Alq ₃ | Ca/Mg |
|----------------|-------|------|---------|-----------------------------|------------------|-------|
| Thickness / nm | 70/5 | 15 | 30 – 75 | 25 | 15 – 60 | 10/5 |

All devices have a constant thickness of the Rubrene:DCJTB doped region since it was shown in Section 4.3.1 that a minimum thickness of ~ 15 nm of the doped region is sufficient. A thicker region would result in a higher driving voltage and does neither lead to an improved spectrum nor to enhanced efficiency. Figure 5.6a shows the efficiency at 20 mA/cm^2 in a 2D plot as a function of STAD and Alq₃ layer thickness. The maximum in efficiency of 1.8 cd/A is observed at a STAD and Alq₃ thicknesses of 35 and 70 nm, respectively. It can be seen from the shape of the efficiency contour lines that the efficiency is more sensitive to the STAD layer thickness than to the Alq₃ layer thickness. The efficiency rapidly drops to only 0.6 cd/A at STAD thicknesses above 70 nm and to almost half of the maximum value at Alq₃ thicknesses below 45 nm. Figure 5.6b shows the operating voltage which is necessary to drive a current density of 20 mA/cm^2 through the devices. As a general trend, the driving voltage increases monotonically with total device thickness from 6.0 to 11.4 V. The operating voltage is clearly more dependent on the Alq₃ layer thickness than on the STAD layer thickness. An increase of the Alq₃ layer thickness by 10 nm leads to a voltage increase of about ~ 0.8 V, whereas the same increase in STAD layer thickness leads to an increase of only ~ 0.6 V.

The spectral characteristic and hence the chromaticity will determine the color gamut in a display. As shown in the previous section, the OLED spectrum exhibits the largest spectral



(a)



(b)

Figure 5.6: Optimizing double-doped Alq₃:Rub:DCJTb OLEDs. (a) Efficiency at 20 mA/cm² as a function of STAD and Alq₃ layer thickness. (b) Driving voltage at 20 mA/cm².

shifts when the distance to the bottom mirror is varied. Therefore, Figure 5.7a shows selected EL spectra at 20 mA/cm^2 with varying STAD layer thickness (30–75 nm) at a constant Alq₃ thickness of 70 nm. With increasing STAD layer thickness, the emission spectrum shifts from 628 to 644 nm and the FWHM increases from 82 to 106 nm. This again illustrates the potential of tuning the spectral characteristic by proper adjustment of the organic layer thicknesses. In addition, it should be mentioned that increasing the current density from $1 \mu\text{A/cm}^2$ to 20 mA/cm^2 leads to a green-shift of the spectrum by $\sim 3 \text{ nm}$ (spectra not shown here). This already suggests that a detailed optical description of doped systems will be more complex than that of undoped Alq₃ systems.

Figure 5.7b shows the reflectance spectra of the red OLED structures (from Fig. 5.7) measured with the setup described in Section 3.5.4. All reflectance spectra exhibit a maximum reflectance of about 70–80% and the maximum position shifts from 470 to 570 nm with increasing STAD layer thickness from 30 to 75 nm. A minimum reflectance of 5% is measured at 640 nm for the device having a STAD thickness of 30 nm. For all devices on the combinatorial substrate (not shown here), the lowest average reflectance in the range from 450 to 650 nm is $\sim 25\%$, which is only obtained in devices with total thicknesses below 60 nm. Devices with a total thickness above 100 nm exhibit a relatively high average reflectance of about 70%. For high contrast ratio, however, low reflectivity in the whole visible range is required. In Figure 5.7b, the devices with 30 and 35 nm STAD thickness show the lowest average reflection of about 45–50%.

The chromaticity is a further criterion for displays and is actually the most apparent one. Figure 5.8 shows the efficiency of the devices in a CIE1931 x,y chromaticity diagram. The efficiency is represented by gray scale and by size of the data point, i.e. large, white symbols correspond to the most efficient devices. The color coordinates of all devices lie on a straight line in the CIE diagram between $x = 0.375, y = 0.62$ and $x = 0.332, y = 0.665$. The maximum efficiency of 1.8 cd/A is achieved in the device having CIE color coordinates of $x = 0.65$ and $y = 0.348$. Devices closest to the red NTSC standard achieve efficiencies of about 0.7 cd/A. The inset shows an overview of the CIE diagram and the position of devices together with the NTSC RGB standards.

Table 5.2 summarizes the trends of the different performance criteria, i.e. efficiency, operating voltage, color coordinates and reflectance. From this table, it can be seen that the best thicknesses for a given criterion are antipodal with the thicknesses for another criterion. In this

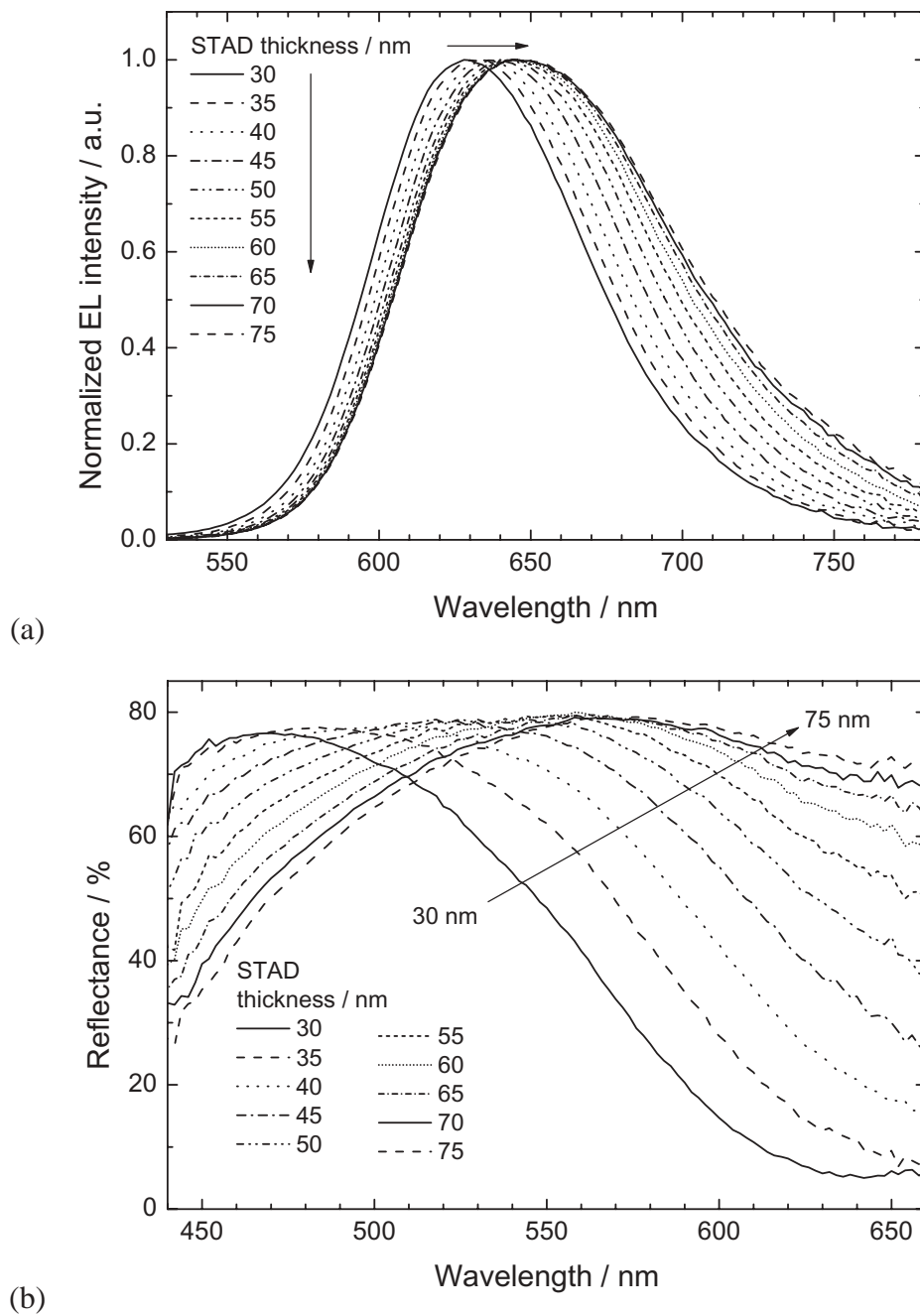


Figure 5.7: (a) Normalized EL spectra of double-doped CuPc/STAD/(Alq₃:Rub:DCJTb) red OLEDs. (b) Reflectance spectra of the complete OLED stacks.

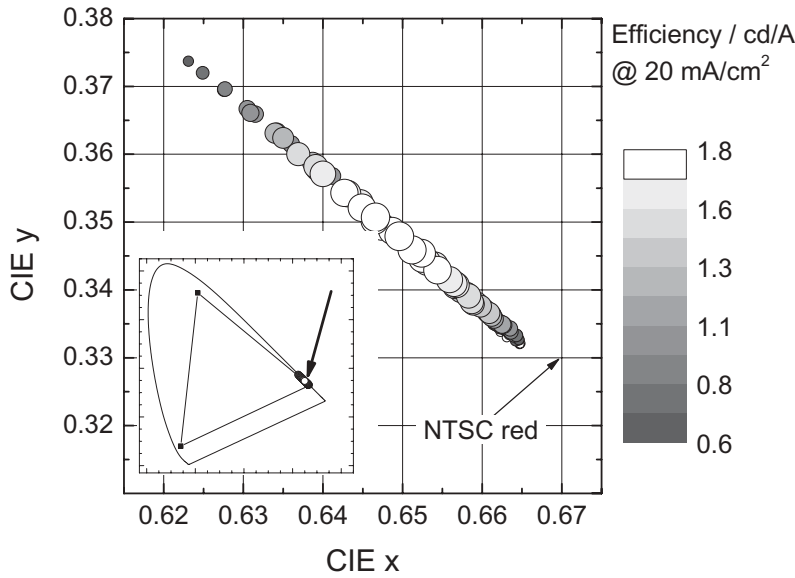


Figure 5.8: CIE1931 x,y coordinates of double doped red OLEDs. The most efficient devices have CIE color coordinates of $x=0.65$, $y=0.35$. The pointer in the inset shows the position of the devices in the CIE diagram together with the NTSC RGB-triangle.

| Criteria | Value | Thickness nm | |
|--|----------------------|--------------|------------------|
| | | NPB | Alq ₃ |
| Efficiency η | >1.7 cd/A | <40 | >55 |
| Operation voltage U | <7 V | <40 | <50 |
| CIE x,y | $x > 0.65, y < 0.34$ | >60 | >45 |
| Average reflectance R | $<30\%$ | <40 | <40 |
| Optimum selection: NPB 35 nm, Alq ₃ 65 nm | | | |
| $\eta = 1.7$ cd/A, $U = 8.1$ V, CIE $x = 0.65, y = 0.35, R = 52\%$ | | | |

Table 5.2: Summary of performance values of a red CuPc/ STAD/ Alq₃:DCJTb combinatorial matrix. The target values and the corresponding STAD and Alq₃ thicknesses are listed in order to find a trade-off for the optimum thicknesses.

case, the criteria are considered in the order of their importance for optimum thicknesses. A good compromise for the above-listed performance criteria are the STAD and Alq₃ thicknesses of 35 and 65 nm, respectively. For these STAD and Alq₃ thicknesses, the device efficiency is 1.7 cd/A, the driving voltage is 8.1 V at 20 mA/cm². CIE color coordinates of $x = 0.65$ and $y = 0.35$ are achieved together with an average reflectance of 52%. The search for optimum layer thicknesses is one strength of the combinatorial approach and has been demonstrated for a red-emitting OLED structure. Naturally, this scheme can be applied to any other material combination.

5.1.3 Summary: Variation of Organic Layer Thicknesses

In summary, it has been shown that combinatorial methods are ideally suited for fabricating a multitude of devices with exactly defined layer thickness variations and combinations. The model structure CuPc/NPB/Alq₃ was used to illustrate the dependence of the spectral emission on the individual layer thicknesses. Two types of interference effects, i.e. wide angle interference and multiple beam interference, determine the spectral characteristic in OLED structures, particularly in top-emitting devices with semi-transparent electrodes. Although the emission material is the same Alq₃ for all devices, the spectral maximum can be shifted from 514 to 580 nm depending on the layer thickness. The distance to the reflective bottom anode is clearly the most critical thickness determining the spectral shift and hence the efficiency. Similar trends will apply to bottom emission devices, e.g. with an ITO anode and a highly reflecting LiF/Al top cathode.

As an example, double-doped red OLED structures based of Alq₃:Rubrene:DCJTb have been optimized via combinatorial device fabrication. The characterization setup automatically provides a complete dataset on I - V EL characteristics, efficiency, chromaticity, and reflectance. This facilitates the search for optimum layer thicknesses by a tradeoff between the above-mentioned performance criteria. The optimum layer thicknesses of STAD 35 nm and Alq₃ 65 nm have been determined in a single evaporation run. The efficiency is 1.7 cd/A at 20 mA/cm² at 8.1 V with CIE color coordinates of $x=0.65$ and $y=0.35$ and an average reflectance of 52%.

5.2 Anode: Influence on Spectral Emission and Device Performance

In the previous section, the importance of the individual organic layer thicknesses and their impact on spectral emission and efficiency have been addressed. Now, the influence of the bottom anode will be illustrated by two extreme cases, i.e. a highly reflecting bilayer anode and a low reflecting three-layer anode. Systematic variations of the relevant thicknesses by means of combinatorial methods show the potential for improvement of optical output by selection of the proper anode for top-emitting OLEDs.

5.2.1 Highly Reflecting Anodes

Anodes for highly efficient top-emitting OLEDs have to fulfill two criteria: first, a high work function material for good hole injection and, second, a high reflectance for improved out-coupling. Several metals with their work functions are listed in Table 5.3 and their spectral reflectance is shown in Figure 5.9. The reflectance of these metals vary from over 90% down

| Material | Ag | Al | Au | Ir | Mg | Mo | Ni | Pt |
|---------------|------|------|-----|------|------|-----|------|------|
| Work function | 4.26 | 4.28 | 5.1 | 5.27 | 3.66 | 4.6 | 5.15 | 5.65 |

Table 5.3: Work function of various metals. Data from [Michaelson, 1977].

to 50% in the visible range. Al, Mg and Ag clearly show the highest reflectance among these metals. However, Al, Ag and Mg with work functions of 4.2 eV, 4.3 eV and 3.7 eV, respectively, are less favorable as hole injecting contacts. In contrast, the high work function metals like Ni, Pt, Ir, etc. exhibit relatively low reflectance compared to Al, Ag and Mg (see Fig. 5.9). Some of these higher work function metals have been investigated for their use as anodes and have proved to show stable device performance [Haskal et al. 1998; Beierlein et al. 2000]. Especially, Ni turned out to be an efficient and a stable hole injection contact after being treated with an oxygen plasma. The drawback of Ni is its $\sim 30\%$ lower reflectance in the whole visible range compared to Ag or Al. Since charge carrier injection is a surface phenomenon, the high work function material is needed only at the interface. The combination of a highly reflecting metal with a thin layer of a high work function metal will lead to improved light output. Combinatorial investigations help exploit the limit of this bilayer anode concept concerning

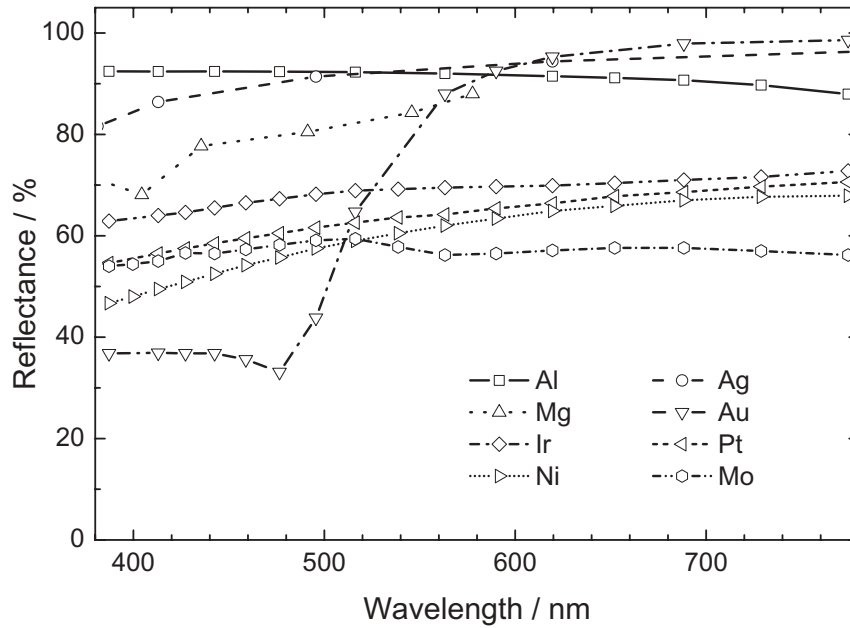


Figure 5.9: Reflectance of various metals. Data taken from [Lide, 1996].

electrical and optical performance. Highly efficient devices based on phosphorescence can be realized [Riel et al. 2003].

Thin layers of high work function metals (Ni, Mo) on a highly reflecting metal (Al) are used in order to combine the best optical reflector with a favorable hole injecting contact. These bilayer anodes are investigated with respect to their optical and electrical properties. Finally, OLED devices are fabricated and characterized on such bilayer anodes.

Optical properties of Al/Ni bilayer anodes

Al/Ni bilayer anodes are fabricated by e-beam evaporation using a sliding shutter in front of the substrate as described in Section 3.3.1. These structures are deposited without breaking the vacuum between the evaporation of Al and Ni in order to prevent native aluminum-oxide being formed. The layer sequence is listed in the following table:

| Material | glass | Al | Ni |
|-----------|--------|-------|-----------|
| Thickness | 1.1 mm | 500 Å | 0 – 500 Å |

The reflectance of the samples is measured with the setup described in Section 3.5.4. Figure 5.10a shows the spectral reflectance of thin Ni layers (0 – 500 Å) on Al (500 Å). In order to calibrate the measurement signal, a blank glass substrate is measured and its reflectance is defined as 8% reference. Since glass exhibits a wavelength-independent reflectance spectrum in the visible range, glass is a suitable reference which leads to consistent reflectance values of $\sim 90\%$ in the visible range for Al. Freshly prepared Ni shows a wavelength-dependent reflectance decreasing from 70% at 650 nm to 55% at 450 nm. The measured values of bulk Al and Ni are in agreement within a few percent with those reported in the literature [Lide 1996; Palik 1991] (see Fig. 5.9). A 500 Å thick Ni layer on Al can be regarded as bulk Ni since there is no difference in reflectance compared to a pure Ni layer with thickness of 1500 Å. At the maximum emission wavelength of Alq₃ ($\lambda_{\text{max}} = 530$ nm) Ni shows a reflectance of only 63%, which is 28% lower than the value of Al. The reflectance at $\lambda = 530$ nm of these bilayer anodes decreases monotonically from 85% to 63% for a 25 and 500 Å thick Ni layer, respectively. A rather large decrease in reflectance is observed between 0 and 25 Å Ni layer thickness. A possible explanation could be non-uniform coverage at such thin layers, i.e. island growth which may result in larger scattering and hence in reduced reflection.

As mentioned before, a high work function is a prerequisite for an efficient anode. It is known that oxygen plasma treatment increases the work function of various materials and improves the reproducibility and the lifetime of OLEDs [Wu et al. 1997; Beierlein et al. 2000]. After an oxygen plasma treatment (for typical process parameters see Sec. 3.4.1) the reflectance is measured again and compared with the unoxidized layers. Figure 5.10b shows the effect of an oxygen plasma treatment on the reflectance of these bilayer anodes. The reflectance (except in the case of Al) is decreased by a few percent after the oxygen plasma treatment. For example, the reflectance at 530 nm of the thick Ni (500 Å) layer is reduced from 63% to 59%, whereas it is reduced only from 85% to 84% for the thin Ni (25 Å) layer.

In summary, extremely thin layers of high work function metals can be deposited on highly reflecting Al to increase the reflectance by $\sim 22\%$. Electrical and optical properties of pure Ni films on glass will be discussed in the next paragraph.

Electrical and Optical Properties of Single Layer Ni films on Glass

Oxygen treatment of Ni leads to the formation of a thin NiO_x layer, which affects the electrical and optical properties of the Ni anodes. An attempt to determine the thickness of this NiO_x

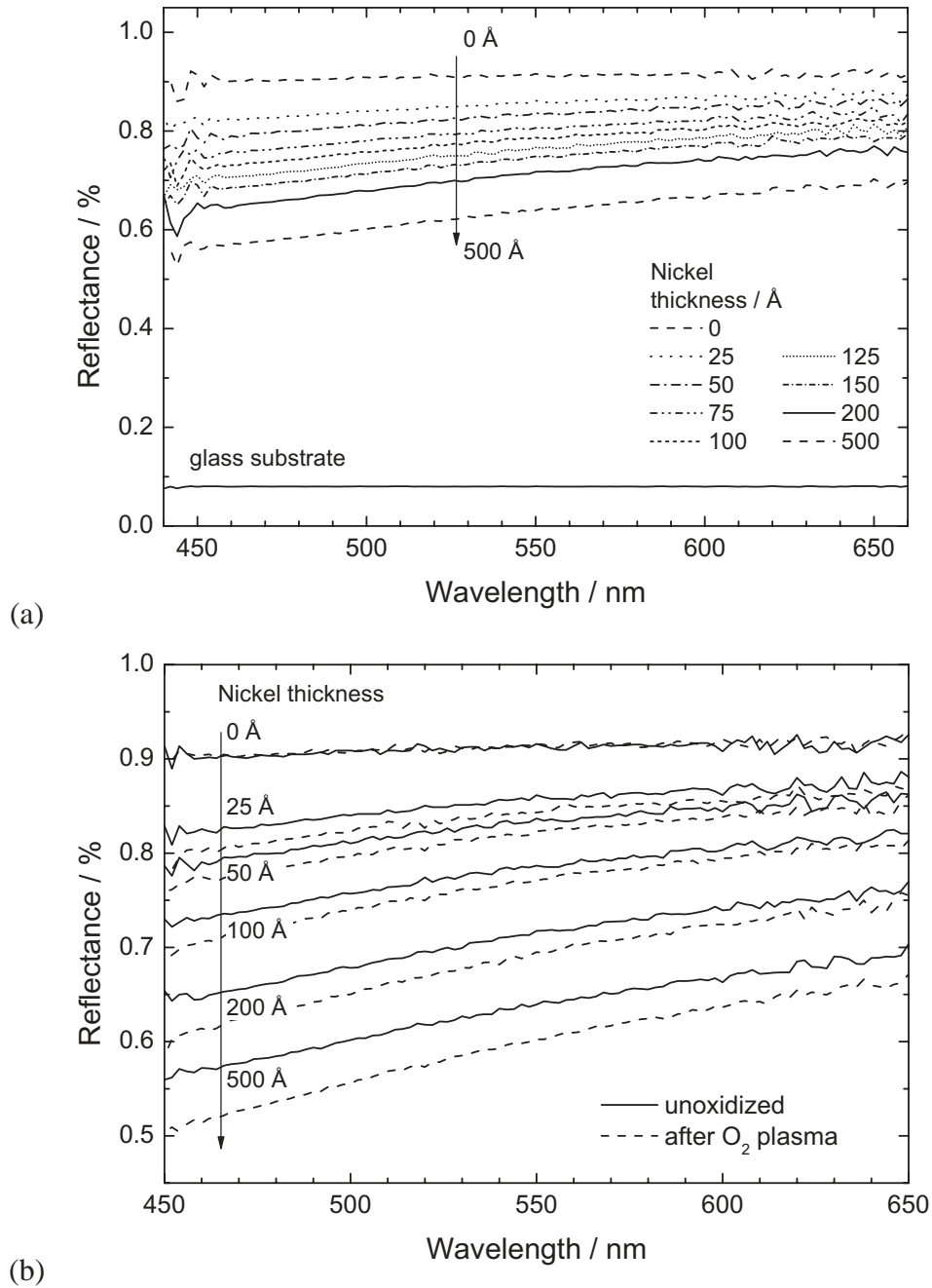


Figure 5.10: (a) Reflectance of thin Ni films on Al (500 Å). A bare glass substrate is taken as a wavelength independent 8% reference. (b) Comparison of reflectance before and after oxygen plasma treatment. The reflectance is reduced by a few percent.

layer is carried out via simple thickness-dependent transmittance and resistance measurements. Therefore, thin Ni layers are deposited directly on glass. Figure 5.11a shows the transmittance of thin Ni films on glass before and after oxygen plasma treatment. The transmittance as a function of Ni thickness shows a decay following Lambert–Beer’s law (Eq. 6.1) and an absorption coefficient of $\alpha = 9.0 \times 10^5 \text{ cm}^{-1}$ can be extracted. The oxygen plasma treated Ni layers exhibit a considerably higher transmittance, indicating that the deposited Ni is turned into transparent NiO_x . In contrast to the untreated Ni, the transmittance of the oxidized layers cannot fully be described by an exponential decay, which indicates uncomplete oxidation of the layers. The transmittance can only be approximated with an exponential decay up to a layer thickness of $\sim 120 \text{ \AA}$ assuming an absorption coefficient of $\alpha = 2.8 \times 10^5 \text{ cm}^{-1}$. Hence, from these optical measurements the NiO_x layer is roughly estimated to be about 120 \AA .

The resistivity is another quantity which can be used to determine the thickness of the NiO_x films. Resistivity has been measured by four point probe on the xy -stage (see Sec. 3.5). Figure 5.11b compares the resistivity of unoxidized and oxidized Ni films on glass. The resistivity of untreated Ni films is as low as $1.3 \times 10^{-5} \text{ \Omega cm}$, almost independent of the thickness, indicating that a continuous films exist and finite size effects do not matter [Klauek et al. 2000]. Since non-stoichiometric NiO_x is a wide band gap p -type semiconductor with rather high resistivity ($\sim 10^{-1} \text{ \Omega cm}$) [Sato et al. 1993] a drastic increase in resistivity $> 10^{-3} \text{ \Omega cm}$ for the oxidized Ni samples is observed at low thicknesses. A rough estimation of the NiO_x thickness of about 120 \AA is derived from Figure 5.11b where two resistivity curves start to diverge. As a consequence, bilayer anodes with Al as reflector have to be oxidized with particular caution. These structures with the second metal layer thicknesses smaller than $\sim 100 \text{ \AA}$ may lead to oxidation of the Al layer and introducing additional serial resistance in the device since aluminum oxide is known as excellent insulator. In the next paragraph, such types of bilayer anodes (Al/Ni as well as Al/Mo) are utilized in OLED structures and characterized with respect to spectral characteristic and efficiency.

OLED Structures on Al/Ni and Al/Mo Bilayer Anodes

In order to illustrate the impact of bilayer anode structures on the OLED device performance, devices with Al/Ni and Al/Mo bilayer anodes are fabricated. The thicknesses of the Ni and Mo layers are varied from 25 to 500 \AA , whereby 500 \AA can be regarded as bulk Ni and Mo. The detailed structure of the OLEDs is listed in the following table:

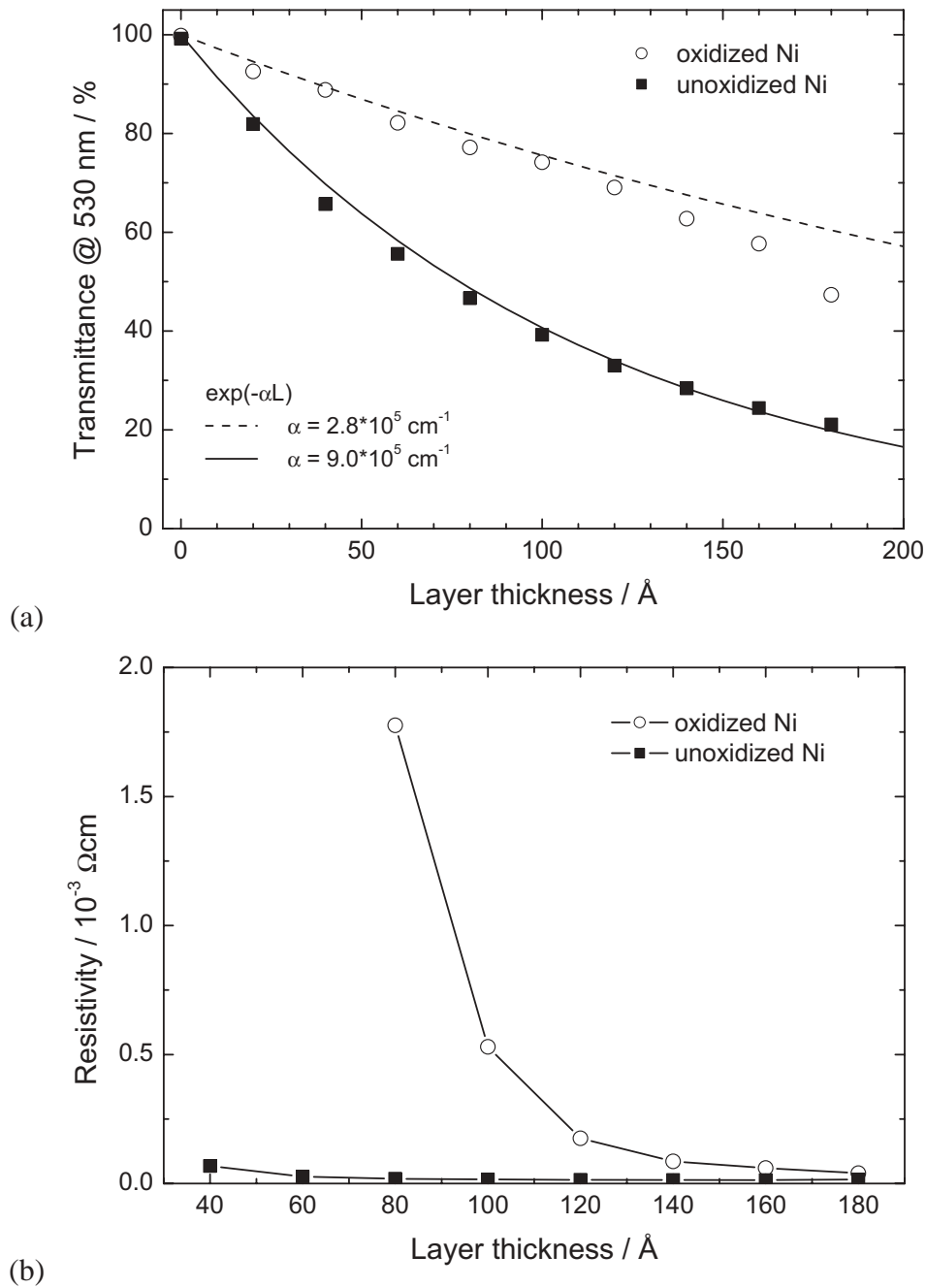


Figure 5.11: Thickness-dependent (a) transmittance and (b) resistivity of thin Ni films on glass. An estimation of the NiO_x thickness is about 120 Å.

| Material | Al | Ni or Mo | CuPc | NPB | Alq ₃ | Ca/Ag |
|---------------|-----|----------|------|-----|------------------|--------|
| Thickness / Å | 500 | 25 – 500 | 150 | 450 | 500 | 30/120 |

All devices have identical organic layers and 10 devices on each substrate have identical anode thickness. The reflectance of Mo is a few percent lower than that of Ni (see Fig. 5.9) but has not been measured separately for the bilayer anode. The I - V characteristics (not shown here) are independent of the Ni and Mo layer thickness up to voltages of 10 V. Only the device with the thinnest Ni layer (25 Å) exhibits a current density, which is reduced about a factor of 2 at voltages above 7 V. This can be explained by an additional series resistance created by the oxidation of the Al layer beneath the thin Ni layer. This is not observed in the case of Mo, which suggests that Mo forms a better barrier against Al oxidation than Ni.

Although the I - V -characteristics are not significantly influenced by the different Ni or Mo layer thicknesses, the light output clearly increases with decreasing Ni and Mo layer thickness. As a consequence, the efficiency of the devices is increased. Figure 5.12 shows the efficiency of the OLED structures having a thin Ni or Mo injection layer on Al. Since an uncalibrated photodiode was used, the efficiencies are given only in arbitrary units normalized to the value for the devices having a bulk (500 Å) Ni or Mo layer, respectively. At higher voltages (>7 V) the efficiencies increase monotonically with decreasing Ni (or Mo) layer thickness. At voltages below 4 V the efficiencies are reduced due to leakage currents in the devices, which are caused by penetration of Ag when evaporated on top of Ca.¹ It is important to note that the functional behavior of the efficiency vs. voltage curve does not change with Ni (or Mo) thickness, but it is shifted in amplitude. This is a clear indication that the injection properties are unchanged and the increase in efficiency is a purely optical effect. Figure 5.13 shows the efficiency for these devices at 8 V normalized to the value of bulk Ni (or Mo). In the case of Ni, the efficiency is increased by a factor of 1.6, whereas in the case of Mo this corresponds to 2.5 fold efficiency.

Figure 5.14 shows the spectra measured at 8 V of the different OLED structures based on Al/Ni and Al/Mo anodes. The samples with the Al/Ni anode exhibit the emission peak at 550 ± 4 nm with a FWHM of 90 nm for the bulk and 78 nm for the thin Ni layer, respectively. OLEDs on the Al/Mo anode exhibit the emission maximum at 540 ± 8 nm with a FWHM of 96 nm for the bulk and 74 nm for the thin Mo layers, respectively. The spectra clearly narrow with decreasing Ni and Mo thickness because of the higher quality of the cavity. The

¹Evaporation of pure Ag on top of Ca led to high leakage currents, therefore, further devices used either pure Ca or Ca/Mg as cathode.

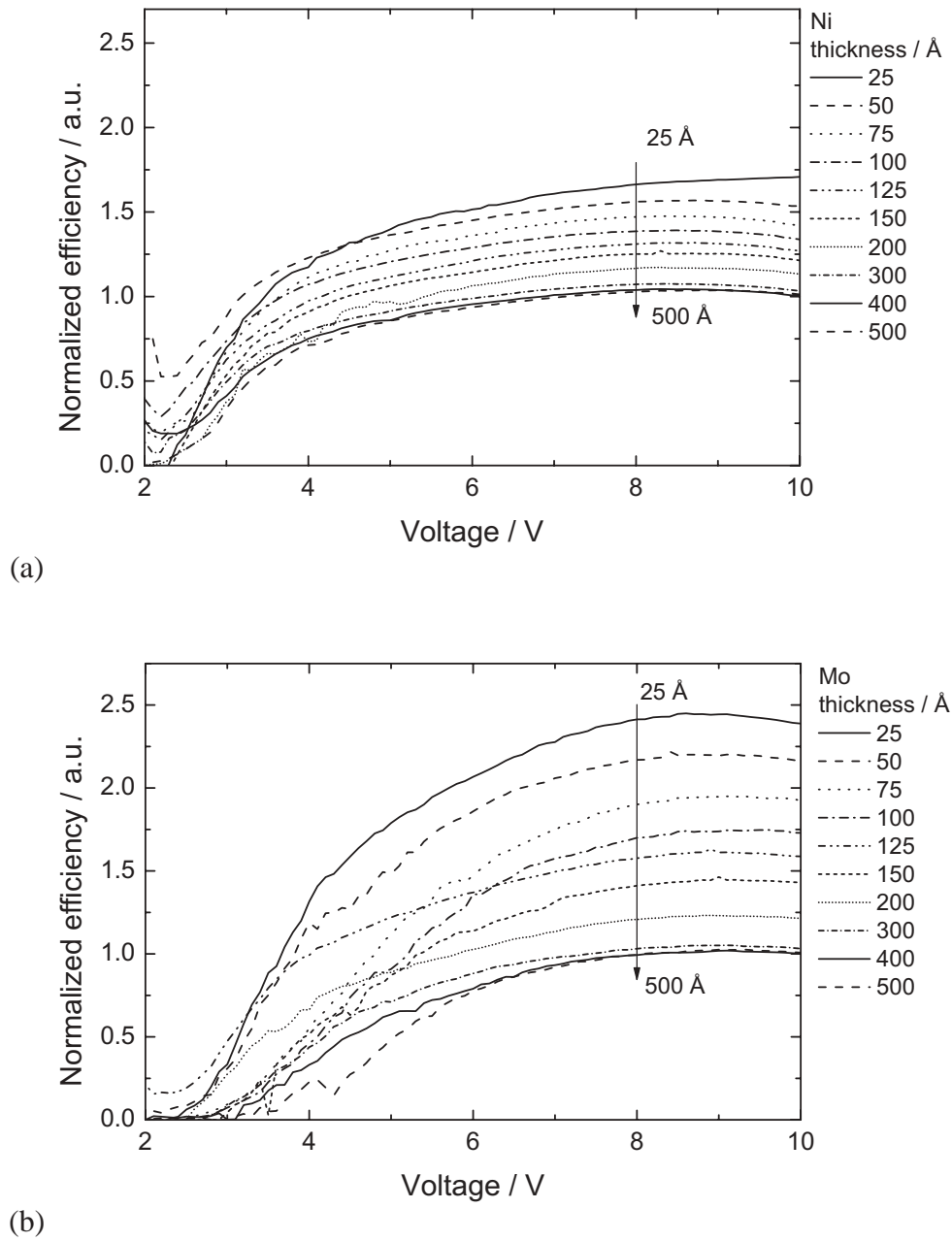


Figure 5.12: Efficiency of OLEDs having bilayer Al/Ni and Al/Mo anode. The efficiencies are relative numbers to the devices with bulk (500 Å) Ni or Mo. The efficiency curves scale with Ni and Mo thickness.

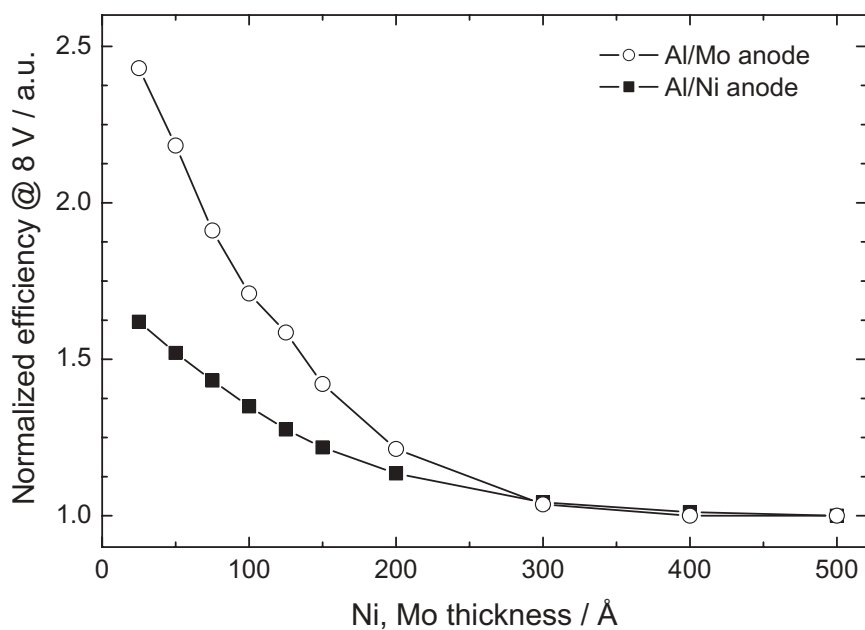


Figure 5.13: Efficiency at 8 V of OLEDs having bilayer Al/Ni and Al/Mo anodes. The efficiencies are relative numbers to the devices with bulk (500 Å) Ni or Mo. An increase in efficiency by factors of 1.6 and 2.5 is achieved for Ni and Mo anodes, respectively.

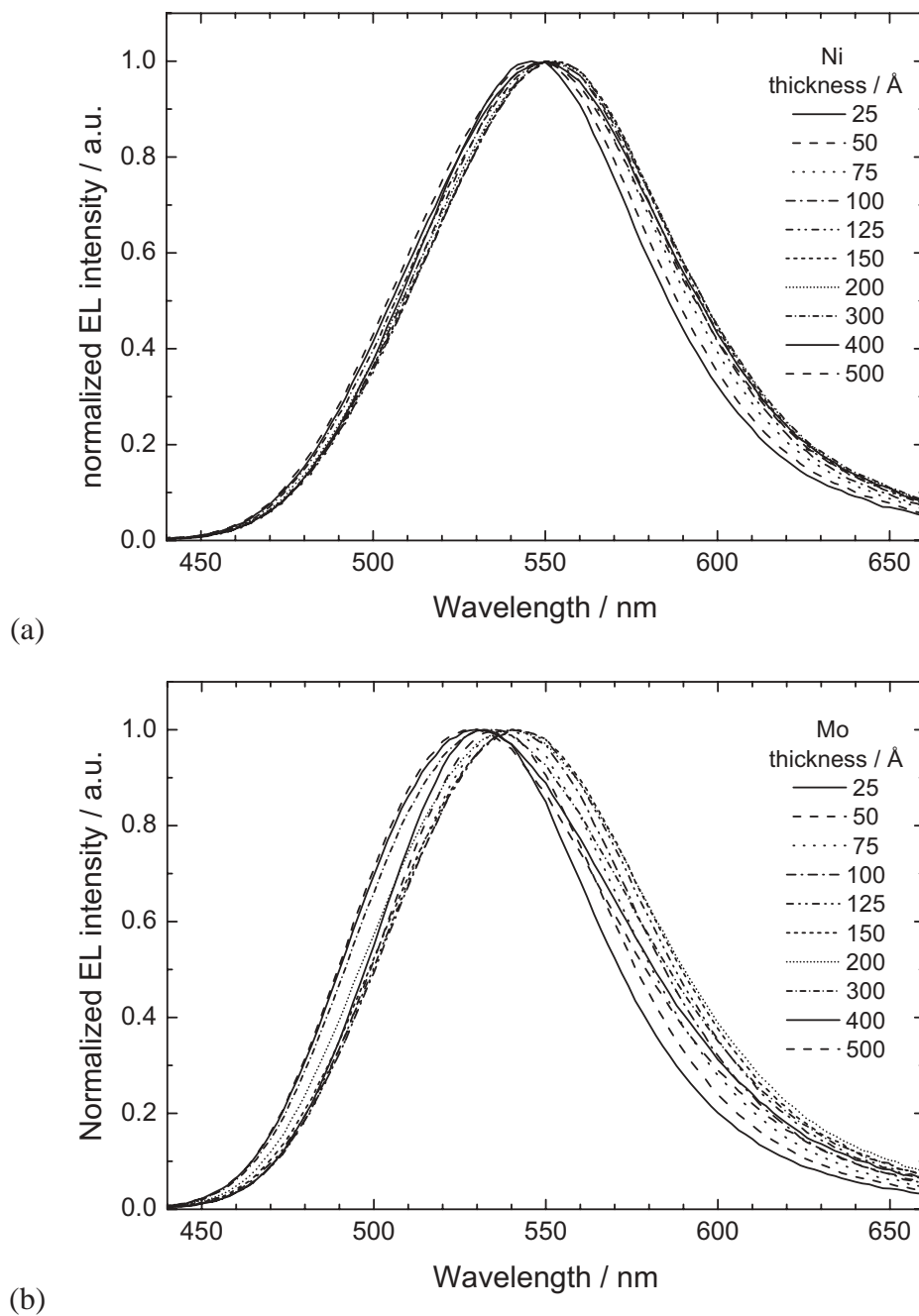


Figure 5.14: EL spectra of CuPc/NPB/Alq₃ OLEDs having bilayer anodes with varying (a) Al/Ni and (b) Al/Mo. The spectral shifts are more pronounced in Mo samples.

higher efficiency and a more directed emission characteristic lead to improved outcoupling and enhanced efficiency. As a detailed treatment of improved outcoupling is beyond the scope of this chapter, the reader is referred to [Neyts 1998; Riel 2002].

In summary, thin layers of high work function metals (Ni, Mo) can be used on highly reflecting Al to achieve identical electrical characteristics to bulk (Ni, Mo) anodes. The electrical characteristics of the device is not changed as long as a certain thickness of the material (25 Å for Ni, <25 Å for Mo) is deposited on Al. However the light output clearly increases with thinner Ni or Mo layer. Since the current density is not affected by the thickness of the injecting metal layer, the change in efficiency can be purely ascribed to optical effects. In the case of thin Ni and Mo layers the efficiencies could be increased by a factor of 1.6 and 2.5 compared to the bulk Ni and Mo values, respectively.

5.2.2 Black Anode Structure

In the previous section, the focus was on maximizing the reflectance of the bottom anode. However, applications under ambient light require high contrast ratios and highly reflecting anodes might actually reduce the contrast. Therefore, in this section, a low reflection electrode structure called a “black anode” is identified, which will be used in Section 5.2.3 as anode for the standard CuPc/NPB/Alq₃ OLED structure. With these black anodes, the reflectance will be reduced which possibly leads to a high contrast ratio between the on- and off-state of an OLED. Furthermore, cavity effects will be reduced, which may alter the emission characteristics. Figure 5.15 shows a schematic view of such a non-reflecting structure². This black anode structure is basically a three-layer structure consisting of a highly reflecting mirror (Al), a transparent spacer (SiO_x) and a semi-transparent high work function anode (Ni). Destructive interference is utilized to suppress reflection in a broad spectral range. Since the OLEDs under investigation are based on Alq₃ emission the reflectance of the black anode was minimized for $\lambda_{\text{Alq}} = 530$ nm. A rough estimate of the transparent SiO_x thickness for minimum reflection at 530 nm can be given by $\lambda_{\text{Alq}}/4 \approx 90$ nm assuming a refractive index of $n = 1.5$ for SiO_x. The thickness of the semi-transparent Ni layer for the layer sequence, which exhibits the lowest reflectance at 530 nm, however, cannot be estimated by a similarly general rule. Therefore, in order to experimentally determine the optimum thickness for a black anode a combinatorial

²Similar structures called BlackLayerTM have been commercialized by Luxell Technologies Inc.

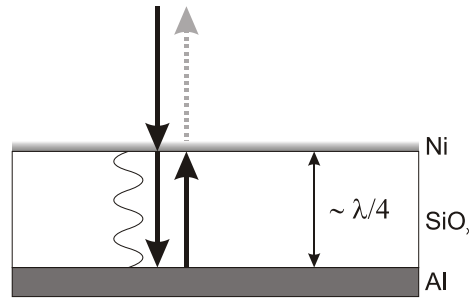
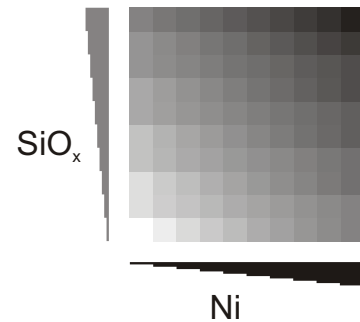


Figure 5.15: Basic principle of a black anode. A highly reflecting mirror (Al) with a transparent spacer (SiO_x) and a semitransparent anode (Ni). The anode is adjusted in a distance $d \approx \lambda_{\text{Alq}}/4$ from the mirror such that due to destructive interference, reflections are reduced.

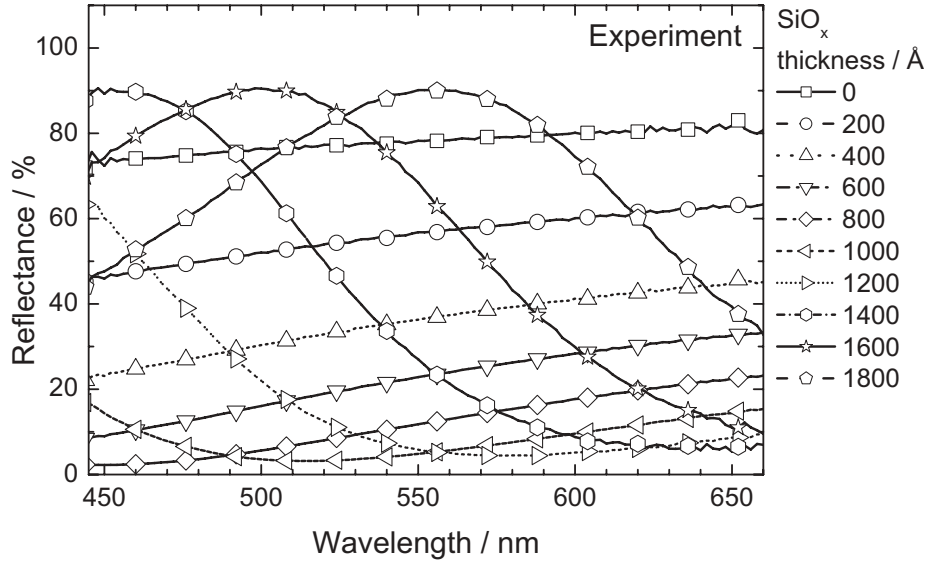
matrix with different SiO_x spacer thicknesses and Ni thicknesses is fabricated. The thicknesses are listed in the following table:

| Material | Ti/Al | SiO_x | Ni |
|---------------|--------|----------------|---------|
| Thickness / Å | 50/700 | 0 – 1800 | 0 – 180 |

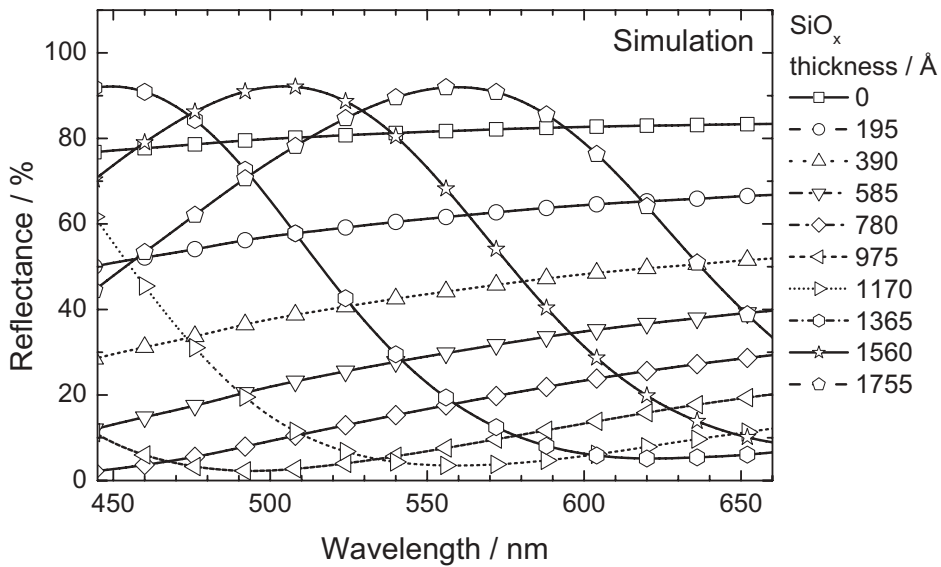


The SiO_x and Ni layers are staircased in 10 equidistant steps from 0 – 1800 Å and 0 – 180 Å, respectively. The spectral reflectance of these matrix structures is measured before and after oxygen plasma treatment with the reflectance setup described in Section 3.5.4.

Figure 5.16 shows 10 out of 100 reflectance spectra of the combinatorial black anode matrix. The structures shown have a fixed Ni thickness of 100 Å and a varying SiO_x spacer thicknesses from 0 to 1800 Å. Reflectance measurements on the samples without SiO_x spacer reproduce the reflectance value of the highly reflecting Al/Ni anodes discussed in Section 5.2.1 (see Fig. 5.10). With increasing SiO_x spacer thickness up to 1000 Å the reflectance in the whole range is decreased and reaches the minimum value of below 5% at 530 nm. A further increase of the SiO_x thickness leads to an increase of reflectance in the short wavelength



(a)



(b)

Figure 5.16: Reflectance of Al/SiO_x/Ni structures with different SiO_x and fixed Ni (100 Å) thickness. (a) Experiment (b) Simulation. Best agreement with experiment is obtained when 2.5% smaller values for the SiO_x thicknesses are assumed in the simulation.

range where a maximum appears, which is then shifted towards longer wavelengths. For a SiO_x spacer thickness of 1800 Å this maximum is located at 555 nm and reaches a value as high as 90%. Figure 5.16b shows the simulated spectra using the optics simulation tool developed by H. Nakamura (see Sec. 2.4) [Nakamura 2002]. The optical constants for e-beam evaporated SiO_x were determined by ellipsometry and the values were found to be close to those of stoichiometric SiO_2 . Excellent agreement between the experimental reflection data and the simulation is obtained when the thicknesses in the optical simulations are adjusted to 2.5% lower values. The accuracy of the optical simulation is also illustrated by comparing the reflectance at 530 nm for all 100 combinatorial devices. Figure 5.17a shows the reflectance extracted at 530 nm of the combinatorial devices in a 2D representation. The structure with SiO_x 1000 Å and Ni 100 Å shows the lowest reflectance at 530 nm with a value below 5% and an average reflectance of only 8% in the range of 450 to 650 nm. This value is further decreased after the oxygen plasma treatment. The optical simulation (Fig. 5.17b) matches the experimental results very well (Fig. 5.17a). As mentioned above, the SiO_x layer thicknesses are adjusted 2.5% lower than the experimental values indicating that the reflectance spectra, especially the position of maximum and minimum reflectance, are very sensitive to small changes in thickness.

In summary, the lowest reflecting Al/ SiO_x /Ni anode structure tailored for 530 nm emission wavelength has been determined experimentally and has been confirmed with numerical simulations. The determined “black anode” structure consists of Al/ SiO_x 1000 Å/ Ni 100 Å and will now be integrated with a standard CuPc/NPB/Alq₃ OLED structure.

5.2.3 OLEDs on Black Anode Structure

In the previous section, a black anode structure with minimum reflectance in the range of Alq₃ emission was experimentally determined. A combinatorial CuPc/NPB/Alq₃ structure is now deposited on top of this black anode in order to study the influence of interference effects on the spectral characteristic and the efficiency. This structure is compared with a structure on a reflecting anode. The following table lists the two combinatorial device structures:

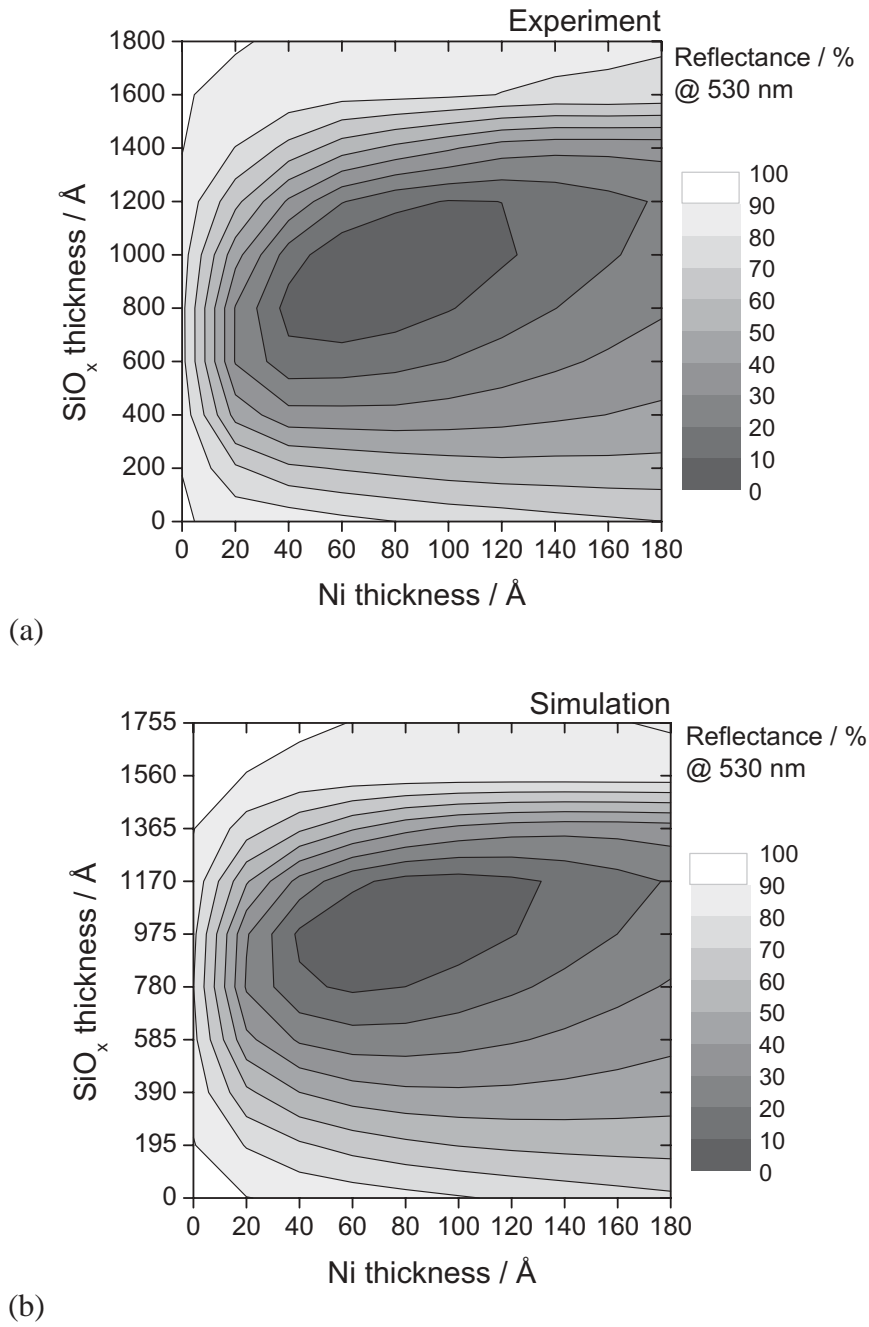


Figure 5.17: Reflectance at 530 nm of combinatorial Al/SiO_x/Ni structures with varying SiO_x and Ni thicknesses. (a) Experiment. (b) Simulation. Best agreement with experiment is obtained when 2.5% smaller thicknesses for SiO_x are assumed in the simulation.

Matrix A:

| | | | | | | |
|---------------------|----------------|----|------|----------|------------------|----|
| (reflecting anode): | Material | Ni | CuPc | NPB | Alq ₃ | Ca |
| | Thickness / nm | 70 | 15 | 10 – 100 | 10 – 100 | 20 |

Matrix B:

| | | | | | | |
|------------------|----------------|-------------------------|------|----------|------------------|-------|
| (“black anode”): | Material | Al/SiO _x /Ni | CuPc | NPB | Alq ₃ | Ca/Mg |
| | Thickness / nm | 70/100/10 | 15 | 10 – 100 | 10 – 100 | 15/5 |

Matrix A is the combinatorial matrix described with regard to electrical and optical aspects in Section 4.1.1 and Section 5.1, respectively. Matrix B has the same organic layer sequence deposited on the mentioned black anode structure. The cathodes of these matrices are different because a thin Mg layer was added to Matrix B in order to prevent the extremely thin Ca layer from oxidation and improving long-term stability. The transmittance of the cathodes are 68% and 50% for Matrix A and Matrix B, respectively. The reflectance of the cathode in Matrix B (34%) is almost twice as high as the reflectance in Matrix A (18%). Although the optical properties of the cathodes are somewhat different the matrices will be compared to discover general trends. The reflectance and transmission values of the Ca and Ca/Mg cathodes are experimental values and will be presented in Section 5.3. Figure 5.18 schematically summarizes the reflectance and transmittance values in these two devices.

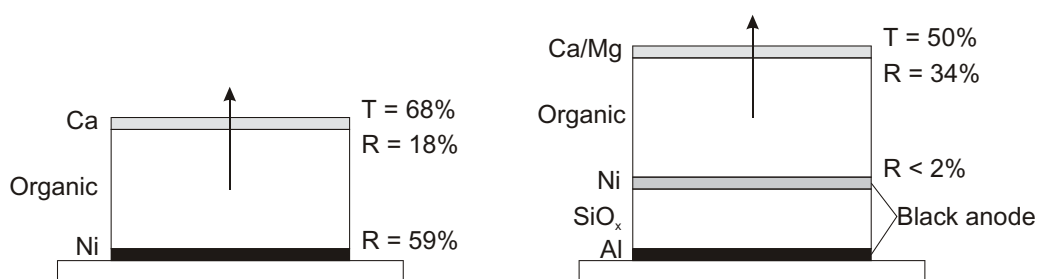


Figure 5.18: Schematic view of OLEDs built on (a) reflecting anode and (b) black anode. The reflectance R and transmittance T values at 530 nm are experimental values determined from single layers on glass (see Sec. 5.3).

Figure 5.19 shows an overview about all normalized spectra from both matrices. Although the same organic structures based on Alq₃ emission are used, a large spectral shift can be observed in both cases. In Matrix A (Fig. 5.19a) the peak wavelength shifts from 520 to 580 nm

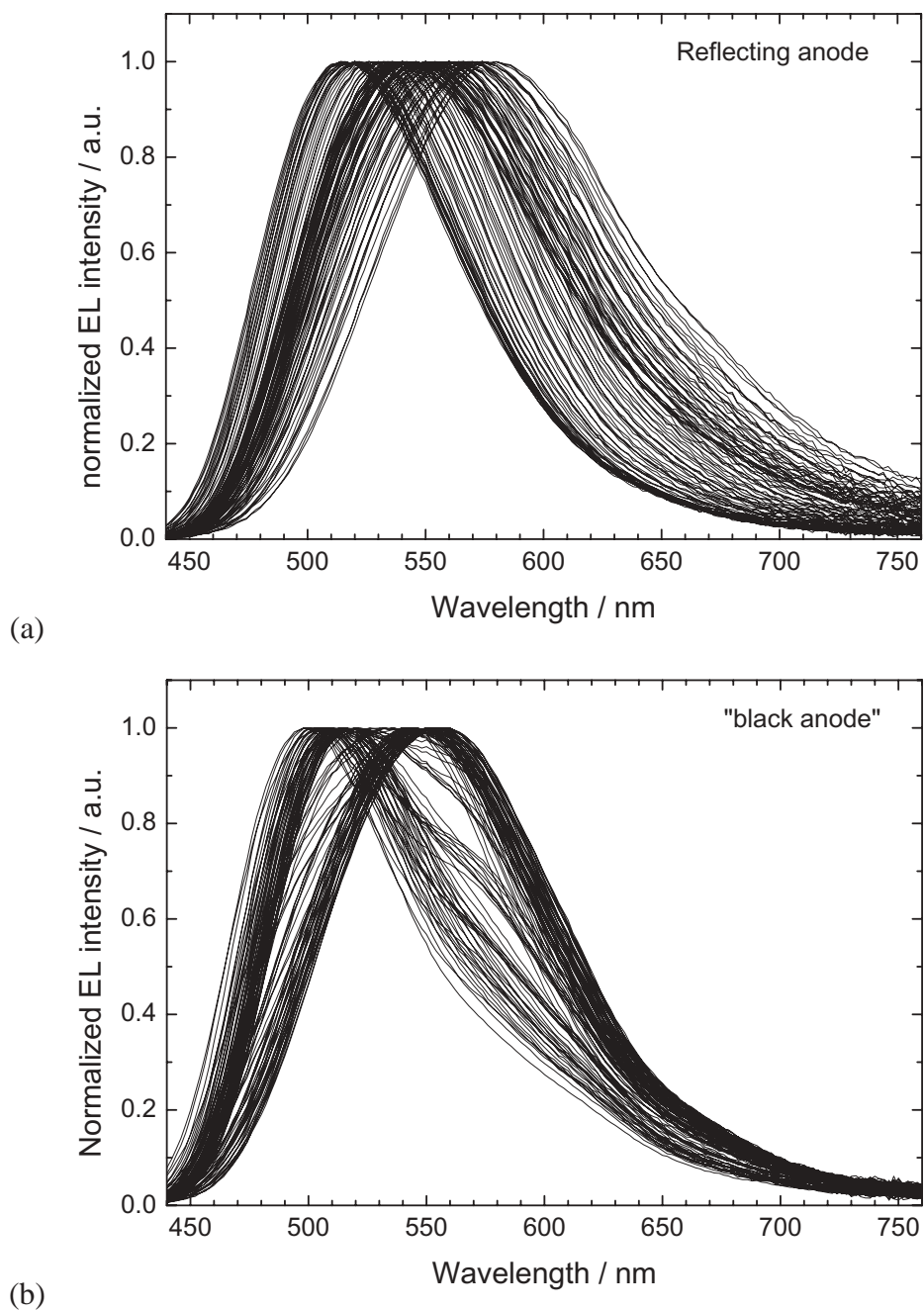
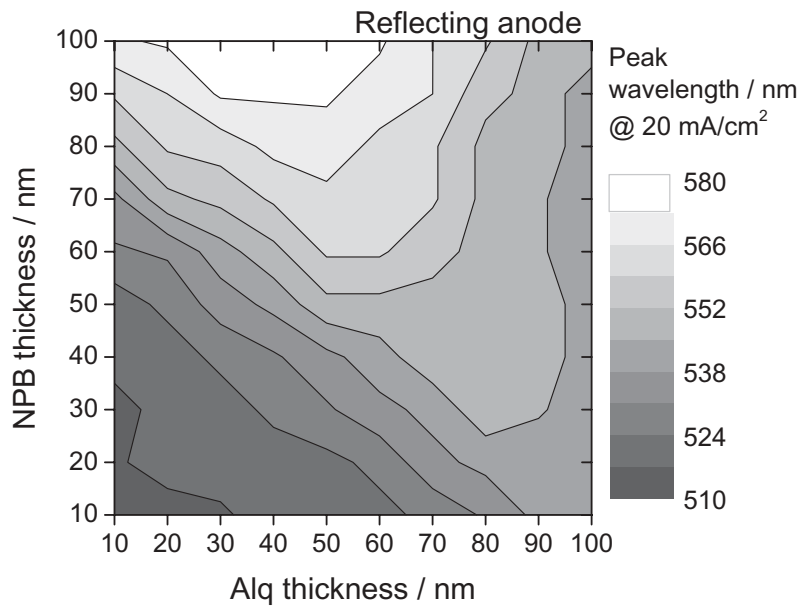


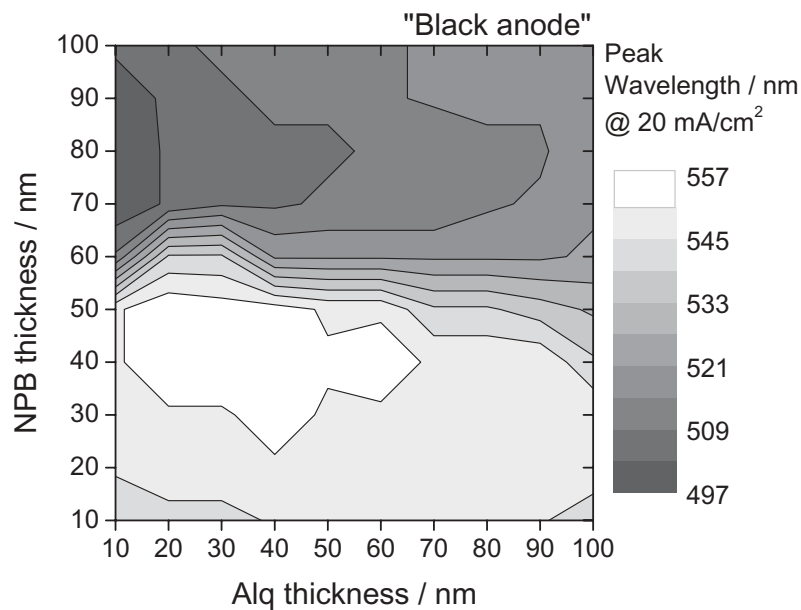
Figure 5.19: Experimental spectra of combinatorial matrix devices at 20 mA/cm^2 (a) Matrix A: reflecting and (b) Matrix B: black anode. A reduced spectral shift is observed on the black anode.

and the FWHM varies from 92 to 138 nm. The devices of Matrix B (Fig. 5.19b) exhibit a peak shift from 500 to 560 nm whereas the FWHM varies between 84 and 148 nm. Another interesting observation for Matrix B besides the smaller peak shift is that the spectra of Matrix B (“black anode”) are bundled into two groups (see Fig. 5.19b). In order to illustrate the most striking differences between Matrix A and B, Figure 5.20 shows the peak emission wavelength as a function of the individual layer thicknesses. For devices on Matrix A (reflecting anode, Fig. 5.20a.) it is observed that for small total thicknesses ($d_{\text{NPB}} + d_{\text{Alq}} \leq 110$ nm) the lines of equal peak wavelength run parallel to the diagonal. This clearly visualizes that the cavity length L basically determines the maximum peak wavelength. For larger total thicknesses the peak wavelength is influenced more strongly by the Alq₃ layer than by the NPB layer thickness. The most red-shifted emission (~ 580 nm) is observed for the device with NPB and Alq₃ thicknesses of 100 and 40 nm, respectively. On Matrix B (“black anode”, Fig. 5.20b), however, the 2D map appears completely different. The peak wavelength is almost independent of the Alq₃ layer thickness because the lines of equal peak wavelength run horizontally in this 2D representation. This indicates that the distance d of the emission zone (see Sec. 5.1) to the bottom electrode, i.e. the NPB layer thickness, determines the peak wavelength. For an NPB layer thickness of 60 nm the emission peak is located at ~ 530 nm. For lower NPB layer thicknesses ($d_{\text{NPB}} < 60$ nm) the peak wavelength is located at ~ 550 nm, whereas it is centered around 510 nm for ($d_{\text{NPB}} > 60$ nm). Furthermore, the broadest spectra are observed for NPB layer thicknesses of 60 nm. The comparison of the two matrices impressively shows that the two basic interference effects, i.e. multiple beam interference and wide angle interference can be separated (see Sec. 5.1.1). Multiple beam interference is predominant on Matrix A (reflecting anode), where the cavity length L is critical. Wide angle interference is predominant on Matrix B (“black anode”) where the wavelength is determined by the distance d of the emitting zone to the bottom electrode. Although the reflection of the black anode matrix is low ($< 8\%$), the predominant effect will be still the wide-angle interference since multiple beam interference relies on multiple reflections, which are hard to achieve in this structure.

Figure 5.21 compares the luminance of the two combinatorial matrices in order to illustrate the influence of interference effects. The 2D map shows the luminance as a function of NPB and Alq layer thickness plotted at a constant current density which basically corresponds to the efficiency since $\eta_{\text{cd/A}} = L/j$. The I - V curves (not shown) of both matrices are comparable since the same organic stack and the same injecting electrodes Ni and Ca are used. Matrix A



(a)



(b)

Figure 5.20: Peak wavelength of combinatorial matrices at 20 mA/cm² (a) Matrix A: reflecting anode. Peak wavelength roughly scales with total device thickness. (b) Matrix B: black anode. Peak wavelength almost independent of Alq₃ thickness.

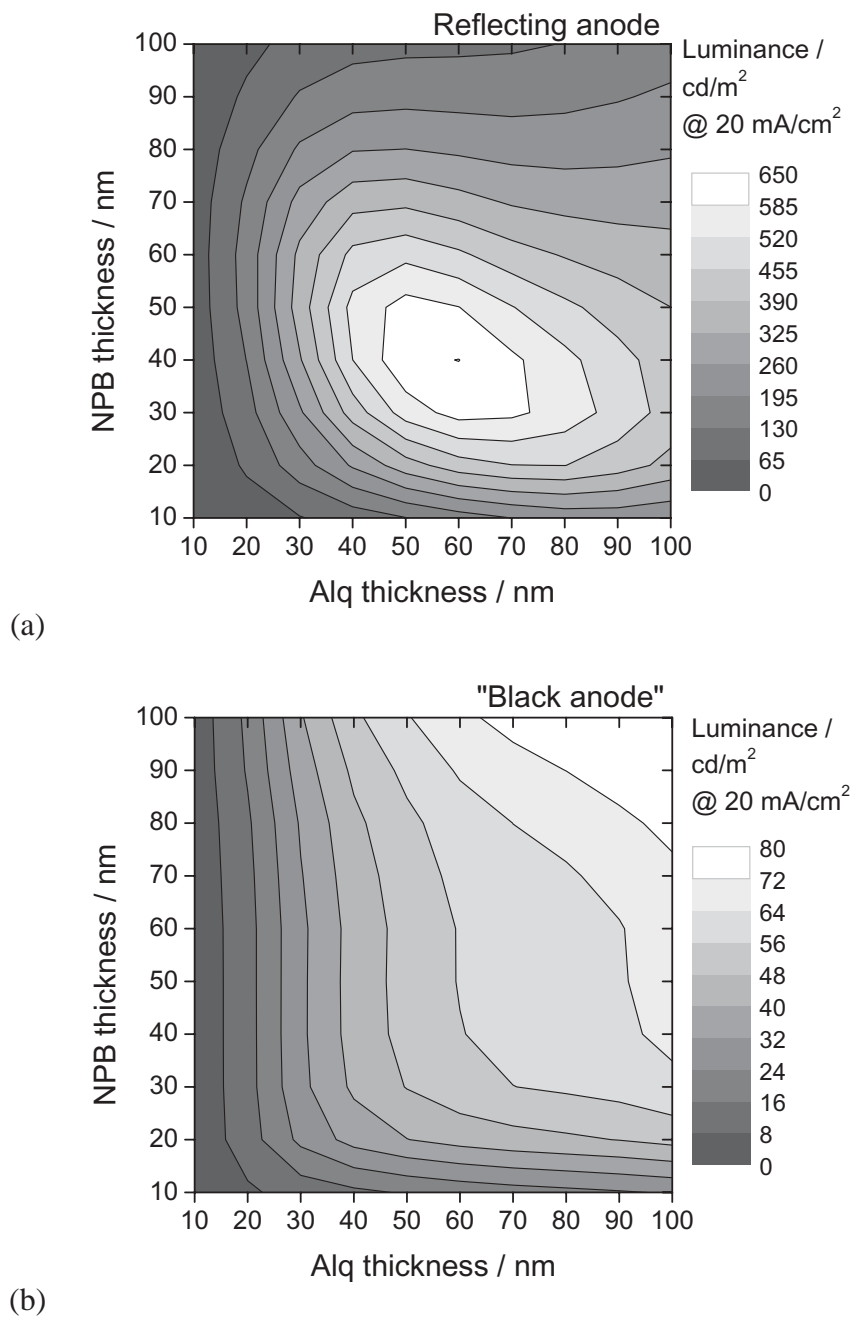


Figure 5.21: Experimental luminance map of NPB/Alq matrices on (a) reflecting Ni anode and (b) black anode Al/SiO_x/Ni. In the latter matrix the luminance maximum is apparently outside the investigated thickness range.

(reflecting anode) shows a clear maximum in the investigated range at 40 nm NPB and 60 nm Alq₃ thickness. This indicates that only one cavity length L (in this case 115 nm) is suitable for maximum efficiency. At thin Alq₃ thicknesses the efficiency drops drastically to less than 10% of the maximum which is attributed to luminescence quenching near the metal cathode. The efficiencies at thin NPB layer thicknesses also drop drastically to below 30%. These values are somewhat higher because emission takes place in Alq₃ layer and NPB acts as exciton blocker and the distance to the anode is increased by the additional CuPc buffer layer. In general, the luminance on Matrix B is roughly a factor of 8 lower than the observed luminance on Matrix A. The 2D-luminance plot of Matrix B (black anode) does not exhibit a distinct maximum in the investigated range. The luminance (i.e. efficiency) is maximal for the thickest device, probably increasing further outside the investigated thickness range. At thin Alq₃ and NPB thicknesses the luminance drops below 10% and 30% of the maximum value, respectively. This is similar to Matrix A, which proves that quenching effects are observed independent of optical interference effects.

5.2.4 Summary: Anode

In summary, extremely thin layers (25 Å) of high work function materials are deposited on highly reflecting Al to increase the reflectance by >22% compared to bulk Ni. The electrical characteristic of the OLEDs is unchanged and the efficiency can be increased by a factor of 1.6 and 2.5 for Al/Ni and Al/Mo bilayer anodes compared to devices with bulk Ni and Mo anodes, respectively. Oxygen plasma treatment leads to formation of NiO_x and the thickness of this layer has been determined to be ~120 Å.

A three-layer anode (“black anode”) consisting of Al/SiO_x/Ni is tailored for minimum reflectance at 530 nm (Al/SiO_x 1000 Å/Ni 100 Å) and employed as anode in a combinatorial matrix of the standard CuPc/NPB/Alq₃ structure. The comparison with a combinatorial matrix on a reflecting anode clearly showed that interference effects determine the efficiency in OLEDs. Quenching effects at low Alq₃ thicknesses are observed independent of optical interference effects. For accurate simulations of the spectral emission and efficiency, optical models have to include quenching near metal electrodes.

5.3 Cathode: Influence on Spectral Emission and Device Performance

As mentioned above, OLEDs always form a microcavity, especially when a semi-transparent and partly reflecting contact is used. In the previous two sections, the anode and the organic stack have been discussed. The cathode requires a careful selection of the material especially for top-emitting structures. An ideal cathode is non-absorbing and provides ohmic injection of electrons into the organic material. Unfortunately, such idealized cathodes do not exist and, hence, the best compromise has to be found. Here as well, the combinatorial approach is useful to investigate the optical properties of such top cathodes and their influence on the spectral characteristic.

5.3.1 Semi-Transparent Metal Cathodes

A straightforward way to achieve good electron injection and high transmittance is the use of extremely thin layers of a low work function metal. At thicknesses below 100 Å the transmittance of such metals is typically on the order of $\sim 50\%$. Table 5.4 lists the work function of various metals that might be used as cathode materials. The complex refractive indices at 530 nm of some cathode metals are listed in Table 5.5. The imaginary part κ of the complex

| Material | Ag | Al | Ba | Ca | Li | Mg | Sr |
|--------------------|------|------|-----|------|-----|------|------|
| Work function / eV | 4.26 | 4.28 | 2.7 | 2.75 | 2.9 | 3.66 | 2.59 |

Table 5.4: Work function of various metals. Data from [Michaelson, 1977].

| Material | $n + i\kappa$ @ 530 nm |
|----------|------------------------|
| Ag | $0.25 + i3.4$ |
| Al | $0.88 + i6.4$ |
| Ca | $0.18 + i2.3$ |
| Mg | $0.56 + i3.3$ |
| Li | $0.21 + i2.4$ |

Table 5.5: Complex refractive indices of various metals. Data from [Lide, 1996].

refractive index at a given wavelength λ is related to the absorption coefficient $\alpha = 4\pi\kappa/\lambda$. It is obvious that Al with its high imaginary part ($\kappa = 6.4$) will not be well suited as semi-transparent cathodes, whereas other metals like Ca, Li might be better choices. The latter metals, however, are highly reactive materials and the optical properties are not readily available and will also depend on fabrication conditions. The combinatorial characterization setup (see Sec. 3.5.4) allows the measurement of transmittance and reflectance of such reactive layers under inert conditions. Figure 5.22 shows the thickness-dependent transmittance of thin Al, Ca, and Ag layers on glass at a wavelength of 530 nm. Al shows an exponential decay in

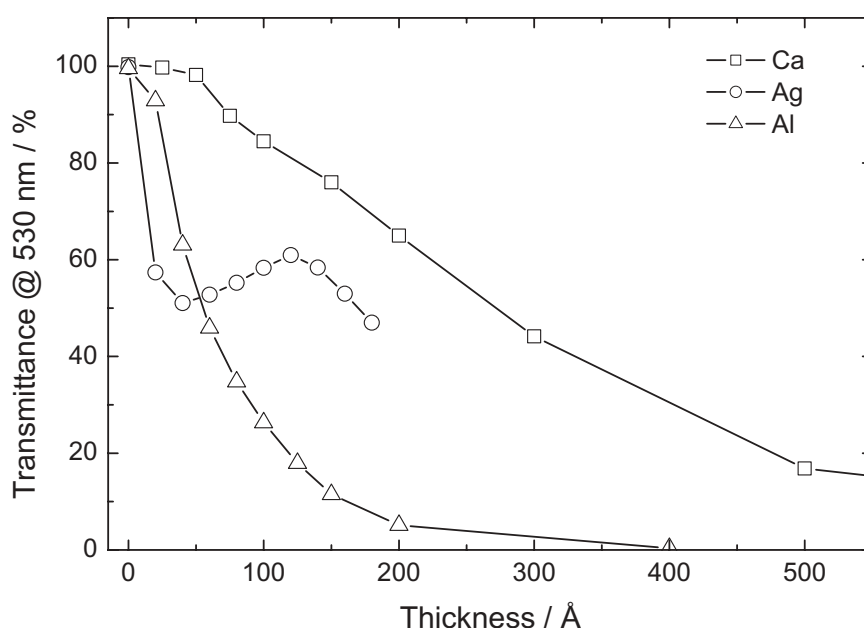


Figure 5.22: Transmittance of typical cathode metals Ag, Al and Ca as a function of thickness measured on glass.

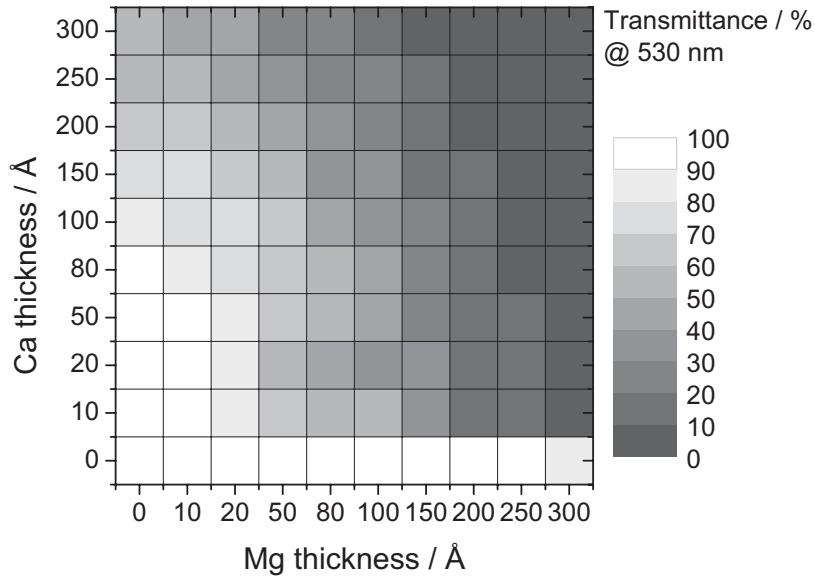
transmittance as is expected from Lambert-Beer's law (see Eq. 6.1). At a thickness of 100 Å the transmitted intensity drops to a value of less than 25%. In contrast, the Ag layers exhibits a transmittance of almost 60% at the same thickness. Furthermore, the transmittance of Ag does not show a monotonic decay in transmittance but a minimum at 40 Å and a maximum at 120 Å thickness. This might be ascribed to a thickness dependent non-uniform coverage, since Ag has a poor adhesion on glass. Ca shows the highest transmittance of these three materials as is expected from the imaginary part $\kappa = 2.3$ in Table 5.5. The transmittance of Ca at 200 Å

is still well above 60%, which makes Ca favorable as semi-transparent cathode. One disadvantage of Ca is its high reactivity, and if not encapsulated under inert conditions, oxygen and moisture will lead to cathode corrosion and device degradation. In this respect, Ag is a more stable metal with a relatively low absorption coefficient. However, pure Ag on top of organic films easily diffuses into the layers and led to leakage currents. Another choice is Mg, which is more stable against oxidation. However, the work function of Mg is less favorable to that of Ca for electron injection (see Tab. 5.4). Therefore, a bilayer cathode will be used consisting of a thin layer of Ca for electron injection and a second thin layer of Mg for protection. This compromises the properties of injection, transmittance and stability. For OLED structures it is now important to know the optical properties, such as transmittance and reflectance, of this double-layer Ca/Mg cathode. Therefore, the following combinatorial matrix is fabricated in a thickness range of Ca and Mg, which seems practical for application in OLEDs:

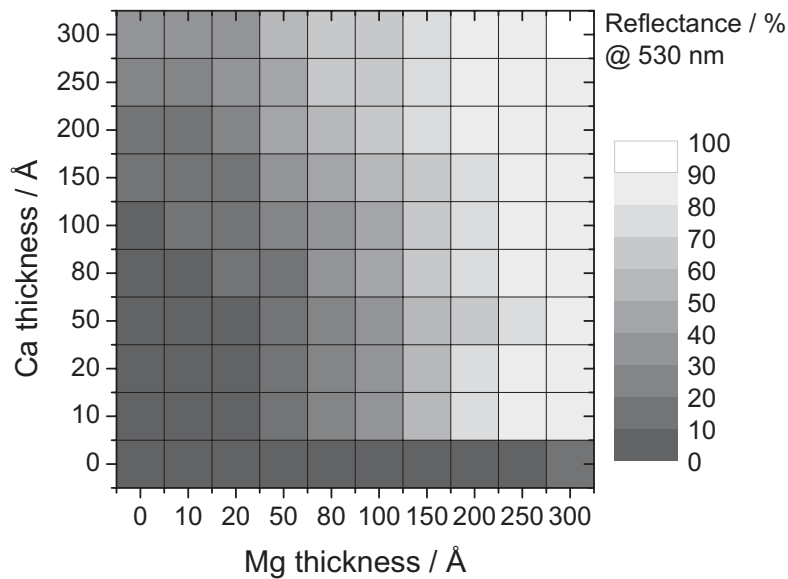
| Material | Ca | Mg |
|---------------|---------|---------|
| Thickness / Å | 0 – 300 | 0 – 300 |

The spectral transmittance and reflectance of this matrix are measured under inert conditions avoiding oxidation by the setup described in Section 3.5.4. For these measurements the blank glass substrate has been taken as 92% and 8% reference for transmission and reflectance measurements, respectively.

Figure 5.23 shows the transmittance and reflectance extracted at a wavelength of 530 nm for Ca/Mg double layers on glass. The total thicknesses of these double layers ranges from 0 to 600 Å and the transmittance values range from 92% to 2%, respectively. The row with only Mg layer on glass (Ca 0 Å) shows overall high transmission, which is attributed to a low sticking coefficient and poor film-forming properties of Mg on glass. This adhesion issue is not observed with Ca. Although the oxygen and water content in the glovebox is low (<1 ppm O₂, <1 ppm H₂O) traces of oxygen on the glass substrate might lead to oxidation of extremely thin Ca layers, so that the actual transmittance might be a few percent lower than the measured values. Figure 5.23 shows the reflectance values measured with the same setup. The reflectance varies from 8%, which corresponds to the value of the glass substrate up to 90% for the thickest Ca/Mg layer. Again the row with Mg shows low reflectance because of the above-mentioned peculiarities of Mg deposition on glass. The reflectance increases steadily with increasing Ca and Mg layer thickness. For use as semi-transparent top cathodes, a trade-off between the transmittance, reflectance and hence absorption has to be found. It is evident



(a)



(b)

Figure 5.23: Ca/Mg double-layer cathode on glass. (a) The transmission varies between 2% for Ca/Mg 300 Å/300 Å and 92% for glass. (b) The reflectance varies between 90% Ca/Mg 300 Å/300 Å and 8% for glass.

that the thinnest Ca/Mg layer shows the highest transmittance and low absorption. Nevertheless, the electrical properties of the metal layer also have to be considered, i.e. the Ca/Mg layer should be thick enough to carry current densities up to about 100 mA/cm^2 without a noticeable voltage drop. From this point of view, a layer thickness in the range of 100 to 200 Å seems reasonable, which in turn would result in a transmittance of 40–60%. In the next section, such a combinatorial bilayer cathode matrix will be deposited onto a CuPc/NPB/Alq₃ standard device structure.

OLEDs with Bilayer Cathodes

In the previous section, Ca/Mg bilayers have been characterized by their transmittance and reflectance. Now, such types of bilayer cathodes are deposited onto a uniform organic multi-layer stack, resulting in 100 OLEDs having an identical organic layer sequence but different cathodes. The detailed device structure is as follows:

| Material | Al/Ni | CuPc | NPB | Alq | Ca | Mg |
|---------------|--------|------|-----|-----|---------|---------|
| Thickness / Å | 700/50 | 100 | 500 | 500 | 0 – 300 | 0 – 300 |

Figure 5.24 shows the efficiency at 20 mA/cm^2 of the above combinatorial matrix. The efficiency varies from 0.5 to 5.9 cd/A in the investigated Ca/Mg thickness range. The hatched area represents the devices that were not operating properly. In these cases, either the cathode was too thin ($d_{\text{Ca}} + d_{\text{Mg}} < 125 \text{ Å}$) or it consisted of pure Mg which obviously results in poor adhesion as it was observed in the transmittance measurements on glass (see Fig. 5.23). It is clearly seen from Figure 5.24 that a Mg thickness greater than 150 Å drastically reduces the device efficiency. For example, the efficiency of devices with a Ca thickness of 150 Å is reduced from 3.1 to 0.8 cd/A when the top Mg layer is increased from 150 to 300 Å. In contrast, the efficiency is less dependent on the Ca thickness. A variation of the Ca thickness from 75 to 250 Å at a constant Mg thickness of 50 Å reduces the efficiency only by ~10% from 4.5 to 4.0 cd/A. The selection of the thicknesses for a semi-transparent Ca/Mg cathode has to trade off efficiency and stability. Via the combinatorial matrix, thicknesses of Ca 150 Å and Mg 50 Å are believed to be a reasonable compromise. This cathode exhibits a transmittance of 50% and a reflection of 34%.

Figure 5.25 shows the spectra of devices with a fixed Ca layer thickness of 150 Å but varying Mg thickness. The normalized representation (Fig. 5.25a) shows that the EL spectra shift

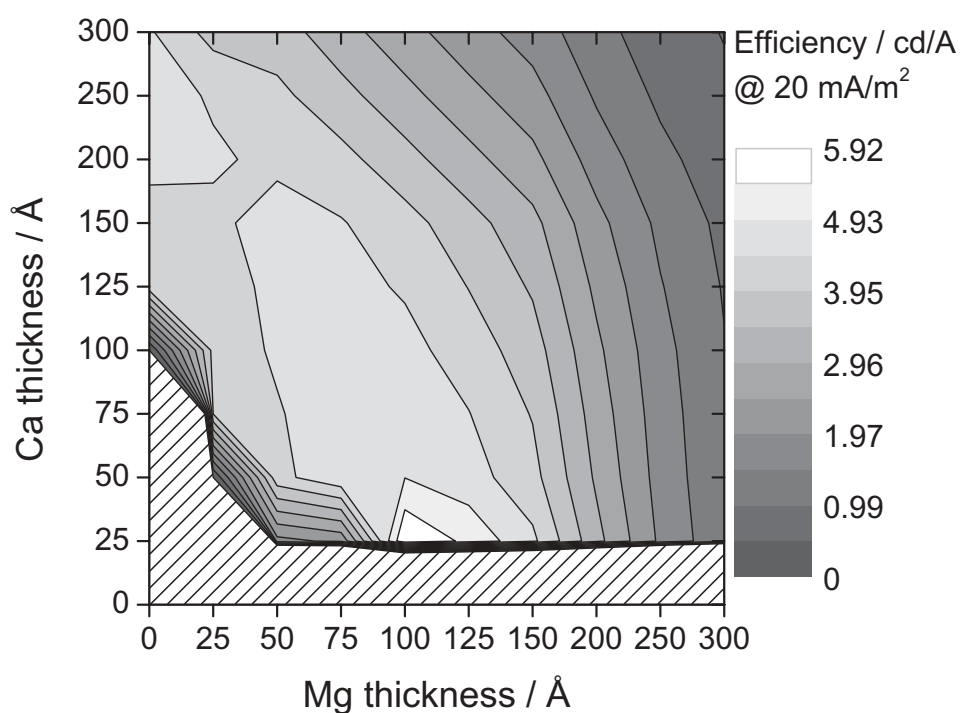


Figure 5.24: Efficiency of CuPc/NPB/Alq₃ OLEDs with Ca/Mg double-layer cathode. The hatched area represents the devices where the cathode was too thin for proper device operation.

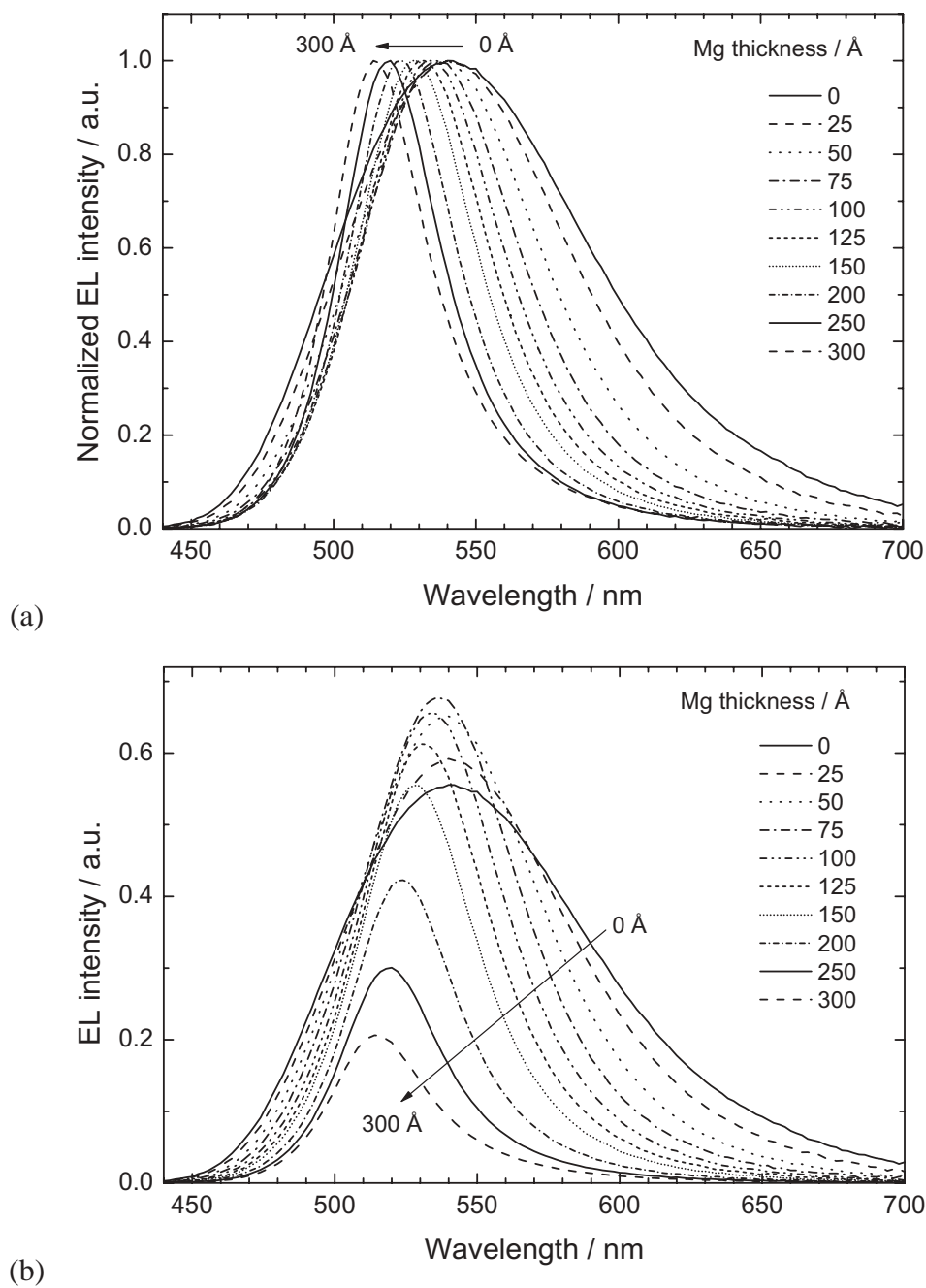


Figure 5.25: EL spectra of CuPc/NPB/Alq₃ OLEDs with semi-transparent Ca/Mg cathode. Ca thickness is 150 Å. (a) Normalized intensity. (b) Absolute intensity.

from 542 to 500 nm with increasing Mg thickness from 0 to 300 Å. Furthermore, the spectral width (FWHM) is decreased from 114 to only 40 nm. This is explained by the enhanced reflectivity of the cathode mirror with increasing Mg thickness, which leads to a higher quality of the cavity. Figure 5.25b depicts the absolute intensity and illustrates again that the EL intensity drops drastically when the Mg layer exceeds 100 Å. This clearly illustrates how sensitively the spectral characteristic is influenced by small changes in thickness of the top cathode. Nevertheless, it could be demonstrated that combinatorial methods are capable of supplying the necessary datasets in order to tackle and verify numerical modeling of the spectra.

5.3.2 Dielectric Capping Layer

In the previous section, the influence of the transmission and reflection of the semi-transparent cathode on the efficiency and spectral characteristic have been demonstrated. It is a known principle that the transmittance of thin metal films can be increased by adding a dielectric layer on top the metal film. An important prerequisite for this concept to work is a high difference in the refractive index Δn . Therefore, dielectric capping layers should have a high index of refraction, e.g. such as HfO ($n = 2.0$), ZnS ($n = 2.3$) or ZnSe ($n = 2.7$), data from [Lide 1996]. It has been demonstrated that this concept can be used to increase the light output of top-emitting OLEDs [Hung et al. 2001; Riel et al. 2003]. Here, this method will be briefly illustrated by applying a uniform capping layer to a complete combinatorial matrix.

Figure 5.26 shows the efficiency map of the red double-doped device discussed in Section 5.1.2. Figure 5.26a shows again the the 2D efficiency map from Figure 5.6 (page 121), here in direct comparison to the matrix with dielectric capping layer. In the uncapped matrix, the most efficient device had thicknesses of STAD and Alq₃ of 35 and 70 nm, respectively. After the first characterization, a capping layer of ZnSe (60 nm) was deposited on top of the combinatorial matrix, which was then remeasured. Figure 5.26b shows the efficiency as a 2D plot of the capped matrix, which exhibits an approximately 12% higher efficiency. The most striking difference is that the most efficient device is now located at layer thicknesses of 50 and 75 nm of STAD and Alq₃, respectively. Another important fact is that the I - V characteristics are unchanged, since the capping layer naturally only affects the optical characteristics. Furthermore, the angular emission dependence, the chromaticity as well as the total reflectance can be tuned by a means of a capping layer. For a more detailed view of capping layers, see [Riel 2002; Riel et al. 2003].

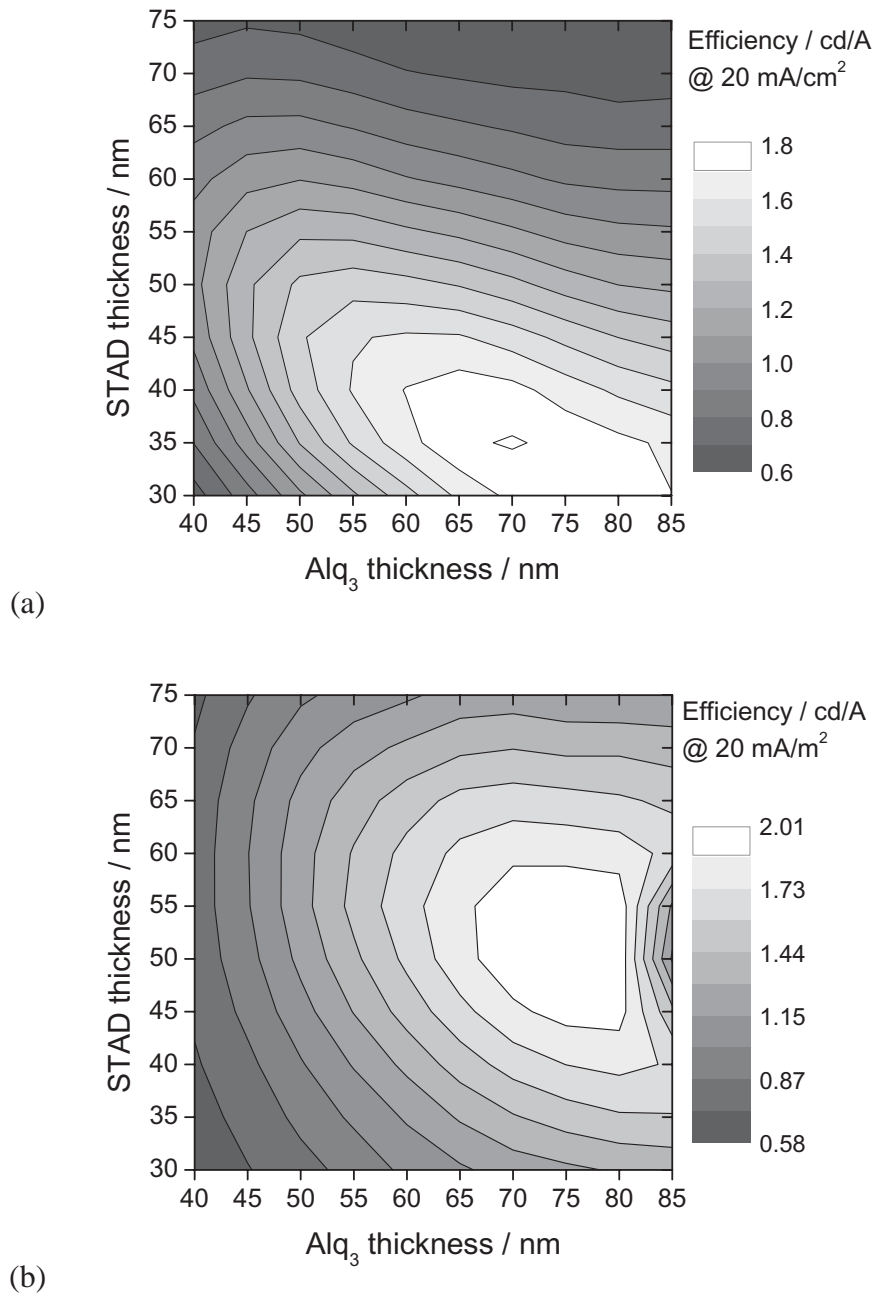


Figure 5.26: 2D efficiency plots of red CuPc/ STAD/ Alq₃:Rub:DCJT B matrices. (a) uncapped (b) After deposition of a 60 nm ZnSe capping layer.

5.3.3 Summary: Cathode

In summary, the combinatorial method has been used to investigate thin semi-transparent metal electrodes for top-emission OLED devices. The cathode has to fulfill two criteria: good electron injection and low absorption. Typical low work function metals, in general, fulfill both requirements, but with the drawback of high reactivity and hence fast degradation. This can be circumvented by a bilayer cathode consisting of a thin layer Ca for injection and a less reactive Mg layer serving as a protective layer against degradation if not encapsulated. Such Ca/Mg structures have been fabricated via combinatorial fabrication and characterized by transmittance and reflectance. These bilayer cathodes have been applied to the standard OLED structure (CuPc/ NPB/ Alq₃). A bilayer cathode of Ca 150 Å/ Mg 50 Å was found to be an acceptable compromise between efficiency and degradation stability. Combinatorial investigations of two layer cathodes will be especially helpful, e.g. in the case of LiF/Al cathodes where the performance of the device depends critically on the LiF thickness. In general, the combinatorial results of EL spectra show the dependence of the semi-transparent cathode and provide the basis of an experimental dataset for future numerical modeling.

It has been sketched on a combinatorial matrix that a capping layer can be used in order to modify the optical output characteristic without affecting the electrical characteristic. Furthermore, it is emphasized that the organic device structure and the capping layer have to be optimized as an entity since the deposition of a capping layer changes the optimum thicknesses for the organic layers.

Chapter 6

Diffusion of Excitons and Quenching at Interfaces

6.1 Quenching of Excitons

It was pointed out in Section 4.1.1 that the EL efficiency is drastically reduced when the emission region is located close to the cathode. In general, the PL or EL efficiency of an organic material is determined by the fraction of the excited states which undergo a radiative transition to the ground state. Various non-radiative mechanisms compete with radiative processes and lead to a quenching of excited states and hence reduce the efficiency in OLED structures. Surface quenching is one extrinsic mechanism that reduces the PL and EL efficiency in organic layers. This process becomes especially important in thin layered structures when the diffusion length of excited states is of the order of the sample thickness. In particular, metals are known to be efficient quenchers of luminescence since energy in a broad range can be transferred efficiently and dissipated non-radiatively [Chance et al. 1978]. Investigations of energy transfer were carried out decades ago on anthracene single crystals with various spacer layers to a metal surface [Vaubel et al. 1971]. In the field of organic light-emitting materials and devices, quenching has been discussed with regard to experimental [Becker et al. 1997; Choong et al. 1998] and theoretical issues [Chance et al. 1978; Burin and Ratner 2000]. It was found that the quenching processes strongly depend on the distance of the emitting species to the quenching site or the interface. For OLEDs it is therefore of great importance to know the critical distances involved. For this purpose, combinatorial sample fabrication is employed

once again to investigate thickness-dependent series of different sample configurations. In order to study surface quenching, a series of PL experiments on Alq₃ layers on various materials (glass, ITO, and Al) are performed. The thickness-dependent PL intensity is described with the aid of Lambert–Beer’s law and with a model that explicitly takes exciton diffusion and quenching at the surface into account.

6.1.1 PL Quenching of Alq₃ on Glass, ITO and Al

Experimental

PL measurements on a series of thin Alq₃ films on different substrates are performed in order to investigate critical quenching distances. The substrates are patterned with interdigitated columns of coated and uncoated glass (see Sec. 3.3.4, Fig. 3.10), i.e. the even and the odd columns have ITO (or Al) and glass as underlayers, respectively. On such substrates staircases of Alq₃ are deposited at the same time onto glass, ITO and Al. The sample structures and surface treatments are listed in the following table:

| substrate | coating | treatment | Alq ₃ thickness |
|-----------|-----------|-----------------------|----------------------------|
| (1A) | – | – | 0 – 2000 Å |
| (1B) | Al 700 Å | – | 0 – 2000 Å |
| (2A) | – | O ₂ plasma | 0 – 2000 Å |
| (2B) | ITO 700 Å | | 0 – 2000 Å |

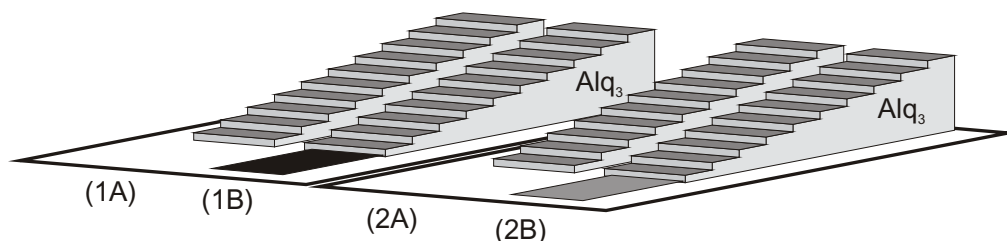


Figure 6.1: Schematic view of thickness series of Alq₃ films on different substrates for PL measurements. (1A,2A) Alq₃ on glass, (1B) Alq₃ on Al and (2B) Alq₃ on ITO.

Figure 6.1 visualizes the experimental sample structures. The Al layer on substrate 1 is fabricated on a clean glass substrate by e-beam evaporation and transferred directly into the vacuum system without further treatment before Alq₃ deposition. Substrate 2 is cleaned and exposed to an oxygen plasma in order to remove residual photoresist and other contaminants from ITO patterning. Before evaporation of the organic films, the reflectivity of the ITO on glass is measured and found to vary only between 8% to 15% in the visible spectral range. The Alq₃ samples ($7 \times 7 \text{ mm}^2$) are excited via a glass fiber with a 355 nm laser (1 mW) and the PL signal is measured in reflection mode as described in Section 3.5.3. All Alq₃ spectra are corrected for the background by subtracting the spectrum of the sample with zero Alq₃ thickness on the corresponding coating.

Results

Figure 6.2 shows an overview of the PL spectra of different Alq₃ thicknesses on glass (10 to 2000 Å). As indicated by the arrow in Figure 6.2a, the PL intensity increases monotonically with increasing Alq₃ layer thickness. The measured PL intensities cover a range of more than three orders of magnitude. Figure 6.2b shows all normalized spectra which exhibit the typical Alq₃ emission with a peak at $530 \pm 2 \text{ nm}$ with a spectral width (FWHM) of $110 \pm 4 \text{ nm}$ indicating that interference effects are negligible in this configuration on glass.

For a quantitative analysis the value of the PL intensities at the peak wavelength is extracted and plotted as a function of thickness. Figure 6.3a shows the PL intensities for two Alq₃ series on glass (Substrate 1A and 2A) as a function of Alq₃ thickness in double logarithmic representation. At thicknesses greater than $\sim 200 \text{ Å}$ the PL intensities of both curves are basically identical showing a linear increase of intensity with slope of approximately 1 in this representation. Below $\sim 200 \text{ Å}$ both data sets deviate from slope 1 and show a steeper decay in PL intensity. Whereas the samples of the untreated substrate exhibit a slope of ~ 1.75 below thicknesses of 90 Å , the samples deposited on the oxygen-plasma-treated substrate show a slope of ~ 1.95 below 170 Å . Since both sample series consist of the same Alq₃, the more pronounced suppression of luminescence on the oxygen-plasma-treated substrate (2A) can be regarded to hint the influence of surface quenching depending on the substrate treatment. Figure 6.3b illustrates the difference of the two measurements by calculating the ratio of the PL intensities from the two substrates. At low thicknesses ($< 200 \text{ Å}$) the ratio steeply drops down below 0.3, clearly indicating that the PL intensity is drastically reduced on the oxygen-plasma-

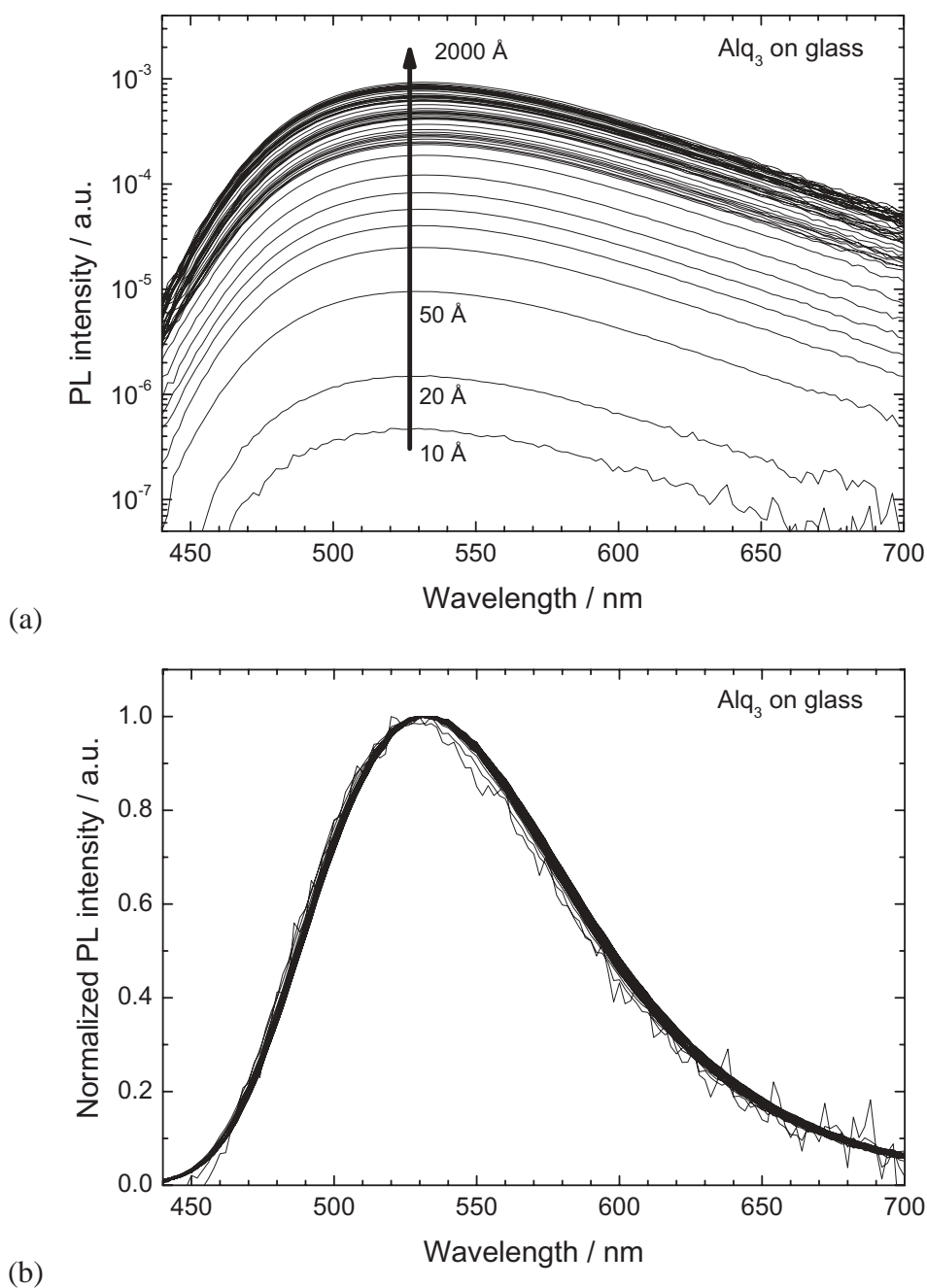


Figure 6.2: Photoluminescence of Alq₃ layers with thicknesses ranging from 10 to 2000 Å on glass. (a) Logarithmic representation illustrating the dynamic range covered by the sensitivity of the spectrophotometer. (b) The normalized linear plot shows the unchanged Alq₃ spectrum at different thicknesses.

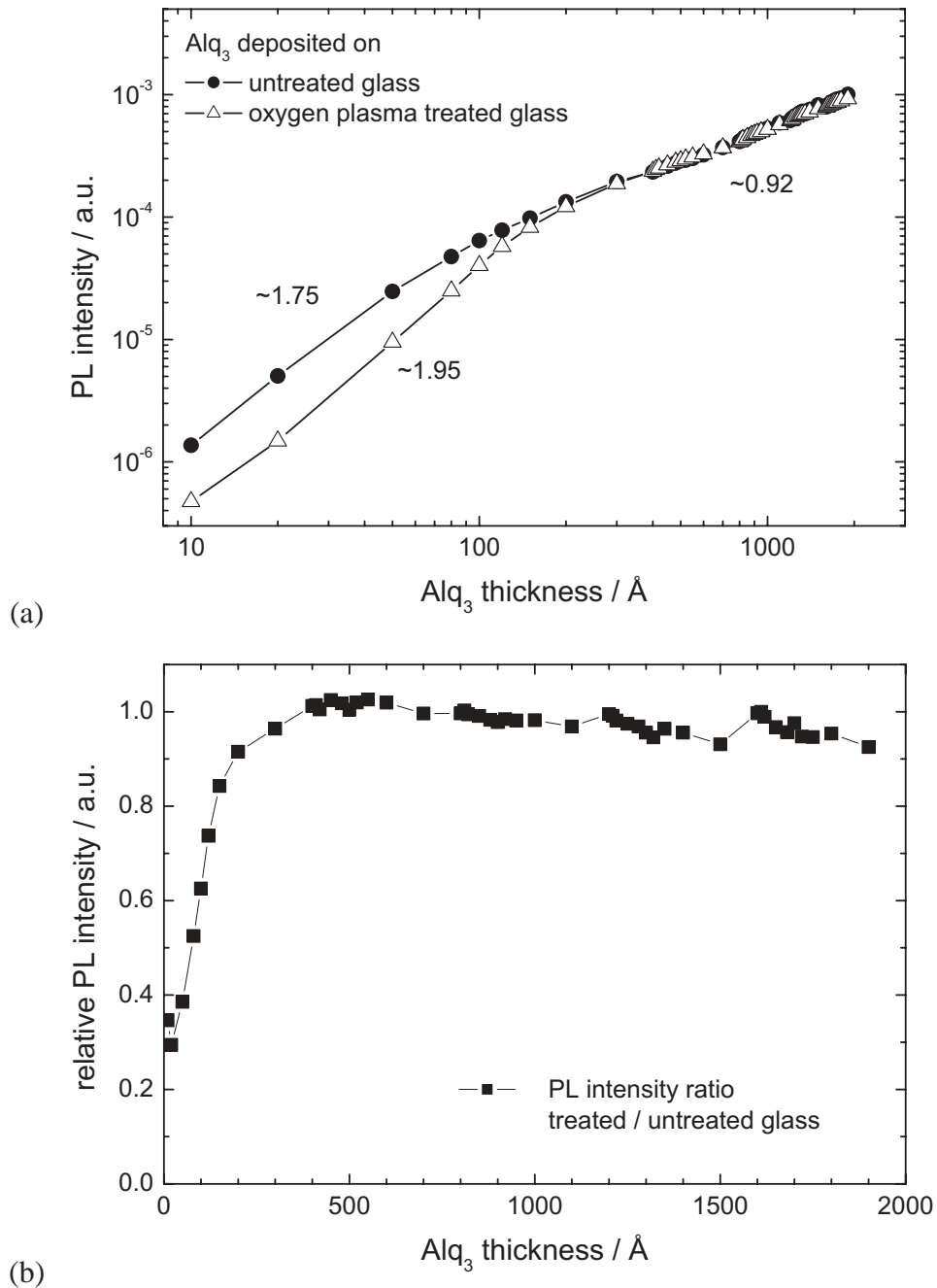


Figure 6.3: (a) Thickness dependent PL intensity of Alq₃ on differently treated glass substrates. Below thicknesses of 200 Å the PL intensity of Alq₃ on the oxygen treated glass shows steeper decrease (~ 1.95) than on untreated substrate (~ 1.75). (b) The ratio of the PL intensities illustrates the drastic reduction of PL at low thicknesses. The constant ratio of 1 at higher thicknesses confirms the reproducibility of the experiments.

treated substrate. The constant ratio of 1 at larger thicknesses confirms the reproducibility of the experiment.

The data shown above illustrates that there is noticeable luminescence quenching even at the glass surface. For OLED structures, quenching at electrodes, e.g. ITO or Al, is of special interest since these materials are typically used as anode or cathode materials. Figure 6.4 shows the PL spectra of Alq₃ on ITO. The logarithmic representation in Figure 6.4a again shows the dynamic range of the PL. Figure 6.4b shows that the PL spectra of Alq₃ on ITO reveal thickness-dependent changes in spectral shape and intensity. The maximum of emission shifts from 514 to 546 nm and the FWHM varies between 96 and 140 nm depending on the Alq₃ layer thickness. The measured PL intensity of Alq₃ on ITO at 2000 Å is about the same compared to the intensity of the sample series on glass.

Figure 6.5 shows the thickness-dependent PL spectra of Alq₃ on Al. Below 50 Å Alq₃ thickness the spectra could not be measured with the setup because of the low intensity and the large background signal of the laser due to the highly reflecting Al. The spectral shift is less pronounced than in the ITO case. The maximum shifts from 520 nm to 540 nm and the FWHM varies within 96 nm to 124 nm. Figure 6.6 shows the extracted PL intensities of the Alq₃ sample series on ITO and Al as a function of thickness. The PL intensity on ITO as a function of thickness exhibits a slope of ~ 1.7 up to 700 Å. However, the PL intensity as a function of thickness does not show a range with slope 1 like the Alq₃ layers on glass. With increasing thickness (>700 Å) the slope is decreased and the intensity seems to saturate to a constant value. In contrast, the Alq₃ samples on Al show a rather different functional behavior. A linear relationship with a slope of ~ 3.1 represents the range from 50 to 500 Å layer thickness. Owing to optical interference effects, at thicknesses >500 Å oscillations can be observed with maxima around 700 and 1500 Å. The quantitative description of the functional behavior of these experimental curves will be the topic of the next section.

6.1.2 Description of PL Intensity using Lambert–Beer’s Law

It is evident that the PL intensity increases with Alq₃ film thickness simply because of the increasing number of molecules which can absorb and re-emit light. Since the excitation beam is attenuated in the absorbing media the intensity profile in the organic film is given by Lambert–Beer’s law:

$$I(x) = I_0 \cdot e^{-\alpha x}, \quad (6.1)$$

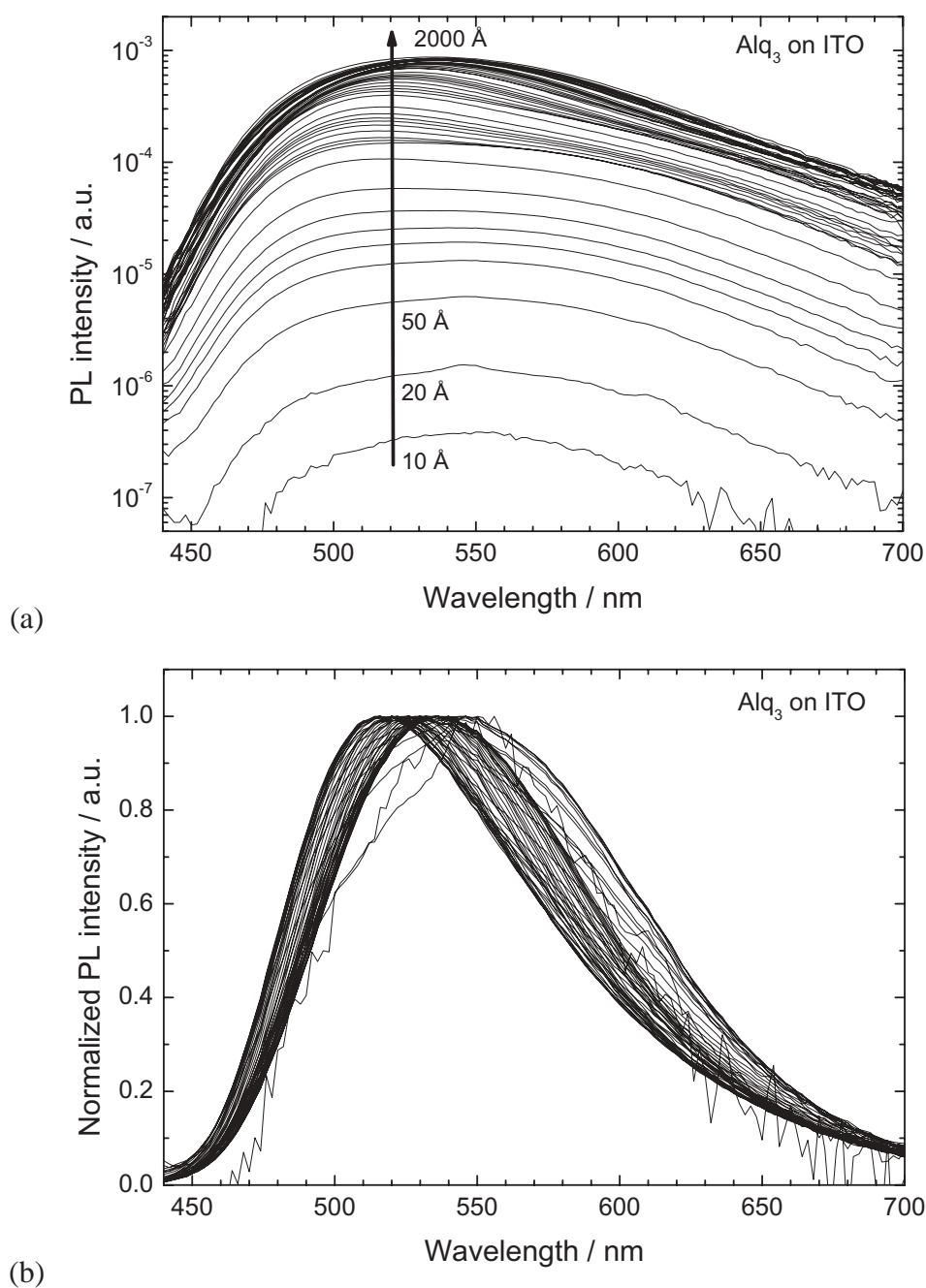


Figure 6.4: PL spectra of Alq₃ layers with thicknesses ranging from 10 to 2000 Å on ITO. (a) Logarithmic representation illustrating the dynamic range. (b) Normalized linear plot showing spectral changes due to thickness-dependent interference.

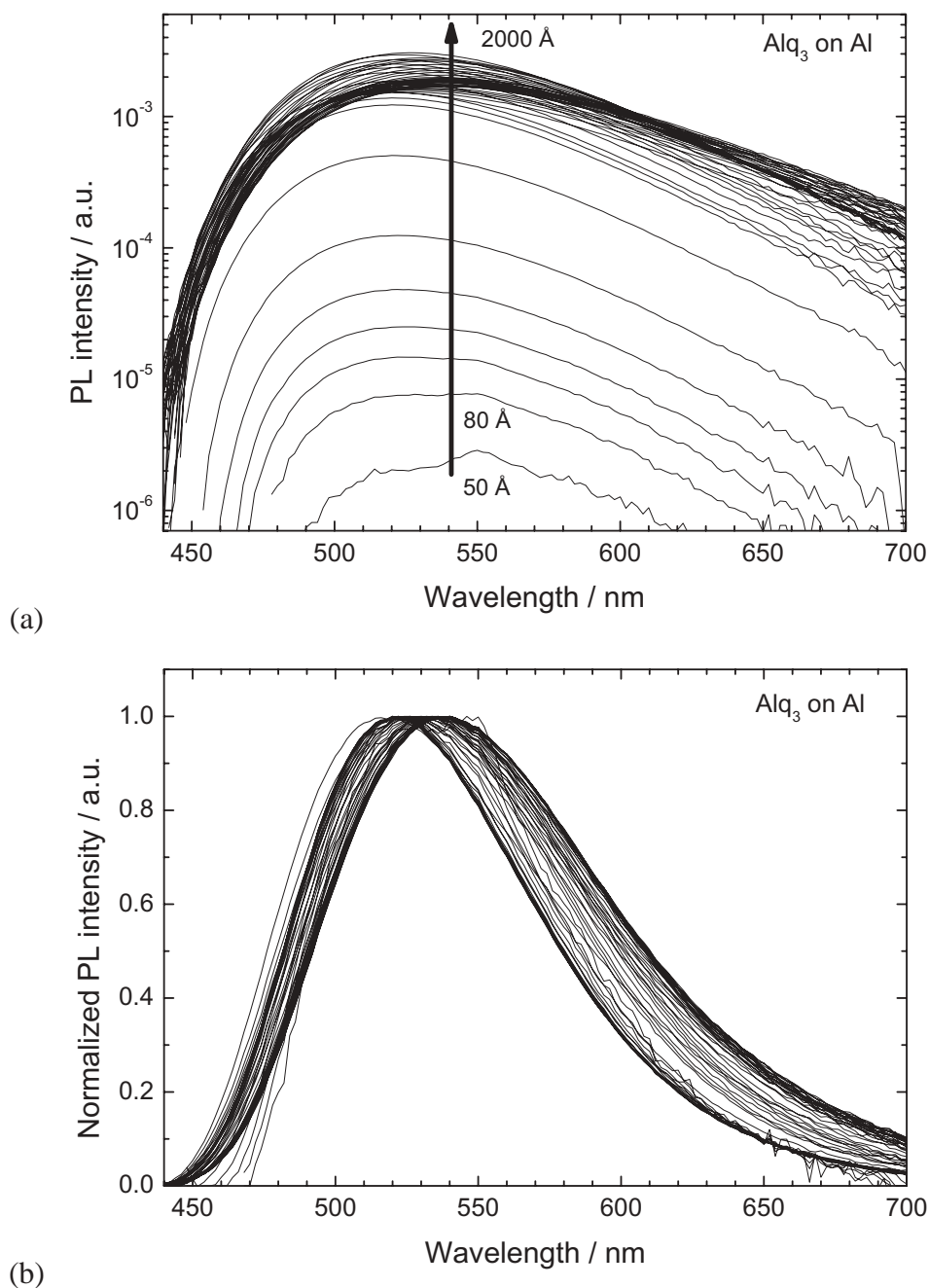


Figure 6.5: Photoluminescence of Alq₃ layers with thicknesses ranging from 10 to 2000 Å on Al. (a) Logarithmic representation illustrating the dynamic range. PL intensities of films with thicknesses < 50 Å could not be measured. (b) Normalized linear plot showing spectral changes due to thickness-dependent interference.

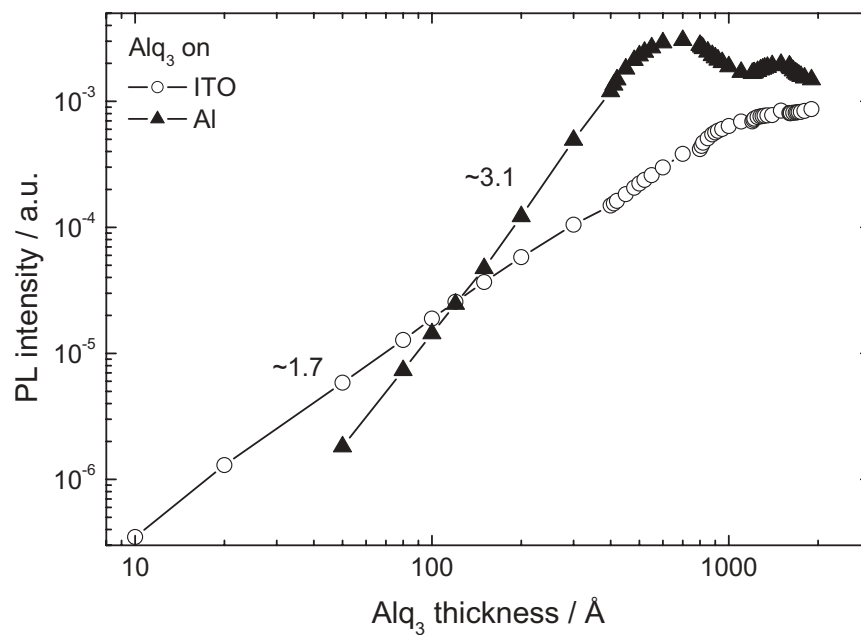


Figure 6.6: Thickness-dependent PL intensity of Alq₃ on ITO and Al. In the low thickness range slopes of ~ 1.7 and ~ 3.1 are observed for ITO and Al, respectively. The highly reflecting Al leads to higher PL intensities. The oscillations in Alq₃ on Al data are due to optical interference effects.

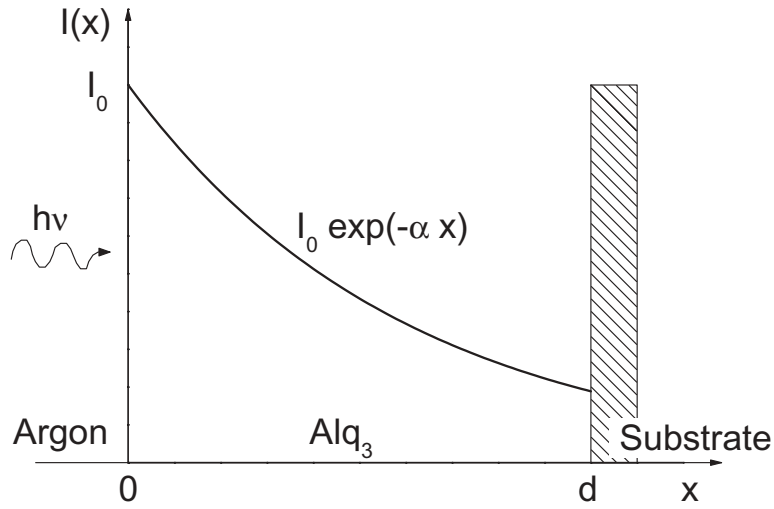


Figure 6.7: Schematic of the excitation intensity in an Alq₃ film on a non-reflecting substrate according to Lambert-Beer's law.

where $I(x)$ is the intensity at location x , I_0 is the excitation intensity, and α the absorption coefficient of the material. Figure 6.7 sketches the boundary conditions and the resulting excitation intensity profile. A quantitative description of the expected PL intensity can now be given with the help of Equation (6.1). The absorbed intensity I_{abs} as a function of x is

$$I_{\text{abs}}(x) = I_0 \cdot (1 - I(x)). \quad (6.2)$$

Assuming a constant molecular absorption coefficient and a constant intrinsic PL quantum efficiency for Alq₃ independent of the position in the layer, the PL intensity is proportional to the absorbed light. In the following, the measured PL intensity will be referenced to the PL intensity $I_{\text{PL}\infty}$ of an infinite thick sample where all excitation light I_0 is absorbed. Hence, all PL intensities are relative values and the excitation intensity I_0 and the absolute PL efficiency of Alq₃ does not need to be known. Thus, the PL intensity I_{PL} of a sample with thickness d is

$$I_{\text{PL}}(d) = I_{\text{PL}\infty} \cdot (1 - e^{-\alpha d}). \quad (6.3)$$

Reabsorption of light and losses due to waveguiding effects are neglected in this description. In order to be able to fit Equation (6.3) to the experimental data, the value of the absorption coefficient α of Alq₃ at 355 nm is needed and has been determined with ellipsometry $\alpha = 3.8 \times 10^4 \text{ cm}^{-1}$. This means that after $4 \cdot \alpha^{-1} \approx 1 \mu\text{m}$ the PL intensity reaches 98% of the maximum

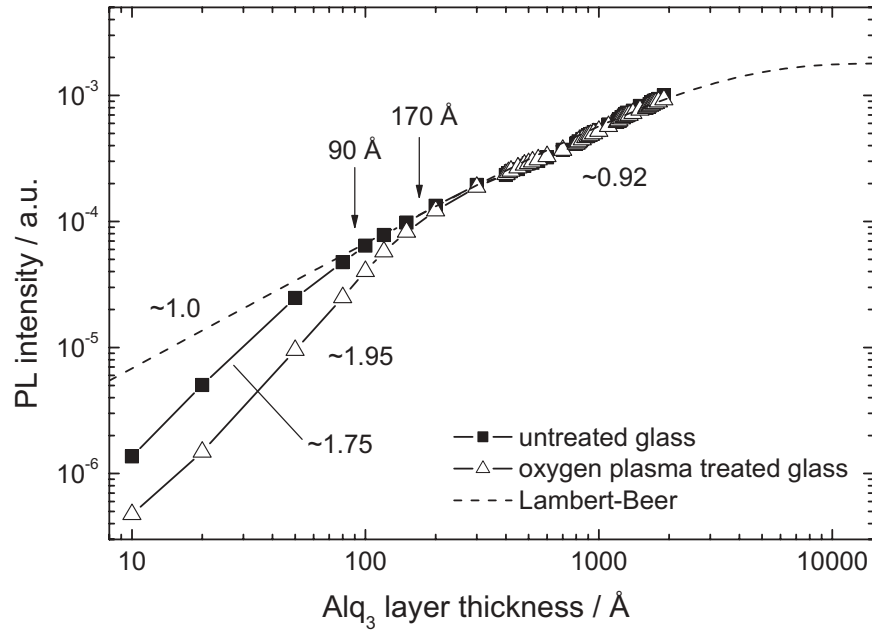


Figure 6.8: PL intensity derived via Lambert-Beer's law compared with experimental values on differently treated glass substrates. At thicknesses below 200 Å the PL intensities on both substrates deviate from the predicted intensities.

intensity $I_{PL\infty}$. However, since the sample thicknesses in this experiments are smaller than 2000 Å this saturation is not observed. Equation (6.3) depends only on two parameters, i.e. the absorption coefficient α and the intensity $I_{PL\infty}$. Since α is determined experimentally, the value of $I_{PL\infty}$ can be unambiguously determined by fitting Equation (6.3) to the experimental data in Figure 6.8. An intensity of $I_{PL\infty} = 1.8 \times 10^{-3}$ (in arbitrary units) can be extracted, which is proportional to the unknown excitation intensity I_0 . This value of $I_{PL\infty}$ will be used below for the experiments on ITO and Al substrates. For low thicknesses, Equation (6.3) shows a linear increase with slope 1.0 in double logarithmic representation (Fig. 6.8). In the range of 200 to 2000 Å the experimental data for both substrates agree very well with the predictions of this simple model. However, below 200 Å both data sets deviate and show a steeper decay in PL intensity, pointing to the influence of exciton quenching at the surface. Whereas the samples of the untreated substrate exhibit a slope of ~ 1.75 below thicknesses of 90 Å, the samples on the oxygen-plasma-treated substrate show a slope of ~ 1.95 below 170 Å. Since the same Alq₃ is used for both sample series these results hint at the influence

of the different substrate treatments on the quenching probability. Oxygen is known to be an efficient luminescence quencher [Birks 1970], therefore, the more pronounced decay in the latter sample series suggests that adsorbed oxygen at the substrate surface acts as a more efficient exciton sink.

In this simple description based on Lambert–Beer’s law (Eq. (6.3)) quenching is not included. Therefore, the experimental trend for Alq₃ layer thicknesses below 200 Å cannot be reproduced. In the following, an improved model will be presented that explicitly takes exciton diffusion and quenching at the interfaces into account.

6.1.3 Exciton Diffusion Model with Quenching at Surfaces

As mentioned above, an improved model has to take into account the observed reduction in photoluminescent efficiency in thin layers. After excitons have been generated in the organic layer, they can diffuse within their lifetime and can be quenched with a certain probability when they reach the surface. Since the samples are excited over a large area (7×7 mm²) and the PL intensity is detected perpendicular to the substrate, the mathematical description is reduced to only one dimension. The one-dimensional stationary diffusion equation for excitons can be written as

$$\frac{\partial S(x)}{\partial t} = g(x) + D \cdot \frac{\partial^2 S(x)}{\partial x^2} - \frac{S(x)}{\tau} = 0, \quad (6.4)$$

The first term $g(x)$ is the local generation rate of excitons, the second term describes exciton diffusion with a characteristic diffusion coefficient D , and the last term considers the decrease of excitons density because of their finite lifetime τ . The local generation rate $g(x)$ due to absorption of the exciting light is derived from Equation (6.2) and is written

$$g(x) = \frac{\partial I_{\text{abs}}(x)}{\partial x} = \alpha I_0 \cdot e^{-\alpha x}. \quad (6.5)$$

Equation (6.5) is valid for non-reflecting substrates. Figure 6.9 gives a schematic illustration of the local exciton generation rate $g(x)$ in a sample of thickness d for non-reflecting and reflecting substrates. Having a reflecting substrate, the incident excitation beam is reflected and passes the sample a second time and thereby increasing the local generation rate of excitons which is then

$$g(x) = \frac{\partial I_{\text{abs}}(x)}{\partial x} = \alpha I_0 \cdot e^{-\alpha x} + \alpha R I_0 e^{-\alpha d} \cdot e^{\alpha(x-d)}, \quad (6.6)$$

where R is the reflection coefficient of the substrate and d the thickness of the sample.

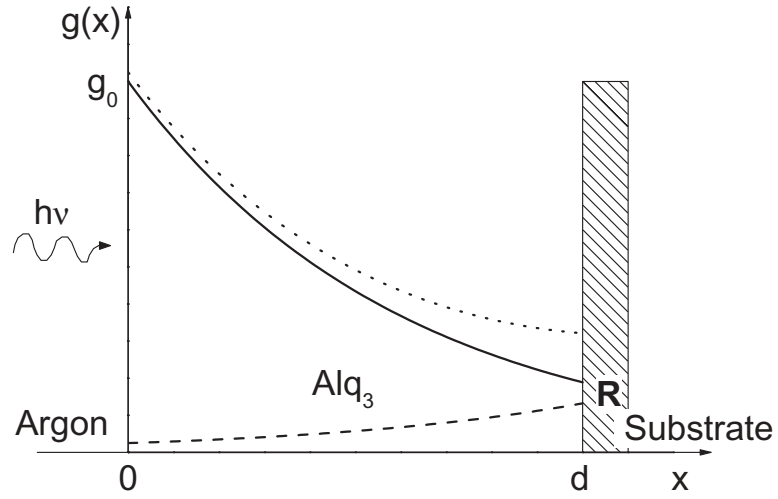


Figure 6.9: Schematic of the local exciton generation rate $g(x)$ in an Alq_3 film of thickness d . Non-reflecting substrate (solid line) and reflecting substrate with a reflection coefficient R (dotted line = solid + dashed line).

The boundary conditions for Equation (6.4) are given by the two interfaces, i.e. Argon/ Alq_3 and Alq_3 /substrate, respectively. It is assumed that the excitons are annihilated by surface-determined processes at a rate q proportional to the concentration of the excitons at these surfaces. This is basically Fick's law, which describes the relation between the concentration of a species and the flow due to diffusion.

$$q_{0,d} \cdot S(x) \Big|_{x=0,d} = -D \cdot \frac{\partial S(x)}{\partial x} \Big|_{x=0,d} \quad (6.7)$$

The parameters q_0 and q_d describe the quenching factor at the Argon/ Alq_3 interface ($x = 0$) and the Alq_3 /substrate interface ($x = d$), respectively. These quenching parameters q_0 and q_d can range between $q = 0$ for no quenching and $q \rightarrow \infty$ for complete quenching at the respective interface. Equation (6.4) can be solved analytically with the generation term $g(x)$ Eq. (6.6) and the boundary conditions Eq. (6.7). Since the full expression is rather long it is not listed here.

It is now helpful to illustrate the solution of the exciton distribution with two examples. Figure 6.10 shows the calculated exciton distribution in a 2000 Å and a 200 Å thick sample for different surface quenching rates on a non-reflecting substrate. For these plots the experimentally determined absorption coefficient for Alq_3 at 355 nm $\alpha = 3.8 \times 10^{-4} \text{ cm}^{-1}$ is used. Furthermore, an exciton diffusion length $L = \sqrt{D\tau}$ for Alq_3 of about 200 Å and an effective

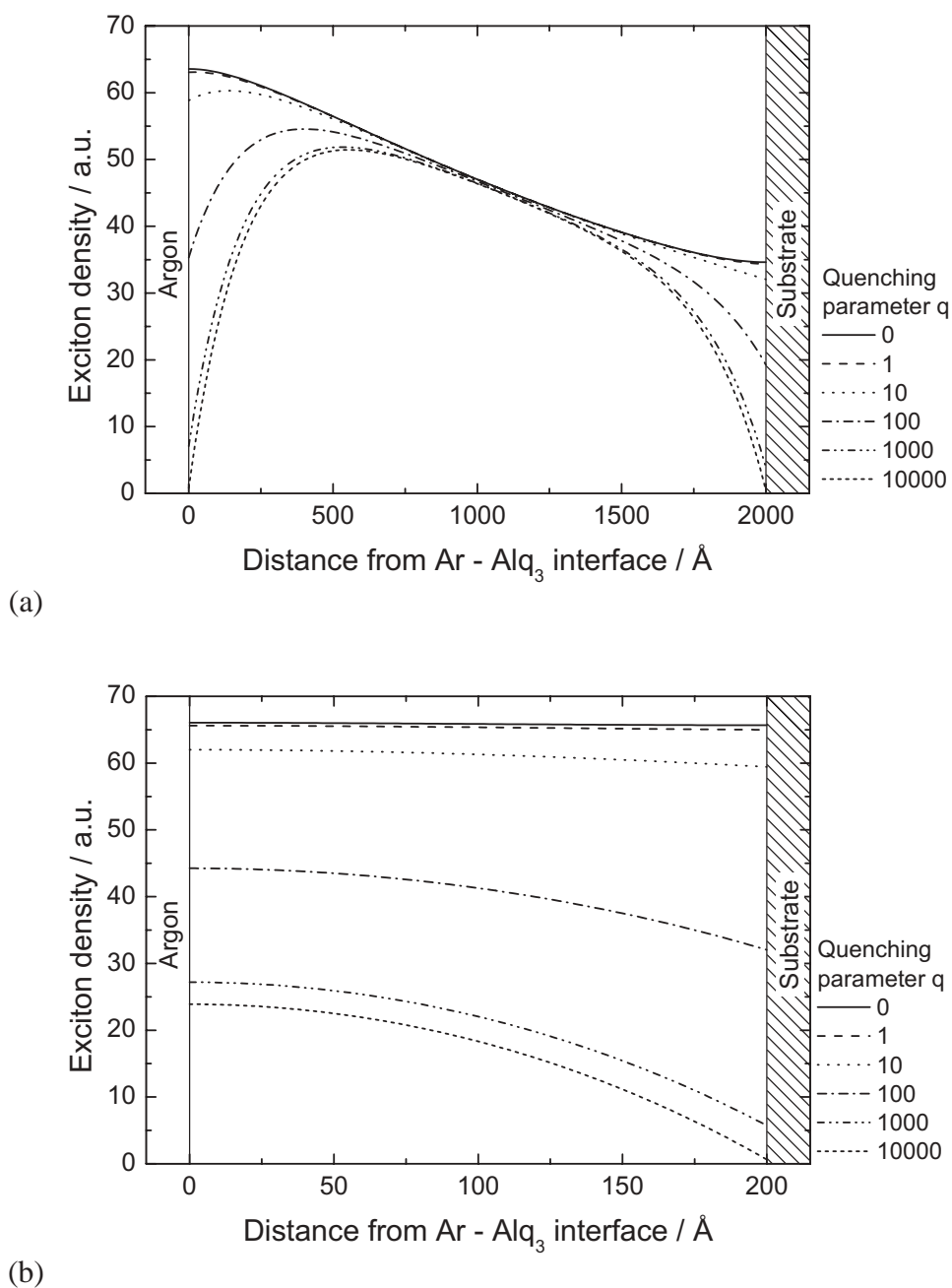


Figure 6.10: Simulated exciton density distribution in an Alq₃ film according to the solution of Equation (6.4). The quenching parameters $q = 0$ correspond to no quenching and $q \rightarrow \infty$ to complete quenching at the surface. (a) Layer thickness 2000 Å. Identical quenching rates at both interfaces are assumed. (b) A layer of 200 Å with quenching only at the substrate interface.

lifetime of $\tau = 16$ ns is assumed which has been reported by [Tang et al. 1989]. Figure 6.10a depicts the calculated exciton distribution in a 2000 Å thick film where equal quenching at both interfaces $q_0 = q_d$ is assumed. For no quenching ($q = 0$) the exciton profile follows the profile of the excitation light and is slightly redistributed by diffusion in such a way that there is no flow across the interfaces, i.e. $\partial S(x)/\partial x|_{x=0,d} = 0$. Large quenching factors ($q > 10^4$) correspond to almost complete quenching and hence the exciton density drops to nearly zero at the interfaces. Figure 6.10b illustrates the case of a thin sample (200 Å) where quenching is assumed only at the substrate interface. It can be clearly seen that the exciton annihilation at the substrate feeds back into the layer and even at the Argon/Alq₃ interface, the exciton density is drastically reduced. Intrinsic quenching at the argon interface is assumed to be less than on the substrate side and will be neglected in the following.

In order to describe the experimentally detected PL signal, the total number of created excitons in the layer is taken as proportional to the actual measured PL intensity. This presumes a constant conversion factor of excitons into photons, i.e. constant quantum efficiency of any Alq₃ molecule independent of the position in the layer. Hence, the detected PL intensity is written as being proportional to the integral of the exciton density $S(x)$:

$$I_{\text{PL}} \propto \int_0^d S(x) dx. \quad (6.8)$$

Equation (6.8) can also be solved analytical but the solution in full length is not given here. Figure 6.11 shows the integrated PL intensity as calculated by Equation (6.8). For this calculation the parameters of $D = L^2/\tau = 2.5 \times 10^{-4}$ cm²/s, $\alpha = 3.8 \times 10^4$ cm⁻¹, $\tau = 16$ ns and $I_{\text{PL}\infty} = 1.8 \times 10^{-3}$ (a.u.) are used. In this case, it is assumed for simplicity that no quenching occurs at the Argon/Alq₃ interface, i.e. $q_0 = 0$. In absence of quenching at the substrate interface, i.e. $q_d = 0$, the calculated PL intensity reproduces the results from the simple model using absorption and re-emission via Lambert-Beer (see Sec. 6.1.2). This is plausible since with no quenching the resulting overall intensity is basically unchanged compared to the Lambert-Beer description (Eq. (6.3)) because the excitons are just redistributed by diffusion. With increasing quenching factor q_d at the substrate interface, the slope gradually increases from ~ 1.0 to almost ~ 3.0 in the case of complete quenching at the substrate surface ($q_d \rightarrow \infty$). The convergence of the different curves in Figure 6.11 shows that under the above assumptions, the influence of surface quenching becomes negligible for thicknesses above ~ 1000 Å.

The quenching parameter q can be transferred into a surface quenching probability P by

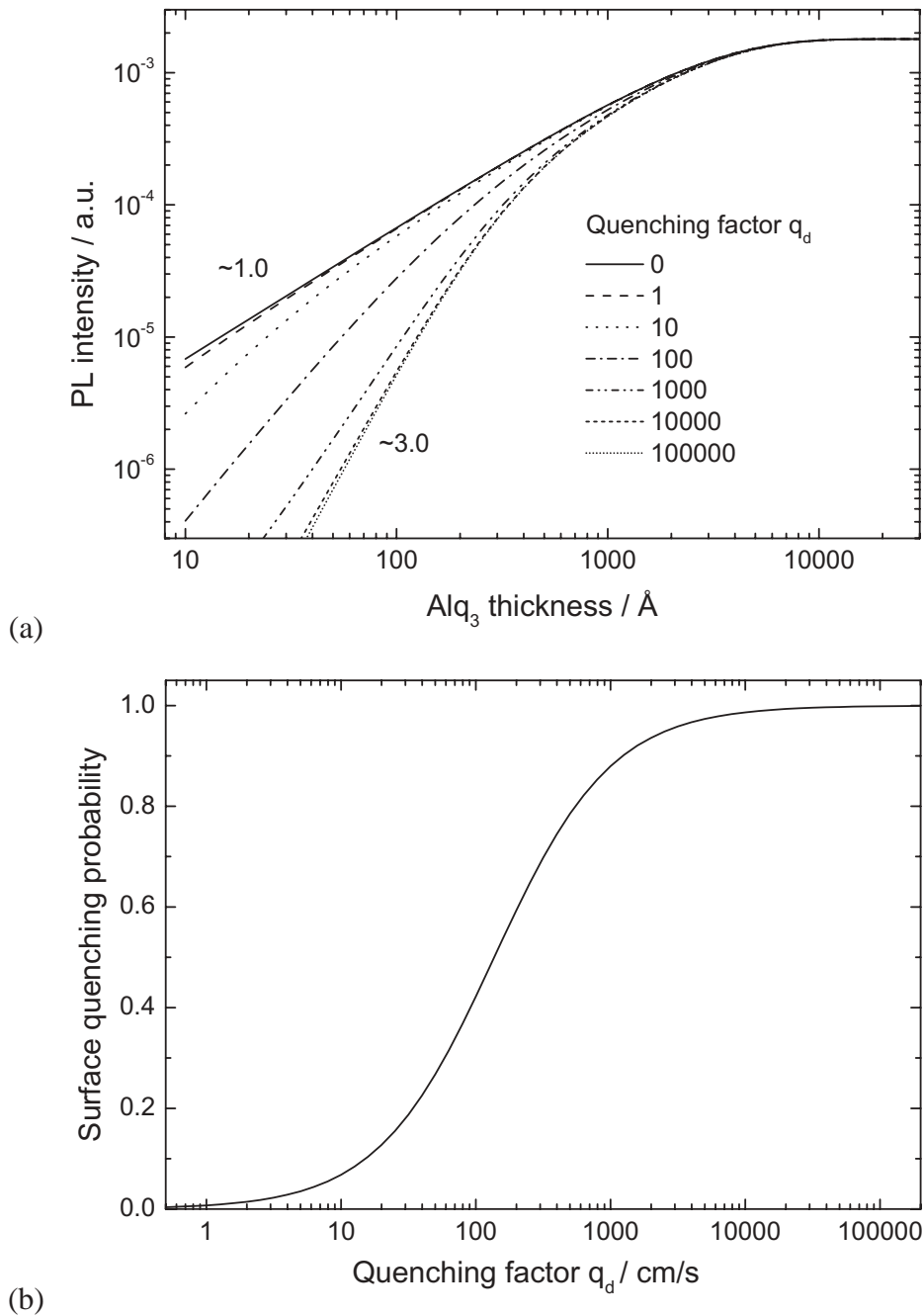


Figure 6.11: (a) Simulated PL intensity according to the solution of Equation (6.8) with different quenching factors: $q_d = 0$ no quenching and $q_d \rightarrow \infty$ complete quenching. Quenching is assumed to occur only at the substrate interface. (b) Relationship between the quenching factor q_d and the percentage P of excitons quenched at the surface. A diffusion constant of $D = 3.0 \times 10^{-4} \text{ cm}^2/\text{s}$ and a life time of $\tau = 16 \text{ ns}$ is assumed.

calculating the ratio of the exciton densities at the surface with and without quenching, respectively. The probability for an exciton being quenched at the surface is therefore

$$P = 1 - \frac{S(d)|_{q=q_d}}{S(d)|_{q=0}}. \quad (6.9)$$

Figure 6.11b shows the relationship of this quenching probability P and the quenching rate q . This can be used in order to quantify different substrates materials and differently treated surfaces by their quenching probabilities. For the calculation a lifetime of $\tau = 16$ ns has been assumed. Here, the value of $D = 3.0 \times 10^{-4}$ cm²/s for the diffusion constant is used, which is extracted from the experimental data as will be shown in the following.

Comparison of Experiment and Model

The model described in the previous section now allows a comparison with experimental data in order to extract material intrinsic and substrate specific parameters. Figure 6.12 depicts the experimental thickness-dependent PL intensity data on top of Al compared to the simulated PL intensities. In the case of a reflecting substrate, the emission from the layer directed into the second half-space is reflected by this mirror into the detector. Thus, the intensity is increased by a factor of $(1 + R)$ compared to the case of a non-reflecting substrate. For Al with a reflection coefficient of $R = 0.92$ the upper limit for the PL intensity in this configuration is almost twice the intensity on glass. Self-absorption in Alq₃ would reduce the maximum detectable intensity but it is not considered here.

At low thicknesses the experimental data is represented by a linear relationship with a slope of 3.0. According to the model described above, the slope of the PL intensity can only be close to 3.0 if complete quenching at the substrate surface is assumed, which is apparently the case for the experimental data on Al. Furthermore, as illustrated in Figure 6.12 this slope of 3 is independent of the diffusion constant D of the organic material. Therefore, a fit of the experimental data on Al can be used to extract the diffusion constant D of excitons in the material. The best fit of the experimental data yields a diffusion constant of $D = 3.0 \times 10^{-4}$ cm²/s. It has to be mentioned that at higher thicknesses (>500 Å) the PL intensities on Al show a rather different functional behavior compared to the simulation and the Alq₃ staircases on glass or ITO. Owing to the highly reflecting mirror a weak microcavity is formed, which modifies the emission spectrum and the intensity via interference effects. The observed oscillation (Fig. 6.12) has maxima at 700 and 1500 Å Alq₃ thickness, which correspond approximately to the length

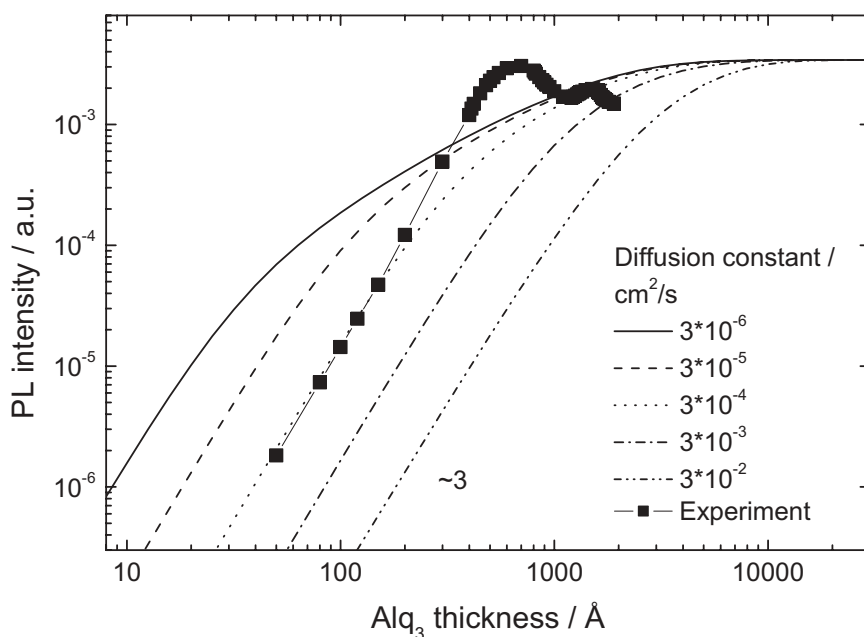


Figure 6.12: Simulated thickness-dependent PL intensity of Alq₃ on Al. Almost complete quenching ($q_d = 10^5$) at the Al interface is assumed. It is important to note that the slope of ~ 3 at low thicknesses is independent of the diffusion constant D . The experimental data at low thicknesses is represented best for $D = 3.0 \times 10^{-4} \text{ cm}^2/\text{s}$ assuming a lifetime of $\tau = 16 \text{ ns}$.

of constructive interference of the Alq₃ emission. An estimation with the peak emission wavelength $\lambda_{\text{Alq}} = 530$ nm and the refractive index of $n_{\text{Alq}} = 1.73$ leads to $\lambda_{\text{Alq}}/4 = 760$ Å and $\lambda_{\text{Alq}}/2 = 1530$ Å, which agree well with the observed maximum positions. It is obvious that in this model optical interference effects are not included. In order to describe the oscillations in the case of Al, optical interference effects have to be included in the description which, however, is beyond the scope of this work.

Since the extracted diffusion constant D is material-parameter-specific for Alq₃, it should be possible to fit all measurements on glass, ITO and Al with the same D and τ . Figure 6.13 shows the comparison of the model to the experimental data on glass and ITO. Assuming the above extracted value for the diffusion constant $D = 3.0 \times 10^{-4}$ cm²/s and the lifetime $\tau = 16$ ns the best fit for the experimental curves is obtained for $q_d = 25$ and 100 cm/s for the untreated and the oxygen-plasma-treated glass substrate, respectively. According to Figure 6.11b, these q -values correspond to quenching probabilities of 15% and 40% for the untreated and the treated substrate, respectively. The best fit for the Alq₃ samples on ITO is obtained for $q = 200$ cm/s, which corresponds to a surface quenching probability of 60% which is significantly higher than the value for the oxygen-plasma-treated glass.

Figure 6.14 shows a more detailed view of Figure 6.12. Here, the PL intensities are plotted versus layer thickness using the exciton diffusion length as parameter. This plot is used in order to extract the exciton diffusion length. The experimental data is compared with various lines in the graph corresponding to different exciton diffusion lengths $L = \sqrt{D\tau}$ in the model assuming a lifetime of $\tau = 16$ ns. Best agreement to the experimental data is achieved for an exciton diffusion length of 220 Å in Alq₃. This plot also illustrates that this method could clearly distinguish between two materials having diffusion lengths of 200 and 250 Å. The combinatorial setup would easily allow a side-by-side comparison of two different materials.

It is important to note that the exciton distribution in an electrically excited OLED is similar to the case discussed above (see Fig. 6.10). As mentioned in Section 5, the exciton generation in CuPc/NPB/Alq₃-based OLED structures is located in Alq₃ close to the NPB layer. Assuming a delta-like exciton generation at this interface, diffusion will lead to an exponential decay of the exciton distribution. This corresponds almost exactly to the exponential decaying exciton generation distribution in the PL experiment by absorbed light. Experiments of electrically excited samples extracting the exciton diffusion length will be discussed in the following section. There, the special case of sensitized fluorescence is described.

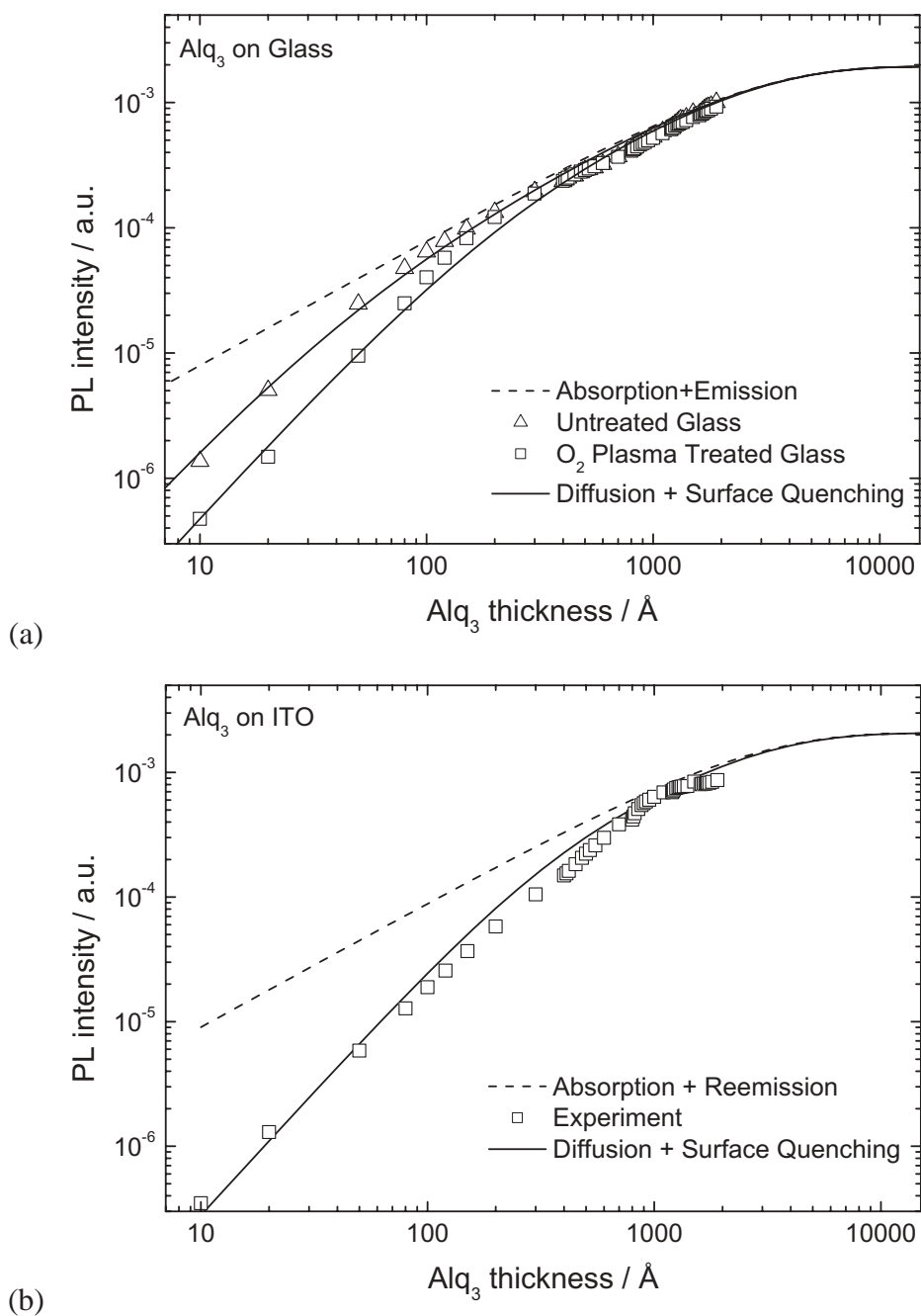


Figure 6.13: Comparison of the experimental PL intensity according to the intensity derived from the diffusion model. (a) Alq₃ on glass. (b) Alq₃ on ITO. A surface quenching probability of excitons of 15%, 40% and 60% can be extracted for untreated glass, oxygen-treated glass and ITO, respectively.

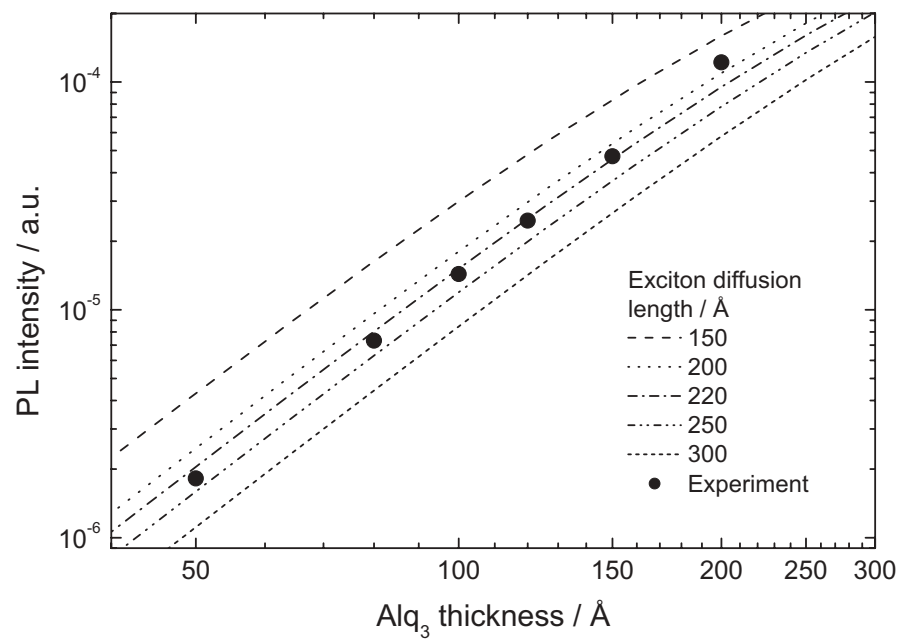


Figure 6.14: Extraction of the exciton diffusion length L in Alq₃ by comparing PL intensity data to the diffusion model assuming a lifetime $\tau = 16$ ns. Several diffusion lengths are compared and best agreement is achieved for an exciton diffusion length of $L = 220$ Å in Alq₃.

6.1.4 Summary: Diffusion of Excitons and Quenching at Interfaces

Thickness-dependent PL measurements demonstrate the effect of luminescence quenching at low layer thickness on glass, ITO and Al. A simple model based Lambert–Beer’s law describes via absorption and emission the PL intensities on glass in a range of 200 to 2000 Å. A clear deviation from this linear increase at thicknesses below 200 Å is observed depending on the substrate pretreatment. The samples on the oxygen-plasma-treated glass substrate show a deviation below 170 Å, whereas the untreated substrate deviates only below 90 Å. An improved model explicitly accounts for exciton diffusion and quenching at the surface with a certain probability depending on the substrate treatment. The loss mechanism at the surface feeds back to the actual exciton density and distribution in the thin layer and thus determines the measured PL intensity. The more pronounced quenching in the case of the oxygen-plasma-treated glass substrate is associated with a higher effective quenching rate caused by adsorbed oxygen on the glass surface. ITO samples exhibit more pronounced quenching than the samples on glass. With this model, the substrates can be quantified by their surface quenching probability and are determined to be 15%, 40% and 60% for untreated glass, oxygen-plasma-treated glass and ITO substrates, respectively. The PL intensity of Alq₃ on Al thickness series at small thicknesses can be described with a d^n behavior, where $n \approx 3$. At thicknesses greater than 500 Å oscillations are observed and their maxima are located at 700 and 1500 Å, which correspond to $\lambda/4$ and $\lambda/2$ of the peak emission wavelength of Alq₃. By comparing the experimental data on Alq₃ with the model, an exciton diffusion constant of $D = 3.0 \times 10^{-4}$ cm²/s and an exciton diffusion length of $L = 220$ Å can be determined. The described method together with the combinatorial setup easily allows the determination and comparison of the exciton diffusion lengths of different materials.

6.2 Delta-Doped Devices

In the previous section, we examined how quenching at interfaces is an important issue for OLED structures. Furthermore, the exciton diffusion length in Alq₃ has been extracted via thickness-dependent PL measurements. In this section, a way to extract the exciton diffusion length by means of EL experiments will be discussed. Moreover, it is essential to know the location and distribution of the emission zone in order to understand and predict the operating mechanisms of OLEDs. To a first approximation, the knowledge of the energy levels and the charge carrier mobilities of the involved materials allow the location of emission zone in the device to be estimated. However, accurate data of the alignment of energy levels and electron and hole mobilities are often not readily available. Furthermore, the preparation conditions might also influence the above-mentioned parameters. First information about the location of the emission zone in a multilayer structure, e.g. in which material the emission zone is located, can be determined by comparing the EL spectra to the PL spectra of the materials used. However, the determination of the exact location and distribution of the emission zone and its voltage dependence calls for more detailed experiments.

A precise and elegant experiment to study recombination and emission in OLEDs or thin fluorescent films is the method of sensitized luminescence [Simpson 1956; Tang et al. 1989]. A thin doped layer consisting of a highly luminescent dye is introduced into the structure. This doping layer is chosen in such a way that it emits with a different emission spectrum which can be readily distinguished from the host emission. The spatial origin of the dopant emission is exactly determined by the position of this layer in the device. This approach is especially well suited for small molecule devices since multilayer structures with arbitrary numbers and sequences of layers can easily be fabricated by vacuum sublimation. Tang et al. adapted this technique for EL devices by inserting a thin layer of a doped region into organic light-emitting diodes in order to estimate the exciton diffusion length in Alq₃ [Tang et al. 1989]. Other authors have used the same technique [Adachi et al. 1991; Mori et al. 1995; Mori et al. 1996; Aminaka et al. 1996; Yamashita et al. 1997; Mori and Mizutani 1997; Lam et al. 2000]. However, the limited number of samples in these publications makes the extraction of device and material parameters difficult and vague. The combinatorial setup described in Section 3 allows the fabrication of a series of ten or more devices in a reliable way for different host/guest systems. In the following section, this technique will be used to investigate an Alq₃ system doped with DCJTb.

6.2.1 Exciton Sensing in Alq₃:DCJTB System

Experimental

In order to map the profile of the emission zone a thin layer (25 Å) of Alq₃:DCJTB ($\approx 1\%$) is inserted into the Alq₃ film at different distances from the NPB/Alq₃ interface as described in Section 3.3.2. Figure 6.15 sketches the cross section of the device series and the schematic energy level diagram where the position x of the dopant layer is varied from 0 to 400 Å. The complete device structure is listed in the following table:

| Material | Al/Ni | CuPc | NPB | Alq ₃ | Alq ₃ :DCJTB | Alq ₃ | Ca |
|---------------|--------|------|-----|------------------|-------------------------|------------------|-----|
| Thickness / Å | 700/50 | 150 | 500 | x | 25 | $475 - x$ | 200 |

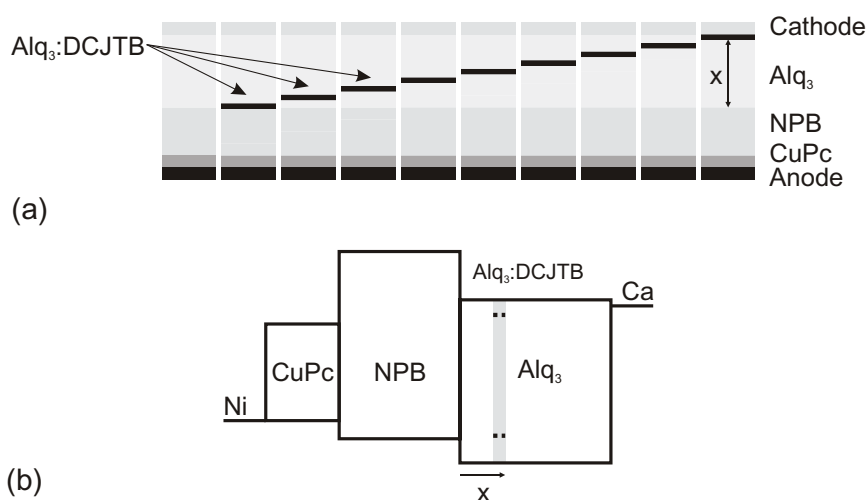


Figure 6.15: Combinatorial device series having a doped sensing layer at different positions. (a) Schematic device cross section. (b) Schematic energy level diagram. The thin (25 Å) Alq₃:DCJTB doped layer is shifted from the NPB/Alq₃ interface towards the cathode.

Results

Figure 6.16 shows the I - V EL curves of nine devices having the sensing layer at various positions x in the Alq_3 layer. All devices show very low reverse currents and excellent rectification ratios ($>10^6$ at ± 5 V). The I - V curves exhibit no significant differences up to a voltage of 7 V, which corresponds to a current density of about 20 mA/cm^2 . As a general trend at higher voltages, the current density is slightly decreased with increasing distance of the sensing layer to the NPB/Alq_3 interface. The photocurrent curves (in Fig. 6.16) show a larger spreading than the I - V curves since the emission spectra depend on the position of the dopant layer as it will be presented in the following.

Figure 6.17 shows the normalized and the absolute EL spectra as a function of the position of the DCJTB in the Alq_3 layer at a current density of 20 mA/cm^2 .

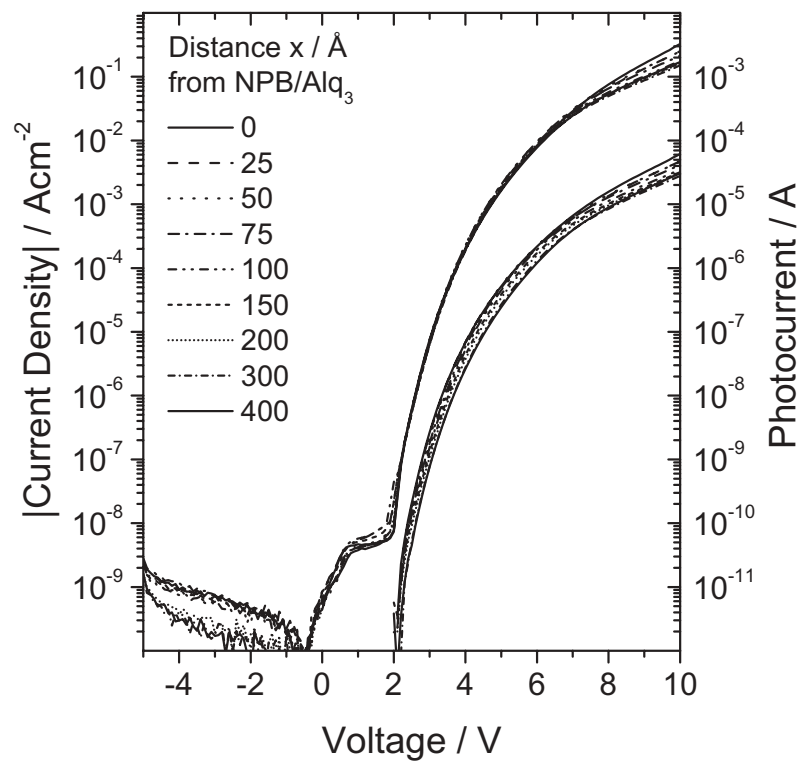


Figure 6.16: I - V EL characteristics $\text{CuPc}/\text{NPB}/\text{Alq}_3$ OLEDs having a delta-doped sensing layer at various distances x from the NPB/Alq_3 interface. The delta doping does not influence the I - V characteristics up to 20 mA/cm^2 . The EL signal exhibit larger variations due to shifts in the emission spectrum.

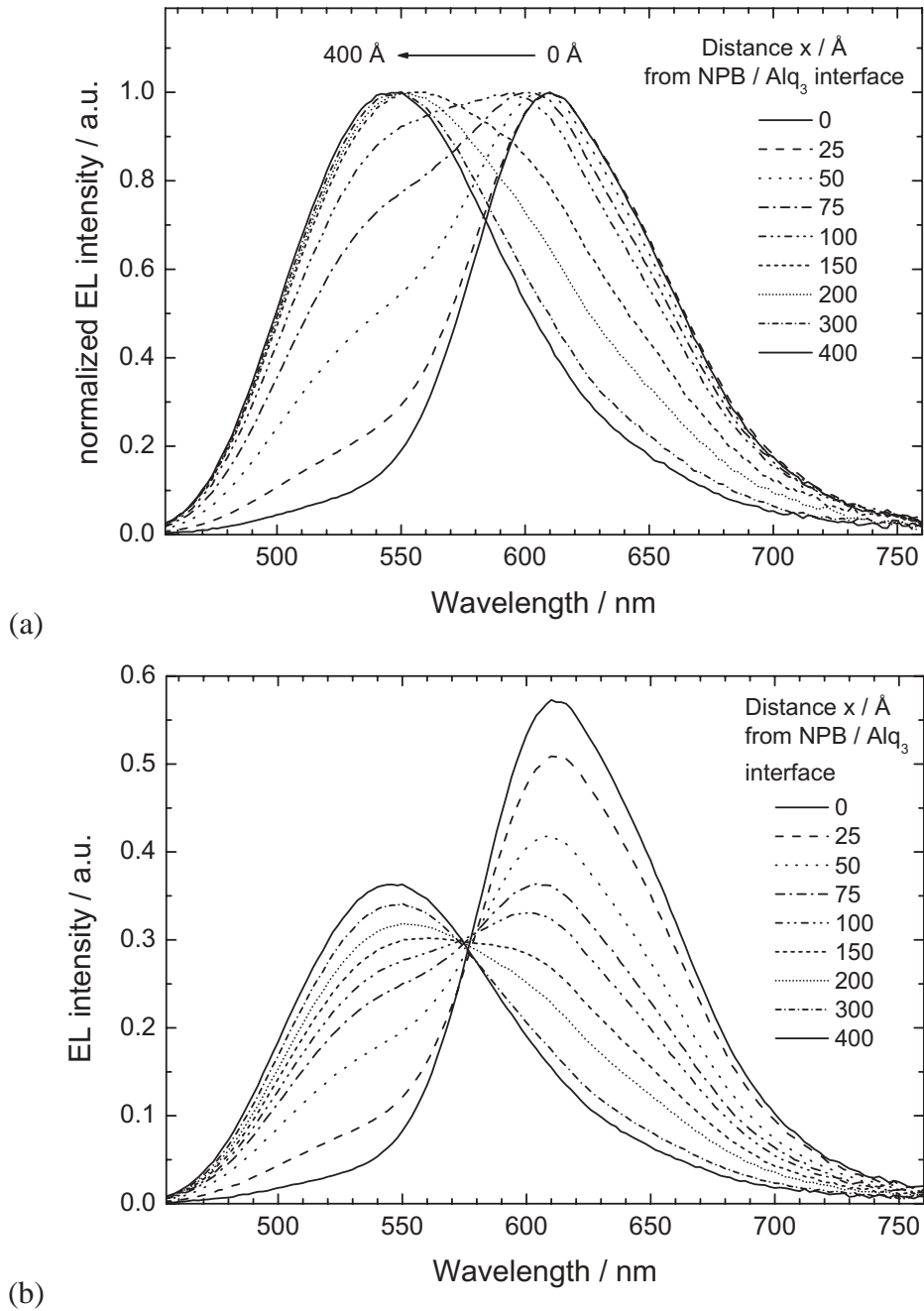


Figure 6.17: EL spectra of devices with delta doping ($\text{Alq}_3:\text{DCJTb}$) at different distances from NPB. (a) Normalized spectra (b) Absolute intensity. The contribution of DCJTb emission decreases with increasing distance x of the doping layer from the NPB/ Alq_3 interface.

In Figure 6.17a a large green-shift of the spectrum is observed with increasing distance x of the doping layer from the NPB/Alq₃ interface. The device with the doping layer next to the NPB/Alq₃ interface ($x = 0$ Å) exhibits the most red-shifted spectrum with an emission peak at 610 nm and a FWHM of 90 nm. This spectrum features a shoulder around 540 nm indicating that some Alq₃ emission is still present. With increasing distance of the dopant layer from the NPB/Alq₃ interface the relative intensity of the dopant emission is reduced and the spectra shift towards Alq₃ emission. The spectra of the device with $x = 400$ Å resembles the spectrum of pure Alq₃ emission (peak at 545 nm in this device configuration). Figure 6.17b shows that the absolute EL intensity of the device with highest DCJTB emission is a factor of ~ 1.5 higher than the intensity of the Alq₃ spectrum. Further measurements reveal that all spectra show a more or less pronounced dependence on current density. In general, Alq₃ emission increases with increasing current density. Figure 6.18 illustrates the current dependence of the spectrum of the device with $x = 100$ Å. By increasing the current density from 0.01 to 100 mA/cm² the emission peak wavelength is shifted from 618 to 594 nm. It is clearly visible that the shoulder

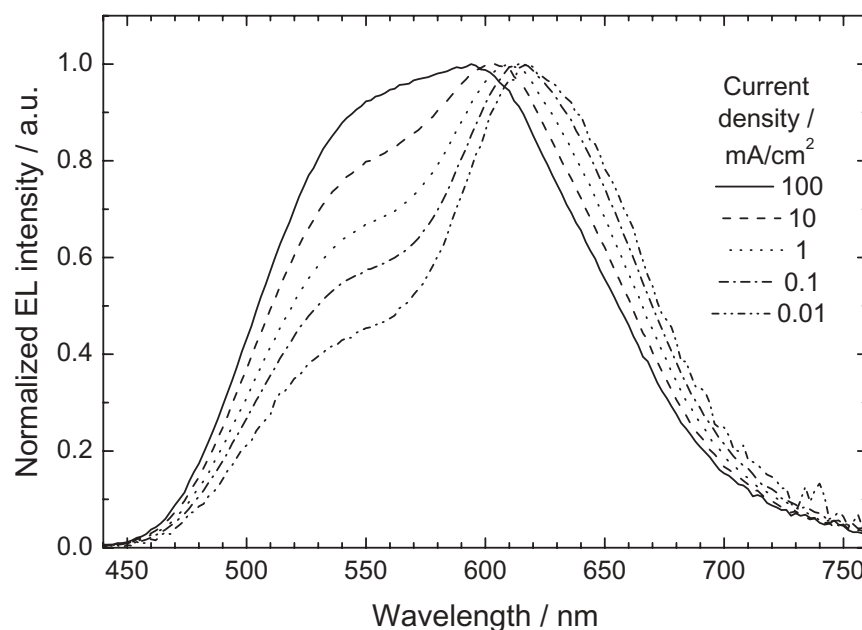


Figure 6.18: Current density dependence of EL spectra in a delta-doped CuPc/NPB/Alq₃ OLED. The distance of the DCJTB doping layer is 100 Å from the NPB/Alq₃ interface. Alq₃ emission increases with increasing current density.

around 540 nm is enhanced, which results in an increase in spectral width from 108 to 150 nm FWHM.

Discussion

In order to explain the spectral shifts, the underlying processes which lead to these observations will be discussed. In general, the recombination zone is determined by the spatial overlap of the electron and hole density distributions in the layer. The local recombination rate $r(x)$ is proportional to the local density of electrons and holes, i.e. $r(x) \propto n(x) \cdot p(x)$. Owing to the large difference in electron and hole mobilities in Alq₃ ($\mu_e/\mu_h \gg 100$) the recombination zone will be confined to a narrow region close to the NPB interface. Numerical simulations also suggest that the generation of excitons is actually confined to a delta-like region close to the hole transporter interface [Ruhstaller et al. 2001]. Since excitons can diffuse in the organic layers within their lifetime, the emission zone will be different from the recombination zone. Assuming a delta-like exciton generation and subsequent diffusion, the excitons diffuse towards the cathode since the larger gap material (NPB) acts as an exciton blocker. As shown in Section 2.3.2 the steady-state distribution of excitons $S(x)$ is then given as an exponential decay

$$S(x) = S_0 \cdot e^{-\frac{x}{L}}, \quad (6.10)$$

where S_0 is the exciton concentration at the NPB/Alq₃ interface, x the distance from this interface and L the characteristic exciton diffusion length in Alq₃. Figure 6.19a sketches the exciton density distribution in the case of an undoped Alq₃ layer. Figure 6.19b depicts the situation when a thin dopant layer is introduced in a distance d from the NPB/Alq₃ interface. The fact that a 25 Å thick layer of Alq₃:DCJTB close to the NPB layer suppresses emission from Alq₃ almost completely (see Fig. 6.17b) leads to the approximation that all excitons reaching this sensing layer decay on DCJTB molecules. In other words, there will be no emission from Alq₃ originating from $x > d$ because all excitons passing $x = d$ in the undoped case now decay on DCJTB. Consequently, the spectral emission of such devices consists of two components, namely the Alq₃ emission originating from $x < d$ and the DCJTB emission from the thin sensing layer. The experimental spectra are a superposition of Alq₃ and DCJTB emission and can be easily deconvoluted because of the large separation of DCJTB ($\lambda_{\max} = 610$ nm) and Alq₃ emission ($\lambda_{\max} \approx 540$ nm). The deconvolution is performed according to the procedure described in the Appendix (see page 196) using pure Alq₃ and DCJTB emission spectra.

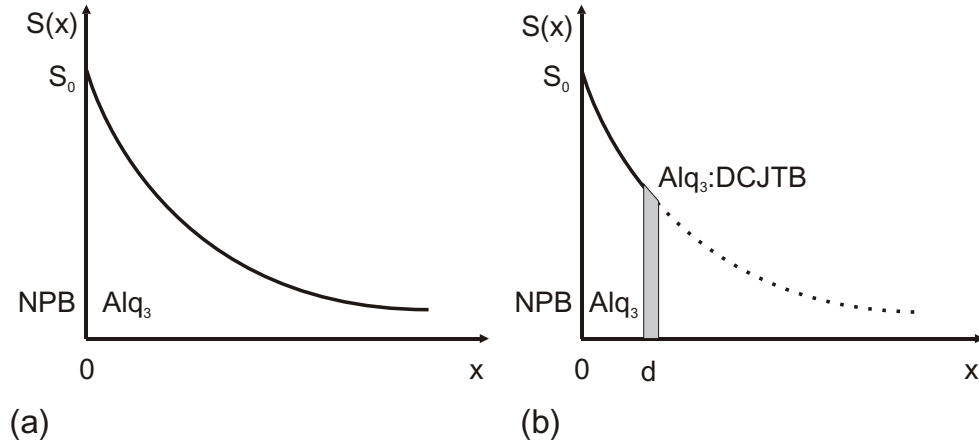


Figure 6.19: Steady-state exciton distribution assuming delta-like exciton generation at the NPB/Alq₃ interface. (a) Undoped case, (b) delta-doped case where all excitons decay in the doped layer. No emission originates from $x > d$.

Figure 6.20 shows the relative spectral contribution of the thin sensing layer for all devices at different current densities ranging from 0.01 to 100 mA/cm². First of all, it can clearly be seen that the spectral contribution of the DCJTB dopant layer steadily decreases with increasing distance from the NPB/Alq₃ interface. If the sensing layer is placed at the NPB/Alq₃ interface, the relative DCJTB emission is greater than 90% for all current densities. The effect of the current density on the EL spectrum is most pronounced for the device which has the dopant layer at $x = 150 \text{ \AA}$. At a current density of 0.01 mA/cm² the DCJTB contribution is as high as 60%, whereas it decreases to 30% at a current density of 100 mA/cm². The device having the sensing layer at $x = 400 \text{ \AA}$ exhibits less than 4% DCJTB emission, which is nearly independent of the current density.

Now, several assumptions will be made in order to describe the above observations. Under constant current drive, the exciton density S_0 at the NPB/Alq₃ interface is assumed to be constant. Furthermore, the EL intensity generated at the location x is proportional to the exciton density $S(x)$. Hence, the experimentally detected EL signal is proportional to the integral over the exciton density:

$$I(x) \propto \int_0^{\infty} S(x) dx = \int_0^{\infty} S_0 \cdot e^{-\frac{x}{L}} dx \quad (6.11)$$

As depicted in Figure 6.19b, excitons located at $x < d$ contribute to Alq₃ emission, whereas all excitons $x > d$ contribute to DCJTB emission. The contribution of excitons to Alq₃ and

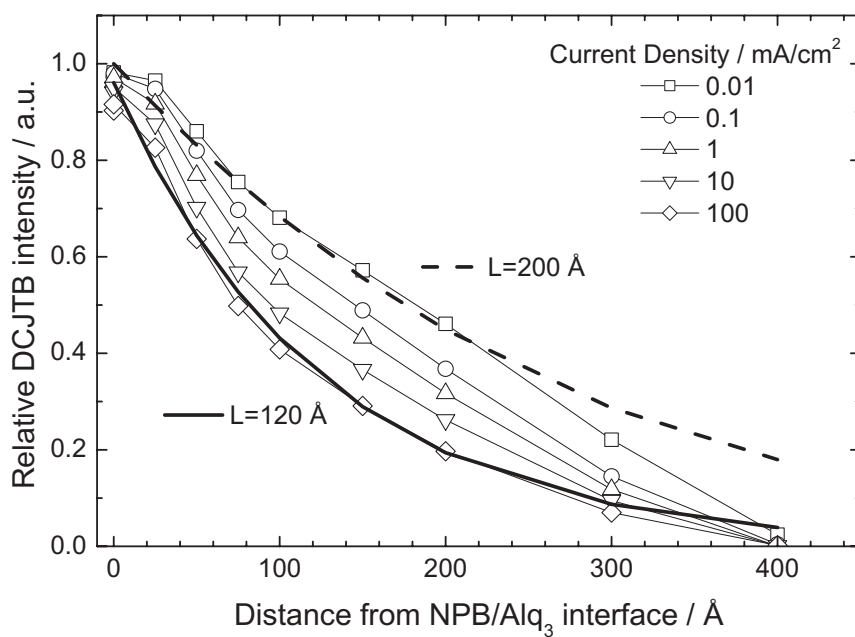


Figure 6.20: *CuPc/NPB/Alq₃ OLEDs with DCJTB sensing layer at various positions. The relative contribution of DCJTB emission is measured as a function of position and current density.*

DCJTB emission can then be calculated as a function of d :

$$S_{\text{Alq}} \propto \int_0^d S_0 \cdot e^{-\frac{x}{L}} dx \quad \text{and} \quad S_{\text{DCJTB}} \propto \int_d^\infty S_0 \cdot e^{-\frac{x}{L}} dx \quad (6.12)$$

The total spectral intensity can therefore be written as

$$I_{\text{total}}(\lambda) \sim (1 - e^{-\frac{d}{L}}) \cdot I_{\text{Alq}}(\lambda) + \eta \cdot e^{-\frac{d}{L}} \cdot I_{\text{DCJTB}}(\lambda), \quad (6.13)$$

where $I_{\text{Alq}}(\lambda)$ and $I_{\text{DCJTB}}(\lambda)$ are the normalized spectra of Alq₃ and DCJTB, respectively. The constant of proportionality η takes the higher EL efficiency of DCJTB into account. This scaling factor can be obtained from Figure 6.17b comparing the Alq₃ and the DCJTB spectrum. The peak intensity of the DCJTB spectrum is a factor of 1.5 higher (in W/(sr·m²·nm)) than that of the Alq₃ spectrum. Calculating the emitted photons per time unit results in a scaling factor of $\eta = 1.4$. The experimentally observed ratio of DCJTB emission to Alq₃ emission as a function of distance d (see Fig. 6.20) can be described by

$$r = \frac{\eta \cdot e^{-\frac{d}{L}}}{(1 - e^{-\frac{d}{L}}) + \eta \cdot e^{-\frac{d}{L}}}. \quad (6.14)$$

The best fit for the data at 100 mA/cm² results in an exciton diffusion length of about $L = 120 \text{ \AA}$. This is considerably smaller than the value of 220 Å extracted in Section 6.1 by means of PL measurements. For lower current densities, Equation (6.14) can be less well fitted to the experimental data in Figure 6.20, but a fit to the data at 0.01 mA/cm² results in a larger diffusion length of $L \approx 200 \text{ \AA}$. However, the exciton diffusion length is a pure material parameter and should not depend on the device structure nor on the driving conditions. This suggests reconsidering the initial assumptions and considering other effects. At low voltages, the recombination zone might be extended further into the Alq₃ layer since holes enter the Alq₃ layer first. At higher voltages, the recombination zone is confined closer to the NPB/Alq₃ interface since the electron mobility increases much faster with field than the hole mobility in Alq₃. Another process which should be taken into account is non-radiative energy transfer via Förster transfer. This process would lead to an increase of the extracted diffusion length since the energy of Alq₃ excitons within the Förster radius ($\sim 50\text{-}100 \text{ \AA}$) [Rabek 1996] will also be efficiently transferred to DCJTB. Furthermore, optical cavity effects have to be taken into account, especially when the sensing layer is shifted over larger distances in the device or placed close to a metal mirror. An important difference of this EL experiment to the PL experiment in Section 6.1 is the presence of charge carriers. This can lead to a reduction of EL efficiency

at higher current densities as it has been observed in $\text{Alq}_3\text{:DCJTB}$ structures in Section 4.3.1 (see Figure 4.15, page 90). This reduction of DCJTB emission has been attributed to quenching by cationic species, either DCJTB^+ or Alq_3^+ [Young et al. 2002]. Since quenching at high current densities reduces the relative DCJTB contribution in the above device structures, a meaningful value for the exciton diffusion length should be extracted from the curve with the lowest current density in Figure 6.20. This would lead to an exciton diffusion length of $L \approx 200 \text{ \AA}$ in Alq_3 which is in good agreement with the value obtained via PL measurements in Section 6.1. Further investigations are necessary in order to evaluate the influence of the individual processes mentioned above, which have been neglected so far. These experiments would include, for example, varying the dopant and electrode materials in order to prove that the extracted exciton diffusion length depends solely on the host material Alq_3 .

6.2.2 Summary: Delta Doped Devices

The method of sensitized fluorescence (or delta-doping) is used for the determination of the exciton diffusion length in Alq_3 via EL measurements. Combinatorial device fabrication is utilized to introduce a thin delta-doped layer at various positions in a standard CuPc/NPB/Alq_3 device structure. Assuming a dirac-like exciton generation rate at the NPB/Alq_3 interface and successive diffusion, the spatial exciton distribution is expected to obey an exponential decay determined by the diffusion length. In order to map the emission zone, the relative spectral contribution of the dopant emission is taken as a measure for the local exciton density. However, at higher current densities, the relative dopant emission is considerably reduced which seems to be related to quenching by charged species. Therefore, the results of this method have to be treated with caution. Nevertheless, for the border case of low current density an exciton diffusion constant of $L \approx 200 \text{ \AA}$ can be extracted, which is in agreement with values reported in the literature and the value extracted via PL measurements in Section 6.1.

Chapter 7

Summary

One goal of this work was to lay the experimental foundations for tackling technological and scientific issues in the field of organic light-emitting diodes (OLEDs) by means of systematic device series. To accomplish this, it was necessary to conceive and develop a completely new UHV (ultrahigh vacuum) evaporation system for combinatorial device fabrication as well as an all-round characterization system, whereby the versatility of both systems was of the highest priority.

OLEDs based on small molecules have been investigated with this system. Today, OLEDs typically consist of three organic layers. Structures having six or more layers or more complex systems usually lead to higher efficiencies. OLEDs are thin-film devices with total device thicknesses of about 100 nm. As such, the electrical and optical properties strongly depend on the thickness of the individual layers. The layer thickness is a parameter that has to be controlled and reproducibly adjusted with high precision. The systematic variation of the thickness and its influence on electrical and optical characteristics can be employed as a tool for investigating many different physical processes and effects. Using the new evaporation system presented here, reliable layer thickness variations as well as electrode variations can be conducted with exceptional reproducibility and complexity, and with an ease otherwise possible only in simulations.

The newly developed UHV evaporation system developed in the framework of this thesis reaches a base pressure of $< 10^{-8}$ mbar. It has twelve independent, temperature-controlled effusion cells, four of which can be used at the same time for co-evaporation. A vacuum load lock permits short loading times for arbitrary substrates and shadow masks up to a maximum

size of $80 \times 80 \text{ mm}^2$. Another load lock allows the refill and exchange of evaporation materials without venting the main chamber to ambient. This required a new concept for effusion cells that can be loaded and unloaded as an entity. The cells can be moved in vacuum to center them below the substrate during evaporation, whereby excellent uniformity ($\pm 3\%$) can be achieved on the active area ($66 \times 66 \text{ mm}^2$) of the substrate. The core of the system is a rotatable sample and mask holder in the recipient. It allows the fabrication of staircase-like structures on the substrate by means of a shutter, which can be controlled precisely from the outside. Furthermore, substrate, shadow mask and the movable shutter can be rotated in 90° steps relative to each other, such that two orthogonal staircase layers form a so-called combinatorial matrix. In such a matrix, 100 thickness combinations in a two-layer system are achieved. Hence, a single substrate holds 10×10 individual samples. For characterization, the substrates are transferred directly to a glovebox, where they are investigated by means of various methods under inert conditions (Argon , $\text{O}_2 < 1 \text{ ppm}$, $\text{H}_2\text{O} < 1 \text{ ppm}$). The computer-controlled, automated characterization setup enables the routine measurement of current–voltage (I – V), luminance–voltage (L – V) as well as photoluminescence (PL), transmittance and reflectance. Furthermore, measurements of photocurrents, transient electroluminescence (EL), and impedance spectroscopy ($Z(\omega)$, C – V) are possible. The setup was designed in a flexible way to permit in principle all measurements in which, on the one hand, samples are electrically or optically excited and, on the other, signals are detected electrically or optically. In addition to the careful acquisition of data and the clear representation of the raw data, it was crucial to handle and process the huge amount of data to calculate, extract and display the quantities of interest. To this end, appropriate programs and scripts were developed.

Such a combinatorial system in conjunction with multi-functional characterization capabilities with such a high degree of flexibility did not exist hitherto. It is conceivable that commercial tool vendors might start to develop similar systems in the foreseeable future.

A further goal of this work was to demonstrate the capabilities of the combinatorial method for layer and device fabrication by means of collected examples. A three-layer OLED structure, like that proposed in 1989 by Tang et al. served as a model device structure. The three layers consisted of CuPc^1 , NPB^2 and Alq_3^3 . This material system was chosen because there are numerous reports in the literature about it. By fabricating a “combinatorial matrix” and

¹copper phthalocyanine

² N,N' -di(naphthalene-1-yl)- N,N' -diphenylbenzidine

³tris(8-hydroxyquinolate) aluminum

varying two of the layers' thicknesses, the most efficient device can be readily determined in a single evaporation run. By means of two-dimensional (2D) efficiency plots the range of maximum efficiency can be determined. This is of great technological interest for the process window. To understand the operation mechanisms, a 2D plot of the driving voltage at a constant current density allows conclusions to be drawn regarding the internal potential distribution in the device. In this device structure, it has been shown convincingly that at low current densities ($<1 \mu\text{A}/\text{cm}^2$) the driving voltage is almost independent of the Alq₃ thickness. At higher current densities ($20 \text{ mA}/\text{cm}^2$), the potential distribution is changed such that the voltage drop across the Alq₃ becomes comparable to that across NPB. The hole mobility in NPB ($\mu_h = 10^{-3} \text{ cm}^2/\text{Vs}$) is much higher than the electron mobility in Alq₃ ($\mu_e = 10^{-5} \text{ cm}^2/\text{Vs}$), which leads to the conclusion that injection across internal organic energy barriers, in particular across the CuPc/NPB interface, regulates the current flow and the internal fields. The internal barriers and the field distribution hence dominate the I - V characteristics of OLEDs. The influence of transport becomes significant only at higher current densities ($>100 \text{ mA}/\text{cm}^2$).

A complementary method for determining the internal potential and field distribution is the method of "potential sensing". The fabrication of samples by means of the combinatorial system allows the introduction of a third electrode, by which the potential can be measured directly under typical operating conditions. The spatial resolution (10 nm) is determined by the thickness of the third metal electrode and can be further improved. From these measurements, the internal field distribution were deduced, and the results are in agreement with the above-mentioned 2D plots of the driving voltage.

The improvement of the device efficiency also means an extension of the operating lifetime, which is a major aim for technical applications. This can be achieved in principle by using an appropriate dopant. The three-layer structure CuPc/STAD⁴/Alq₃ is extended by an Alq₃:DCJT⁵B doped layer. A combinatorial experiment reveals that the width of this doped region must be at least 150 Å thick for emission originating only from DCJT⁵B. By knowing this minimum thickness the efficiency can be kept high and the driving voltage kept low. The flexibility of the new evaporation system allows a direct comparison of two different dopants. By means of co-evaporation from three effusion cells, red-emitting OLED structures have been fabricated that possess two dyes (Rubren⁶ and DCJT⁵B doped into the emission zone. Via this

⁴2,2',7,7'-diphenyl-amino-spiro-9,9'-bifluorene

⁵4-(dicyanomethylene)-2-*t*-butyl-6(1,1,7,7-tetramethyljulolidyl-9-enyl)-4*H*-pyran

⁶5,6,11,12-tetraphenylnaphthacene

double-doping an efficiency increase of about 15% compared to the single-doped structure (DCJTb) has been achieved accompanied by a slightly red-shifted spectrum. The major advantage of this double-doped structure is revealed in terms of the lifetime, which increased by a factor of 3 to an extrapolated value of 16.000 h at 100 cd/m².

The future of efficient OLEDs, however, lies in the employment of phosphorescent materials because their emission makes use of the excited singlet and triplet state. Moreover, their theoretical internal efficiency may reach 100%. Such a structure based on the phosphorescent dopant Ir(ppy)₃⁷ was proposed in 1998 by Baldo et al. These highly efficient devices require an additional layer to keep the triplet excitons from diffusing during their long lifetime to adjacent layers, where they would decay with lower efficiency or even become radiationless. With the help of the combinatorial methods presented here, the influence of this exciton-blocking layer as well as the position and the width of the emitting layer have been investigated. For example, a 50-Å-thick layer of the material BCP⁸ is enough to increase the efficiency by a factor of 2 up to ~20 cd/A, whereby the driving voltage is not increased significantly. The position of the emission zone has a significant influence, whereas its width plays a secondary role in the range from 150 to 250 Å.

The OLED devices investigated here are exclusively top-emitting structures, i.e. light is emitted through the second electrode to the top. The results of various combinatorial matrices clearly demonstrate that the efficiency of OLEDs of a given material set is determined mainly by optical interference effects. The electrodes play an important role because the reflectivity of the mirrors determines how well the cavity is defined. On the one hand, reflectivity can be enhanced by the use of two-layer anodes (e.g. Al/Ni, $R > 85\%$). On the other hand, it can be drastically reduced by a three-layer (“black”) anode ($R < 5\%$). The latter was realized by Al/SiO_x/Ni, and reflection measurements show that numerical simulations can very well reproduce the experimental results. However, it is not sufficient to optimize single components, e.g. the anode to high or low reflectivity. In fact the OLED must be regarded in its entirety. In order to achieve a good contrast ratio under ambient light conditions the reflectivity of the entire OLED has to be minimized. Preliminary measurements of red-emitting OLEDs show that the most efficient LED does not necessarily exhibit the lowest reflectivity. Tuning by an additional transparent dielectric layer can be used to adjust this. In OLEDs with semi-transparent cathodes (“top-emitting”) the transmission and reflection of these electrodes play

⁷tris(2-phenylpyridine) iridium

⁸2,9-dimethyl-4,7-diphenyl 1,10-phenanthroline

an important role. The optical properties of reactive cathode materials, e.g. Ca and Mg, can be measured with the characterization system under inert conditions. This forms the basis for numerical simulations.

In addition to technological questions, the combinatorial setup also allowed more basic aspects of OLEDs to be addressed. Luminescence quenching is one effect that can drastically reduce efficiency and which is hence to be avoided. Thickness-dependent photoluminescence of Alq₃ layers provide information about the critical distances to be considered. To describe thickness-dependent photoluminescence, a model was established to account for exciton diffusion and quenching at the substrate interface. The experimental data on glass, ITO (indium-tin-oxide), and aluminum can be described by this model. Furthermore, the quenching probability at the surface can be quantified and is 15% and 40% for an untreated and an oxygen plasma-treated glass substrate, respectively. On typical electrode materials, e.g. ITO and Al, surface quenching probability is 60% and 100%, respectively. Based on this model, an exciton diffusion length in Alq₃ of about $L = 220 \text{ \AA}$ can be extracted.

The “sensing layer” experiment is an alternative method for determining the exciton diffusion length. By inserting a thin (25 Å) doped layer at various positions in an OLED structure, the distribution of the emission zone in OLED structures can be measured. The relative intensity of the dopant can be regarded approximately as a measure for the local exciton density. In the case of a CuPc/NPB/Alq₃ OLED with DCJTb as dopant, the resulting profile strongly depends on the current density which points to luminescence quenching by charged species. For the border case of low current density and with several simplifications, the exciton diffusion length in Alq₃ can be estimated to be about $L \approx 200 \text{ \AA}$. Similar experiments have been performed, although the data sets were limited and the samples were fabricated in series. With the combinatorial setup presented here, this type of experiment can be conducted even with different dopants without excessive effort, whereby direct comparisons in the same evaporation run are possible.

All the experimental approaches presented here make use of combinatorial methods, which allow the fabrication of numerous samples with distinct differences. The structure of the device itself is used as a parameter, quasi as an additional “measurement instrument”. As there are numerous organic materials, electrode configurations, and possible combinations thereof, detailed device operation must still be studied in each specific case. For quantitative simulations of OLEDs, particularly to simulate their electrical behavior, sophisticated models are

needed. Such models must be described and verified on the basis of rich and reliable data sets. Systematic experimental data are indispensable to obtain reliable descriptions of and to understand OLEDs. The next goal will be to extend the description of simple structures together with separately measured material parameters to describe more complex device structures. A first important step in this direction has been achieved with the present work. The necessary data can be obtained efficiently and with high precision and reproducibility with the aid of the combinatorial evaporation system presented here.

Appendix

A.1 CIE Coordinates and Maximum Efficiencies

From a given spectrum the maximum efficiency can be calculated in the following way:

$$\eta_{max} = 683 \text{ lm/W} \cdot \int_{380\text{nm}}^{780\text{nm}} V_{\lambda} S(\lambda) d\lambda, \quad (\text{A.1})$$

where V_{λ} is the spectral response of the human eye as shown in Figure 3.14 (page 51) and $S(\lambda)$ the spectral power density $S(\lambda)$ in $\text{W}/(\text{sr} \cdot \text{m}^2)$. The CIE coordinates are calculated as follows:

$$X = \int_{380\text{nm}}^{780\text{nm}} S(\lambda) X_{\lambda} d\lambda \quad Y = \int_{380\text{nm}}^{780\text{nm}} S(\lambda) Y_{\lambda} d\lambda \quad Z = \int_{380\text{nm}}^{780\text{nm}} S(\lambda) Z_{\lambda} d\lambda \quad (\text{A.2})$$

where X_{λ} , Y_{λ} , and Z_{λ} are tristimulus values which are shown in Figure A.1. For details see [Keller 1997].

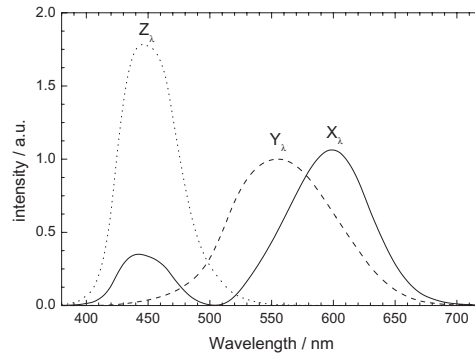


Figure A.1: CIE 1931 tristimulus curves.

The CIE x,y color coordinates are then calculated as follows:

$$x = \frac{X}{X + Y + Z}, \quad y = \frac{Y}{X + Y + Z} \quad (\text{A.3})$$

A.2 Deconvolution of Spectra

The spectral emission of doped OLEDs is in general a superposition of the host and guest emission spectra and can be deconvoluted by linear regression. As it was shown in Section 5.1 small changes in layer thickness may lead to a drastic change in spectral characteristic. Therefore, the base spectra from the host and the dopant emission should be taken from the same substrate, thus avoiding uncertainties due to different layer thicknesses in the organic stack or the electrodes. The base spectra are vectors $\vec{b}_1, \dots, \vec{b}_n$ where $n = 2$ or $n = 3$ is number of base

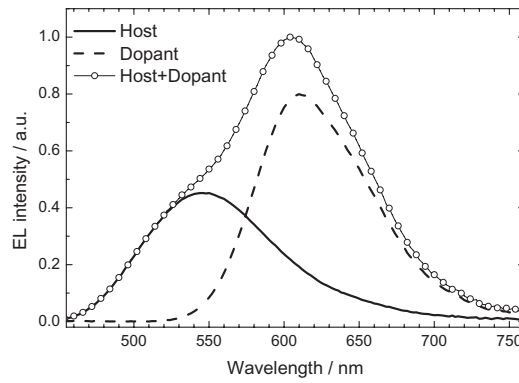


Figure A.2: Deconvolution of guest and host spectra in a doped system via linear regression.

spectra. The vector \mathbf{k} consists of n constants k_1, \dots, k_n which are the factors by which the base spectra b_1, \dots, b_n have to be multiplied to get the target vector of the mix spectrum \mathbf{t} .

$$(b_1, \dots, b_n) \begin{pmatrix} k_1 \\ \vdots \\ k_n \end{pmatrix} = (t), \quad B\mathbf{k} = \mathbf{t} \quad (\text{A.4})$$

The solution to this overdetermined equation system is $B^T B\mathbf{k} = B^T \mathbf{t}$ and with $A = B^T B$ and $\mathbf{z} = B^T \mathbf{t}$ this leads to $A\mathbf{k} = \mathbf{z}$ and the solution for \mathbf{k} is

$$\mathbf{k} = A^{-1}\mathbf{z}. \quad (\text{A.5})$$

A.3 HOMO and LUMO Levels of Organic Materials

| | E_{HOMO} | E_{LUMO} | E_{gap} | Reference |
|----------------------|-------------------|-------------------|------------------|---|
| Alq ₃ | 5.8 – 5.9 | 3.1–3.2 | 2.7 | [Hill et al. 2000] |
| | 5.8 | 3.1 | 2.7 | [Chen et al. 2001] |
| Almq ₃ | 5.9 | 3.2 | 2.7 | [Kido and Iizumi 1997] |
| BCP | 6.4 – 6.5 | 2.9 – 3.4 | 3.5 | [Hill et al. 2000] |
| | 6.7 | 3.2 | 3.5 | [Adachi et al. 2000] |
| CBP | 6.0 – 6.3 | 2.9 – 3.2 | 3.1 | [Hill et al. 2000] |
| | 6.3 | 3.2 | 3.1 | [Adachi et al. 2000] |
| CuPc | 5.1 – 5.2 | 3.5 – 3.6 | 1.6 | [Hill et al. 2000] |
| DCM1 | 5.3 | 3.1 | 2.2 | [Lam et al. 2000] |
| DCM2 | 5.26 | 3.11 | 2.15 | [Hamada et al. 1999] |
| DCJMTB | 5.2 | 3.1 | 2.1 | [Chen et al. 2001] |
| DCJTB | ? | ? | ? | |
| Gaq ₃ | 5.4 | 2.9 | 2.5 | [Chen et al. 2001] |
| Inq ₃ | 5.7 | 3.4 | 2.3 | [Chen et al. 2001] |
| Ir(ppy) ₃ | 5.2 | 2.8 | 2.4 | [Ikai et al. 2001] |
| MTDATA | 5.0 | 1.85 | 3.15 | [Hamada et al. 2001; Mäkinnen et al. 2002] |
| NPB | 5.4 – 5.6 | 2.3 – 2.5 | 3.1 | [Hill et al. 2000] |
| PTCDA | 6.7 | 4.5 | 2.2 | [Hill et al. 2000] |
| Rubrene | 5.36 – 5.41 | 3.15 – 3.21 | 2.2 | [Hamada et al. 1999; |
| | | | | Hamada et al. 2001] |
| STAD | 5.3 | 2.2 | 3.1 | (Covion) |
| TAZ | 6.6 | 2.6 | 4.0 | [Adachi et al. 2001] |
| TPD | 5.4 | 2.4 | 3.0 | [Lam et al. 2000] |
| TPP | 5.4 | 3.8 | 1.6 | [Sawatani et al. 2000] |

Table A.1: HOMO and LUMO levels of various organic materials.

References

- C. Adachi, M. A. Baldo, and S. R. Forrest (2000). Electroluminescence mechanisms in organic light emitting devices employing a europium chelate doped in a wide energy gap bipolar conducting host. *J. Appl. Phys.* 87(11), 8049–55.
- C. Adachi, M. A. Baldo, S. R. Forrest, and M. E. Thompson (2000). High-efficiency organic electrophosphorescent devices with tris(2-phenylpyridine)iridium doped into electron-transporting materials. *Appl. Phys. Lett.* 77(6), 904–6.
- C. Adachi, M. A. Baldo, M. E. Thompson, and S. R. Forrest (2001). Nearly 100% internal phosphorescence efficiency in an organic light emitting device. *J. Appl. Phys.* 90(10), 5048–51.
- C. Adachi, S. Tokito, T. Tsutsui, and S. Saito (1988a). Electroluminescence in organic films with three-layer structure. *Jpn. J. Appl. Phys.* 27(2), L269–71.
- C. Adachi, S. Tokito, T. Tsutsui, and S. Saito (1988b). Organic electroluminescent device with a three-layer structure. *Jpn. J. Appl. Phys.* 27(4), L713–5.
- C. Adachi, T. Tsutsui, and S. Saito (1991). Electroluminescent mechanism of organic multilayer thin film devices. *Optoelectron. Devices Technol.* 6(1), 25–36.
- E. Aminaka, T. Tsutsui, and S. Saito (1996). Effect of layered structures on the location of emissive regions in organic electroluminescent devices. *J. Appl. Phys.* 79(11), 8808–15.
- H. Aziz, Z. D. Popovic, N.-X. Hu, A.-M. Hor, and G. Xu (1999). Degradation mechanism of small molecule-based organic light-emitting devices. *Science* 283, 1900–2.
- U. Bach, K. D. Cloedt, H. Spreitzer, and M. Grätzel (2000). Characterization of hole transport in a new class of spiro-linked oligotriphenylamine compounds. *Adv. Mater.* 12(14), 1060–3.

- M. A. Baldo and S. R. Forrest (2000). Transient analysis of organic electrophosphorescence: II. transient analysis of triplet-triplet annihilation. *Phys. Rev. B* 62(16), 10967–77.
- M. A. Baldo, S. Lamansky, P. E. Burrows, M. E. Thompson, and S. R. Forrest (1999). Very high-efficiency green organic light-emitting devices based on electrophosphorescence. *Appl. Phys. Lett.* 75(1), 4–6.
- M. A. Baldo, D. F. O'Brien, Y. You, A. Shoustikov, S. Sibley, M. E. Thompson, and S. R. Forrest (1998). Highly efficient phosphorescent emission from organic electroluminescent devices. *Nature* 395, 151–4.
- Z. Bao, A. J. Lovinger, and A. Dodabalapur (1996). Organic field-effect transistors with high mobility based on copper phthalocyanine. *Appl. Phys. Lett.* 69(20), 3066–8.
- S. Barth, P. Müller, H. Riel, P. F. Seidler, W. Rieß, H. Vestweber, and H. Bässler (2001). Electron mobility in tris(8-hydroxy-quinoline)aluminum thin films determined via transient electroluminescence from single- and multilayer organic light-emitting diodes. *J. Appl. Phys.* 89(7), 3711–9.
- H. Bässler (1993). Charge transport in disordered organic photoconductors. *Phys. Stat. Sol. B* 175, 15–56.
- H. Becker, S. E. Burns, and R. H. Friend (1997). Effect of metal films on the photoluminescence and electroluminescence of conjugated polymers. *Phys. Rev. B* 56(4), 1893–905.
- T. A. Beierlein, W. Brütting, H. Riel, E. I. Haskal, P. Müller, and W. Rieß (2000). Kelvin probe investigations of metal work functions and correlation to device performance of organic light-emitting devices. *Synth. Met.* 111-112, 295–7.
- T. A. Beierlein, H.-P. Ott, H. Hofmann, H. Riel, B. Ruhstaller, B. Crone, S. Karg, and W. Rieß (2002). Combinatorial device fabrication and optimization of multilayer organic LEDs. In *Proc. SPIE*, Volume 4464, pp. 178–86.
- S. Berleb (2001). *Raumladungsbegrenzte Ströme und Hoppingtransport in organischen Leuchtdioden aus Tris-(8-hydroxyquinoline)-Aluminium (Alq₃)*. Ph. D. thesis, Universität Bayreuth.
- A. Bernanose, M. Comte, and P. Vouaux (1953). Sur un nouveau mode d'émission lumineuse chez certain composés organiques. *J. Chim. Phys. Phys. Chim. Biol.* 50, 64–8.

- J. B. Birks (1970). *Photophysics of Aromatic Molecules*. New York London: Wiley – Interscience.
- P. J. H. Bloemen, M. J. van de Vorst, M. T. Johnson, R. Coehoorn, and W. J. M. de Jonge (1994). Magnetic layer thickness dependence of the interlayer exchange coupling in (001) Co/Cu/Co. *J. Appl. Phys.* 76(10), 7081–3.
- M. Born and E. Wolf (1999). *Principles of Optics: Electromagnetic Theory of Propagation, Interference and Diffraction of Light*. Cambridge University Press.
- W. Brütting, S. Berleb, and A. G. Mückl (2001). Device physics of organic light-emitting diodes based on molecular materials. *Org. Electronics* 2(1), 1–36.
- W. Brütting, H. Riel, T. Beierlein, and W. Rieß (2001). Influence of trapped and interfacial charges in organic multilayer light-emitting devices. *J. Appl. Phys.* 89(3), 1704–12.
- V. Bulović, A. Shoustikov, M. A. Baldo, E. Bose, V. G. Kozlov, M. E. Thomson, and S. R. Forrest (1998). Bright, saturated, red-to-yellow organic light-emitting devices based on polarization-induced spectral shifts. *Chem. Phys. Lett.* 287, 455–60.
- A. L. Burin and M. A. Ratner (2000). Exciton migration and cathode quenching in organic light emitting diodes. *J. Phys. Chem. A* 104, 4704–10.
- J. H. Burroughes, D. D. C. Bradley, A. R. Brown, R. N. Marks, K. Mackay, R. H. Friend, P. L. Burns, and A. B. Holmes (1990). Light-emitting diodes based on conjugated polymers. *Nature* 347, 539–41.
- I. H. Campbell, M. D. Joswick, and I. D. Parker (1995). Direct measurement of the internal electric field distribution in a multilayer organic light-emitting diode. *Appl. Phys. Lett.* 67(21), 3171–3.
- R. R. Chance, A. Prock, and R. Silbey (1978). Molecular fluorescence and energy transfer near interfaces. *Adv. Chem. Phys.* 37, 1–65.
- B. Chen, X. Lin, L. Cheng, C. Lee, W. A. Gambling, and S. Lee (2001). Improvement of efficiency and colour purity of red-dopant organic light-emitting diodes by energy levels matching with the host materials. *J. Phys. D* 34, 30–5.
- C. H. Chen, C. W. Tang, J. Shi, and K. P. Klubek (2000). Recent developments in the synthesis of red dopants for Alq₃ hosted electroluminescence. *Thin Solid Films* 363, 327–331.

- V.-E. Choong, Y. Park, Y. Gao, M. G. Mason, and C. W. Tang (1998). Photoluminescence quenching of Alq₃ by metal deposition: A surface analytical investigation. *J. Vac. Sci. Technol. A* 16(3), 1838–41.
- E. Danielson, J. H. Golden, E. W. McFarland, C. M. Reeves, W. H. Weinberg, and X. D. Wu (1997). A combinatorial approach to the discovery and optimization of luminescent materials. *Nature* 389, 944–8.
- D. L. Dexter (1953). A theory of sensitized luminescence in solids. *J. Chem. Phys.* 21(5), 836–50.
- T. Förster (1948). Zwischenmolekulare Energiewanderung und Fluoreszenz. *Ann. Phys.* 6(2), 55–75.
- E. W. Forsythe, M. A. Abkowitz, and Y. Gao (2000). Tuning the carrier injection efficiency for organic light-emitting diodes. *J. Phys. Chem. B* 104, 3948–52.
- E. W. Forsythe, M. A. Abkowitz, Y. Gao, and C. W. Tang (2000). Influence of copper phthalocyanine on the charge injection and growth modes for organic light emitting diodes. *J. Vac. Sci. Technol. A* 18(4), 1869–74.
- R. H. Fowler and L. Nordheim (1928). Electron emission in intense electric fields. *Proc. R. Soc. London Ser. A* 119, 173–81.
- C. Giebeler, S. A. Whitelegg, A. J. Campbell, M. Liess, S. J. Martin, P. A. Lane, and D. D. C. Bradley (1999). Optical studies of electric fields in poly(2-methoxy-5-ethyl (2'-hexyloxy) para-phenylene vinylene) light-emitting diodes. *Appl. Phys. Lett.* 74(24), 3714–6.
- Y. Hamada, H. Kanno, T. Tsujioka, H. Takahashi, and T. Usuki (1999). Red organic light-emitting diodes using an emitting assist dopant. *Appl. Phys. Lett.* 75(12), 1682–4.
- Y. Hamada, N. Matsusue, H. Kanno, H. Fujii, T. Tsujioka, and H. Takahashi (2001). Improved luminous efficiency of organic light-emitting diodes by carrier trapping dopants. *Jpn. J. Appl. Phys.* 40(7B), L753–5.
- H. Hänsel, H. Zettl, G. Krausch, C. Schmitz, R. Kisselev, M. Thelakkat, and H.-W. Schmidt (2002). Combinatorial study of the long-term stability of organic thin-film solar cells. *Appl. Phys. Lett.* 81(11), 2106–8.

- E. I. Haskal, H. Vestweber, H. Schmid, and P. F. Seidler (1998). Substrate designs and contacts for organic light-emitting displays. In *Proceedings SPIE*, Volume 3476, pp. 243–9.
- T. K. Hatwar, G. Rajeswaran, J. Shi, Y. Hamada, H. Kanno, and H. Takahashi (2000). Red emitting organic electroluminescent devices with improved stability. In H. Kobayashi and T. Tsutsui (Eds.), *10th Int. Workshop on Inorganic and Organic Electroluminescence, Hamamatsu*, pp. 31–4.
- I. G. Hill, D. Milliron, J. Schwartz, and A. Kahn (2000). Organic semiconductor interfaces: electronic structure and transport properties. *Appl. Surf. Sci.* 166, 354–62.
- M. Hiramoto, K. Koyama, K. Nakayama, and M. Yokoyama (2000). Direct measurement of internal potential distribution in organic electroluminescent diodes during operation. *Appl. Phys. Lett.* 76(10), 1336–8.
- H. Hofmann (2001). Kombinatorische Methoden für organische Leuchtdioden: Automatisierung des Meßsystems und Charakterisierung von Mehrschichtstrukturen. Diploma thesis, Fachhochschule München.
- S. Hoshino and H. Suzuki (1996). Electroluminescence from triplet excited states of benzophenone. *Appl. Phys. Lett.* 69(2), 224–6.
- L. S. Hung, C. W. Tang, M. G. Mason, P. Raychaudhuri, and J. Madathil (2001). Application of an ultrathin LiF/Al bilayer in organic surface-emitting diodes. *Appl. Phys. Lett.* 78(4), 544–6.
- IDTech (2003). <http://www.idtech.co.jp/en/news/press/20030312.html>. Press release.
- M. Ikai, S. Tokito, Y. Sakamoto, T. Suzuki, and Y. Tag (2001). Highly efficient phosphorescence from organic light-emitting devices with an exciton-block layer. *Appl. Phys. Lett.* 79(2), 156–8.
- K. C. Kao and W. Hwang (1981). *Electrical Transport in Solids With particular Reference to Organic Semiconductors*. Pergamon Press.
- P. A. Keller (1997). *Electronic Display Measurement*. New York: Wiley & Sons.
- R. G. Kepler, P. M. Beeson, S. J. Jacobs, R. A. Anderson, M. B. Sinclair, V. S. Valencia, and P. A. Cahill (1995). Electron and hole mobility in tris(8-hydroxyquinolino-N1,O8) aluminum. *Appl. Phys. Lett.* 66(26), 3618–20.

- J. Kido and Y. Iizumi (1997). Efficient electroluminescence from tris(4-methyl-8-quinolinato)aluminum(III). *Chem. Lett.*, 963–4.
- J. Kido, K. Nagai, Y. Okamoto, and T. Skotheim (1991). Poly(methylphenylsilane) film as a hole transport layer in electroluminescent devices. *Appl. Phys. Lett.* 59(21), 2760–2.
- H. Klauk, J. R. Huang, J. A. Nichols, and T. N. Jackson (2000). Ion-beam deposited ultra-thin transparent metal contacts. *Thin Solid Films* 366(1-2), 272–8.
- M. Klessinger and J. Michel (1995). *Excited states and photochemistry of organic molecules*. Weinheim: VCH.
- D. Y. Kondakov, J. R. Sandifer, C. W. Tang, and R. H. Young (2003). Nonradiative recombination centers and electrical aging of organic light-emitting diodes: Direct connection between accumulation of trapped charge and luminance loss. *J. Appl. Phys.* 93(2), 1108–19.
- J. Lam, T. C. Gorjanc, Y. Tao, and M. D'Iorio (2000). Selective doping of multilayer organic light emitting devices. *J. Vac. Sci. Technol. A* 18(2), 593–6.
- S. Lamansky, P. Djurovich, D. Murphy, F. Abdel-Razzaq, H.-E. Lee, C. Adachi, P. E. Burrows, S. R. Forrest, and M. E. Thompson (2001). Highly phosphorescent bis-cyclometalated iridium complexes: Synthesis, photophysical characterization, and use in organic light emitting diodes. *J. Am. Chem. Soc.* 123, 4304–12.
- Lide, D. R. (Ed.) (1996). *CRC Handbook of Chemistry and Physics* (77th ed.). CRC Press, Inc.
- Y.-Y. Lin, D. J. Gundlach, S. F. Nelson, and T. N. Jackson (1997). Pentacene-based organic thin-film transistors. *IEEE Trans. El. Dev.* 44(8), 1325–31.
- D. Ma, C. S. Lee, S. T. Lee, and L. S. Hung (2002). Improved efficiency by a graded emissive region in organic light-emitting diodes. *Appl. Phys. Lett.* 80(19), 3641–3.
- A. J. Mäkinen, I. G. Hill, and Z. H. Kafafi (2002). Vacuum level alignment in organic guest-host systems. *J. Appl. Phys.* 92(3), 1598–603.
- M. Matsumura and Y. Miyamae (1999). Current-voltage characteristics of organic EL devices with a Cu-phthalocyanine buffer layer. *Proc. SPIE* 3797, 283–9.
- H. Mattoussi, H. Murata, C. D. Merritt, and Z. H. Kafafi (1998). Absolute photoluminescence quantum yield of molecular organic thin films: effects of doping with the strongly

- fluorescent rubrene. *Proc. SPIE* 3476, 49–60.
- E. Moderegger, F. P. Wenzl, S. Tasch, G. Leising, U. Scherf, and K. O. Annan (2000). Comparison of the internal field distribution in light-emitting diodes and light-emitting electrochemical cells. *Adv. Mater.* 12(11), 825–7.
- T. Mori, K. Miyachi, and T. Mizutani (1995). A study of the electroluminescence process of an electroluminescence diode with an Alq₃ layer using a dye-doping method. *J. Phys. D* 28, 1461–7.
- T. Mori and T. Mizutani (1997). Application of energy transfer model to partially DCM-doped Alq₃ light-emitting diode. *Polym. Adv. Technol.* 8, 471–6.
- T. Mori, K. Obata, K. Imaizumi, and T. Mizutani (1996). Preparation and properties of an organig light emitting dide with two emission colors dependent on the voltage polarity. *Appl. Phys. Lett.* 69(22), 3309–11.
- S. Naka, H. Hiroyuki, H. Onnagawa, J. Kido, and T. Tsutsui (1999). Time-of-flight measurement of hole mobility in aluminium (III) complexes. *Jpn. J. Appl. Phys.* 38(11A), L1252–4.
- H. Nakamura (2002). Classical calculation model for dipole radiation in stratified structure — quantitative outcoupling efficiency —. unpublished.
- K. A. Neyts (1998). Simulation of light emission from thin-film microcavities. *J. Opt. Soc. Am. A* 15(4), 962–71.
- K. A. Neyts, P. D. Visschere, D. K. Fork, and G. B. Anderson (2000). Semitransparent metal or distributed Bragg reflector for wide-viewing-angle organic light-emitting-diode microcavities. *J. Opt. Soc. Am. B* 17(1), 114–9.
- E. D. Palik (1991). *Handbook of Optical Constant of Solids II*. Academic Press.
- Pankove, J. I. (Ed.) (1980). *Display devices*. Berlin Heidelberg: Springer-Verlag.
- M. Pope, H. Kallmann, and P. Magnante (1963). Electroluminescence in organic crystals. *J. Chem. Phys.* 38, 2042–3.
- M. Pope and C. E. Swenberg (1999). *Electronic Processes in Organic Crystals and Polymers* (2nd Edition ed.). Oxford University Press.
- Z. D. Popovic, H. Aziz, N.-X. Hu, and A. I. ad P. N. M. dos Anjos (2001). Simutaneous electroluminescence and photoluminescence aging studies of tris(8-hydroxyquinoline)

- aluminum-based organic light-emitting devices. *J. Appl. Phys.* 89(8), 4673–5.
- Z. D. Popovic, H. Aziz, C. P. Tripp, N.-X. Hu, A.-M. Hor, and G. Xu (1998). Improving the efficiency and stability of organic light-emitting devices by using mixed emitting layers. *Proc. SPIE 3476*, 68–73.
- Z. D. Popovic and E. R. Menzel (1979). Electric field-induced fluorescence quenching in organic photoconductors. *J. Chem. Phys.* 71(12), 5090–6.
- J. F. Rabek (1996). *Photodegradation of Polymers*. Berlin: Springer.
- H. Riel (1997). Grading of internal organic-organic barriers in OLEDs. IBM Internal Report.
- H. Riel (1998). Ladungsträgerinjektion, Transport und Rekombination in organischen LEDs: Von Einschichtstrukturen zu effizienten blauen OLEDs. Master's thesis, Universität Erlangen-Nürnberg.
- H. Riel (2002). *Optimization of multilayer organic light-emitting diodes*. Ph. D. thesis, Universität Bayreuth.
- H. Riel, T. A. Beierlein, S. Karg, and W. Rieß (2003). The role of copper-phthalocyanine in multilayer organic LEDs based on small molecules. *Proc. SPIE 4800*, 148–55.
- H. Riel, W. Brütting, T. Beierlein, E. Haskal, P. Müller, and W. Rieß (2000). Influence of space charges on the current–voltage characteristic of organic light-emitting devices. *Synth. Met.* 111-112, 303–6.
- H. Riel, S. Karg, T. Beierlein, W. Rieß, and K. Neyts (2003). Tuning the emission characteristic of top-emitting organic light-emitting devices using a dielectric capping layer: An experimental and theoretical study. *J. Appl. Phys.*.. to be submitted.
- H. Riel, S. Karg, T. Beierlein, B. Ruhstaller, and W. Rieß (2003). Phosphorescent top-emitting organic light-emitting devices with improved light outcoupling. *Appl. Phys. Lett.* 82(3), 466–8.
- H. Riel, H. Vestweber, and W. Rieß (1998). Influence of charge carrier injection on the device performance of blue organic light-emitting diodes. In *Proc. SPIE Int. Conf. on Polymer Photonic Devices*, San Jose, CA.
- W. Rieß, H. Riel, T. Beierlein, W. Brütting, P. Müller, and P. F. Seidler (2001). Influence of trapped and interfacial charges in organic multilayer light-emitting devices. *IBM J. Res.*

- Develop.* 45(1), 1–13.
- F. Rohlfling, T. Yamada, and T. Tsutsui (1999). Electroabsorption spectroscopy on tris-(8-hydroxyquinoline) aluminum-based light emitting diodes. *J. Appl. Phys.* 86(9), 4978–84.
- B. Ruhstaller (2000). *Poylmer composite and multilayer organic light-emitting diodes*. Ph. D. thesis, University of California, Santa Cruz.
- B. Ruhstaller, S. A. Carter, S. Barth, H. Riel, W. Rieß, and J. C. Scott (2001). Transient and steady-state behavior of space charges in multilayer organic light-emitting diodes. *J. Appl. Phys.* 89(8), 4575.
- T. Sano, Y. Hamada, and K. Shibata (1996, August). Stability of dye electroluminescent devices. In R. H. Mauch and H.-E. Gumlich (Eds.), *Inorganic and Organic Electroluminescence*, Berlin, pp. 249–54. Wissenschaft & Technik Verlag.
- H. Sato, T. Minami, S. Takata, and T. Yamada (1993). Transparent conducting *p*-type NiO thin films prepared by magnetron sputtering. *Thin Solid Films* 236, 27–31.
- Y. Sato, S. Ichinosawa, and H. Kanai (1996, August). Improved stability of doped organic electroluminescent diodes. In R. H. Mauch and H.-E. Gumlich (Eds.), *Inorganic and Organic Electroluminescence*, Berlin, pp. 255–8. Wissenschaft & Technik Verlag.
- Y. Sato, S. Ichinosawa, and H. Kanai (1998). Operation characteristics and degradation of organic electroluminescent devices. *IEEE J. Sel. Topics Quantum Electron.* 4(1), 40–8.
- T. Sawatani, Y. Ohmori, and K. Yoshino (2000). Enhanced electroluminescence in organic light-emitting diodes utilizing co-doped emissive layer for red light emission. *IEICE Trans. Eletron.* E83-C(7), 1022–5.
- H.-W. Schmidt, C. Schmitz, P. Pösch, and M. Thelakkat (1999). Combinatorial methods for screening and optimization of materials and device parameters in organic light emitting diodes. *Proc. SPIE* 3797, 58–65.
- C. Schmitz (2001). *Investigation of Opto-Electronic Thin-Layer Devices Using a Combinatorial Approach*. Ph. D. thesis, University of Bayreuth.
- C. Schmitz, M. Thelakkat, and H.-W. Schmidt (1999). A combinatorial study of the dependence of organic LED characteristics on layer thickness. *Adv. Mater.* 11(10), 821–6.

- J. Shi and C. W. Tang (1997). Doped organic electroluminescent devices with improved stability. *Appl. Phys. Lett.* 70(13), 1665–7.
- A. A. Shoustikov, Y. You, and M. E. Thompson (1998). Electroluminescence color tuning by dye doping in organic light-emitting diodes. *IEEE J. Sel. Topics Quantum Electron.* 4(1), 3–13.
- J. Simon and J.-J. André (1985). *Molecular Semiconductors*. Springer-Verlag, Heidelberg.
- O. Simpson (1956). Electronic properties of aromatic hydrocarbons III. diffusion of excitons. *Proc. R. Soc. London Ser. A* 238, 402–11.
- S. K. So, W. K. Choi, L. M. Leung, and K. Neyts (1999). Interference effects in bilayer organic light-emitting diodes. *Appl. Phys. Lett.* 74(14), 1939–41.
- H. Spreitzer, H. Schenk, J. Salbeck, F. Weissoertel, H. Riel, and W. Rieß (1999). Temperature stability of OLEDs using amorphous compounds with spiro-bifluorene core. *Proc. SPIE* 3797, 316–24.
- T. Strite and T. A. Beierlein (1997). unpublished results.
- T. X. Sun and G. E. Jabbour (2002, April). Combinatorial screening and optimization of luminescent materials and organic light-emitting devices. *MRS Bulletin*, 309–315.
- S. M. Sze (1981). *Physics of Semiconductor Devices*. John Wiley and Sons.
- C. W. Tang and S. A. Van Slyke (1987). Organic electroluminescent diodes. *Appl. Phys. Lett.* 51(12), 913–5.
- C. W. Tang, S. A. Van Slyke, and C. H. Chen (1989). Electroluminescence of doped organic thin films. *J. Appl. Phys.* 65(9), 3610–6.
- T. Tsujimura, Y. Kobayashi, K. Murayama, A. Tanaka, M. Morooka, E. Fukumoto, H. Fujimoto, J. Sekine, K. Kanoh, K. Takeda, K. Miwa, M. Asano, N. Ikeda, S. Kohara, S. Ono, C.-T. Chung, R.-M. Chen, J.-W. Chung, C.-W. Huang, H.-R. Guo, C.-C. Yang, C.-C. Hsu, H.-J. Huang, W. Rieß, H. Riel, S. Karg, T. Beierlein, D. Gundlach, S. Alvarado, C. Rost, P. Müller, F. Libsch, M. Mastro, R. Polastre, A. Lien, J. Sanford, and R. Kaufmann (2003). A 20-inch OLED display driven by super-amorphous-silicon technology. *SID 2003 Technical Digest*, Vol. XXXIV, Book I, 6–9.
- T. Tsutsui and K. Yamamoto (1999). Evaluation of true luminous efficiency from experimental luminance values. *Jpn. J. Appl. Phys.* 38(5A), 2799–803.

- T. Tsutsui, M.-J. Yang, M. Yahiro, K. Nakamura, T. Watanabe, T. Tsuji, Y. Fukuda, T. Wakimoto, and S. Miyaguchi (1999). High quantum efficiency in organic light-emitting devices with iridium-complex as a triplet emissive center. *Jpn. J. Appl. Phys.* 38(12B), L1502–4.
- N. J. Turro (1991). *Modern Molecular Photochemistry*. University Science Books, Sausalito CA.
- S. A. Van Slyke, C. H. Chen, and C. W. Tang (1996). Organic electroluminescent devices with improved stability. *Appl. Phys. Lett.* 69(15), 2160–2.
- G. Vaubel, H. Baessler, and D. Möbius (1971). Reaction of singlet excitons at an anthracene/metal interface: Energy transfer. *Chem. Phys. Lett.* 10(3), 334–6.
- H. Vestweber and W. Rieß (1997). Highly efficient and stable organic light-emitting diodes. *Synth. Met.* 91, 181–185.
- P. S. Vincett, W. A. Barlow, R. A. Hann, and G. G. Roberts (1982). Electrical conduction and low voltage blue electroluminescence in vacuum-deposited organic films. *Thin Solid Films* 94, 171–83.
- C. C. Wu, C. I. Wu, J. C. Sturm, and A. Kahn (1997). Surface modification of indium tin oxide by plasma treatment: An effective method to improve the efficiency, brightness, and reliability of organic light emitting devices. *Appl. Phys. Lett.* 70(11), 1348–50.
- T. Yamada, F. Rohlfiing, D. Zou, and T. Tsutsui (2000). Internal electric field in tris-(8-hydroxyquinoline) aluminum (Alq) based light emitting diode. *Synth. Met.* 111-112, 281–4.
- K. Yamashita, T. Mori, and T. Mizutani (1997). Electroluminescence properties of an organic triple-layer light-emitting diode with two different dye-doped regions. *Synth. Met.* 91, 203–4.
- R. H. Young, C. W. Tang, and A. P. Marchetti (2002). Current-induced fluorescence quenching in organic light-emitting diodes. *Appl. Phys. Lett.* 80(5), 874–6.
- L. Zou, V. Savvate'ev, J. Booher, C.-H. Kim, and J. Shinar (2001). Combinatorial fabrication and studies of intense efficient ultraviolet–violet organic light emitting device arrays. *Appl. Phys. Lett.* 79(14), 2282–4.

List of Publications

1. T. A. Beierlein, B. Ruhstaller, D. J. Gundlach, H. Riel, S. Karg, C. Rost, W. Rieß "Investigations of internal processes in organic light-emitting devices using thin sensing layers", *Synthetic Metals* (2003) vol. 138, 213-221.
2. H. Riel, S.Karg, T. Beierlein, B. Ruhstaller, W. Rieß "Phosphorescent top-emitting organic light-emitting devices with improved light outcoupling", *Appl. Phys. Lett.* 82(3), (2003) 466-468.
3. T. A. Beierlein, H. Riel, B. Ruhstaller, H. Hofmann, B. K. Crone, S. Karg, W. Rieß "Tuning of electrical and optical properties of organic LEDs using combinatorial device fabrication", *Journal of the SID* 10(4), (2002) 311-315.
4. H. Riel, T. A. Beierlein, S. Karg, W. Rieß "The Role of Copper-Phthalocyanine in Multilayer Organic LEDs Based on Small Molecules", *Proc. SPIE 2002*, vol. 4800, 148-155.
5. T. A. Beierlein, H.-P. Ott, H. Hofmann, H. Riel, B. Ruhstaller, B. Crone, S. Karg, W. Rieß "Combinatorial Device Fabrication and Optimization of Multilayer Organic LEDs," in *Organic Light-Emitting Materials and Devices V*, edited by Zakya H. Kafafi, *Proc. SPIE* (SPIE, Bellingham, 2002), vol. 4464, 178-186 (invited).
6. W. Brütting, H. Riel, T. Beierlein, W. Rieß "Influence of Trapped and Interfacial Charges in Organic Multilayer Light-Emitting Devices," *J. Appl. Phys.* 89(3), (2001) 1704-1712.
7. H. Riel, S. Barth, T. Beierlein, W. Brütting, S. Karg, P. Müller, W. Rieß "Grading Interfaces — A New Concept to Improve Device Performance in Organic Multilayer Light-Emitting Diodes," *Organic Light-Emitting Materials and Devices IV*, edited by Z. H. Kafafi, *Proc. SPIE*, Vol. 4105 (SPIE, Bellingham, 2001), 167-174.

8. W. Riess, H. Riel, T. Beierlein, W. Brütting, P. Müller, P.F. Seidler "Influence of Trapped and Interfacial Charges in Organic Multilayer Light-Emitting Devices," IBM J. Res. Develop. 45(1), 77-88 (2001).
9. T. Beierlein, W. Brütting, H. Riel, E.I. Haskal, P. Müller, W. Rieß "Kelvin Probe Investigations of Metal Work Functions and Correlation to Device Performance of Organic Light-Emitting Devices," Synthetic Metals 111-112 (2000) 295-297.
10. H. Riel, W. Brütting, T. Beierlein, E. Haskal, P. Müller, W. Rieß "Influence of Space Charges on the Current-Voltage Characteristic of Organic Light-Emitting Devices," Synthetic Metals 111-112 (2000) 303-306.

Patents

US6580090 "Organic light-emitting devices"

US6552364 "Organic light-emitting devices"

US6548961 "Organic light-emitting devices"

US6501217 "Anode modification for organic light emitting diodes"

US6433358 "Method for producing an organic light emitting device and a concerning device"

Danksagung

Zum Schluss möchte ich mich bei all denjenigen bedanken, die in verschiedenster Weise zu dieser Arbeit beigetragen haben:

Prof. Markus Schwoerer für die Übernahme der Erstkorrektur und sein Interesse an dieser externen Doktorarbeit,

Prof. Hans-Werner Schmidt, dem Pionier der OLED-Kombinatorik, für die bereitwillige Übernahme der Zweitkorrektur,

Dr. habil. Walter Rieß für die kompetente Betreuung, seinen unermüdlichen Optimismus und die Freiheit bei der Realisierung der „Columbus HPO“,

Hanspeter Ott, dem Namenspatron der „Columbus HPO“, für die unzähligen Stunden Arbeit daran und das gemeinsame Austüfteln von „Masken-Dreh-Wende-Schiebe-Aufdampfmechanichtsutz“ und „Verdampferzellenschiebekippklappschutzichtsutzblechmechanismus“

Meinrad Tschudy, für die vielen kleinen und größeren Ergänzungen überall im Labor, die immer flexibel und multifunktionell sein mussten,

Dr. Heike Riel für die gemeinsame Zeit seit U(h)r-Zeiten im Büro, optische Simulationen und ihre stets freundliche Hilfsbereitschaft,

Dr. Dave Gundlach für die gemeinsame Zeit an der „Columbus HPO“, die Herstellung wichtiger Proben und „his worldly wisdoms“,

Dr. Siegfried Karg für so manche Korrekturlesung und sein immer offenes Ohr für allerlei Fragen über organische Elektrolumineszenz und vieles mehr,

den weiteren Mitgliedern der OLED Gruppe Dr. Santos Alvarado, Constance Rost, Thomas Brunschwiler und Marilyne Sousa, sowie den Ex-IBMern Dr. Beat Ruhstaller und Dr. Brian Crone für Unterstützung in verschiedenster Weise,

Horst Hofmann für die Programmierung der LabView Programme zur Ansteuerung des automatischen Messplatzes,

Dr. Haijme Nakamura vom IBM Tokyo Research Lab für die Verwendung seines optischen Simulationsprogrammes und die Anpassung an HPO Matrizen,

どうもありがとう,

Dr. Paul Seidler und der IBM Corporation für die Genehmigung des nötigen „Kleingeldes“ zur Realisierung der „Columbus HPO“,

Ute Drechsler für vielerlei Hilfe im Reinraum und die frühmorgendlichen Besprechungen, den Mitarbeitern der Werkstatt und des Elektronik Service, insbesondere Peter Müller, Kurt Wasser, Simon Schefer und Jörg Schmid,

Lilli-Marie Pavka und Charlotte Bolliger für Nachhilfe in Englisch und Deutsch,

allen Mitarbeitern des IBM Forschungslabors Rüschtikon für die einzigartige Infrastruktur und die angenehme Arbeitsatmosphäre,

meinem Vater für seine langjährige Unterstützung in jeder Hinsicht,

und zu guter letzt meiner lieben Sandra (Δεα) für ihre endlose Geduld, sowie ihr Verständnis und ihren aufbauenden Zuspruch.